Liquid-injection atomic layer deposition of cerium-doped hafnium oxide dielectric films

Functional Materials Group

School of Engineering

Thesis submitted in accordance with the requirements of the University of Liverpool for the degree of Doctor in Philosophy

by

Nam Hung Pham

October 2010

Acknowledgements

During the whole of my research as a PhD student, I need to thank and appreciate the helps that I have received from many people. Although it is impossible to make a complete list here, I would like to say special thanks to anyone that might helpfully involve with me during these four years.

Firstly, I would like to express my deepest appreciations to my primary supervisor, Dr. Richard Potter. Without his help, sympathy and patience, I could have never approached this ending stage of my PhD. Moreover, as his student, I have also learnt a lot from him in many research areas, particularly with Physics issues that I have always found challenging to cope with. Furthermore, he has helped me a lot in many aspects involved with the practical work, which was another area that I have been struggling to accomplish. I am also very grateful to my secondary supervisor, Prof. Paul Chalker, for providing me invaluable advices and guidance during the whole research period to help me gain important insights from complicated matters.

I also would like to express my gratitude to many postdoctoral and research staffs that have provided me countless helps during the experimental stage. The first one is Dr. Matthew Werner, who has given me many kindly helps and assistances in acquiring MEIS data, as well as instructing and helping me a lot in problems with MEIS analysis. He also provided me many useful instructions and explanations for the electrical measurements. Likewise, I am very grateful to Dr. Kate Black and Dr. Paul Marshall for their concerns and aids during the film growth stages and film characterisations, to name but a few. I would like to say many thanks as well to Dr. Tim Joyce for providing me great assistance in AFM study, Dr Bob Murray and Dr. Simon Romani for helping me in some TEM data collection and interpretation. I also gratefully acknowledge Mr. David Atkinson for always being helpful and kind to help me out in any problems related to general practical works, especially with equipment setups and operations.

To the other PhD colleagues, I also would like to appreciate their friendly help during my research period. It has been such a great time to work and have fun with Darren Potter, Adam Clare, Peter King and Karl Dawson. Especially with Ziwen Fang, I am very grateful to him as helping me so much in acquiring MEIS data and aiding me with analysis.

I also wish to thank all of my friends here in the UK and also the ones in my country for their supports. Among them, I particularly would like to appreciate the help from Dr. Nhan Le who has kindly spent a lot of her precious time to help me edit my thesis format and setup.

Finally, I really have to say that I am greatly indebted to the members of my family. While my parents have continuously supporting and encouraging me throughout the whole period I have been away from home, my sister and her husband have provided me many warm moments either in the UK or in France. Their supports and encouragements are surely one of the most important factors that motivating me to pursuit my research in such a long time being abroad.

Abstract

The work presented in this thesis concerns studies of stabilising the higher-k phases in hafnium oxide film by cerium doping as an oversized tetravalent dopant with the aim for potential high-k oxide in future CMOS devices. Ce-doped Hf-oxide films were grown on n-type Si(100) substrates from two single source $Ce(thd)_4$ and $[(MeCp)_2$ HfMe(OMe)] precursor solutions 0.05M in anhydrous toluene at 300°C with Ozone as co-reactant by using Liquid-Injection Atomic Layer Deposition (LIALD) technique. The amount of cerium incorporated into the films was found to be proportional to the ratio of ALD cycles between two precursors, resulting in films with 5%, 8%, 10%, 17% and 34% Ce.

The microstructure studies of Ce-doped Hf-oxides were carried out for films annealed between 600°C and 1000°C in air and at 900°C in N_2 and vacuum. Results obtained from XRD and UV Raman showed that regardless of annealing environments, the dominant stabilised phase found in all films adopted a form of "metastable tetragonal" resembling closely the fluorite-type cubic phase in pure HfO_2. Films with 5%, 8% and 17% Ce were also found to contain a varying fraction of monoclinic phase. The film with 10% Ce was found to have the highest distortion from the cubic structure, especially under vacuum condition. In addition, TEM and MEIS analysis indicated that the use of vacuum was mandatory to prevent internal oxidation and intermixing between the high-k oxide film and the silicon substrate underneath.

Electrical characterisations of films with approximately 10% cerium and annealed in vacuum were investigated by using C-V, I-V and C-f measurements. The effect of vacuum annealing on these films was demonstrated in substantial improvement of frequency dispersion and significant reduction of fixed oxide charges and interface states compared to the as-grown examples. Higher leakage current density were observed in annealed films and attributed to the leakage pathways induced by crystallisation. A permittivity of 34 measured at 100 kHz was found for 23 nm thick film annealed at 900°C in 15 minutes. This result showed a good agreement with theoretically predicted enhancement of dielectric constant (k~32) by doping HfO_2 with cerium. The highest k-value of 44 was observed for a 15 nm thick film annealed at 800°C in 100 minutes. Films with respective thickness 6, 10.5 and 19.5 nm annealed at 800°C in 10 minutes were found to yield permittivity in the range between 30 and 34, which suggested a good scaling capability.

Table of contents

List of figures

List of tables

Abbreviations and symbols

α	Polarisability
Δ	Phase difference
ε''_r	Imaginary part of the complex dielectric permittivity
ε'_r	Real part of the complex dielectric permittivity
ε_0	Permittivity of vacuum
θ	Diffraction angle
$\theta/2\theta$	Bragg-Brentano geometry
λ	Radiation wavelength
μ	Carrier mobility
Φ'_m	Metal work function after contact
Φ_{fp}	Semiconductor bulk potential
Φ_m	Metal work function before contact
Φ_{MS}	Metal-Semiconductor work function
Φ_{s0}	Surface potential
χ	Electron affinity of the semiconductor before contact
χ'	Electron affinity of the semiconductor after contact
χ_i	Electron affinity of SiO_2
<Z>	Mean atomic number
A	Capacitor area
AFM	Atomic Force Microscopy
ALD	Atomic Layer Deposition
C	Capacitance density of the gate insulator
CB	Conduction band
CET	Capacitance Equivalent Thickness
C-f	Capacitance-Frequency
CMOS	Complimentary Metal-Oxide-Semiconductor
C_p	Cyclopentadienyl
C-V	Capacitance-Voltage
CVD	Chemical Vapour Deposition
d	Interplanar spacing
DRAM	Dynamic Random Access Memory

E_C	Conduction energy level
E_F	Fermi energy level
E_g	Bandgap
EOT	Equivalent Oxide Thickness
E_V	Valence energy level
fcc	Face centred cubic
FET	Field Effect Transistor
IBAD	Ion Beam Assisted Deposition
IC	Integrated Circuit
ISS	Low energy ion scattering
I-V	Current-Voltage
k, ε	Dielectric constant (permittivity)
L	Channel length
LIALD	Liquid-injection Atomic Layer Deposition
MBE	Molecular Beam Epitaxy
Me	Methyl
MEIS	Medium Energy Ion Scattering
MFC	Mass flow controller
MOCVD	Metal-organic Chemical Vapour Deposition
MOS-C	Metal-Oxide-Semiconductor Capacitor
MOSFET	Metal-Oxide-Semiconductor Field Effect Transistor
N_{av}	Average number of bonds per atom
PCSA	Polariser-Compensator-Sample-Analyser
PEALD	Plasma-enhanced Atomic Layer Deposition
R_a	Arithmetic surface roughness
RBS	Rutherford back scattering
SPM	Scanning Probe Microscopy
STM	Scanning Tunnelling Microscope
t	Oxide thickness
t', t"	Metastable tetragonal structures
tan(Ψ)	Amplitude ratio upon reflection
TEA	Toroidal sector electrostatic analyser
TEM	Transmission Electron Microscopy

thd	tetrakis (2,2,6,6-tetramethyl-3,5-heptanedionato)
t_{SiO2}	SiO_2 thickness
UHV	Ultra high vacuum
VB	Valence band
V_{FB}	Flatband voltage
V_G	Gate voltage
V_m	Molecular volume
V_{ox}	Potential drop across the oxide
V_T	Threshold voltage
W	Transistor width
XAS	X-ray Absorption Spectroscopy
XPS	X-ray Photoelectron Spectroscopy
XRD	X-ray Diffraction

Chapter 1 INTRODUCTION

The Field Effect Transistor (FET) has been the centrepiece of the semiconductor industry since it was opted for mass-production in the 1950's. Since then, the unprecedented growth and development of many important electronic devices such as logic gate, memory unit and integrated circuits (ICs) have been based on the foundation of FET. There are a number of different types of FET, but one of the most important and popular type is the Metal-Oxide-Semiconductor FET (MOSFET). The huge success of the MOSFET has in part been due to the highly compatible combination of insulating silicon dioxide (SiO_2) on top of semiconducting silicon (Si). This natural parent-child combination has provided a simple yet powerful way to increase the processing speeds of IC devices while reduce the fabrication cost over the last 40 years. The shrinkage of individual components and the growth in circuit density has happed at an outstanding and yet predictable rate, with circuit density doubling approximately every 2 years, this has led to the so called Moore's law [1]. The number of transistors on a single chip over that last four decades is the best illustration for this law: from just over 2000 transistors in 1971 up to more than one billion in 2010. This huge increase in the number of transistors per unit area would not be possible if it were not for the excellent insulating properties of SiO_2. However, it was predicted about 20 years ago that this trend would eventually reach the physical and operational limits imposed by the decreasing thickness of the SiO_2 layer. As the thickness of this insulating layer approaches a few atomic layers thick, the leakage current becomes unacceptably high and thus, leading to enormous power dissipation and device unreliability As a result, the search for alternative materials with higher permittivity than SiO_2, the so-called high-k dielectrics, began more than 10 years ago and remain an ongoing focal point today. The high-k dielectrics can help resolve the aforementioned problems with SiO_2 induced by miniaturisation because they can offer the same capacitance storage with a physically thicker insulating layer than SiO_2 due to their higher dielectric constants and hence, reduces the leakage current.

By employing a high-k dielectric in place of SiO_2, the scaling trend in MOSFETs production can be maintained without compromising the performance and cost of next-generations devices. Numerous studies, both theoretical and experimental, have been devoted to this topic and one of the most fruitful results recently was the introduction of Hf-based oxides into 45 nm node processor from Intel in 2007. Dubbed as the "first high-k generation" by the company, Hf-based devices have solved the problems of transition from SiO_2 to high-k dielectric as a current and near-term solution to the demand of the market.

To maintain the scalability of devices in the longer-term, higher-k materials will be required in addition to solutions to various other issues relating to design and production. The International Technology Roadmap for Semiconductors (http://www.itrs.net/), a global organisation created to guide research directions and address manufacturing demands in the semiconductor industry, has stated the necessity of high-k materials with substantially higher dielectric constants than Hf-based in future devices in 5-10 years to come [2].

This pressing demand has motivated numerous focused studies on higher-k dielectrics to improve electrical performances compared to HfO_2. Various types of materials, which potentially offers higher k-values compared to "first generation Hf-based dielectric", have been evaluated and assessed, for example perovskite materials such as $Ba(Sr)TiO_3$. Another approach which has also attracted much attention is the modification of the microstructures of materials such as HfO_2 and ZrO_2 using dopants. The addition of various different elements to these basic oxides can be used to alter the crystal structure, which in turn can lead to the enhancement of the dielectric constant. It is due to the fact that tetragonal or cubic phases in HfO_2 were proved to yield substantially higher permittivity than either the amorphous form or monoclinic phase, which is typically the thermodynamically stable phase found at room temperatures [3]. The pursuit of doped HfO_2 materials to increase k-value is also the main motivation of the works in this project, with the interest focusing on using cerium as a potential dopant, which was investigated among various other elements proposed from theoretical studies [4-6].

In this thesis, cerium-doped hafnium oxide films were grown using the state-of- the-art Liquid-injection Atomic Layer Deposition (LIALD). The films were then analysed using a variety of techniques to investigate how doping influences the crystal structure and electrical characteristics of these materials. The main theme of the project is the modification of film microstructures, and is reported as the effect of phase stabilisations in HfO_2 by adding cerium and its consequence on the dielectric constants of selected deposited films. The thesis will be divided into various chapters. Chapter 2 provides a literature review which will put the current work into context; it covers both the basic operating principles of MOSFET devices and also reviews the developments and issues involved with high-k materials as well as phase stabilisation. The experimental techniques used in this project are presented in chapter 3, which includes descriptions of the operational principles, data acquisition and methods of analysis. Chapter 4 is the first of two results chapters, in which the experimental results will be presented and discussed. In the first part of chapter 4, the main LIALD growth results are presented, the incorporation of cerium into the films is also discussed in light of compositional analysis using Medium Energy Ion Scattering (MEIS). The chapter also covered individual LIALD growth studies of CeO_2 and HfO_2 and the justifications in process conditions to conduct ternary oxide film growths based on the "ALD window" match of two single source precursors.
The crystal structures, phase compositions and electrical performances of these films are then presented in chapter 5. The effects of doping concentrations and annealing conditions on the microstructure and electrical properties of the films are investigated using X-ray Diffraction, UV Raman scattering, Atomic Force Microscopy, Ellipsometry, C-V and I-V measurements. Finally, chapter 6 provides a summary of the work, highlighting the main conclusions as well as providing some recommendations for future research within this particular direction.

References

1. Moore, G. E. (1965) Cramming more components onto integrated circuits. *Electronics,* **38** (8), 114-117.
2. Technology Roadmap for Semiconductors (2009 Edition): Process Integration, Devices and Structures: http://www.itrs.net/Links/2009ITRS/2009Chapters_2009Tables/2009_PIDS.pdfInternational
3. Zhao, X. and Vanderbilt, D. (2002) First-principles study of structural, vibrational, and lattice dielectric properties of hafnium oxide. *Physical Review B,* **65** (23), 233106.
4. Cockayne, E. (2008) Effect of ionic substitutions on the structure and dielectric properties of hafnia: A first principles study. *Journal of Applied Physics,* **103**.
5. Fischer, D. and Kersch, A. (2008) The effect of dopants on the dielectric constant of HfO_2 and ZrO_2 from first principles. *Applied Physics Letters,* **92** (1).
6. Lee, C. K., Cho, E. N., Lee, H. S., Hwang, C. S. and Han, S. W. (2008) First-principles study on doping and phase stability of HfO_2. *Physical Review B,* **78** (1).

Chapter 2 LITERATURE AND BACKGROUND

2.1 Introduction

The last 50 years have seen the huge development and massive growth of the semiconductor industry since it was formed as a viable business in 1960. At the heart of this unprecedented success, the Complementary Metal Oxide Semiconductor (CMOS) Field Effect Transistor (FET) has been undoubtedly the key player. This very "basic" electronic component is the cornerstone of microprocessors and memory units amongst many other important applications. The dominance of this electronic device is due to its low power consumption and because of its performance improvement over 40 years according to Moore's Law of scaling [1]. This law predicts that the aerial density of devices on an integrated circuit increases exponentially, doubling over a 2–3 year period and the minimum feature size in a transistor decreases exponentially each year. This empirical law still holds true today and dictates the development of this industry in the foreseeable future. The *International Technology Roadmap for Semiconductors* (IRTS) maps out the technology milestones, projected performances and future demands for research, development and production. This online document is revised annually as a guide for the whole industry to maintain its healthy position in the market [2].

Until very recently, the huge success of the whole semiconductor industry has been mainly relying on one simple system, Si/SiO_2. As a semiconductor, Si is just only an average quality choice among others. However, it does have the benefit of having a high quality oxide form, which can act as an insulator, is easy and cheap to produce and is very stable on top of the silicon itself. As an insulator, SiO_2 possesses many excellent properties such as large band gap, good thermal stability, low defect concentrations and easy-to-grow by thermal oxidation to name but a few. Additionally, this native oxide enables device improvements in terms of speed and cost to be achieved quite simply by scaling down the device dimension as proposed by Moore's law.

Nevertheless, the scaling of SiO_2 has now already reached its limit thickness (~2 nm) [3] and hence, needs to be replaced to keep the conventional device-scaling scenario still practical and economical. The main reasons why the much needed replacement(s) of SiO_2 has been so important is the problem of increasing carrier leakage as the dielectric layer thickness decreases. Carrier leakage occurs due to quantum tunnelling and direct leakage and results in increasing power consumption and ultimately, failure of the devices. In fact, the search for alternative high-k dielectric materials has already been going on for at least last 10 years [4] and remains an important research topic within both academic and industrial groups.

This chapter thus will present and discuss many issues involved with such a process from literature with a specific concentration on Hf-based materials. Firstly, the basic structure of CMOS devices and their operation is discussed as a background for particular focus on insulator layer afterwards. The requirements and issues of high-k materials are then discussed along with a details review of recent work in this field. The concepts behind the stabilisation of crystalline oxide phases using dopants, with a particular focus on Ce-doped HfO_2, is then discussed, which is central to the work that has been carried out here. Finally, the chapter concludes with a discussion about the various deposition techniques that can be used for thin film dielectric deposition, with a particular focus on atomic layer deposition (ALD).

2.2 MOS device technology

2.2.1 MOSFET: basic structure and function

Firstly, consider the typical structure of a n-type MOSFET as illustrated in Figure 2-1.

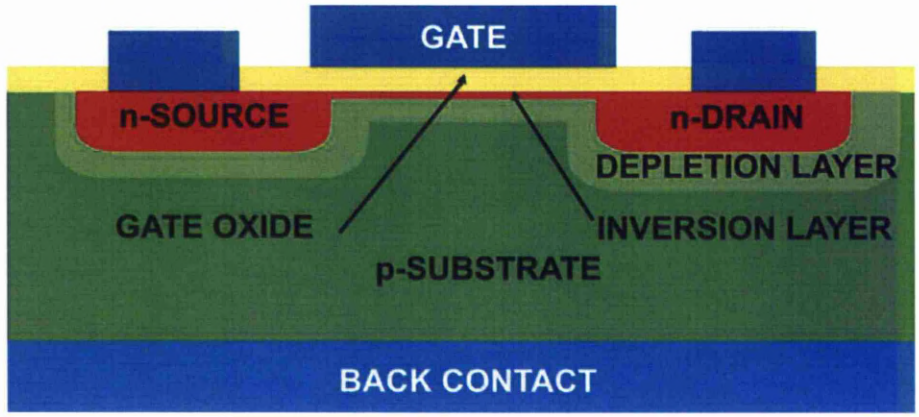

Figure 2-1: Cross-sectional diagram of an n-type MOSFET [5].

As can be seen from the diagram, an n-type MOSFET consists of a source and a drain which are two highly conductive n-type semiconductor regions. The term n-type refers to the negative charge of electrons, which are the main type of charge carriers flowing between the source and the drain when the device is operated. The complementary p-type device uses positively charged holes as carriers instead, but for the time being, let us just concentrate on the n-type MOSFET. The source and drain regions form p-n junctions with the p-type substrate and as a result, are isolated from the substrate by the depletion regions that naturally form. The source and drain are separated spatially from each other by the gate region, which is essentially a MOS-capacitor structure. Without gate bias, the area under the gate forms another depletion region, and as a result, the source and the drain are electrically isolated from each other. Together, this effectively creates the source-channel-drain circuit that forms a p-n-p junction and hence, inhibits current flowing in either direction through the p-type channel. A metal or poly-crystalline Si gate covers the region between source and drain .The gate is separated from the semiconductor by the gate oxide, typically SiO_2.

A MOSFET is "on" when the inversion layer, i.e. an electrically conductive path, is formed along the channel between the source and drain. A voltage (positive in the case of an n-type device) applied to the gate creates an electric field and controls the flow of electrons from the source to the drain. Firstly, the electric field generated by this applied gate voltage concentrates the electrons at the interface between the semiconductor and the gate oxide.

When this electric field is strong enough, a conducting channel is formed due to the accumulation of minority charge carriers (electrons in this case), which produces an inversion layer. Once this inversion layer has formed, electrons can flow freely between the source and the drain. In order to create and maintain this electric field, an insulating layer (the gate oxide in this case) is necessary to separate the source, the drain and the channel. Thus at a fixed operational voltage, the electric field strength in the inversion layer varies proportionately with the dielectric constant of the oxide and inversely with the oxide's thickness. As mentioned before, due to the scaling trend, the device dimension has been shrinking continually and hence, so has the oxide thickness (SiO_2) to maintain the required capacitance. This, however, has a practical limit due to the reduction of the oxide thickness still has to be in the region of a few nanometres. Beyond this thickness, quantum effects such as electron tunnelling (Fowler-Nordheim) [1] are so severe that they render the device unserviceable.

2.2.2 MOS physics

In this section, key physical principles and parameters of MOS devices for both MOS-C (MOS Capacitor) and MOSFET operations are explained alongside some other issues involved, particularly the effect of device scaling.

2.2.2.1 Accumulation, depletion and inversion

Consider an nMOS capacitor structure formed on a p-type Si substrate and under various gate bias conditions as shown in Figure 2-2.

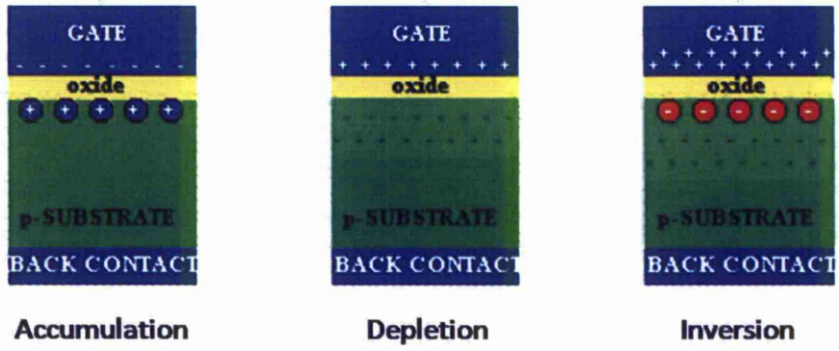

Figure 2-2: Charge distribution in an nMOS with different bias voltages [5].

Accumulation occurs for when a negative voltage is applied to the gate, the negative charge on the gate attracts holes from the substrate to the oxide-semiconductor interface. Depletion occurs when the applied voltage becomes positive as the major charge carriers (positive holes) in the substrate are repelled away from the interface. As this happens, the semiconductor immediately under the gate oxide is depleted of mobile carriers and a negative charge, which is formed by the ionised acceptor ions, is created in this space charge region. Inversion occurs if the applied voltage exceeds a critical value, namely the threshold voltage (V_T). In inversion, the electric field starts to attract minority charge carries from the bulk of the substrate, towards the oxide/semiconductor interface, this charge builds up to form an inversion region.
The voltage separating the accumulation and depletion regime is referred to as the flatband voltage, V_{FB}. The concept of V_T and V_{FB} will be discussed after the definition of Metal-Semiconductor work function (Φ_{MS}) in the next section.

2.2.2.2 Metal-Semiconductor work function (Φ_{MS})

The Metal-Semiconductor work function (Φ_{MS}) is normally referred in literature simply as work function. It is the energy difference required to remove an electron from the Fermi level to vacuum for the metal and the semiconductor respectively. To illustrate this term visually, an energy band diagram for an nMOS structure is shown at thermal equilibrium, (i.e. the Fermi levels of the metal and the semiconductor are equivalent) in Figure 2-3. The band structure is shown before and after the contact is established to illustrate how the band energies are modified. As can be seen in Figure 2-3 (b), the band energies of the Si bend towards the semiconductor-oxide interface after the contact.

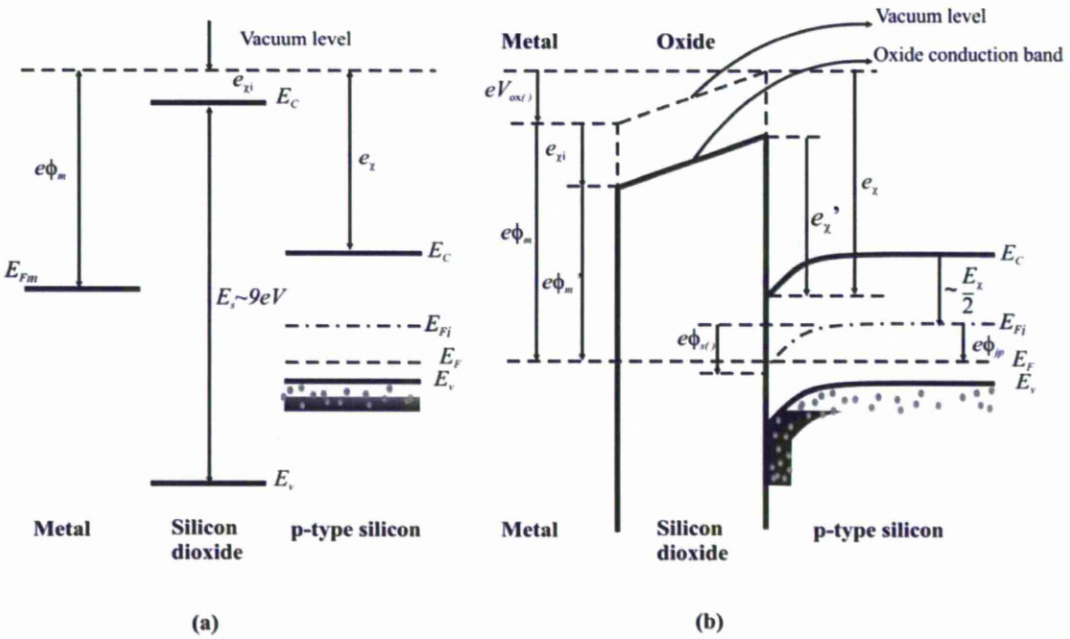

Figure 2-3: Band diagram of an nMOS structure before (a) and after (b) the contact (at zero gate voltage applied) [6].

Where: E_{Fm}: Metal Fermi level of, E_{Fs}: Semiconductor Fermi level, E_{Fi}: intrinsic energy level,

($E_{Fi} = (E_C+E_V)/2$, E_C: Conduction energy level, E_V: Valence energy level, Φ_m and Φ'_m: metal work function before and after contact, χ and χ': electron affinity of the semiconductor before and after contact, χ_i: electron affinity of SiO_2, V_{ox0}: potential drop across the oxide, Φ_{s0}: surface potential.

2.2.2.3 Flatband voltage (V_{FB})

Flatband voltage is a term that referred to a value of applied gate voltage that inducing no band bending in the semiconductor. At this voltage, there is zero potential at the semiconductor/oxide interface, all energy bands become flat (flatband condition). Because of the work function difference and possible trapped charges in the oxide, the voltage that exists across the oxide layer is not necessarily zero in practice. Figure 2-4 shows a band diagram for an nMOS structure at flatband voltage.

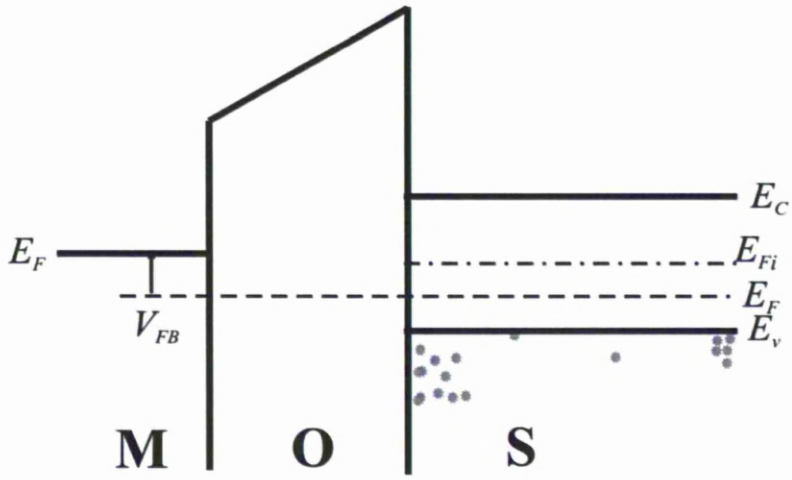

Figure 2-4: Energy band diagram for an nMOS capacitor at flatband condition [6].

2.2.2.4 Threshold voltage (V_T)

The threshold voltage (V_T) of a MOSFET is defined as the gate voltage where an inversion layer forms at the interface between the oxide and the semiconductor substrate. Effectively, this inversion layer will allow current flows between the source and the drain under an applied voltage and hence, the device switches on. In a MOS structure, this voltage is the specific value required to achieve the threshold inversion point. By definition, the threshold inversion point is the condition when the surface potential Φ_s is twice the value of the semiconductor bulk potential (Φ_{fp}). Figure 2-5 presents band diagram of an nMOS structure under threshold conditions. For a given semiconductor, oxide and gate material system, the value of V_T is a function of the doping of the semiconductor, the oxide thickness and charges. Because this value is very important in order to define the operations of the MOSFET, i.e. "on" or "off" state, it is of great concern in device design.

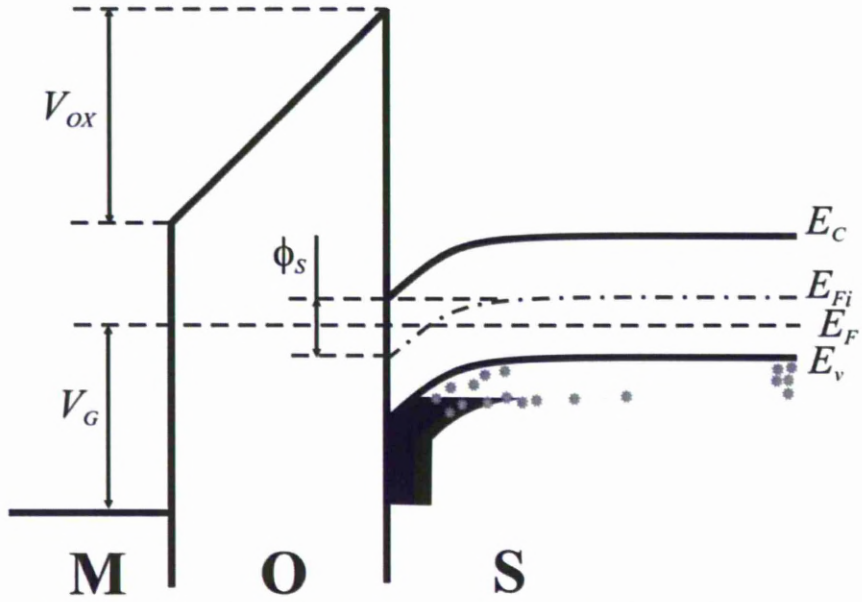

Figure 2-5: Energy band diagram of an nMOS structure at threshold voltage [6].

V_G: threshold voltage, V_{OX}: voltage across the oxide at the threshold inversion point.

2.2.2.5 Device scaling

Device scaling has served to increase processing speed while reduce the cost of manufacturing. It is done by increasing the number of transistors per unit area, thus improving the performance by offering higher device density and device operating frequency while reducing power consumption. One key parameter that dictates the speed of a MOSFET is the saturated "ON" current, this can be estimated by equation 2.1 [6]. This equation relates the drive current to the physical parameters of the MOSFET as well as its operational parameters as follows.

$$I \approx \frac{W}{2L}\mu C\left(V_g - V_T\right)^2 \qquad \text{(Equation 2.1)}$$

Where W: transistor width, L: channel length, μ: carrier mobility, C: capacitance density of the gate insulator, Vg: gate voltage, V_T: threshold voltage.

The capacitance density of the gate insulator can be approximated as:

$$C = \frac{k\epsilon_0}{t} \qquad \text{(Equation 2.2)}$$

k: relative permittivity of the oxide, ε_0: permittivity of vacuum, t: oxide thickness.

As the device shrinks, to maintain a constant drive current requires either an increase in the capacitance of the oxide layer or an increase in the difference between the gate voltage and the threshold voltage. However, in practice, the latter case is considered as very limited due to electrical problems. To increase the difference between the gate voltage and the threshold voltage either requires an increase in gate voltage or a decrease in threshold voltage. While a very high gate voltage can result in undesirable field effect across the device, a low threshold voltage will eventually prevent the device from operating as the difference between on and off states becomes negligible. These factors effectively render the option of increasing the capacitance as virtually the only practical option. In fact, such approach has been favourably utilised in MOS structures with SiO_2 employed as oxide insulator simply by reducing the thickness of the SiO_2 layer. However, as this thickness approaches about 1.5 nm [1, 7], many serious problems occurs. Severely high leakage currents due to tunnelling effect were reported [1, 4, 7, 8], which creates serious problem for power dissipation, especially in low-power and portable devices. Moreover, this issue also accelerates the degradation of the very thin SiO_2 film and eventually leads to electrical breakdown. Therefore, the need for high-k materials to replace SiO_2 is the most practical way to mitigate the limitations of this capacitance increase approach. The higher dielectric constant enables thicker dielectric layer to be used while still maintaining the desirable value of capacitance. The physically thicker layer reduces the problem of tunnelling and other issues confronted with SiO_2 scaling. However, simply replacing SiO_2 by high-k dielectrics is not the entire answer to the aforementioned problem. In the following sections, issues involved with high-k materials will be discussed, mainly from the material selection viewpoint. The integration into the conventional MOSFET structure is also briefly explained, which has been so far one of the most challenging issue particularly within industrial research in this field.

2.3 High-k dielectric materials

In order to maintain the stringent requirements from the market and its own development governed by the Moore's law, the semiconductor industry has no choice but to look for an alternative high-k dielectrics to replace SiO_2, at least for the near and medium- term future.

It has been proposed [4] that to replace traditional MOS structure which employs SiO_2 as gate dielectric, a new structure has to be developed to accommodate the high-k materials used as next-generations gate dielectric. Figure 2-6 shows a gate stack which illustrates all of the main components that are required to ensure that the high-k dielectrics perform in the desired way.

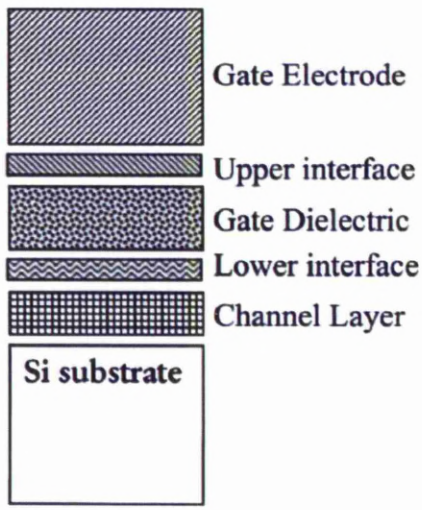

Figure 2-6: A schematic view of a MOS structure utilising high-k material as gate dielectric[4].

Many issues involved with high-k materials and their influences on gate stacks will be outlined in the following sections. The physical principle behind obtaining high dielectric constants is firstly discussed as it is the starting point of the whole research theme Important considerations that affect the desirable properties of the high-k prospects are then outlined. A review of some of the main groups of materials that have recently been investigated or emerged as prospective gate dielectrics is also given.

2.3.1 Physics of high-k dielectrics

For normal dielectric materials (non-ferroelectric), the overall electric polarization can result from a combination of up to four physical components [9]. They are electronic, ionic (also known as lattice vibration), orientational and space charge polarisation. Figure 2-7 shows the AC frequency response of a dielectric to illustrate the contributions of these different mechanisms to the overall polarisation.

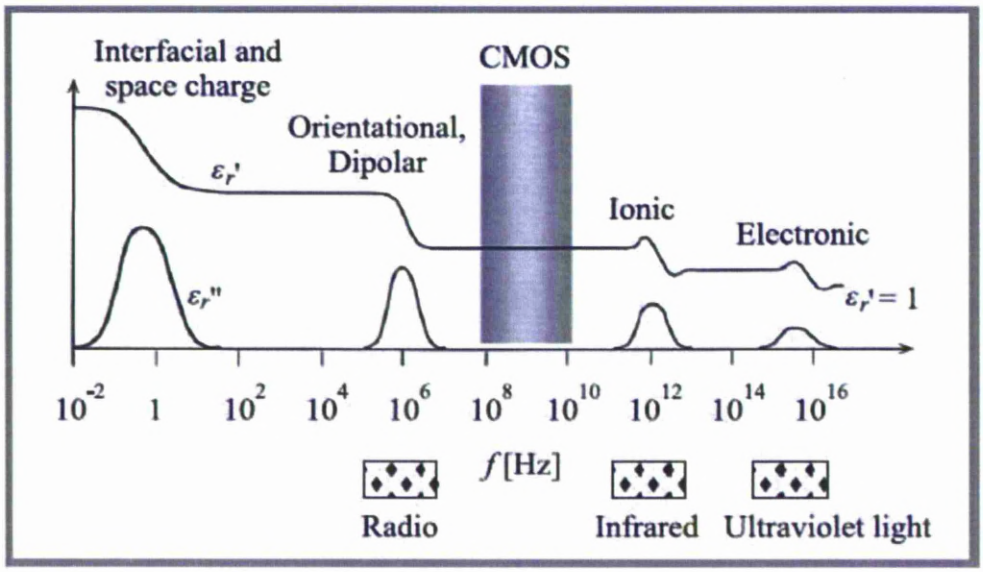

Figure 2-7: The frequency dependence of different polarisations to the dielectric function ($\varepsilon_r = \varepsilon'_r r + i\varepsilon''_r$, where ε'_r is the real part and ε''_r– imaginary part of the complex dielectric permittivity) with respect to the CMOS "window" [10].

As Figure 2-7 illustrates, the two attributes of polarisations for any insulating materials suitable for CMOS application will be from ionic and electronic contributions. Basically, an atom with large atomic radius, such as those with a high atomic number, will generate a large electronic polarisation in response to the external electric field [4]. However, this contribution is only limited to an extent. It has been shown [8] that the electronic contribution to the overall dielectric constant is typically less than 16. Moreover, quantum treatment of the electronic polarisability [9] shows that the larger this contribution to the material, the smaller the band gap will be. This has been experimentally observed by many researchers [1, 8, 11].

The bandgap of the dielectric materials is another important consideration for high-k materials research. A large bandgap is desirable to ensure that charge carriers cannot get over the potential barrier produced by the dielectric layer. As a result, increasing the dielectric permittivity by increasing the electronic contribution is not entirely desirable as it results in a reduced bandgap, which leads to carrier leakage. Therefore, in order to look for high-k dielectrics, materials with a large contribution from ionic (lattice) component have been paid a great attention. This tendency is included within the well-known Clausius-Mossoti equation (equation 2.3) [11], showing the dependence of the overall dielectric constant on material properties.

Figure 2-8 presents results of a recent study about the variations of dielectric constant against the mean atomic number, <Z>, for rare-earth oxides and other neighbouring elements in period 5 and 6 of the periodic table. This trend implies the role of molecular volume besides the polarisability, especially in terms of different crystal structures for a given oxide.

$$k = \frac{1+\frac{2}{3}4\pi\frac{\alpha}{V_m}}{1-\frac{1}{3}4\pi\frac{\alpha}{V_m}} \qquad \text{(Equation 2.3)}$$

α: polarisability, V_m: molecular volume

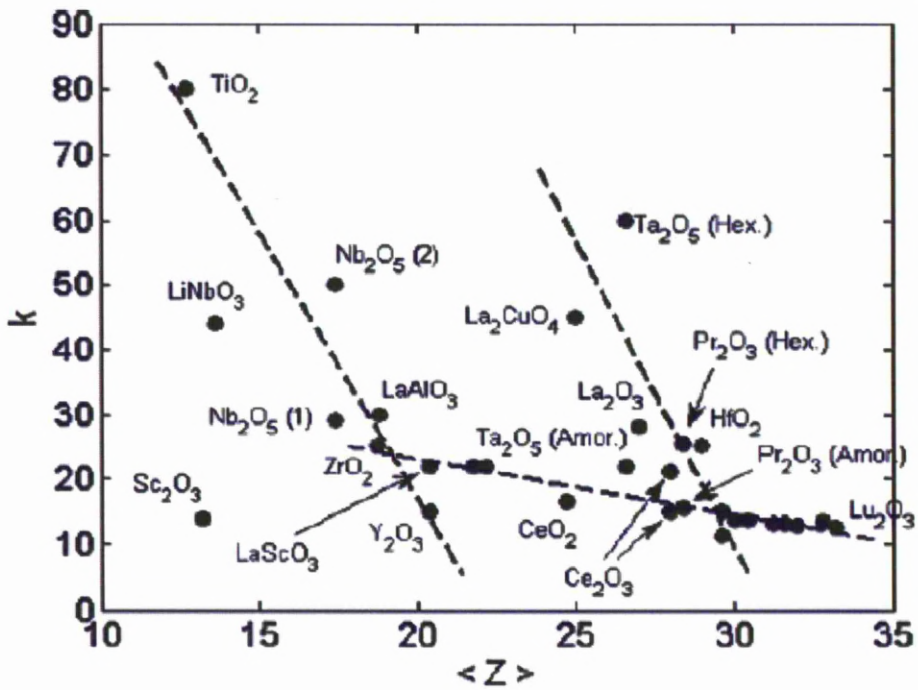

Figure 2-8: Variations of dielectric constants k of various potential oxides as function of mean atomic number <Z> [11].

Essentially, the enhancement in ionic contribution to the overall dielectric constant can be found via two main groups of materials. The first one, namely perovskite crystals, consists of materials with ferroelectric property such as (Ba, Sr)TiO_3 and (Pb, Zr)TiO_3. Below the Curie temperature, the Ti atoms in each unit cell of the crystal are uniformly displaced in response to an applied electric field and hence, it is possible to generate a very high polarisation throughout the material.

As a result, very high k-value can be achieved, values up to several thousands have been reported [1, 4]. In the other group of potential candidates (transitional oxides/ rare earth oxides and their aluminates or silicates), the rise in the dielectric constant can be achieved by a different approach. Instead of relying on ionic polarisation as in the case of perovskites, these materials can generate polarisation by some forms of lattice vibrations, hence the name lattice polarisation. This phenomenon can be explained by the effect of soft phonons [4]. Atoms with large number of electrons can resonate in their bonding structures at low vibrational frequency modes, which produce a so-called soft phonon mode. These phonons then make a lattice contribution to the overall polarisability, and therefore to the permittivity of the material. This trend has been demonstrated mathematically in [1], which paves the way for modelling and first-principle calculations for various high-k oxides.

2.3.2 Properties required for high-k gate dielectrics

It has been generally agreed that a high-k gate dielectric has to pass multiple criteria to be integrated successfully into modern CMOS devices. Although disparities exist among different authors or between academic and industrial approach, essentially the group of critical properties can be divided into 3 main classes [7]. Class I refers to basic properties as a dielectric, which includes the permittivity and the band gap. Class II relates to the processing of the materials and devices, and includes factors relating to interface quality and deterioration of the various gate stack layers during processing. Class III relates the choice of the dielectric for the overall performance in a microelectronic device. Obviously, there are some interdependence and scope for compromise especially when the huge cost of past investment and preference to maintain the manufacturing flow processes in the semiconductor industry are concerned. All of these key demands will be presented in the following sections; together these will form a framework to assess any prospect high-k material of interest from different perspectives.

2.3.2.1 Dielectric permittivity and band gap/band offset constraint

Because the primary reason behind the search for high-k dielectrics is to replace SiO_2 (k=3.9) to enable future scaling, a high value of dielectric constant is desirable.

However, for a material to act properly as a gate dielectric, it must also have a reasonably large band gap (in consideration with SiO_2 offering a band gap ~ 9eV). Unfortunately, many high-k materials have been shown to have relatively small bandgaps; their band gaps are inversely proportional to their dielectric constants. Figure 2-9 demonstrates this trend for many different candidates.

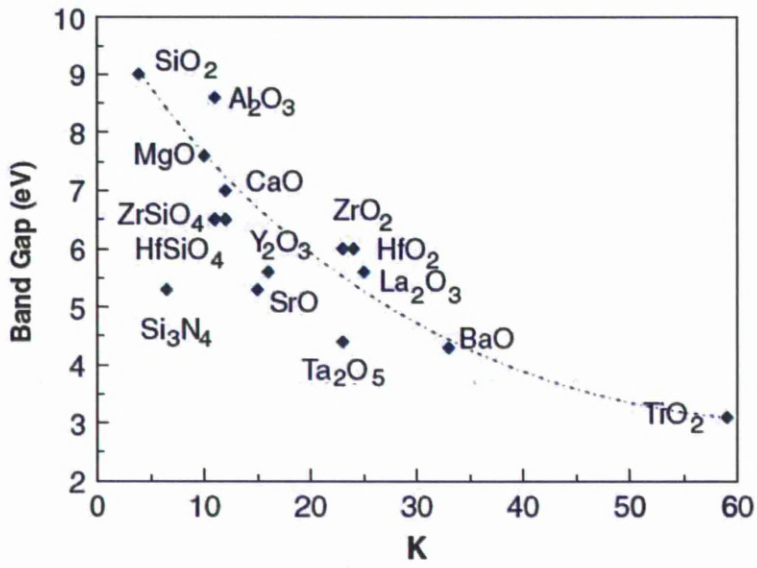

Figure 2-9: Variations of band gaps against dielectric constants for various high-k materials [1].

As can be seen from this figure, Al_2O_3 can offer very large band gap but quite small k-value while TiO_2 can offer quite high k-value but suffer from a small band gap. Some other potential oxides, namely ZrO_2, HfO_2 and La_2O_3 locate somewhat in the middle of the trend-line curve. In fact, these oxides have been the most extensively investigated candidates to date, probably because they offer the acceptable compromise between dielectric constant and band gap.

It has been pointed out that for the near term future, a material with a k-value between 25 and 30 is desirable [1]. However, it has to be kept in mind that the choice for a value of dielectric constant is also strongly dependent on the structure of the gate stack [4, 8]. If, let say a high-k simply replace SiO_2 in a conventional MOS structure, than a medium k-value mentioned above or even slightly lower is sufficient for a number of years to come.

However, if a low-k interlayer needs to be inserted between the gate dielectric and the semiconductor substrate reduce the density of interface states that can affect device performance, higher k-values may be necessary as demonstrated by Eisenbeiser [8]. In fact, very high-k materials attracts a great attention when the application of DRAM is concerned rather than the gate dielectric for microprocessors. Materials such as $SrTiO_3$ or Ta_2O_5 [12] were reported to have very high-k values, but offer very low band gaps. For gate dielectric application, very high-k materials are not desirable not only because of their unacceptable low band gaps but also because such very high k-values will create undesirable phenomena in device operations, such as short channel effects [1, 8]. Moreover, high-k dielectrics based on perovskites are ferroelectric materials, which mean they are very sensitive to temperature, operating conditions and material properties.

Besides a reasonable band gap ($E_g \geq 5eV$) to ensure the dielectrics function properly, it is also noteworthy that the band alignments, i.e. the band offsets for conduction and valence bands of the oxide with respect to Si, are of great importance. SiO_2 is considered an excellent insulator because aside from a very large band gap it also has large band offsets with respect to the silicon [8]. When the thickness of the dielectric layer is increased by employing a high-k material, tunnelling leakage will be significantly reduced. However, another form of potential leakage can affect the function of the device severely, namely thermionic emission current [8]. This leakage mechanism can be explained by the injection of electrons to the conduction band or holes to the valence band of the insulating layer from the silicon. To prevent this, the potential barrier at each band must be over 1 eV in order to inhibit conduction by the Schottky emission of electrons or holes into the oxide bands.

In practice, it has been found that the conduction band (CB) offset is typically smaller than the valence band (VB) offset [1]. Figure 2-10 shows various calculated band offset values for a range of potential high-k materials. The CB offset is one of the important criteria used to screen out candidates, especially at the early stage of modelling and theoretical calculations from first-principles.

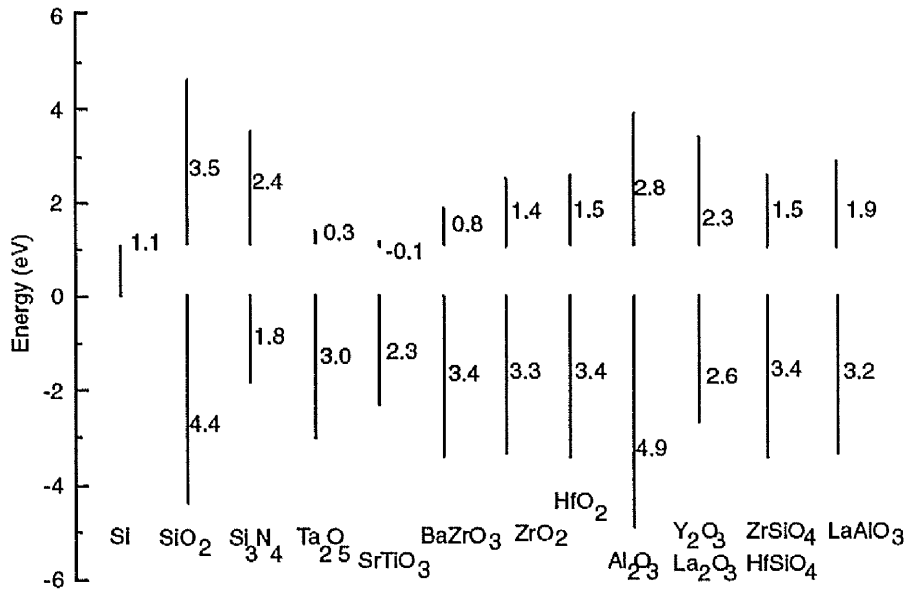

Figure 2-10: Calculated CB and VB offsets with consideration to Si [1].

2.3.2.2 Thermodynamic stability

If the high-k film is in direct contact with the silicon substrate, then the interface with between the two plays a key role in determining the overall electrical properties of the devices. It is also important that this high-k film remains stable in terms of its microstructure and unwanted phase transformation during processing and operation. Given the fact that most of the potential candidates are transition-metal oxides or rare-earth oxides and many of them undergo phase transformations from amorphous to polycrystalline forms, this issue is even more complicated and challenging in terms of integrating such prospective materials into current CMOS process flows.

Firstly, consider some possible reactions that can happen between Si and a simple oxide. Navrotsky [8] has carried out extensive work on the thermodynamics of relevant oxides and considers a wide range of these reactions. These reactions can be grouped as follows.

- Substrate oxidation

$$ySi + A_xO_y \rightarrow SiO_2 + xA$$

- Formation of silicide or/and silicate

$$Si + A_xO_y \rightarrow A_xSi + SiO_2$$

$$Si + A_xO_y \rightarrow A + A_xSiO_y$$

$$Si + A_xO_y \rightarrow A_xSi_y + A_xSiO_y$$

- silicate layer formation, due to a very thin SiO_2 interlayer either (i) intentionally left on the Si substrate to aid the high-k film growth or to improve the electrical performance or (ii) oxygen diffusion through the dielectric layer during film growth or annealing in an oxidising environment or with traces of oxygen via the reaction:

$$Si + A_xO_y + O_2\ (gas) \rightarrow SiO_2 + A_xO_y$$

that eventually leads to the formation of either amorphous or crystalline silicate:

$$SiO_2 + A_xO_y \rightarrow A_xSiO_y$$

- During processing at low oxygen pressures, oxygen deficient dielectric oxides may form. These oxides will have different thermodynamic properties to the fully oxidised materials. In addition, SiO gas may also form and diffuse through the oxide thin film:

$$Si + A_xO_y \rightarrow A_xSi_y + SiO\ (gas)$$

The reactions mentioned above can happen individually or in succession depending on the types of oxides and/or the processing conditions. In contrast to SiO_2 that can be formed easily by thermal oxidation, all the oxides have to be deposited, mostly under non-equilibrium conditions. This factor, coupled with the subsequent processing steps, many of which involved high temperatures that the material will be exposed to during device fabrication, may add more complexities to the control of the desired composition and/or phase(s). Main concerns regarding this issue will be discussed in terms of the oxidation of Si substrate and the formation of silicate.

The problem with silicide formation has been much less researched compared to the other two and data are scarcely addressed in literature.

The oxidation of the silicon substrate during high-k film growth or subsequent annealing processes is quite a major issue, particularly for oxides such as ZrO_2, HfO_2 and CeO_2. The last one is well-known for its high oxygen conductivity and thus is used in fuel cell [13, 14]. For transitional metal oxides like ZrO_2 and HfO_2, it has been reported that they have quite high oxygen diffusivity [1, 4]. Although HfO_2 and to a lesser extent ZrO_2 are considered quite stable in direct contact with silicon [8], this potentially high level of oxygen transportation through the films is still a concern. Another potential problem has been found with some oxide films, particularly those deposited by Atomic Layer Deposition (ALD), is excessive oxygen or sometimes, trapped water [1, 8] (as water is the most typical oxidant used in ALD). The role of water or other OH-groups to the oxidation of Si is still not clear. However, it has been shown that excessive oxygen from the HfO_2 film can be responsible for the growth of a SiO_2 interlayer [15] even when the film was annealed in ultra pure N_2. For rare-earth (RE) oxides, it is well-known that they are highly hygroscopic with La_2O_3 being the most hydroscopic [16]. La_2O_3 also has a high affinity with CO_2 and at intermediate temperature, can form an amorphous by-product with water vapour, which in turn can be decomposed at higher temperatures[8]. It has been speculated about the use of RE oxides in modern CMOS devices due to their nature as excellent catalysts though various reported experimental data seem to support thermodynamic stability with Si [17]. RE oxides can catalytically decompose O_2 into atomic oxygen, which may in turn promote internal oxidation of the silicon to form a SiO_x interlayer.

The formation of a silicate layer between the high-k oxide and Si substrate is somewhat less serious than the SiO_2 interlayer. It is due to the fact that to form such silicate compounds, most of the potential high-k oxides typically need to react first with Si to create an intermediate SiO_2 layer. Therefore, most of the efforts to maintain a sharp interface between high-k oxide and Si substrate have concentrated on the inhibition of such SiO_2 layer or any Si-based components.

A number of solutions have been proposed to prevent silicate formation including the using a barrier layer sandwiched between the high-k oxide and Si substrate to reduce the diffusion of oxygen (see Figure 2-6) or "alloying" the high-k oxide with some other element to form more stable compounds such as aluminates or oxy-

nitrides [1]. However, the latter case will reduce the k-value substantially because such stable compounds normally have quite lower k-values and hence, are less favourable.

2.3.2.3 Film characterisations

Beside its large band gap and band offsets with Si, amorphous SiO_2 also forms a very good interface with Si, resulting in a low interface state density as well as a low bulk fixed charge density [1]. Moreover, the microstructure of SiO_2 is very stable over a wide range of thermal conditions and operational environments, both in the bulk of the film and at the interface with Si. All of these excellent characteristics highlight many challenges that exist for next generation high-k materials to overcome if they are to replace SiO_2. As a result, the understanding and the ability to control the microstructure of high-k materials play a major role in determining and optimising the high-k gate stack. Main concerns of film microstructure are morphology, interface quality and defects. The influence of these factors will be outlined and discussed in this section.

It has been argued that amorphous films are superior to a polycrystalline one with grain boundaries for a couple of reasons [4, 8]. The main concern with a polycrystalline film is the potential leakage currents and possible diffusion paths for dopants provided by grain boundaries. In addition, grain size and orientation changes throughout a polycrystalline film can cause significant variations in the local permittivity, leading to undesirable and unstable properties during processing flows and operations. Unfortunately, most of the oxides considered as potential candidates, e.g. HfO_2, ZrO_2 or La_2O_3, suffer from crystallisations, either during the growth or during subsequent processing at elevated temperatures. Moreover, many of them show phase separations or alterations even at intermediate temperature compared to the thermal budget found in CMOS annealing (typically 1000°C, 5 seconds) [1, 7, 8]. The problem is further complicated because in thin film, the kinetics of crystallisations can be very different from the kinetics of bulk materials and hence, may introduce various non-stoichiometric or metastable compounds co-existing with the desired composition and/or phase [18]. However, reports on the leakage currents of amorphous and nanocrystalline HfO_2 [1, 3, 19] indicate that the difference is only

minor. Therefore, it is still a debatable issue which phase is preferable for these types of oxide. The divergence of ideas also has been demonstrated in industrial preferences. Whereas companies such as Intel and Freescale choose to pursuit binary oxides because of their higher k, Texas Instruments favours lower-k silicates due to their easier integration and lower trap densities [1]. Hence, it is important to put the use of any potential high-k oxide in the context of the gate stack structure. If a barrier layer is used (typically N-based compounds), then the use of pure binary oxides should not be a problem and the choice is thus expanded. However, this comes at the price of introducing a complicated gate structure and possibly potential problems in terms of interface control. If the absolute emphasis is to retain the amorphous phase, the choice is limited only to either silicates or aluminates due to the fact that SiO_2 and Al_2O_3 are good glass formers. By "alloying" high-k oxides with either SiO_2 or Al_2O_3, the resulting compounds can have high crystallisation temperatures and will remain amorphous after device processing while still offer higher dielectric constants than SiO_2. Moreover, by adjusting the composition, the k-values can be gradually increased because for silicates and aluminates, the dielectric constants of the compounds were reportedly to roughly follow the rule of mixture [1, 4]. Between these two, aluminates seems to be the preferred choice because they offers higher permittivities than the silicates [1]. Nevertheless, silicates and aluminates still have relatively low k-values compared to their oxide counterparts and thus only offer limited scalability.

A crucial objective of any potential high-k gate dielectric is to achieve and maintain a sufficiently high-quality interface with the Si channel and ideally, as close as possible to that of SiO_2. Compared to SiO_2, most high-k oxides reportedly have one to two orders of magnitudes higher interface state density [4]. In fact, the quality of the interface has been demonstrated empirically to be influenced by bond constraint expressed by the term the average number of bonds per atom, N_{av}. Defect density increases proportionally with a corresponding degradation in device performance when $N_{av} > 3$ [4]. Metal oxides with high coordination number such as Ti or Ta are thought to create an over-constrained interface with Si while other having less co-ordination numbers such as Ba or Ca will in contrast, create under-constrained interface in their corresponding oxides. Any oxide that can create an over- or under-constrained interface with respect to Si is expected to result in a large density of

defects near the interface, which in turn results in poor electrical properties. According also to Wilk et al [4], these bonding constraints are critical to the silicide formation in the gate dielectric or even to any M–Si bonding (not necessarily a full silicide phase). The unfavourable bonding conditions that are found in any kind of silicide bonding will lead to potential leakage current and degradation of electron mobility. Therefore, it is desirable to have no metal oxide or silicide phases present within the proximity of the channel interface. Robertson has pointed out some key advantages of amorphous high-k oxide film as a gate dielectric [1] in terms of interface quality. Firstly, it provides the most cost-effective solution and is the most compatible with the existing process. In addition, an amorphous oxide can significantly reduce the number of interface defects by configuring its interface bonding. As previously mentioned in the issue of morphology, it is possible to gradually vary the composition of an amorphous oxide without creating a new phase; for example as in silicate alloys, or interfacial layers, or when adding nitrogen. Additional advantages of using amorphous oxides include the isotropic nature of the material which results in uniform permittivity and the absence of grain boundaries, which reduces carrier scattering. The main disadvantage of amorphous oxides is the low-k values of such materials. If the k-value is the first priority, epitaxial oxides grown on Si can provide the solution. The main issue with epitaxial oxides currently is the films have to be grown by Molecular Beam Epitaxy (MBE) technique. This process is quite complicated, costly and not popular in semiconductor industry.

As a result, it turns out that in order to improve the interface quality a buffer layer between the dielectric and Si is currently a realistic solution. So far, SiO_2 interlayers a few Angstroms thick are used as buffer layers in high-k gate stacks. This layer is beneficial to the use of high-k oxide for two main reasons. Firstly, it can help the growth of the high-k oxides by providing nucleation sites, particularly if ALD is used and HfO_2 is the oxide of choice [20]. The SiO_2 layer also improves the overall electrical quality of the Si-oxide interface [1] due to its high quality interface in contact with Si. A SiO_2 layer also separates the Si channel from the high-k oxide and hence, it can reduce the problem with reduction in carrier mobility due remote scattering. However, this SiO_2 buffer layer also has some disadvantages, of which the biggest is the influence on Equivalent Oxide Thickness (EOT).

EOT is a term used to compare the dielectric performance of the high-k material with the performance of SiO_2. It shows the thickness of SiO_2 (t_{SiO2}) that would be required to obtain the same gate capacitance as the one obtained with the physically thicker high-k material ($t_{high\text{-}k}$). If a thin interlayer of SiO_2 is added to the gate stack, then it acts as a second capacitor in series with the high-k layer. Consider a 2-layer MOS capacitor comprising of a SiO_2 layer in series with a high-k film.

The overall capacitance can be described as:

$$\frac{1}{C} = \frac{1}{C_{SiO_2}} + \frac{1}{C_{high-k}} \qquad \text{(Equation 2.4)}$$

which will lead to:

$$CET = t_{SiO_2} + t_{high-k} \qquad \text{(Equation 2.5)}$$

Thus, an extra SiO_2 layer is undesirable as it adds to the overall EOT and hence, reduces the scalability. This problem can be somewhat mitigated by (i) using oxides with higher k-values (up to a point) to compensate for the loss of EOT caused by the SiO_2 interlayer, (ii) replacing SiO_2 with some other buffer layers which either have higher k-values than SiO_2 and/or exhibit better barrier. In the first case, it still requires extreme care to be able to control the thickness of the intentional SiO_2 layer. As mentioned before, many potential oxides have been reported to have high oxygen diffusivity and hence, this behaviour can alter the thickness of this beneficial SiO_2 in interface, particularly during subsequent annealing. In the other cases, they complicate further the process of integrating high-k oxides into the gate stack because they require the search for alternative buffer layers.

The last issue that has strong influence on the device operation from the microstructure viewpoint is the defects from potential high-k oxides. It is well-known that most of transitional and RE oxides have a much higher concentrations of bulk defects compared to SiO_2 [7, 8, 17, 20-23], these are mainly oxygen vacancies and oxygen interstitials. The main reason why these high-k oxides have high concentrations of defects is due to their chemical nature.

In contrast to SiO_2, all of these oxides are poor glass-formers [1]. Moreover, they have relatively higher co-ordination numbers and they are highly ionic. As a result, these oxides have larger non-equilibrium defect concentrations than SiO_2. Although they have high heats of formation, i.e. the equilibrium defect concentrations should be low, the non-equilibrium defect concentration is still high because the oxide network is less able to relax easily to rebond and remove defects. That is also the reason why oxygen vacancy and oxygen interstitial defects are the two main types prevailing in these oxides due to their lower formation energy compared to metal defects. These defects can exist either as bulk fixed charges or as surface states at the interface with the silicon channel. They were reportedly responsible for creating strong electric fields, altering band offsets, contributing to dielectric loss and because of their diffusions in an electric field, inducing a phenomenon similar to electrolysis [1, 21]. Unstable threshold voltage and low carrier mobility were also attributed to these defects [24].

Because these detrimental effects will lead to unstable device operations, the concentrations of defects must be minimised and controlled as far as possible. The choice of film growth methods can significantly affect the density of defects and hence, needs to be evaluated with great care. Other processing factors such as substrate preparation, subsequent annealing and gate stack structure also contribute to the density of defects. Alteration in the structure of the oxide itself can also help to somewhat mitigate the problem, e.g. incorporating La into HfO_2 was demonstrated to suppress the formation of oxygen vacancy [25].

2.3.2.4 Compatibility with gate electrode

Until very recently, poly-Si has been the industrial choice for the gate electrode on top of SiO_2 in conventional MOS devices. These gates are not actually metals but heavily doped n- and p-type poly-Si. They are still a favourable choice though because dopant implant conditions can be tuned to create the desired threshold voltage V_T for both nMOS and pMOS. In addition, the process integration schemes for poly-Si are well established in industry. Poly-Si also has the advantage that it is refractory, easily deposited and compatible with SiO_2.

However, when the SiO_2 is replaced by a high-k oxide, the use of poly-Si as gate electrode is arguably no longer suitable.

Firstly, materials such as HfO_2 and ZrO_2 can react with the poly-Si during the dopant implant annealing process resulting in the formation of silicides [1], which in turn leads to carrier leakage paths and influenced the functions of the oxides. Diffusion of dopants, particularly Boron, from the poly-Si gate through the oxide can also occur [1, 4]. Moreover, because poly-Si gates are not real metals, they have a relatively low carrier density and hence, add a depletion length of a few Angstroms to the Equivalent Capacitance Thickness (ECT) of the gate stack [1]. As a result, it is necessary to deploy alternative metal gate electrodes simultaneously with the integration of high-k oxides in to the new gate stack structures. In fact, research in metal gates has also been a very active area in parallel with the field of high-k oxides. Some of the main challenges of metal gates are the compatibility with the processing and thermal stability with the high-k oxides. In addition, there is the challenge of fine-tuning work functions for nMOS and pMOS separately. Some of extensively researched simple metals or alloys reportedly showed promising results are Ru, TiN, TaC_x and TaN, etc. [1].

2.3.2.5 Manufacturing compatibility and device reliability

From the viewpoint of manufacturing, integration of high-k oxide into the process flows requires very strict conformation to the overall design and production of ICs and preferable, demands the least change in any subsequent steps. It is mainly due to the massive cost and deep know-how in the past for Si semiconductor and still seemingly the dominant choice for years to come. In addition, since the gate dielectric properties and thickness have a strong impact on the performance of the device, these properties must be very well controlled in practical conditions within current or expected industrial environment to manufacture large ICs with a high yield. Because these properties are typically a function of deposition technique, the dielectric must have repeatable, well-controlled properties across a large area wafer and also from batch to batch. Moreover, whatever the deposition technique to be used, it also needs to be a cost effective process with a high throughput.

Device reliability is another major issue which demands a lot of works in developing and validating new methods in metrology and theoretical investigations. This issue involves many different experimental factors such as device lifetime, modes of failures for oxide breakdown at operational voltages, etc. [26]. Theoretical studies deal with critical questions relating to the performances of high-k oxides that not known before to the semiconductor industry community [7], mainly due to the much more complex nature of such materials compared to the well-characterised SiO_2.

2.4 Stabilisation of higher-k phases in HfO_2-based dielectrics

Among all high-k oxides investigated as gate dielectric in advanced CMOS devices, HfO_2 and its "twin oxide" ZrO_2 have attracted the most attentions because of their reasonable k-values (k=15~25), wide band gap (E_g~ 6 eV) and good thermal stability on Si. Between these two, HfO_2 has been more favourable due to its higher thermal stability with Si and better resistance to silicide formation[1]. In fact, it is Hf-based oxide that chosen in the 45 nm node production which Intel introduced in 2007 as their preferred high-k gate dielectric. However, according to the latest edition of the ITRS published in 2009 [27], the need for a higher-k material (k>30) is mandatory to maintain the scalability of devices in near future. In addition, due to the necessity of a buffer layer between the Si substrate and high-k oxide, it is also necessary to require higher-k values to compensate for the loss in EOT that subjected to continuous scaling. As a result, the search for a higher k-value compared to the initial requirement (k=20~25) has been started with two main approaches. The first one involves some emerging candidates, which are RE-oxides and perovskite oxides such as (Sr, Ba)TiO_3. These materials have attracted extensive interest due to their potentially high k-values, particularly in the case of perovskites. However, their chemical instabilities (in the case of RE oxides such as highly hygroscopic and catalytic nature) or difficulties in growth conditions (perovskites require MBE and very sensitive in layer compositions) have been so far not fully resolved and hence, still a serious technical barrier to overcome. Another class of materials have also been considered promising, in fact, is derivatives of pure HfO_2 (ZrO_2). Zhao and Vanderbilt predicted theoretically [28] that the high-temperature phases, i.e. cubic or tetragonal, of materials such as HfO_2 should have significantly higher permittivity (k can be increased up to 70 for tetragonal phase) than the thermodynamically stable

monoclinic phase (k~16). Following this study, many investigations have been done to investigate ways of stabilising these high temperature phases and to assess their suitability of CMOS devices as successors of HfO_2 (see, for example [8, 29-32] among many others). Many other experimental studies, mainly involved HfO_2 thin films doped with RE elements, have shown encouraging electrical results (see section 2.4.3 for more details).

Because HfO_2 has become the most important high-k oxide available at the current time due to its recent adoption into mass-production microelectronics, derivatives of this system are desirable for next generation advanced CMOS circuits. This section will present an overview of this trend as the main context and motivation for the work undertaken within this study. Firstly, the microstructure of HfO_2 will be outlined, followed by the mechanisms of phase stabilisation by doping with different elements. The last part will review some experimental results reported in the literature to demonstrate and correlate crystal structure and dielectric property relationship with considerations to progressive scaling demands.

2.4.1 HfO_2 polymorphs: stable and metastable phases

It has long been known in the ceramics industry that Hf, together with other elements such as Ti, Zr, Ce, U, Th and Pu form a variety of binary and multi-component oxides based on the fluorite structure of CaF_2 [18]. These materials are generally refractory and find a wide variety of applications ranging from structural ceramics, thermal barrier coatings, nuclear fuels and nuclear waste ceramics through to solid electrolytes for oxide fuel cells, sensors and catalysts. For Hf and Zr binary oxides, three stable phases can be formed at the atmospheric pressure depending on temperature. The monoclinic phase is the most thermodynamically stable at room temperature, while the other two are stable at higher temperatures. Figure 2-11 schematically shows these three phases and their transformational temperature accordingly.

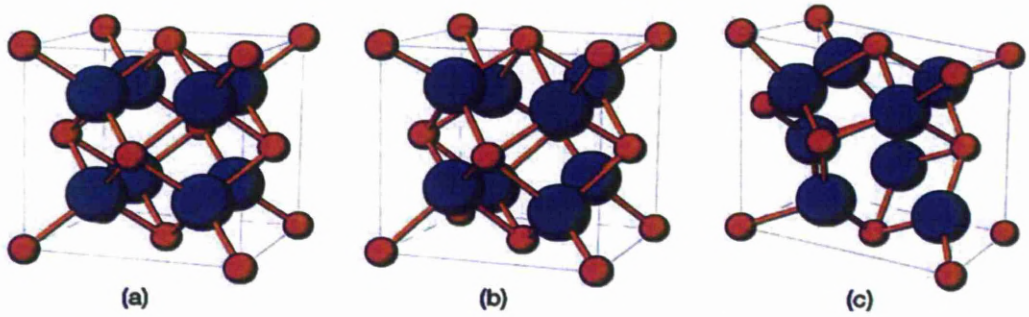

Figure 2-11: Ball and stick schematic illustrations for (a): cubic, (b): tetragonal and (c): monoclinic structures of HfO_2 [18]. (The large ball represents O^{2-}; the small one represents Hf^{4+}). Monoclinic ↔ tetragonal (1510°C - 2000°C on heating, 1288°C - 1800°C on cooling), tetragonal ↔ cubic at 2700°C [33].

In cubic and tetragonal phases, the cation in the network has a co-ordination number of 8 while for the monoclinic phase, it just only has 7. The monoclinic phase is considered a distortion of the parent structure while the tetragonal is typically described as a distorted cubic with oxygen displacement along the z-axis [33-35]. In contrast to other oxides based on large tetravalent cations such as Ce, Th and U (with the exception of Ti), the high-temperature phases of HfO_2 and ZrO_2, cannot be quenched to retain their forms at room temperature [18, 36]. This can be explained by two effects: (i) Zr^{4+} and Hf^{4+} have small ionic radii and hence, cannot accommodate the co-ordination number of 8 required for tetragonal or cubic phases at low temperature [37-39] and (ii) at temperature below the transformation point, the monoclinic phase has the lowest interfacial energy and hence, is the most thermodynamically stable phase at atmospheric pressure [40]. In addition to the three main phases, other orthorhombic phases have also been reported to exist under very high pressure and elevated temperature [36]. However, these orthorhombic phases are not of particular interest here as it is highly unlikely that these phases could be stabilised under any growth conditions and subsequent processing which would be compatible with CMOS fabrication.

Besides the thermodynamically stable phases, "metastable phases" in both pure ZrO_2 and HfO_2 have also been studied [35, 36]. The term "metastable" refers to the fact that although these phases are not as stable as the monoclinic phase, they can be obtained at temperatures below the standard transformational boundaries. The observation of "metastable tetragonal" in ZrO_2 powder was firstly reported by Garvie [40].

In his work, hypotheses are made about the formation of such phase as a function of crystallite size and surface energy. Following this study, numerous investigations, both experimental and theoretical, have been devoted to this complex yet interesting phenomenon of phase transformation and phase stabilisations. Much of this has focused on applications within the bulk ceramics industry due to importance of these oxides as control rod (HfO_2) in water-cooled nuclear reactors [36] or electrolyte in solid-oxide fuel cell (ZrO_2) [35].

One of important observations about the phase transformation in ZrO_2 and HfO_2 alike was the diffusionless nature of such reversible phase transformation, especially for the monoclinic $\leftrightarrow$ tetragonal regime [41]. All of these studies have led to general agreement about the conditions required for tetragonal and/or cubic phase to be retained in undoped HfO_2 and ZrO_2 and how to study these effects by metastable-stable phase diagrams [35]. Essentially, proposed factors involve the critical size of crystallites and its interplay with interface or surface energies.. The latter factor is particularly important in thin films rather than in bulk materials. A number of studies involving ALD of HfO_2 films have illustrated this interdependence by looking at the effects of film thickness and growth conditions [42-44]. These studies also mentioned the influence of annealing conditions, such as the oxygen partial pressure, to the formation and stabilisation of these metastable phases. This factor will be discussed in more details in the next part of this section. To visually illustrate this complicated relationship, Figure 2-12 demonstrates how the phase variations can be obtained by controlling the crystallite size in nanocrystalline ZrO_2. The equivalent film thickness is also shown and illustrates the influence of surface energy (in terms of coarsening effect) to phase stabilisation.

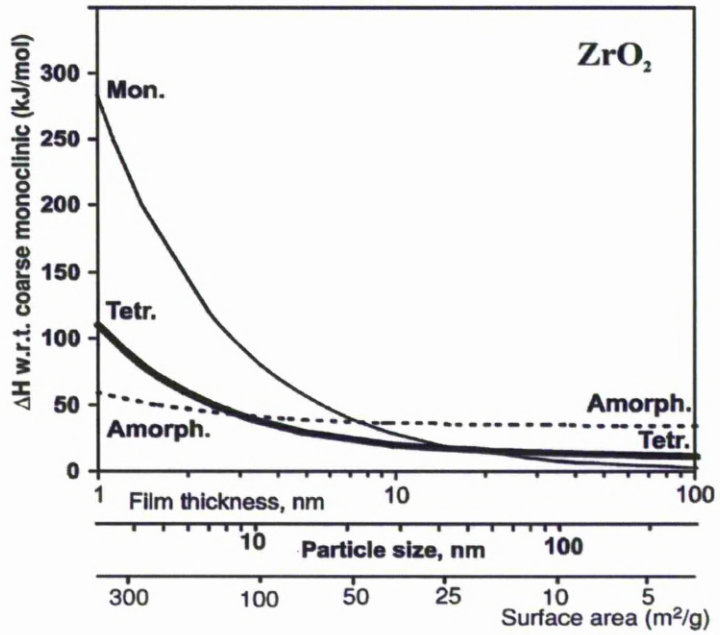

Figure 2-12: Excess enthalpy of nanocrystalline ZrO_2 against particle size (in log scale) [8] and its correspondent phases: amorphous (amorph.), tetragonal (tetr.) and monoclinic (mon.)

2.4.2 Phase stabilisation in HfO_2 by doping with other elements in bulk ceramics

One of the most effective ways to induce the phase stabilisation in ZrO_2 and HfO_2 is to introduce dopant(s) into the matrix of these host oxides [35, 36]. Numerous investigations have been done, mainly for ZrO_2 and to a lesser extent for HfO_2, since the discovery of toughening transformation in ZrO_2 in the 1970's for tetragonal and cubic phases at much lower transformation temperatures [36]. Probably the first and the most extensively studied system is yttria stabilised zirconia (YSZ), followed by other solid solutions with dopants such as Ca, Mg and Ce. Another group of dopants which have also been investigated are the RE elements. Thanks to these thorough and extensive studies, many important mechanisms effecting phase stabilisation are understood. Theoretical insights into the formation of various metastable phases have also been advanced in this particular field. Theoretical studies into the mechanisms for the formation of these phases within a single system or the microscopic interactions between guest and host cations in the network and their influences to the ultimate structures of the doped systems have been reported.

One of the most thorough studies so far in this field involving microstructure analysis with a wide range of dopants was carried out by Li et al [37-39] using X-ray Absorption Spectroscopy (XAS) for zirconia stabilisations. Another excellent review on hafnia and its toughened derivatives was published by Wang et al [36]. Because the work on phase stabilisation of hafnia is far less advanced than the work on zirconia, it is inevitable to postulate various findings and theories found from ZrO_2 studies to HfO_2 investigations. Nevertheless, given the nearly identical physical and chemical properties between these two "twin oxides", it is reasonable and necessary to do so. As a result, this part will highlight key points in the context of phase stabilisations of HfO_2 and ZrO_2 alike based on these aforementioned core papers plus important information found in various studies from literature. Many studies involved the built-ups or modifications of phase diagrams for various systems, which have also the main source of discrepancies and controversies between different authors. This factor will also be taken into account when microstructures and phase compositions are concerned and arguably, one of the most puzzling issues in this interesting area.

In the following sections, two different mechanisms of stabilisations are reviewed. They are based on the addition of trivalent or tetravalent cations respectively, which also constitute the majority of elements investigated, into Zr/Hf oxide networks. Pentavalent dopants were demonstrated to have a hybrid mechanism for the aforementioned cases [39] and hence, can be understood in a similar way. The use of divalent cations so far is limited to Ca and Mg only and can be found in [36]. To conclude this part, some other important observations reported in "metastable phases" for Zr- and Hf-based systems will be briefly illustrated and discussed.

2.4.2.1 Stabilisation based on Oxygen vacancy

The ionic radii of Zr^{4+} and Hf^{4+} are considered to be too small to accommodate a stable 8-fold co-ordination with oxygen in tetragonal and cubic phases (only exist in high temperature conditions). A revised phase diagram of ZrO_2 doped with Y^{3+} [45] showed tetragonal or cubic phase stabilisation and was firstly explained by the role of oxygen vacancies created to compensate for charge balance [46].

This in turn resulted in the co-ordination number of Zr^{4+} being reduced to around 7.5 in tetragonal or cubic configuration, which meant that they were more stable because they were closer to the strongly favoured co-ordination number of 7 between Zr and O. A number of other studies were also conducted with other dopants but the mechanism for the role of oxygen vacancy and how the stability of tetragonal/cubic phase vary with such factors were not well understood. This was the main motivation in the work of Li et at [38] to study the influence of oxygen vacancy in aiding the phase stabilisation of ZrO_2 in a systematic way with different trivalent cations at various concentrations. One of the main advantages this study had was the employment of XAS, a powerful technique with the capability to probe local structures. According to the author, XAS provides high resolution in differentiating the dopant and host cation networks even at low doping concentrations. It was particularly important when the ionic radii of dopants compared to Zr were concerned and all previous studies could not provide satisfactory explanations regarding this issue. As a result, more understandings about how trivalent cations affect the phase stabilisations in ZrO_2 were developed and validated.

The local microstructure in this study can be summarised as the following key notes:

- Oxygen vacancies created by introducing trivalent cations into ZrO_2 networks are responsible for the stabilisation of tetragonal and cubic phases. They are also found to be associated with the Zr cations in the case of oversized dopants and with two dopant cations in the case of undersized dopants.
- Oversized dopants (Y and Gd) form solid solutions adopting the zirconia structure, in terms of both dopant-oxygen bond length and dopant-cation distance. These oversized dopants also accommodate 8-fold configuration and leave oxygen vacancies for Zr host cations.
- Undersized dopants (Fe and Ga) substitute randomly for Zr ions in the network and have very limited solubility in zirconia solid solutions. They exist in 6-fold co-ordinations and compete with Zr ions for the oxygen vacancies.

- The tetragonal-to-cubic transformation in zirconia solid solutions involves distortion of the nearest-neighbour Zr-O shell whereas the tetragonal-to-monoclinic transformation requires distortion of both the nearest-neighbour Zr-O shell and the next nearest-neighbour Zr-Zr shell.

These findings lead to some important consequences in terms of phase stabilisations. Firstly, in order to achieve the same stabilising effect, the amount of undersized dopants needs to be used much more than their oversized counterparts. The undersized dopants also create much more distortion in the host cation network compared to the oversized ones. This behaviour is reflected in their much lower solubility in Zr cation networks and hence, cubic solid solutions are found to be very difficult to form. In terms of tetragonal stabilisation, both types of dopants are found to be capable of suppressing monoclinic distortion though similarly to cubic phase, the undersized dopants are much less effective. For the oversized dopants, increasing the doping levels will result in a decrease of tetragonality, which can be represented by the ratio of ZrO_7/ZrO_8 [46]. The tetragonal-cubic boundary is determined at the concentrations of oversized dopants that yield this ratio equivalent to unity. In cubic structure, ZrO_7 is the elementary structural unit while in tetragonal, it is the ZrO_8 that is the dominant one.

2.4.2.2 Stabilisation based on cation network stabilisers

Besides the extensively researched topic of stabilising high-temperature phases in ZrO_2 using trivalent cations, some other studies were also conducted with tetravalent cations such as Ti, Ce and Ge [47-49]. All of these studies demonstrated that by alloying ZrO_2 with the oxides from these elements, tetragonal and/or cubic phases could be retained at room temperature with appropriate doping concentrations. However, the mechanism of stabilisation in these systems was not well understood. In contrast to the systems doped with trivalent cations, these systems do not create oxygen vacancies within the network especially at low doping concentrations and hence, the stabilisation cannot be explained by the same mechanism applied for the trivalent dopants.

Therefore, the stabilisation by adding tetravalent cations into ZrO_2 networks requires an alternative explanation. Li et al in their second study using XAS [37] followed the same approach used by the previous study of trivalent cations. Ce was used as an oversized dopant and Ge as a undersized dopant, these were introduced to ZrO_2 matrix are various concentrations to assess their influence on the host network as well as the effect on oxygen bonding. At this point, it is also important to recall that tetragonal zirconia may be viewed as a layer structure, in which tetragonality is attributed to the strong bonding of Zr-O_I (2.10Å) within the layers whereas weak bonding of Zr-O_{II} (2.34 Å) between the layers [50]. The main results from Li's XAS work can be summarised as the followings.

- Both the oversized (Ce^{4+}) and undersized (Ge^{4+}) tetravalent dopants have significantly different oxygen coordination from that of the host cation (8-fold in the case of Ce and 4-fold in the case of Ge). While Ce is found to form a random substitutional solid solution with Zr, Ge associates in the cation sublattice within ordered domains. For both dopants, the cation-cation distance in the network is not affected by alloying.
- Oversized CeO_8 polyhedra are observed in tetragonal zirconia with a Ce-O bond length of 2.30 Å, which is longer than the mean Zr-O distance of the host network but shorter than the Ce-O distance in pure CeO_2.
- The undersized Ge in zirconia solid solutions is tetrahedrally coordinated with O with a Ge-O distance of 1.81 Å. This distance longer than the Ge-O in pure GeO_2. However, it is shorter than the Zr-O_I bond and hence, is thought also stronger.

These differences in microstructures exert their impact on the stability of tetragonal zirconia and are visually illustrated in Figure 2-13. The c/a ratio is depicted as a function of tetragonality, i.e. the higher this ratio, the more stable tetragonal structure can be formed (c is the length of the unit cell in z-direction and also conventionally used as c-axis. For tetragonal structure, a=b≠c, and tetragonality in ZrO_2 and HfO_2 alike is defined by anisotropic elongation or contraction mainly along the c-axis).

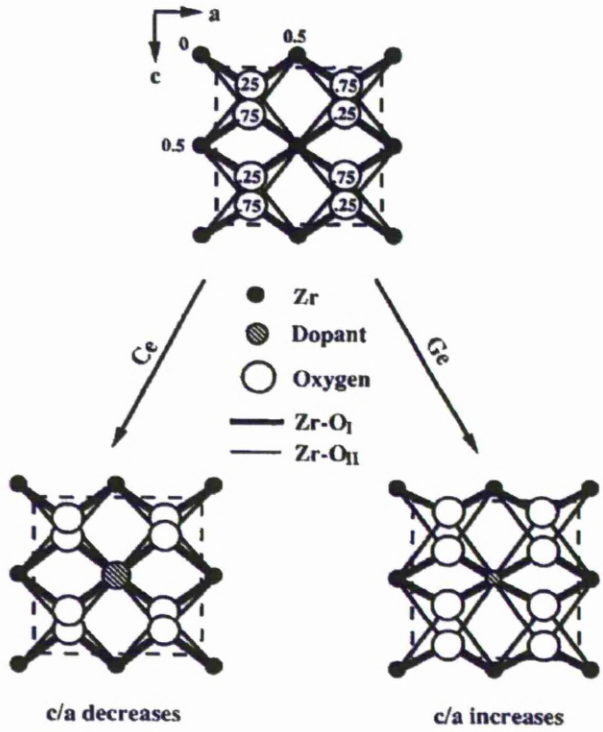

Figure 2-13: Schematic view for variation of tetragonality of zirconia solid solutions with Ce and Ge dopants. (Numbers indicate atom positions in b direction) [37].

For the oversized tetravalent Ce dopant, the tetragonality decreases when the doping concentration increases. It is because of the introduction of Ce^{4+} ions in sufficient amount, which themselves adopt a more symmetric 8-fold coordination of fluorite-like structure. Due to their larger size, these ions create the effect of assimilating two types of bonding in tetragonal ZrO_2 and hence, destabilise the layer structure. However, it is also noteworthy that this effect from oversized tetravalent Ce^{4+} is less than that of the oversized trivalent cations, reflecting in the critical concentrations needed to a complete phase from tetragonal to cubic (18% for M_2O_3 compared to 70% of CeO_2). In addition, for CeO_2-ZrO_2 system, two-phase system of tetragonal-cubic can be found between 18% and 70% of Ce doping level at intermediate temperatures [48], which is likely one of the main source for controversies found in many different studies regarding the tetragonal-cubic transformation boundary and some forms of "metastable tetragonal" phases within this doping range. This issue will be mentioned in the next part of this section.

In the case of undersized tetravalent Ge dopant, the opposite trend to the Ce doping is observed. The tetragonality of zirconia solid solution increases proportionally with the Ge doping concentrations. This is due to the stabilising effect achieved by cation ordering. The oxygen overcrowding, which prevents the tetragonal phase of ZrO_2 from being stable, is relieved by the full development of bifurcated tetrahedral bondings for both Zr-O and Ge-O in the layer-like structure. Therefore, the tetragonal zirconia solid solutions are found to be much more stable compared to the case of Ce doping. However, one noteworthy observation is that no cubic solid solution can be obtained using Ge dopants. This can be expanded to all undersized tetravalent dopants and can be explained by the absence of oxygen vacancies in these systems to aid the ZrO_7 polyhedron formation. In contrast, oversized dopant such as Ce can form cubic phase in significant quantity because CeO_2 itself is a cubic fluorite-type structure. Although no oxygen vacancies are generated by the Ce dopant, the cubic structure can be explained by its formation once the percolation limit for Ce in the fcc lattice (19.8%) is exceeded. Under these conditions, a locally "cubic" environment surrounding Ce can be created to form cubic domains, which in turn triggers the phase separation into tetragonal and cubic regions. This two-phase regime continues until the Zr ions become the minority species and fully surrounded by the cubic matrix, which will lead to a cubic-like structure. This tendency is also thought to be applicable to all other oversized tetravalent dopants.

2.4.2.3 Intermediate "metastable tetragonal" phases in Zr- and Hf-based oxides

While the term "metastable phases" in Zr- and Hf-based systems generally refers to the high-temperature phases stabilised and retained at room temperature against the monoclinic distortion, it can also relate to other intermediate phases exist between the two-phase regime in various phase diagrams particularly at low and intermediate doping levels. These intermediate tetragonal phases have been detected and distinguished from the stable tetragonal/cubic phases as distorted fluorite-type structure evolved via diffusionless transformation and termed as t' and t" respectively besides the high-temperature tetragonal phase, t [33, 35, 51, 52] mainly in systems doped with trivalent cations. More recently, similar intermediate phases were also reported for Ce-doped hafnia [53] and for very thin undoped HfO_2 films [43].

Of these two structures, the t" tetragonal form resembles a very similar structure to the cubic one, with a c/a ratio equivalent to unity. This similarity between phases has been the main cause of many contradictions between various phase diagrams constructed prior to this discovery by diffraction techniques, such as X-ray Diffractions (XRD) [35], although the existence of these phases had been acknowledged for quite a long time. The underlying reason, as has been identified [33, 35], was due to the fact that the distortion in these two "metastable tetragonal phases" are caused by the oxygen displacement along the c-axis. Thanks mainly to the advances of Raman microscopy and its high sensitivity to light element displacement, which is not available from XRD, these structures were resolved and validated. Figure 2-14 illustrates different phases found in Zr- and Hf-based oxides and how oxygen displacement exist in t' and t" tetragonal forms. In this schematic view, the small solid black circles present Zr (Hf) atoms while the large white circles represent oxygen atoms. Displacements along the c-axis involving oxygen atoms are indicated by the arrows. The t" tetragonal form and the cubic phase are undistinguishable from the crystallographic viewpoint because firstly, they both can be characterised by only one unit cell parameter, a; and secondly, light elements such as oxygen have a very low X-ray scattering cross section. Only by detection of the vibrational mode, which is made possible by technique such as Raman scattering, it is possible to differentiate between these similar structures. Neutron diffraction can also in principle detect the displacement of the oxygen atoms as its has a much higher sensitivity of oxygen scattering factor compared to XRD [53]. However, as many Hf-based oxides exhibit high neutron absorption coefficients [36], the use of neutron diffraction is quite limited in practice.

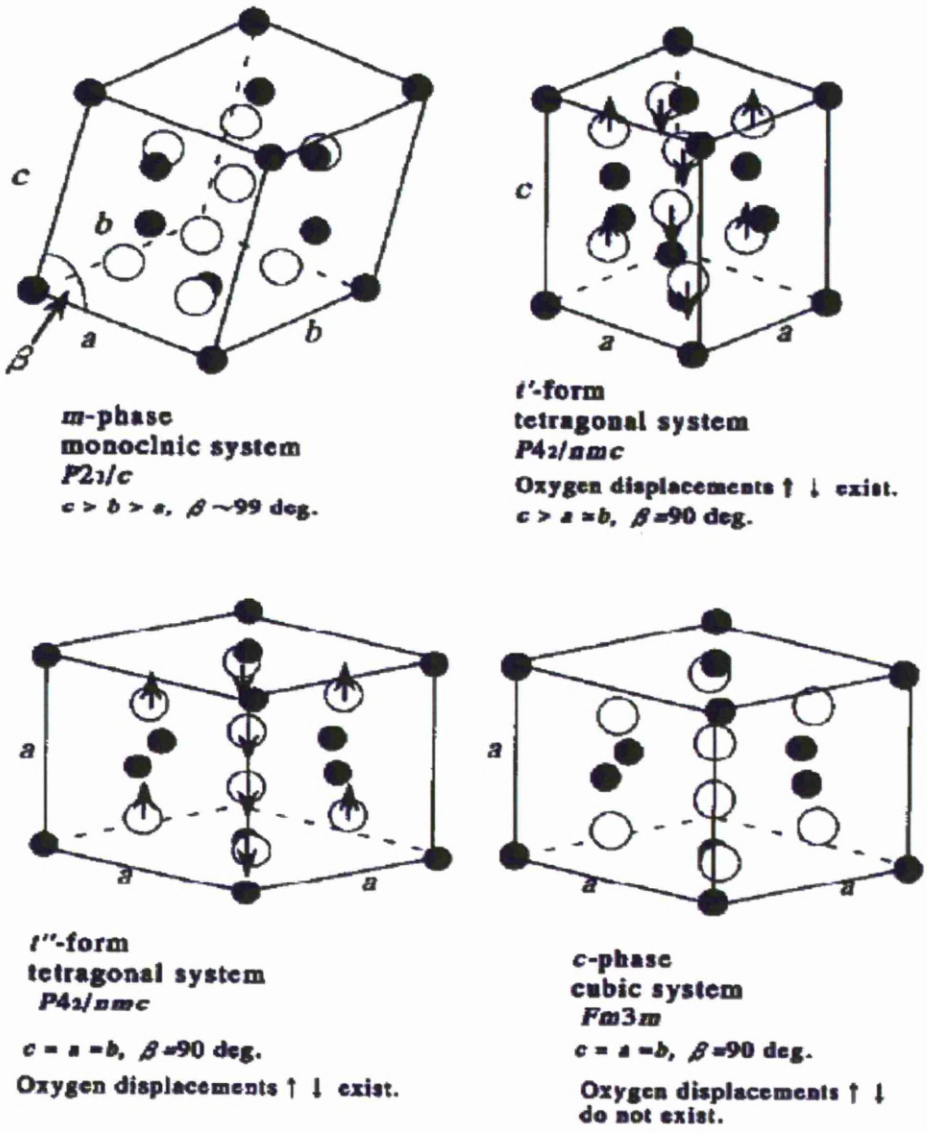

Figure 2-14: Monoclinic (m), tetragonal (t' and t'') and cubic phases in Zr- and Hf- based oxides [35].

2.4.2.4 Some recent progress in high-k research from Hf-based thin films

The first theoretical study investigating the effect of phase on the permittivity of HfO_2 was undertaken by Zhao and Vanderbilt [28] in 2002. This work revealed an interesting insight into how it might be possible to obtain significantly higher permittivity from HfO_2. Their reported k-values were 70, 29 and 16 for tetragonal, cubic and monoclinic phase respectively. Following this initial investigation, some other first-principle and ab initio studies were also done to further corroborate this structure-property relationship [8, 30, 31].

These studies also confirmed the enhancement of permittivity in Hf-based oxides by stabilising its high-temperature crystal structures although the calculated k-values were somewhat different between authors. One significant variation among these studies is the discrepancy in dielectric constant for tetragonal phase (k~70) estimated by Zhao and Vanderbilt and another result from Rignanese [8] in his ab initio study about IVB transitional metal oxides and silicates (k~29). The values calculated for the cubic phase were however, in reasonable agreement. Despite the difference between the predicted values in these two studies, it is clear that a significant enhancement should be possible by obtaining and stabilising the tetragonal or cubic phase. At the same time, the bandgap of the material should remain virtually unchanged or may even be slightly improved [1].

Motivated by these studies and also by the need of higher-k oxides to succeed HfO_2 in next CMOS generations, many experimental studies have been done to investigate the feasibility of enhancing k-value in Hf-based thin films. Trials were undertaken by doping HfO_2 with La [54], Gd, Er, and Dy [29, 55, 56], Ce [57] as well as Sc [55], Y [58] and Si [59, 60] typically at low doping levels (typically up to 20%). Electrical results such as leakage current, fixed oxide charges, surface density states, etc. were quite encouraging though varied between different groups. Some degree of variation is inevitable because the differences in growth methods, film thickness, annealing conditions, nature of dopants, doping levels, MOS structure, etc. As far as the dielectric constants are concerned, these studies however yielded two maximum experimental dielectric constants of 28 and 32, except in the study of La-doped HfO_2 which gave a significantly higher permittivity of 38. These values are quite close to the value of the cubic or tetragonal HfO_2 predicted by Rignanese mentioned previously but far lower than the tetragonal k-value estimated by Zhao and Vanderbilt. While these results are very promising from the viewpoint of high-k applications, there remained some questions about the accurate determination of phases in these materials. Most authors relied mainly on the evolutions of XRD patterns to argue the crystal structure of their correspondent films as tetragonal or cubic, while some others could not deduce the structure unambiguously.

As mentioned before, XRD alone is not sufficient to distinguish between the various configurations of tetragonal and cubic phases, particularly if the dopant level is low. The issue is further complicated by the broadening effect and peak convolution in XRD spectra due to small crystallites and the potential co-existence of different phases in the films. It is thus remaining a very challenging yet very interesting area to conduct more investigations about crystal structures in these Hf-based thin films and gain a better understanding about the dielectric constant variations against phase composition and/or microstructure alteration. Moreover, doing so can also possibly reveal some optimal conditions such as annealing environments and temperatures, doping levels required to achieve a specific value of permittivity and other electrical properties, etc.

2.5 Deposition techniques for dielectric thin films

The shift to a high-k dielectric material in CMOS production represents a fundamental change in processing towards deposited thin dielectric films rather than the native oxide that can be grown directly on crystalline silicon. To ensure good electrical performance of the resulting devices, the deposited dielectrics must have an excellent thickness uniformity and superior interfacial and bulk properties. Clearly, the search for such a perfect technique is not easy because any potential method will have its own advantages and disadvantages. Research projects in laboratory require a flexible and capable tool to accomplish testing a wide range of materials whereas industrial applications dictate a critical balance between financial investment, quality control and yields. This section will outline some of the most popular deposition techniques particularly suitable for growing dielectric thin films and used in both research laboratory and industrial environment. The main focus of this section will be on Atomic Layer Deposition (ALD), a derivative of the Chemical Vapour Deposition (CVD) family, which is the technique used in the current research and has also been adopted for production by many leading companies in semiconductor industry. Other competing or alternative techniques will also be briefly reviewed.

2.5.1 Atomic Layer Deposition (ALD)

The development of Atomic Layer Deposition (ALD), originally known as Atomic Layer Epitaxy (ALE), is widely accredited to Suntola and Antson from Finland, who developed the technique in the 1970s for the commercial production of high-quality, large-area flat panel displays based on thin film electroluminescence (TFEL) [61]. However, the process was also developed and investigated extensively as early as 1960s by many former Soviet Union researchers although far less well-known until much later [62].

Since then, it has become a very useful and versatile technique for depositing a wide range of materials, ranging from elemental metals through to oxides, nitrides and a range of other types of compounds [62] for various applications. Recently, worldwide interest in ALD has increased due to the driving force of the semiconductor industry and its ongoing demand for scaling devices. The demand for a method capable of depositing very thin, conformal, atomically flat and highly-insulating oxide layers at the nanometre thickness scale, are all met by ALD [61]. The so-called high-k oxides, which mostly comprise refractory materials, are not easily processed in a controlled manner by thin film deposition techniques other than ALD. The reason why ALD is thought of as the most capable technique to be employed in high-k thin film application owes much to its characteristics as a very distinct method to provide "digitised control" of film thickness.

One of the most important concepts of ALD is its growth cycle. Figure 2-15 and Figure 2-16 demonstrate two simplified but typically representative ALD growth cycles in two different fashions [63]. They are referred to as chemisorption-saturation and reaction-sequence ALD respectively, both rely on the strong chemical adsorptions of gaseous precursors, which are in various forms of metal complexes or compounds, to the substrate. Another type of adsorption that can also exist is physisorption. However, the influence of this in ALD is not very strong for most film growths and generally a minor effect. A detailed discussion about the growth kinetics, mechanisms and surface chemistry can be found in [62]. For both of these aforementioned ALD growth pathways, a purge of inert gas is applied in step 2 and 4 to remove all excessive precursors and gaseous by-products.

As each step of the ALD cycle is self limiting, it is possible to accurately control film thickness simply by controlling the number of cycles. In theory, each cycle can form a full monolayer (ML), however, in practice, only a fraction of ML is produced in most processes due to steric hindrance of the precursors on the surface.

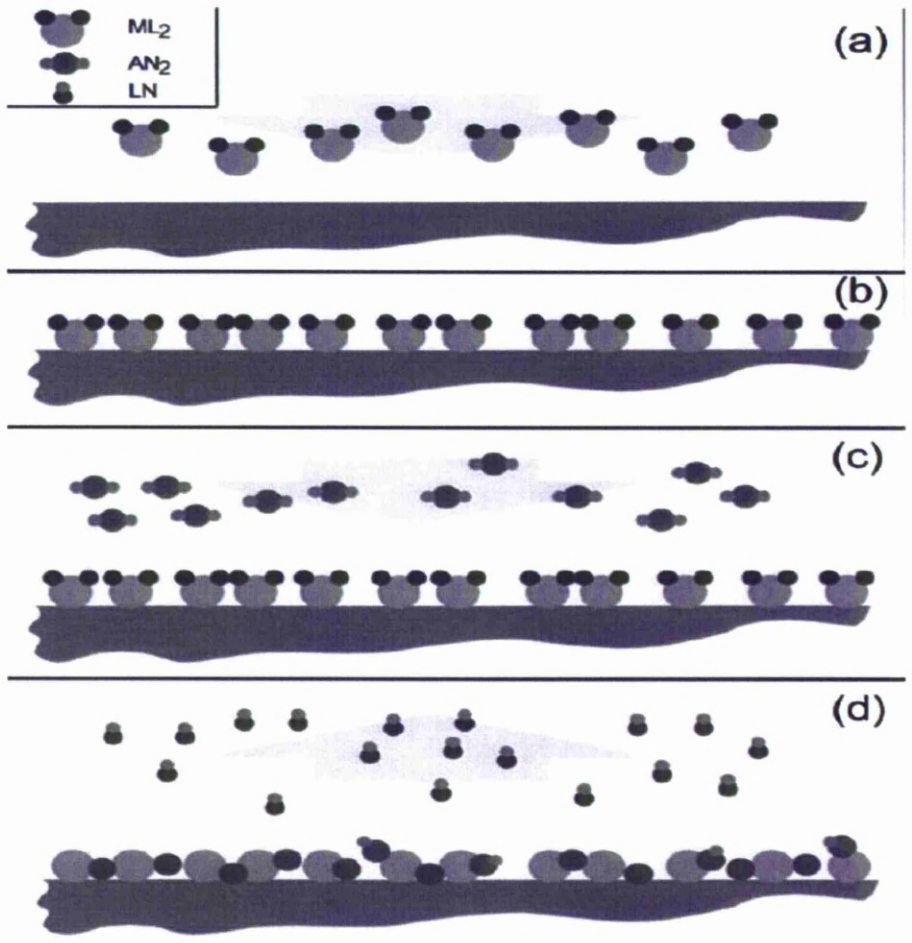

Figure 2-15: Sequence of steps in chemisorption-saturation ALD: (a) Substrate is exposed to the first molecular precursor, ML_2; (b) first molecular precursor forms a saturated layer on the substrate; (c) the adsorbed layer of the first precursor is exposed to the second precursor, AN_2; and (d) the exchange reaction between the precursors produces the film and eliminates the by-products [63].

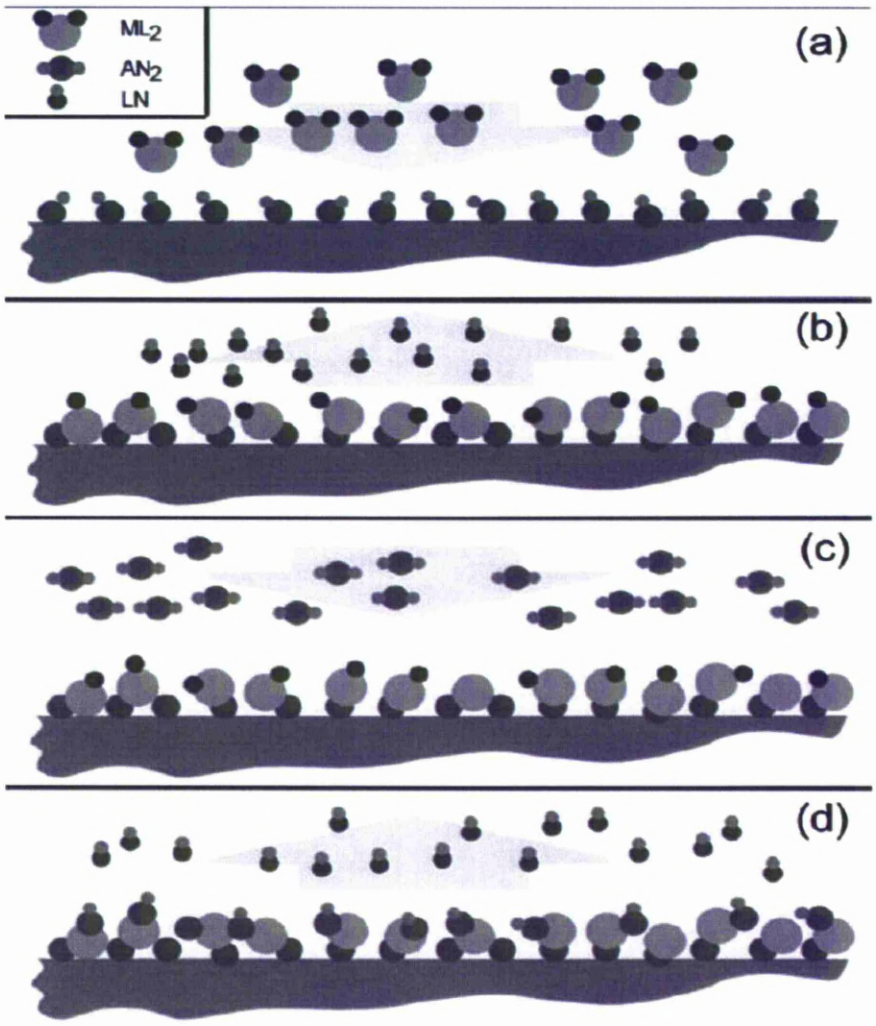

Figure 2-16: Sequence of steps in reaction-sequence ALD: (a) The surface is activated with *AN* groups and this surface is exposed to ML_2 molecules; (b) ML_2 molecules react with *AN* groups to produce volatile *NL* by-product molecules and attach *ML* groups to the *A* elements of the surface *AN* groups. The reaction self-saturates when all the *AN* groups are converted to *AML* groups. The *AML* species cannot further react with the exposing ML_2 precursor; (c) After removal of excess ML_2, the *ML*-terminated surface is exposed to the second precursor AN_2 and (d) AN_2 molecules react with the surface *ML* groups to produce *NL* volatile by-product and attach *AN* to the surface *M* atoms. The reaction self-saturates once all surface *ML* groups are converted into *MAN* that cannot further react with AN_2 precursor [63].

One of the most important characteristic of ALD is the self-limitation nature of the process. ALD is characterised by two central parameters: steric hindrance of the ligands and the number of reactive sites available on the surface [62]. These two parameters in turn depend on various factors such as precursor doses, growth temperatures, chemical structures of precursors, etc. For a given system of precursors including metal-contained reactant and oxidising agent providing that both are used at sufficient quantities to cause surface saturation, ALD growth process can be

characterised by the growth rate against growth temperature. Figure 2-17 illustrates the typical effects of growth temperature on the growth rate that may be observed in typical ALD processes. The central part of this graph (region "a") is referred to as the growth window and is the typical region used for deposition as the growth rate per cycle is insensitive to temperature [61]. Possible different behaviours of a film growth can also be observed during the course of temperature evolution and they are also illustrated within this figure.

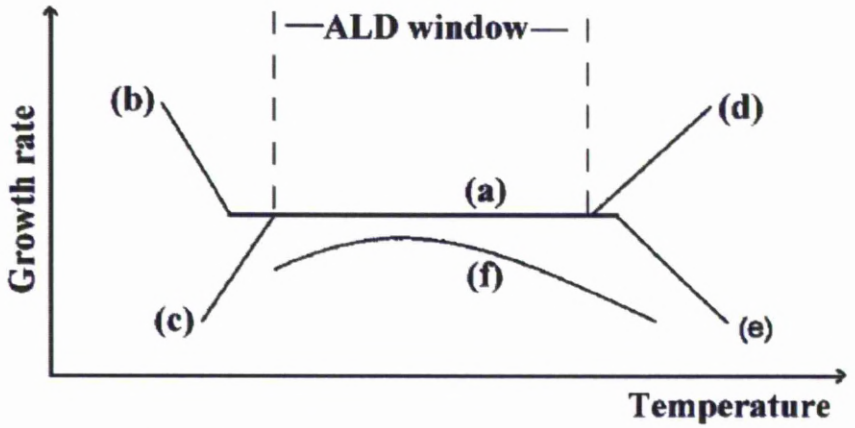

Figure 2-17: Schematic illustration of ALD processing window with various characteristics responses of growth rates against temperatures: (a) ALD processing window with constant growth rate; (b) precursor condensation; (c) insufficient reactivity; (d) precursor decomposition and (e) precursor desorption. If the deposition rate is dependent on the number of available reactive sites as in (f), actual ALD window cannot be observed, i.e. surface-saturation cannot be achieved [61].

As can be seen from the figure above, if an ALD window can be found for a particular growth process, the growth rate (typically represented by nm/cycle) should be constant. This characteristic of an ALD window implies that it can provide a simple and accurate way to achieve the desired thickness regardless of reactant flux homogeneity. This is one of the greatest strengths of ALD, besides excellent uniformity and conformity particularly for high aspect ratio structures, compared to other deposition methods. However, it is also a limitation for certain applications.

Because the growth rate of typical ALD processes tends to be rather low compared to many other thin film processes, it requires a more time-consuming process to achieve a given thickness.

However, given the fact that the high-k oxide layer is within the order of a few nanometres, the advantages offered by ALD still much outweighs its limitation in the control of film thickness, particularly in industrial batch processing.

Another important aspect affecting the evolution of ALD technique is the utilisation of an increasingly wider range of chemical precursors. Together with the development of the ALD hardware, precursor chemistry has played an important role in expanding the varieties of materials that can be deposited by ALD. From the chemical viewpoint, precursors suitable for high-k oxides can be mainly grouped into the following categories: halides, alkoxides, β-diketonates, cyclopentadienyl-type compounds and amido complexes [62-64]. Among many critical requirements for a good ALD precursors [61, 64], thermal and chemical stability, sufficient volatility and reactivity are the most important factors, especially when the growth conditions at low or intermediate temperatures are concerned. Traditionally, these properties have been some of the limiting factors in expanding the application envelope of thermal ALD due to the constraints imposed by the available and suitable chemicals. However, the recent development in precursor chemistry, particularly in organometallics, has partly helped remove that barrier.

Other recent developments of ALD in terms of technique improvements are Liquid-injection (LI) ALD and Plasma-enhanced (PE) ALD. The LI derivative has been developed to overcome the problem with many precursors for thermal ALD: low volatility at temperatures below the decomposition thresholds. By dissolving the precursors in inert organic solvents such as anhydrous toluene or heptanes and transporting the precursors to the reaction chamber in the vapour form of dilute precursor solution, LIALD helps to reduce the high temperatures required to evaporate pure precursors and hence, more types of precursors can be employed. The PE derivative, on the other hand, has been developed to provide a more sufficient ALD pathway by providing energetic radicals or ions by means of plasma generation to remove ligands or surface activation. Since these radicals or ions can react with the surface ligands with minimal to no activation energy barrier, PEALD generally results in an increased reaction rate and an improved removal of volatile products at lower temperatures compared to thermal ALD process.

2.5.2 Chemical Vapour Deposition (CVD)

Chemical vapour deposition (CVD), like ALD, is the process involving a volatile compound of a material to be deposited, with other gaseous reactants, to produce a non-volatile solid that deposits atomistically on a suitably placed substrate. However, in CVD, both reactants are introduced simultaneously and react on the substrate via a thermally assisted reaction. A large variety of films and coatings including metals, semiconductors and insulators in either crystalline or amorphous form have been investigated by CVD. Compared to several other methods, one of the most distinct advantages that CVD offers is a very high growth rate, even at low temperature. In addition, other advantages making this technique quite favourable include the affordable cost of the equipment and operating expenses, the suitability for both batch and semi-continuous operation, and the compatibility with other processing steps. Aside from conventional CVD, some other derivatives have been developed to improve the performances of the method or for specific application such as Metal-organic CVD (MOCVD), Liquid-injection MOCVD, Plasma-enhanced CVD and laser-enhanced CVD [65]. In terms of processing pressure conditions, CVD can be classified into two main groups: atmospheric and low-pressure, of which the latter one has been used extensively in thin film deposition for semiconductor industry [66].

The basic principle of CVD can be presented by the following primary steps: (i) the introduction of precursor(s) into a reaction chamber, (ii) gas phase collisions between precursor molecules, (iii) transport of precursors to the substrate, (iv) absorption of the precursors onto the substrate, (v) the adatoms migration and film-forming chemical reactions on the substrate, (vi) desorption of the adsorbed molecules, (vii) surface nucleation, and (viii) desorption of the gaseous by-products of the reaction. Depending on the growth temperatures, two main CVD operational regimes can be categorised. They are mass-transport limited regime at high temperatures and surface-reaction limited regime at low temperatures respectively [66]. The role of precursor chemistry hence has a strong influence on the development of CVD in a similar way to ALD.

As mentioned before, one of the main advantages of CVD is the high growth rate. However, for applications that require very thin films, this can also be a disadvantage. For applications such as dielectric deposition for MOS devices, CVD cannot give the level of thickness control required and ALD is highly advantageous in this case. Another issue with CVD for application such as CMOS fabrication comes from the high demand of uniformity and conformity of ultrathin films, which is another drawback compared to ALD.

2.5.3 Molecular Beam Epitaxy (MBE)

Molecular Beam Epitaxy (MBE) is a deposition technique originally designed to undertake epitaxial film growth on a crystalline substrate at ultrahigh vacuum (UHV) and low temperature. Traditionally, it has been used to grow single crystal films such as GaAs and other compounds from group III and V in the periodic tables as well as elemental metals [67]. Many of these compounds are important constituents in modern microwave electronics and optoelectronics, high speed digital and analogue devices and ICs, etc. The main operational principle of MBE involves controlling the flux of atomistic beams of ultra-pure metallic sources directed towards a heated substrate. The flux of metals on the surface results in deposition of material and if the conditions are correct, epitaxial formation of the required material. In solid-source MBE, ultra-pure elements such as Ga and As are heated in separate Knudsen effusion cells until they begin to slowly sublimate. The gaseous elements then condense on the substrate, where they may react with each other to form the single crystal film with desired structure, e.g. GaAs. The term "beam" means that evaporated atoms nearly do not interact with each other or vacuum chamber gases until they reach the wafer, due to the long mean free paths of the atoms. Actuation of open/close function of the source shutters allows film growth to be controlled at the atomic level within a monolayer. This in turn offers the ability to precisely control epitaxial film growth and composition, making it a highly attractive technique for many academic and industrial scientists.

The main advantage of MBE is the ability to grow very high quality epitaxial growths or complicated structures that are virtually impossible to obtain by other techniques. MBE also prevails over other techniques in terms of impurities within

the films due to its high UHV processing conditions and the heterointerfaces can be kept to the minimum. MBE also offers highly accurate film compositions and complex films can be deposited without the need of complex chemical delivery system as typically required by other methods. In terms of process control, it has the most advantageous position among all the growth methods because the UHV conditions are highly compatible with a wide range of in situ surface analytical equipments, which can be either directly attached or connected to the growth chamber. These equipments enable the monitoring of the chemical composition and physical structure of the so-called epilayers throughout the growth process, thus provide excellent control. The main disadvantages of MBE are its relatively slow growth rate, complex and expensive equipment due to its high vacuum demand and associated components and difficulty to integrate with other techniques at industrial production level.

Recently, the use of MBE for high-k oxides has focused on the growth of perovskite films for applications in both gate logic structure and DRAM [66]. Given the fact that perovskite materials offer very high k-values and the continuously pressing demand for higher-k oxides to succeed HfO_2 in CMOS devices, MBE may be the competing method of choice against ALD in the future, at least at the research level in laboratory.

2.5.4 Ion Beam Assisted Deposition

The concept of ion beam assisted deposition (IBAD) relies on energetic ions to stimulate the surface reactions of precursor atoms that are generated with an electron-beam evaporator and deposited on a substrate. Because the process utilises ions as reactant, ion bombardment is the key factor to control the film properties in the IBAD process. Regarding the application of high-k oxide films, HfO_2 was reportedly deposited by this technique in [43] and ZrO_2 elsewhere [66]. For IBAD application of high-k dielectric materials, energetic oxygen ions in a vacuum system are used to convert deposited surface metal atoms into metal oxides for thin film deposition. The stoichiometric composition of the oxide films can be altered by the transport ratio of the metal vapour against the oxygen beam and the ion energy.

This is a potential advantage of this technique since various stoichiometries of oxide films can be created to investigate their impacts on film structures. Another advantage that this technique can provide is the ability to form complex metal oxides without the use of many chemical precursors.

References

1. Robertson, J. (2006) High dielectric constant gate oxides for metal oxide Si transistors. *Reports on Progress in Physics,* **69** (2), 327-396.
2. International Technology Roadmap for Semiconductors, http://www.itrs.net/home.html.
3. Gusev, E. P., Narayanan, V. and Frank, M. M. (2006) Advanced high-k dielectric stacks with poly-Si and metal gates: Recent progress and current challenges. *IBM Journal of Research & Development,* **50** (4/5), 387-410.
4. Wilk, G. D., Wallace, R. M. and Anthony, J. M. (2001) High-k gate dielectrics: Current status and materials properties considerations. *Journal of Applied Physics,* **89** (10), 5243-5275.
5. Principle of semiconductor devices, http://ecee.colorado.edu/~bart/book/book/chapter6/ch6_2.htm.
6. Neamen, D. A. (2003) *Semiconductor Physics and Devices - Basic principles (3rd edition),* McGraw-Hill,
7. Stoneham, A. M., Gavartin, J. L. and Shluger, A. L. (2005) The oxide gate dielectric: do we know all we should? *Journal of Physics-Condensed Matter,* **17** (21), 2027-2049.
8. Demkov, A. A. and Navrotsky, A. (2005) *Materials Fundamentals of Gate Dielectrics,* Springer,
9. Kao, K. C. (2004) *Dielectric phenomena in solids,* Elsevier Academic Press,
10. Hall, S., Buiu, O., Mitrovic, I. Z., Lu, Y. and Davey, W. M. (2007) Review and perspective of high-k dielectrics on silicon. *Journal of Telecommunications and Information technology,* **2**, 33-43.
11. Engstrom, O., Raeissi, B., Hall, S., Buiu, O., Lemme, M. C., Gottlob, H. D. B., Hurley, P. K. and Cherkaoui, K. (2007) Navigation aids in the search for future high-k dielectrics: Physical and electrical trends. *Solid-State Electronics,* **51**, 622-626.
12. G. D. Wilk, R. M. W., J. M. Anthony (2001) High-k gate dielectrics: Current status and materials properties considerations. *Journal of Applied Physics,* **89** (10).
13. Maruyama, T. (2000) Cerium dioxide thin films prepared by chemical vapor deposition from cerium dipivaloylmethanate. *Journal of Materials Science Letters,* **19** (19), 1723-1725.
14. Paivasaari, J., Putkonen, M. and Niinisto, L. (2002) Cerium dioxide buffer layers at low temperature by atomic layer deposition. *Journal of Materials Chemistry,* **12** (6), 1828-1832.
15. Ho, M. T., Wang, Y., Brewer, R. T., Wielunski, L. S. and Chabal, Y. J. (2005) In situ infrared spectroscopy of hafnium oxide growth on hydrogen-terminated silicon surfaces by atomic layer deposition. *Applied Physics Letters,* **87** (13).
16. Narayanan, V., Guha, S., Copel, M., Bojarczuk, N. A., Flaitz, P. L. and Gribelyuk, M. (2002) Interfacial oxide formation and oxygen diffusion in rare earth oxide – silicon epitaxial heterostructures. *Applied Physics Letters,* **81** (22), 4183-4185.
17. Fanciulli, M. and Scarel, G. (2007) *Rare Earth Oxide Thin Films,* Springer-Verlag Berlin Heidelberg,

18. Navrotsky, A. (2005) Thermochemical insights into refractory ceramic materials based on oxides with large tetravalent cations. *Journal of Materials Chemistry,* **15** (19), 1883-1890.
19. Zhu, W. J., Tamagawa, T., Gibson, M., Furukawa, T. and Ma, T. P. (2002) Effect of Al inclusion in HfO_2 on the physical and electrical properties of the dielectrics. *IEEE Electron Device Letter,* **23** (11), 649-651.
20. Deshpande, A., Inman, R., Jursich , G. and Takoudis, C. (2006) Characterization of Hafnium oxide grown on silicon by atomic layer deposition: Interface structure. *Microelectronic Engineering,* **83** (3), 547-552.
21. Foster, A. S., Gejo, F. L., Shluger, A. L. and Nieminen, R. M. (2002) Vacancy and interstitial defects in hafnia. *Physical Review B,* **65** (17).
22. Houssaa, M., Pantisanoa, L., Ragnarssona, L. A., Degraevea, R., Schrama, T., Pourtoisa, G., De Gendta, S., Groesenekena, G. and Heyns, M. M. (2006) Electrical properties of high-k gate dielectrics: Challenges, current issues, and possible solutions. *Materials Science and Engineering Reports,* **51** (4-6), 37-85.
23. Ganduglia-Pirovano, M. V., Hofmann, A. and Sauer, J. (2007) Oxygen vacancies in transition metal and rare earth oxides: Current state of understanding and remaining challenges. *Surface Science Reports,* **62**, 219-270.
24. Gavartin, J. L., Ramo, D. M., Shluger, A. L., Bersuker, G. and Lee, B. H. (2006) Negative oxygen vacancies in HfO_2 as charge traps in high-k stacks. *Applied Physics Letters,* **89** (8).
25. Umezawa, N., Shiraishi, K., Sugino, S., Tachibana, A., Ohmori, K., Kakushima, K., Iwai, H., Chikyow, T., Ohno, T., Nara, Y. and Yamada, K. (2007) Suppression of oxygen vacancy formation in Hf-based high-k dielectrics by Lanthanum incorporation. *Applied Physics Letters,* **91**.
26. Ribes, G., Mitard, J., Denais, M., Bruyere, S., Monsieur, F., Parthasarathy, C., Vincent, E. and Ghibaudo, G. (2005) Review on high-k dielectrics reliability issues. *IEEE Transactions on Device and Materials Reliability,* **5** (1), 5-19.
27. International Technology Roadmap for Semiconductors (2009 Edition): Emerging Research Materials , http://www.itrs.net/Links/2009ITRS/2009Chapters_2009Tables/2009_ERM.pdf.
28. Zhao, X. and Vanderbilt, D. (2002) First-principles study of structural, vibrational, and lattice dielectric properties of hafnium oxide. *Physical Review B,* **65** (23), 233106.
29. Govindarajan, S., Boscke, T. S., Sivasubramani, P., Kirsch, P. D., Lee, B. H., Tseng, H. H., Jammy, R., Schroder, U., Ramanathan, S. and Gnade, B. E. (2007) Higher permittivity rare earth doped HfO_2 for sub-45-nm metal-insulator-semiconductor devices. *Applied Physics Letters,* **91** (6).
30. Cockayne, E. (2008) Effect of ionic substitutions on the structure and dielectric properties of hafnia: A first principles study. *Journal of Applied Physics,* **103**.
31. Fischer, D. and Kersch, A. (2008) The effect of dopants on the dielectric constant of HfO_2 and ZrO_2 from first principles. *Applied Physics Letters,* **92** (1).

32. Lee, C. K., Cho, E. N., Lee, H. S., Hwang, C. S. and Han, S. W. (2008) First-principles study on doping and phase stability of HfO_2. *Physical Review B,* **78** (1).
33. Yashima, M., Takahashi, H., Ohtake, K., Hirose, T., Kakihana, M., Arashi, H., Ikuma, Y., Suzuki, Y. and Yoshimura, M. (1996) Formation of metastable forms by quenching of the HfO_2-$RO_{1.5}$ melts (R=Gd,Y and Yb). *Journal of Physics and Chemistry of Solids,* **57** (3), 289-295.
34. Teufer, G. (1962) Crystal structure of tetragonal ZrO_2. *Acta Crystallographica,* **15** (Nov), 1187.
35. Yashima, M., Kakihana, M. and Yoshimura, M. (1996) Metastable-stable phase diagrams in the zirconia-containing systems utilized in solid-oxide fuel cell application. *Solid State Ionics,* **86-88**, 1131-1149.
36. Wang, J., Li, H. P. and Stevens, R. (1992) Hafnia and hafnia-toughened ceramics. *Journal of Materials Science,* **27** (20), 5397-5430.
37. Li, P. and Chen, I. W. (1994) Effect of dopants on zirconia stabilization - An X-ray Absorption study .2. Tetravalent dopants. *Journal of the American Ceramic Society,* **77** (5), 1281-1288.
38. Li, P., Chen, I. W. and Pennerhahn, J. E. (1994) Effect of dopants on zirconia stabilization - An X-ray Absorption study .1. Trivalent dopants. *Journal of the American Ceramic Society,* **77** (1), 118-128.
39. Li, P., Chen, I. W. and Pennerhahn, J. E. (1994) Effect of dopants on zirconia stabilization - An X-ray Absorption study .3. Charge-compensating dopants. *Journal of the American Ceramic Society,* **77** (5), 1289-1295.
40. Garvie, R. C. (1965) Occurrence of metastable tetragonal zirconia as a crystallite size effect *Journal of Physical Chemistry,* **69** (4), 1238.
41. Wolten, G. M. (1963) Diffusionless phase transformations in zirconia and hafnia. *Journal of The American Ceramic Society,* **46** (9), 418-422.
42. Holgado, J. P., Espinos, J. P., Yebero, F., Justo, A., Ocana, M., Benitez, J. and Gonzales Elipe, A. R. (2001) Ar stabilization of the cubic/tetragonal phases of ZrO2 in thin films prepared by ion beam induced chemical vapour deposition. *Thin Solid Films,* **389** (1-2), 34-42.
43. Manory, R. R., Mori, T., Shimizu, I., Miyake, S. and Kimmel, G. (2002) Growth and structure control of HfO_{2-x} films with cubic and tetragonal structures obtained by ion beam assisted deposition. *Journal of Vacuum Science & Technology A - Vacuum Surfaces and Films,* **20** (2), 549-554.
44. Gusev, E., Cabral, C., Copel, M. J., Emic, C. D. and Gribelyuk, M. (2003) Ultrathin HfO_2 films growth on silicon by atomic layer deposition for advanced gate dielectrics applications. *Microelectronic Engineering,* **69**, 145-151.
45. Scott, H. G. (1975) Phase relationships in the zirconia-yttria system. *Journal of Materials Science,* **10** (9), 1527-1535.
46. Ho, S. M. (1982) On the structural chemistry of zirconium oxide. *Materials Science and Engineering,* **54** (1), 23-29.
47. Lefevre, J. (1963) Fluorite-type structural phase modifications in systems having a zirconium or hafnium oxide base. *Annales de Chimie (Paris),* **8** (1-2).
48. Tani, E., Yoshimura, M. and Somiya, S. (1983) Revised phase diagram of the system ZrO_2-CeO_2 below 1400 degrees C. *Journal of the American Ceramic Society,* **66** (7), 506-510.

49. Pandolfelli, V. C., Rodrigues, J. A. and Stevens, R. (1991) Effects of TiO_2 addition on the sintering of ZrO_2-TiO_2 compositions and on the retention of the tetragonal phase of zirconia at room temperature. *Journal of Materials Science,* **26** (19), 5327-5334.
50. Michel, D., Mazerolles, L. and Jorba, M. P. Y. (1983) Fracture of metastable tetragonal zirconia crystals. *Journal of Materials Science,* **18** (9), 2618-2628.
51. Sheu, T. S., Tien, T. Y. and Chen, I. W. (1992) Cubic-to-tetragonal (t') transformation in zirconia-containing systems. *Journal of the American Ceramic Society,* **75** (5), 1108-1116.
52. Yashima, M., Morimoto, K., Ishizawa, N. and Yoshimura, M. (1993) Diffusionless tetragonal-cubic transformation temperature in zirconia-ceria solid solutions. *Journal of the American Ceramic Society,* **76** (11), 2865-2868.
53. Fujimori, H., Yashima, M., Sasaki, S., Kakihana, M., Mori, T., Tanaka, M. and Yoshimura, M. (2001) Internal distortion in ceria-doped hafnia solid solutions: High-resolution X-ray diffraction and Raman scattering. *Physical Review B,* **64** (13).
54. He, W., Zhang, L., Chan, D. S. H. and Cho, B. J. (2009) Cubic-structured HfO_2 with optimized doping of lanthanum for higher dielectric constant. *IEEE Electron Device Letters,* **30** (6), 623-625.
55. Adelmann, C., Sriramkumar, V., Van Elshocht, S., Lehnen, P., Conard, T. and De Gendt, S. (2007) Dielectric properties of dysprosium- and scandium-doped hafnium dioxide thin films. *Applied Physics Letters,* **91**.
56. Losovyj, Y. B., Ketsman, I., Sokolov, A., Belashchenko, K. D., Dowben, P. A., Tang, J. and Wang, Z. (2007) The electronic structure change with Gd doping of HfO_2 on silicon. *Applied Physics Letters,* **91**.
57. Chalker, P. R., Werner, M., Romani, S., Potter, R. J., Black, K., Aspinall, H. C., Jones, A. C., Zhao, C. Z., Taylor, S. and Heys, P. N. (2008) Permittivity enhancement of hafnium dioxide high-k films by cerium doping. *Applied Physics Letters,* **93** (18).
58. Kita, K., Kyuno, K. and Toriumi, A. (2005) Permittivity increase of yttrium-doped HfO_2 through structural phase transformation. *Applied Physics Letters,* **86** (10), 3.
59. Tomida, K., Kita, K. and Toriumi, A. (2006) Dielectric constant enhancement due to Si incorporation into HfO_2. *Applied Physics Letters,* **89** (14).
60. Böscke, T. S., Govindarajan, S., Kirsch, P. D., Hung, P. Y., Krug, C., Lee, B. H., Heitmann, J., Schröder, U., Pant, G., Gnade, B. E. and Krautschneider, W. H. (2007) Stabilization of higher-k tetragonal HfO_2 by SiO_2 admixture enabling thermally stable metal-insulator-metal capacitors. *Applied Physics Letters,* **91**.
61. Niinistö, L., Päiväsaari, J., Niinistö, J., Putkonen, M. and Nieminen, M. (2004) Advanced electronic and optoelectronic materials by Atomic Layer Deposition: An overview with special emphasis on recent progress in processing of high-k dielectrics and other oxide materials. *Physica Status Solidi A - Applied Research,* **201** (7), 1443-1452.
62. Puurunen, R. L. (2005) Surface chemistry of atomic layer deposition: A case study for the trimethylaluminum/water process. *Journal of Applied Physics,* **97** (12).

63. Sneh, O., Clark-Phelps, R. B. and Londergan, A. R. (2002) Thin film atomic layer deposition equipment for semiconductor processing. *Thin Solid Films,* **402** (1-2), 248-261.
64. Fischer, R. A. (2005) *Topics in Organometallic Chemistry: Precursor Chemistry of Advanced Materials CVD, ALD and Nanoparticles,* Springer-Verlag Berlin Heidelberg
65. Ohring, M. (2002) *Materials Science of Thin Films: Deposition and Structure (2nd Edition),* Elsevier Inc.,
66. Huff, H. R. and Gilmer, D. C. (2005) *High Dielectric Constant Materials - VLSI MOSFET Applications,* Springer-Verlag Berlin Heidelberg
67. Seshan, K. (2002) *Handbook of thin film deposition processes and techniques: Principles, Methods, Equipment and Applications (2nd Edition),* Noyes Publications / William Andrew Publishing,

Chapter 3 EXPERIMENTAL METHODS

3.1 Introduction

Details of main experimental techniques employed in the work of this thesis are described in this chapter. Firstly, the growth method of Ce-doped Hf-oxide films is presented, including details of precursors and other parameters involved in LIALD process. Following the film growth, principal analytical techniques used to characterise the films are described, comprising instrumental details and analytical procedure. They are XRD, UV Raman, MEIS, AFM, ellipsometry and weight gain analysis. Electrical properties of the films are extracted by using C-V, I-C and C-f measurements. Because of the thin film nature, some equipments not originally designed for thin film characterisation have been optimised in terms of data acquisition procedure to improve the quality of data obtained. Alongside with instrumental descriptions and setups, methods employed to analyse data are also presented with discussions about issues involving during the analysis.

3.2 ALD film growth

3.2.1 Introduction

As mentioned in the previous chapter, one of the most common techniques currently used to deposit thin films for microelectronics applications is Atomic Layer Deposition (ALD) (see chapter 2 for details). All the films investigated in this research project were deposited by a modified ALD process called Liquid-injection ALD. The method was initially developed for Metal-Organic Chemical Vapour Deposition (MOCVD) and later adopted for ALD. The main difference between conventional ALD and Liquid-injection ALD is the way in which the precursors are delivered into reaction chamber. While the former method relies on the thermal evaporation of precursors often with the aid of a flowing inert gas, the latter uses flash evaporation of precursor solution at point of use.

The precursors are dissolved in organic solvents and are then sprayed into a heated vaporiser as and when required, the precursor and solvent are flash evaporated and carried to the reaction chamber by flowing inert gas. Because the precursor is stored at room temperature and is only heated as required, it is potentially possible to employ a much wider variety of precursors. Precursors which might not be suitable for conventional delivery due to poor thermal stability or ones that suffer from low vapour pressures can often be used via direct liquid injection delivery. Moreover, this technique does not require constant heating of the precursors and hence, degradation of precursors is reduced and shelf life increased. A range of materials have been successfully deposited by this method [1-4] in our research group and the method is attracting significant interest from industry.

The following sections will describe the Aixtron AIX 200FE, which is the reactor used to produce all the films by Liquid-injection ALD. Details of growth parameters are given and discussed afterwards.

3.2.2 Liquid-injection ALD

3.2.2.1 Aixtron AIX 200FE

The Aixtron AIX 200FE system is a Liquid-injection MOCVD reactor, originally designed for deposition of various oxide materials on different types of substrates. The system has three independently controlled metal-organic precursor sources with Jipelec TriJet® liquid precursor delivery and evaporation system, a horizontal CVD quartz reactor with infrared lamp heating and a 2" wafer susceptor mounting stage with Gas Foil Rotation® and manual loading. A schematic of the system with its main components is shown in Figure 3-1.

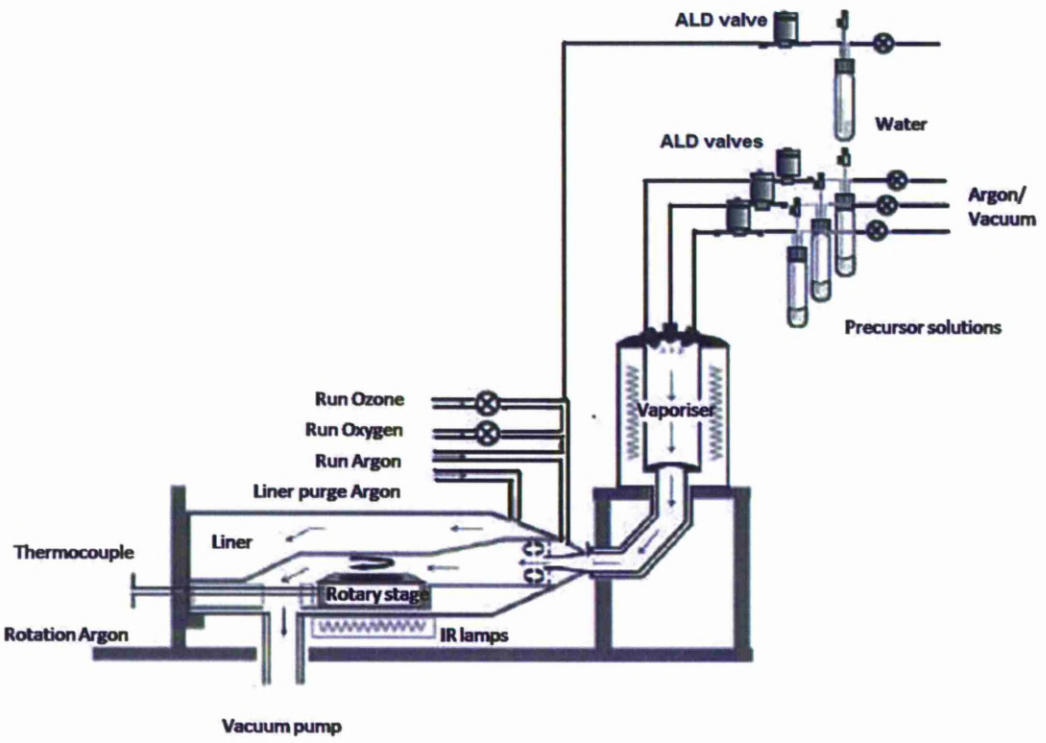

Figure 3-1: Schematic illustration of Aixtron AIX 200 FE system [2].

Precursors are dissolved in inert organic solvent (anhydrous toluene in this research) and stored in pressurised (1200 mbar) glass containers connected to the liquid injectors by stainless steel tubes. The liquid precursor delivery system comprises three separate liquid injectors and hence, enables a maximum of three different precursors to be injected individually with preset intervals (for ALD mode) or simultaneously (for CVD mode). To ensure that the required precursor is transported into and through the vaporiser, each injector tip is constantly supplied with a stream of heated Argon carrier gas. Depending on the amount of precursors required for the growth process, the injectors can be controlled via an integrated control system, which also allows different operating modes of the injectors, i.e. continuous or pulsed supply. For the LIALD process, the injectors are always set to operate in the pulsed mode. The frequency and opening times of the pulsed injectors are controlled by the pulse generators; the signals are amplified and sent to the injectors via the CACE control system. CACE controls when the signal is actually allowed to pass through to the injectors and when it is not, hence allowing control of precursor dosing.

In addition to the MO-precursor sources, co-reactants in the form of water, oxygen or ozone are also available on the system. Depending on which one of them is used, the supply of this oxidizing agent can be transferred to the reaction chamber via vapour (in the case of water) or through gas supply system (in the case of O_2). The water is supplied by a vapour draw source, controlled by a high-speed Swagelok ALD valve. If O_3 is required (the case of this research) then O_2 will be fed into an O_3 generator and subsequently fed into the reaction chamber.

In order to ensure that the precursors are thoroughly vaporised before entering reaction chamber, the vaporiser is fitted with embedded heating cartridges and thermocouples in five independent zones. This configuration allows the temperature of the vaporiser to be controlled consistently up to maximum 250 °C.

The substrate temperature is controlled by a graphite susceptor, which is heated by a set of five infrared lamps and controlled by a thermocouple embedded inside the susceptor. The substrate can be rotated via the gas driven mounting stage, which is driven by Argon gas, it can improve thickness uniformity, and particularly for CVD. Mass flow controllers (MFCs) are used on all gas supplies to ensure that the reactor flow conditions are stable and controllable in a repeatable fashion. An MFC is also used to pressurise the precursor containers.

All gases and by-products from the growth process are sucked out of the system by a vacuum pump after passing through a water-cooled filter situated at the outlet of the reaction chamber, where non-volatile materials will be condensed and separated. To maintain the required reactor pressure, a butterfly throttle valve is utilised at the pump inlet and controlled by a pressure gauge.

All of the aforementioned features are integrated and controlled by the CACE control software. This software allows the user to set up various operational parameters to suit any specific growth recipes as well as control the growth process in a programmable fashion.

3.2.2.2 Growth method

This section will presents the initial works carried out to characterise each of the individual precursors to determine their ALD growth windows, it also discuss the growth of the Ce-doped Hf-oxide. Firstly, all growth parameters used to deposit Ce-doped Hf oxide films are presented in Table 3-1 below.

Table 3-1: Summarised growth data for Ce-doped Hf oxide films on Si substrates

Evaporator temperature	**160°C**
Reactor pressure	**5 mbar**
Injection rate	**2.5µl/pulse (4 pulses/cycle)**
Solvent	**Toluene**
Precursor concentration	**0.05M**
Argon flow	**200 sccm**
Pulse sequence (precursor/purge/O_3/purge)	**2 / 2 / 0.5 / 3.5 sec.**
No. of cycles	**15 - 300**
Ce:Hf precursor ratio's	**1:2; 1:4; 1:9; 1:12; and 1:19**

All these parameters have been chosen after many trials to determine the optimal reactor conditions for the growths from various growth studies carried out in this reactor before. Specifically, the chosen temperature was selected as the result of initial studies of ALD characteristics from each individual precursor to match the optimal growth rate. To create the Ce-doped Hf oxide films, two single sources were employed, namely $Ce(thd)_4$ (thd = tetrakis(2,2,6,6-tetramethyl-3,5-heptanedionato) and $[(MeCp)_2HfMe(OMe)]$ ($MeCp=CH_3C_5H_4$). Initial attempts to grow with the $Ce(thd)_4$ with water as a co-reactants in the ALD process failed, however, this was not particularly surprising as thd -based compounds are known to be too stable for this reaction. As a result, ozone was used instead of water; the use of ozone for this particular precursor were also reported in some previous studies involving the growth of CeO_2 [5, 6].

In order to find out the suitable temperature for the growth of this binary oxide film, ALD studies were conducted for each individual precursor with 300 cycles over a range of temperatures. The results are shown in Figure 3-2 to illustrate the growth rates of CeO_2 and HfO_2 respectively with ozone used as oxygen source.

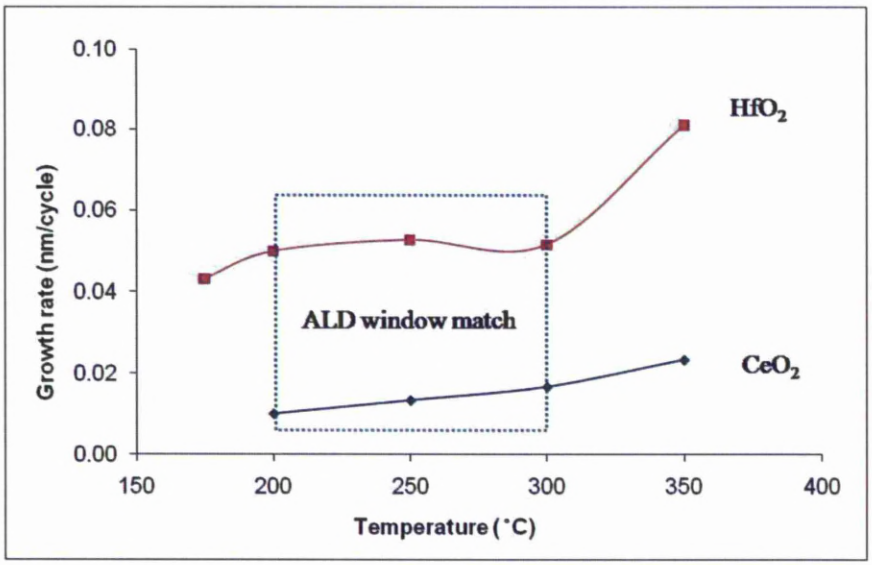

Figure 3-2: ALD growth curves for $Ce(thd)_4$ and $[(MeCp)_2HfMe(OMe)]$ with ozone.

The ALD growth curves obtained from each single precursor shown above indicates that the ALD window for HfO_2 is the temperature range from 200 °C to 300 °C while in the case of CeO_2, the ALD window is not clear. Therefore, the growth temperature for the growth of Ce-doped Hf oxide films was chosen at 300 °C to maximise the reactivity of $Ce(thd)_4$ within the upper limit of HfO_2 ALD regime.

The cerium percentages within different films were controlled by varying the ALD cycle ratios between these two precursors as presented in Table 3-1 above. Accordingly, the mixed oxide was formed by a growth process essentially following nano-laminate style deposition. In other words, several cycles of one process (HfO_2 ALD cycles) were carried out before the second process was introduced (CeO_2 ALD cycles).

3.2.2.3 Sample preparation for subsequent characterisations

After the films were grown, all of them were stored in sealed boxes to prevent them from dusts and moistures. For following heat treatments and subsequent characterisations such as XRD, Raman, MEIS, etc. each sample was cut into small pieces approximately 1 cm x 1 cm. Before and after characterisations, all pieces from different samples were wrapped with optic-grade tissues and kept inside plastic boxes or air-tighten bags to avoid scratches and contaminations from the ambient environment.

3.3 X-ray Diffraction (XRD)

3.3.1 Introduction

X-ray diffraction (XRD) has been used extensively within this research to investigate the crystal structures and the phase compositions of the films. The technique provides important information about the structural evolutions and phase stabilisations following different post-thermal treatments and particularly, the role of cerium in stabilising the desirable phase derived from pure HfO_2.

3.3.2 Background

After the discovery of X-rays by W.C.Rontgen in 1895 and the first diffraction experiment undertaken from a single crystal by Max von Laue in 1912, XRD has become a powerful tool in the study of crystallographic structures of different types of materials. Initially developed and used extensively in mineralogy, it has been successively utilised by many branches of sciences.

The widespread use of this technique relies on a phenomenon called diffraction which is an effect observed when electromagnetic waves interact with matters. Essentially, there are three different types of possible interactions that can happen when a material is exposed to radiations (X-ray in this case). The first one is called photoionisation, which is an inelastic scattering process. In this process, the electrons can be released from their bound state with the atoms due to the energy and momentum is transferred from the incoming beam.

Another second inelastic scattering, named the Compton effect, can also take place. The energy from the X-ray is transferred to the electrons similar to the photoionisation but not liberating electrons from their bindings with the atoms. The last process, which is named the Thomson scattering effect, is an elastic scattering. In this process, the wavelength of the impinging X-ray remains unchanged in contrast to the two scattering processes mentioned above. This is the very scattering effect that responsible for the phenomenon of diffraction caused by X-ray radiation.

During the course of the interactions, if the radiation wavelength is on the same scale as the interatomic distance in the periodic structures, it gives rise to diffraction patterns at specific positions in spaces. The interferences between X-ray and matters can either be constructive or destructive. Constructive interference occurs when certain geometrical constraints are satisfied, also known as the Bragg condition. This principle is schematically shown in Figure 3-3.

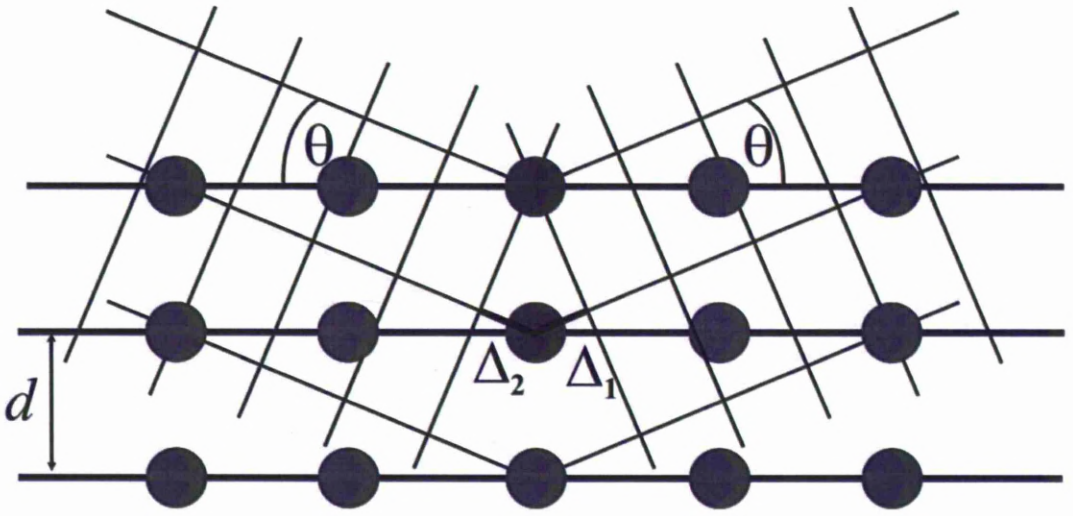

$$\Delta_2+\Delta_1=2d\cos(90^\circ-\theta)=2d\sin\theta$$

Figure 3-3: Basic diffraction geometry by Bragg's law [7].

Consider a set of crystallographic lattice planes comprising of parallel layers of atoms separating by a distance d as shown in Figure 3-3. When this structure is irradiated by X-rays at an incidents angle of θ, the phase shift of the plane wave for two adjacent atoms will be the sum of Δ_1 and Δ_2.

This sum is equal to 2dsin θ as a simple trigonometrical calculation is performed. For constructive interference of the reflected waves, they must be in phase with the incoming ones. In other words, the phase shift has to be a multiple of incident wavelength. This is the very condition for a simple diffraction geometry which was first formulated by W.H.Bragg and W.L.Bragg in 1919, hence the name Bragg's law:

$$2d \sin\theta = n\lambda \qquad \text{(Equation 3.1)}$$

n: integer; d: interplanar spacing (Å); λ: radiation wavelength (Å); θ: diffraction angle (°)

To make use of the diffraction technique to study crystal structures of ordered matters, the radiation wavelength used has to be comparable to the magnitude of the interplanar spacings. This can be achieved by using various types of metals to generate a range of X-rays with different wavelengths depending on the specific material under investigation. One of the most popular sources used is Copper, which generates an X-ray with wavelength about 1.5418 Å. This X-ray source was used within this work to study the crystal structures and phase stabilisations of Ce-doped Hf oxide films. The diffraction data from all the films were collected by utilising the θ/2θ scan configuration, which essentially detects and plots the intensities against incident angles (see section 3.3.3 for more details). By obtaining data from this scan configuration, important information such as structure, phase, interplanar spacing, crystallite size, .etc can be derived (see section 3.3.4).

In terms of identifying the structures or phases existing in a sample of material, the diffraction data is often compared to database data files. Two of the most common sources of references are ICDD (International Centre for Diffraction Data) and CSD (Cambridge Structural Databases), which cover a wide range of materials and are continually updated.

By comparing the obtained diffractograms with available references, unknown structures and phases from the investigated material can be revealed. This process, however, requires some basic understandings about periodicity existing in any given crystalline materials. In crystallographic study, any ordered material can be illustrated in 3-D construction by using the well-known Miller index system.

Any crystalline material comprises of atoms or molecules arranged in many different ways called lattice planes. These specific planes are parallel to each other and intersect the axes of crystallographic unit cell. The unit cell on its own is not a real image of how atoms or molecules are located but rather a mathematical concept to illustrate arrays of points, any of which must have exactly the same surroundings in the same direction specified. The index of any plane mentioned above involves three integers *h, k, l* which represents the intersection points of the plane *h/a, k/b* and *l/c* respectively with a chosen unit cell with arbitrary dimensions *a, b* and *c*. An example for some Miller-indexed planes in a simple cubic unit cell is given in Figure 3-4 .

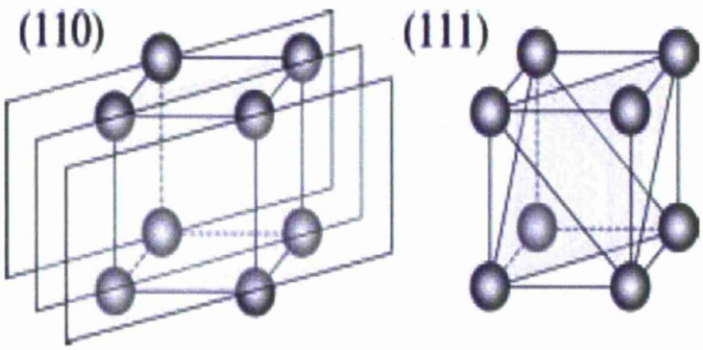

Figure 3-4: Lattice plane (110) and (111) for a simple cubic structure.

To investigate the crystallographic structures of any given materials, powder diffraction is normally carried out to ensure all possible planes can be detected and all plane orientations are random. By doing so, crystal structure databases are built up and used as standard references.

However, the Ce-doped Hf oxide system under investigations in this work was formed in thin film deposited on crystalline silicon substrates. This can lead to some difficulties in terms of interpreting the XRD spectra and comparing them with powder references. Some common problems include that thin films normally found to be polycrystalline with potential preferred orientations, the influence from the substrate, small crystallite sizes and the possibility for co-existence of various phases, etc. Hence, the interpretation of thin film diffraction data has to be performed with all of these factors taken into account to yield reliable results.

3.3.3 Rigaku Miniflex XRD system

The system used to carry out all of the XRD study in this work was Rigaku Miniflex powder diffractometer. The equipment was designed originally to perform XRD studies on powder samples. However, it is also capable of doing diffraction studies on other types of samples. In the case of thin film samples, the volume of material available results in lower signal to noise ratio compared to powder samples. A brief description of the equipment main components and their operations will be given in the following paragraphs together with system calibration and optimisation for thin film data acquisition.

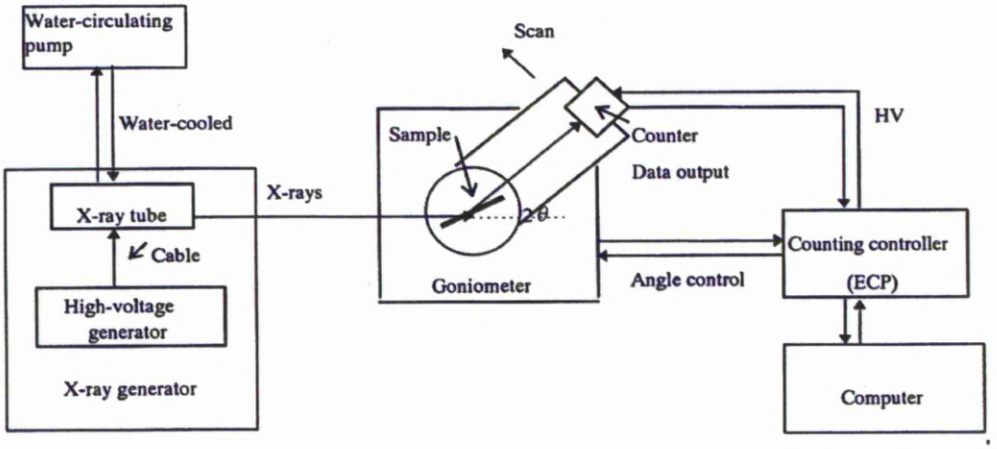

Figure 3-5: Main components of Rigaku Miniflex [8].

A block diagram illustrating the main components of the system is presented in Figure 3-5.At the centre of this system is the goniometer which is used to collect diffraction data from the sample. As mentioned before, the scan configuration of this system is θ/2θ, also known as Bragg-Brentano geometry. Therefore, the operation of the goniometer is dictated by this mode. A schematic representation of this scan mode is shown in Figure 3-6.

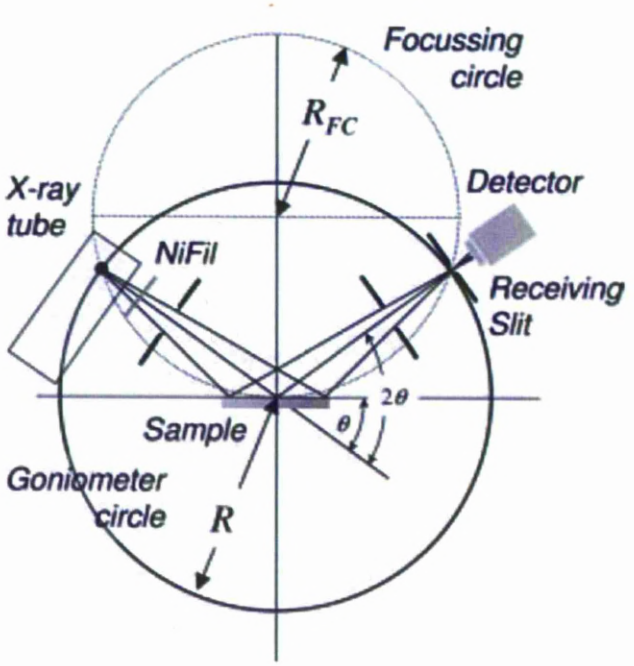

Figure 3-6: θ/2θ diffraction in Bragg-Brentano geometry [7].

Essentially, the goniometer rotates the sample to vary the incidence angle of the X-rays (θ) while at the same time moving the detector to an angle of 2θ to collect scattered radiation that meets the Bragg condition. For this instrument, the X-ray source is kept fixed during the scan while the sample and the detector are simultaneously rotated by an angle θ and 2θ respectively. The sample holder of this equipment is designed to accommodate either a relatively chunky sample such as a metal sheet or a revolving system comprising six circular container. The latter is particularly convenient when a large number of samples either in powder or thin film forms have to be analysed in succession. It also allows different automated scan configurations to be set up in a way that the data of each individual sample is recorded.

Another important part of the system is the X-ray tube and its related components. The wavelength of the X-rays generated by the tube is dependent on the type of target material used. For the current work, a Copper X-ray source with a Nickel filter was used to generate X-rays with a wavelength of 1.5418 Å. A sketch of a typical commercial X-ray tube is given in Figure 3-7.

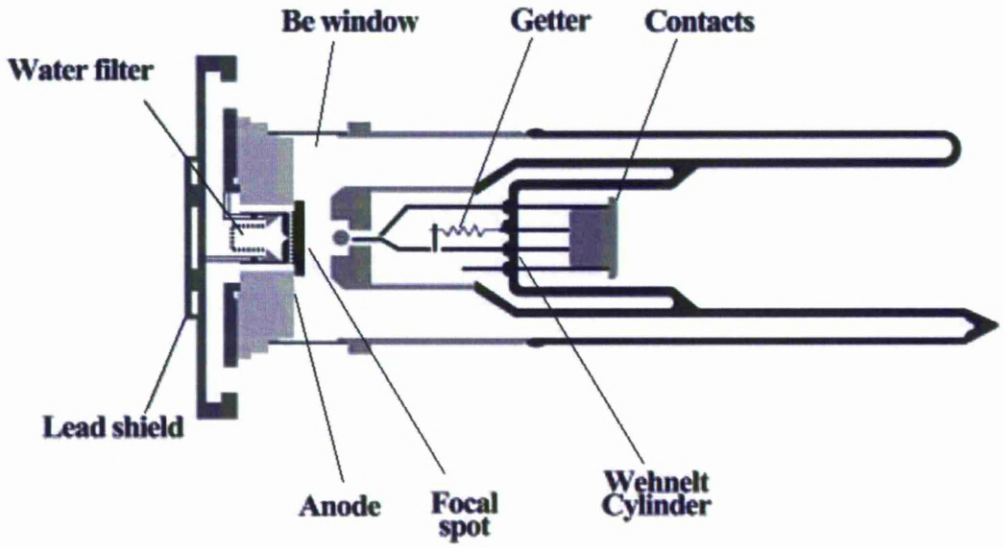

Figure 3-7: Schematic of a typical X-ray source [7].

X-rays are emitted when accelerated electrons from the cathode filament strike the anode, which is made from high purity metal. The choice of anode materials depends on the specific wavelength required by the analysis. Common metals used in anode fabrication are Copper, Molybdenum or Chromium to name but a few. The current flows between the filament and anode is in the order of a few tens of milliamps. The applied acceleration voltage typically varies between 5 kV and 25 kV. When the accelerated electrons hit the anode, X-rays are emitted. This is the result of ionisation and relaxation process of electrons bound to the atoms of the target material. Consequently, different characteristic radiation peaks will be produced such as Kα, Kβ, Lα, etc. These peaks, which are indicative of their sequent electron shell undergoing the processes of ionisation and relaxation, are embedded in a continuous background called Bremsstrahlung (German for braking radiation). For most applications, the Kα emission line is of the most importance as it gives the highest intensity emission compared to the other emission lines.The appearance of Kβ is not desirable for XRD since it is very close to the Kα line and as a result, severely affects the interpretation of diffraction patterns. As a result, the Kβ is often suppressed using a filter. For the Copper source used here, a Nickel filter is used to absorb Kβ line.

To make use of the Kα radiation for diffraction analysis, it is noteworthy to take into account of its doublet nature. In fact, Kα is not a single emission line, but is composed of two individual ones, namely $K\alpha_1$ (λ=1.5406 Å) and $K\alpha_2$ (λ=1.5444 Å). The existence of the $K\alpha_2$ line only affects the resolution of diffracted patterns at high scattering angles and in the case of polycrystalline thin films, is not commonly observed [7]. Hence, in this work, a typically weighted Kα line with an average wavelength 1.5418 Å is used.

In order to calibrate the system, a SiO_2 standard powder sample supplied with the equipment is used. The data from this standard sample is compared to a reference spectrum also supplied by the manufacturer or compare with other reference data available for SiO_2 powder. Necessary adjustments to the system can be done based on regular checks to ensure proper operation and accuracy of acquired data.

In terms of sample setup, the films of interest had to be accommodated within the central part of the sample holders by using a form of tacky rubber ("blue tag") to keep them stationary during the scans. In order to ensure the consistency of the measurements and minimise the errors during the scans, the flatness of the samples was of great importance. A piece of clean glass was used to gently pressed on top of the samples to align them at the same height with the holders, which in turn ensured the samples were parallel to the bases of the holders.

Because the system was originally designed to undertake powder diffraction study, it is necessary to optimise the scan conditions for thin films. For the Rigaku miniflex system, most hardware parameters are fixed and it is only the scan speed and data sampling method that can be optimised to give optimal signal-to-noise quality. The scan step is typically set to the recommended value by the manufacturer as 0.02°/ min, which is nearly the smallest value the system can achieve. Therefore, the quality of the obtained spectra is strongly influenced by the scan speed. Decreasing the scan speed will improve the signal-to-noise ratio of the spectra but only to a limited extent, in addition, there is always a compromise between, the signal quality and the overall scan duration.

To establish the optimal scan conditions for the thin film studies carried out in this work, initial studies were carried out to investigate the effect of scan speed on signal quality.

As the thickness range of the films within this research was between 15 nm to 25 nm, an initial study with a 20 nm thick HfO_2 film was carried out to optimise the scan speed. The scan speed of the system can be set between 0.01°/min and 100°/min and test scans were run using each of the two scanning modes available, namely continuous or fixed time mode. The main difference between them lies in the way the goniometer rotates during data acquisition. In continuous mode, the goniometer scans at a constant velocity, set by the operator, and the detector and electronics are set-up to collect and average the output for fixed periods of time during the scan. In contrast, the fixed time (FT) mode works by stepping the goniometer by a user defined angle and remains at this position for the required acquisition sampling time before stepping to the next angle. In terms of scan duration, the time required to complete one specific range of scattering angle is interchangeable between these two modes and can be converted from one to another. Therefore, the scan time for this initial study was presented in min/deg, which is the way the FT mode is set up. In fact, some other previous studies also performed with air annealed HfO_2 films revealed that the peak positions, the intensities of the peaks and the peak broadening were not influenced significantly by the scan speed. This issue is even more important in this study due to the fact that the signal-to-noise quality from thin films typically quite low and strong interference with the silicon substrate as well as the amorphous matrix possibly existed in some cases. To determine the optimal scan speed, the standard deviation of the background signal was measured as a function of scan speed. A lower standard deviation indicates a better signal-to-noise ratio and hence, peak identification and the resolution of the spectra can be improved. A graph of scan speed against background standard deviation is shown in Figure 3-8. From this, it is clear that both scan modes yielded similar trend. Thus, the scan speed chosen for all the concerned films throughout this work was determined as 0.2°/min in continuous mode, which is equivalent to 5 mins/degree as in FT mode shown in the graph.

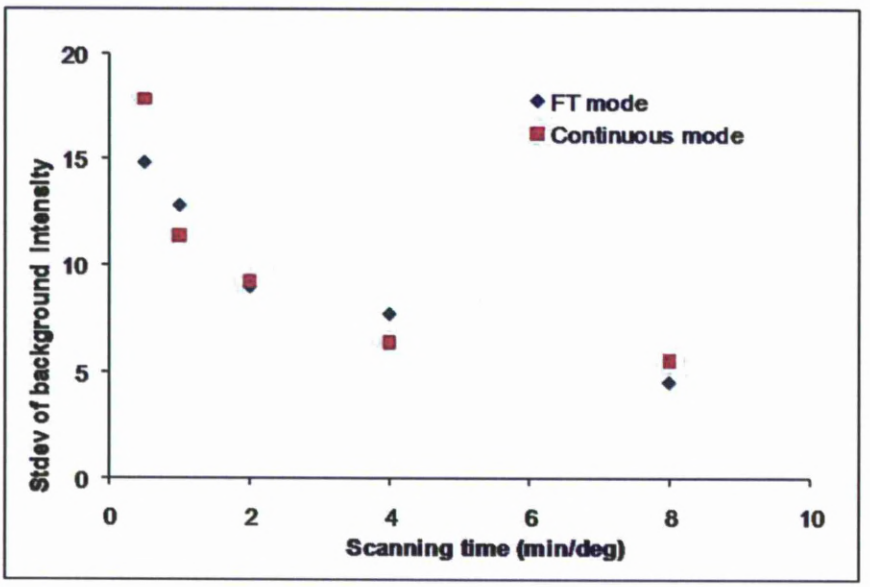

Figure 3-8: Spectra quality against scan speed for a 20 nm HfO_2 film

3.3.4 Data acquisition and analysis

Because the very nature of the samples was in thin film form, not all the peaks expected to appear in any given spectrum would match the reference spectra from powder samples. Hence, data analysis was only concentrated in a relatively narrow range of scattering angles, i.e. $2\theta = 20^{\circ} - 40^{\circ}$ only. This range of scattering angle was chosen after some preliminary trials in much wider ranges that possible to the scanning range available from the equipment to find out possible diffracted patterns from the films. Fortunately, most characteristic features of all HfO_2-based polymorphs are within this range and hence, sufficient information about crystal structures and phases can be determined.

In order to extract useful information from the diffracted patterns, the raw data requires some preliminary processing. For powder samples, this process typically involves the following steps: background subtraction to remove broad features that are usually associated with amorphous scattering, smoothing, $K\alpha_2$ stripping to remove shoulders on each peak caused by the weak $K\alpha_2$ emission line of the x-ray tube and finally peak searching and profile fittings to allocate unambiguously diffracted features [9]. This process was used as a guide to the data interpretation within this research.

Each of these steps can be done either manually or by various computer programmes developed for powder diffraction analysis. However, for thin film analysis, this process is not easily performed automatically as in the case of powder samples. The main reason is that in thin films only a few diffracted features can be detected and hence, preventing the profile fittings and structure refinements which normally require the whole patterns to be simultaneously analysed and fitted, for instance in Rietveld's method. Therefore, the data analysis for all the films in this work had to be done manually and some processing steps previously mentioned would be omitted as being explained in the following paragraphs.

The raw data collected from each sample was processed and analysed using Origin software, which is a specifically designed for graphical processing and analysis. The spectra then would be subjected to background subtraction to eliminate as much as possible the contribution of substrate interference and equipment noise. After that step, the peaks of interest would be identified. The smoothing and $K\alpha_2$ stripping were omitted in contrast to the powder diffraction data processing. The first reason for doing so were due to the fact that the following peak-fitting did not require smoothing as the programme would do it during this step. Moreover, as previously mentioned, the contribution of $K\alpha_2$ to the overall resolution in thin film diffraction was very little compared to $K\alpha_1$ and hence, the average wavelength $K\alpha$ was used instead. After this point, the raw data were ready for the next step, peak-fitting, and also the most important one in determining useful information about the crystal structures of the films under investigation.

The peak-fitting offered some peak shapes typically used in XRD data interpretation. They are Gauss, Lorentz, Pearson-VII and pseudo-Voigt functions. More details about mathematical descriptions and manipulations of those peak shapes can be found in [9] and other XRD text books. In this work, all the peak shapes adopted Lorentzian distributions mainly because of its simplicity in choosing fitting parameters compared to the other two latter functions, which are essentially the products of blending the two former functions in different proportions. In addition, this function has an advantage over the Gaussian type because it offers a better match to the peaks commonly found from thin films, i.e. long tails at the base and

relatively low intensities. If required, convoluted peaks appeared in films with mixed phases, e.g. monoclinic and cubic, could be separated by applying deconvolution process from the programme. The results from peak-fittings revealed that the errors for peak positions were between 0.02°and 0.05°; Full Widths at Half Maximum (FWHMs) were approximately between 0.01 radians and 0.03 radians. These errors were very small compared to the values yielded from peaks' parameters and hence, would be neglected in subsequent data analysis.

After the peaks were fitted, some important information about crystal structures could be derived, including the interplanar spacings, unit cell and crystallite sizes. The d-spacing of the various atomic planes can be calculated using:

$$d = \frac{\lambda}{2\sin\theta} \qquad \text{(Equation 3.2)}$$

d: interplanar spacing (Å); λ: X-ray wavelength (Å); θ: diffraction angle (°)

For a fluorite-type cubic structure such as Ce-doped Hf oxide in this work, the unit cell could be represented by one of its side, *a*. Thus, this parameter could be calculated based on the above d-spacing by using a basic relation:

$$\frac{1}{d^2} = \frac{1}{a^2} + \frac{1}{b^2} + \frac{1}{c^2}$$

Because the unit cell is a cubic, hence $a = b = c$ which gives:

$$a = d\sqrt{3} \qquad \text{(Equation 3.3)}$$

In the current work, this will be used as a rough approximation as Ce-doped Hf oxide is not strictly cubic, it is a metastable tetragonal with very small distortion from its fluorite-type parent form. However, as can be seen later from chapter 5, the results obtained from this calculation still agreed quite well with the cubic structure from pure HfO_2, which confirmed the validity in using this estimation.

The crystallite size contributing to the broadening observed in any diffracted feature can be estimated using the well-know Debye-Scherrer equation (Eq. 3.4).

In fact, the broadening effect from a sharp diffracted line is the sum of small crystallite effect with microstrain and instrumental error. However, these latter factors are very small and hence, could be neglected from this estimation.

$$\tau = \frac{K\lambda}{\beta \cos\theta} \qquad \text{(Equation 3.4)}$$

τ: mean crystallite size (Å), K: constant (K=0.9 typically), β: FWHM (radians), λ: X-ray wavelength (Å), θ: diffraction angle (radians)

3.4 Raman scattering

3.4.1 Introduction

The Raman effect, which was named after the Indian physicist C.V. Raman, has become an important tool in determining vibrations in molecules. Since its discovery in 1922, Raman scattering has provided researchers in many fields with a simple yet powerful source of information about molecule configurations, chemical structures and physical forms of various substances in different matter states. Coupled with recent advances in instrumental technology particularly in lasers, it is now widely regarded as one of the most important analytical techniques to deal with molecule structural investigations.

Within the scope of this work, the use of Raman scattering was necessary due to its ability to help tackle some unresolved issues in crystal structure analysis given by XRD study. In addition, it also provided a clearer insight into the phase stabilisation of Ce-doped Hf oxide films to obtain the desirable high-k phase against the stable monoclinic from pure HfO_2.

3.4.2 Background

When light interacts with matters, it mainly scatters by Rayleigh scattering, which is an elastic scattering process. The scattered photons will have exactly the same frequency and wavelength as the incident ones. However, there is also a small probability (1 photon in every 10^6-10^8) that the incident photon will be scattered with a slightly different frequency due to inelastic interactions with the scattering

molecule. Inelastic scattering occurs when the incident photon interacts with the vibrational states of the scattering molecule, this is the basis of the Raman effect.

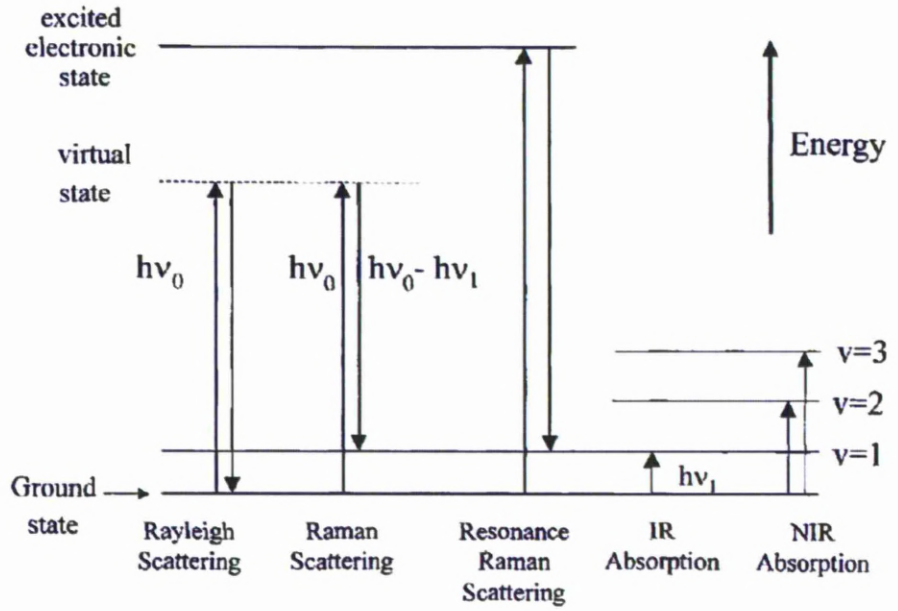

Figure 3-9: Various interactions of an incident light with matter [10].

In Figure 3-9, different types of interactions between an incident light with frequency ν_0 and matter are illustrated. When molecules with different vibrational quantum states $\nu_1, \nu_2, \nu_3 \ldots$, are exposed to this light, various processes can take place. Firstly, the well-known Infra Red (IR) and Near Infra Red (NIR) absorption processes can happen if the energy of the incident light is equivalent to the energy difference between the ground state and other higher vibrational modes. Consequently, IR absorption will take place when light at certain frequencies interacts and causes a change in molecular dipoles by vibrational modes. The loss of energy from the incident light will match exactly the energy required to excite oscillations of atomic bonds in heteronuclear molecules.

Besides absorption, another phenomenon called scattering can also happen. Basically, this is the result of interaction between the incident light with the electron clouds surrounding the nuclei of the molecules. This sort of interaction will create a virtual energy state which is unstable and hence, considered as a short-lived state. If only the electrons are involved in this process, the scattered photon will have the same energy as the incident one as illustrated in Rayleigh scattering.

However, if nuclear motion is induced by the interaction, then the result will be a shift in energy between the incident and scattered photons, i.e. Raman scattering. Raman scattering itself can be subdivided into two processes, namely Stoke scattering and anti-Stoke scattering. The main difference between them is the way the molecules interact with the incident light. If the molecules absorb energy, then the resulting scattered photon will have lower energy than the incident one and hence, have a higher wavelength, this is called the Stoke scattering. If on the other hand, the molecule imparts energy to the scattered photon, then this is known as anti-Stoke scattering. Furthermore, another competing process with Raman scattering but with much higher order of magnitudes can concurrently take place, which is known as fluorescence. Although both of them happen in the same way, they differ to the other fundamentally. In Raman scattering, the effect can take place at any frequency and hence, it is not a resonant process. In contrast, fluorescence can only happen after a certain resonance lifetime and at specific frequencies. In practice, fluorescence often appears strongly in the background of the Raman spectra and is undesirable as it interferes strongly or even hinders the Raman features. Therefore, great care is required to reduce fluorescence from the background in order to detect the actual Raman features.

Within this work, all the Raman spectra were recorded at room temperature in the Stoke scattering mode. This is due to the fact that at room temperature, the number of low energy states far exceeds the number of higher energy excited states, and hence Stoke scattering is stronger than anti-Stoke scattering. Conventionally, the unit typically used in Raman spectra recording on the horizontal axis are relative wavenumbers (cm^{-1}). These units are used as it is the change (shift) in frequency that is of interest rather than the absolute wavelength of the scattered photons.

In order to extract useful information from any given Raman spectrum, it is important to understand some basic principles about how a scattering peak appears, particularly when the material under investigation is in thin film form. Firstly, the incident light, usually from a highly monochromatic laser, has to induce a change in electronic polarisability within the molecule by creating some form of atomic displacement, which in turn corresponds to some type of vibrational mode. In contrast, the activation of any IR vibrational mode requires the change in dipole

moment induced by the incident light. Therefore, these two techniques are generally complimentary to each other when structural information about any given substance is of concern. These two different rules also lead to another rule, the so-called mutual exclusion rule. This rule essentially states that no IR and Raman band can be observed at the same frequency if the molecule under investigation has a centre of inversion. Another noteworthy point is besides the active modes due to vibrations of individual or groups of atoms and molecules, Raman scattering peaks can also be observed for phonons in crystalline materials, which are essentially due to the lattice vibrations in solids. Several detailed treatments on the vibrational modes and phonon vibrations can be found in many textbooks about vibrational spectroscopy and solid state physics. It is also of importance to be able to predict all possible active Raman modes for any given substance to interpret the scattering spectrum and find out information about its structure or phase evolution. However, this process is very complex and requires very complicated treatment using group theory, which is beyond the scope of this work. Rather than that, the Raman spectra obtained from experiments has been compared with available literature references dealing with Ce-doped Hf oxides or some other closely related materials with careful assertions and arguments.

3.4.3 Horiba Jobin Yvon Labram HR 800

All Raman spectra obtained from the films in this work were carried out by the Labram HR 800 system. The equipment was designed to undertake fast and accurate measurements not only for Raman scattering but also photoluminescence study over a wide range of laser wavelengths. The system is also equipped with a temperature-controlled cell to perform temperature-dependent Raman scattering analysis, which is mainly used in organic chemistry analysis and other temperature-sensitive substances. In order to give the most flexibility to the users to suit various analytical demands, the equipment is supplied with a range of laser choices comprising visible laser (red 633nm, green 515nm and blue 488nm), UV 325nm and NIR (768nm) lasers as well.

As mentioned earlier, one main serious issue with Raman scattering study is the co-existence of fluorescence, particularly in the visible range. This is also the problem

encountered at first efforts utilising Raman to study the crystal structures and phase evolutions of thin films in this project. All available lasers with this Raman system were tried but none of them returned any Raman scattering peaks from the films. The spectra either only showed background noise (likely fluorescence) in the case of blue and green laser or simply feature of silicon substrate (red and NIR lasers). One likely explanation for the failure to yield any Raman signals from these lasers might be due to their lower photon energies compared to the UV laser and hence, yielded lower scattering intensities. This was due to the fact that the Raman scattering intensity of any vibrational mode approximately scaled with the fourth power of the laser frequency employed. In addition, the employment of UV laser would also help reduce a large amount of fluorescence either from the sample or from other impurities which normally found on the film's surface and from the ambient environment.

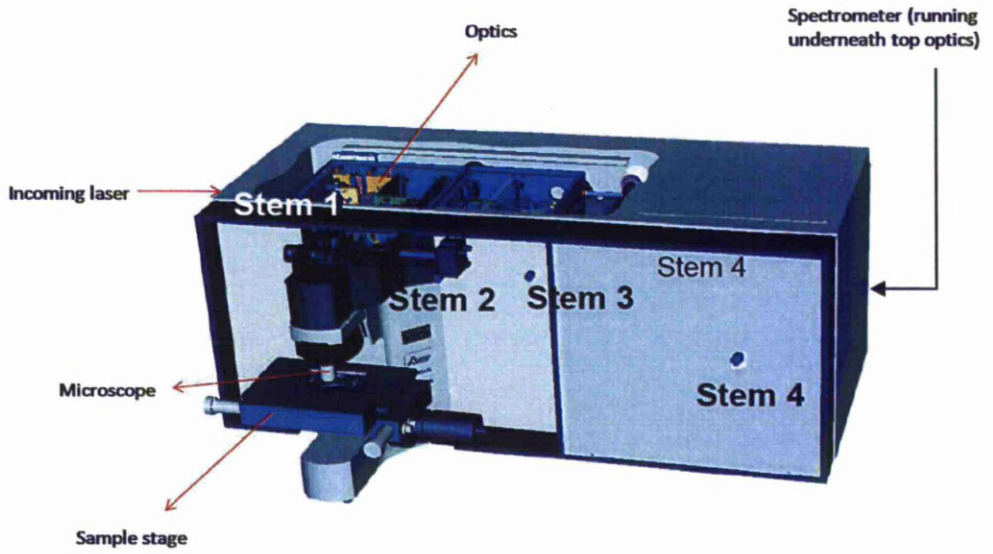

Figure 3-10: Labram HR 800 layout [11]

The layout of the Labram HR 800 is illustrated in Figure 3-10 for its main components. The system comprises four main parts which are the laser, the microscope, the spectrometer and the optics. The laser of choice is guided through a system of optics and focused onto the sample through a confocal lens, which provides the highest spatial resolution with maximum signal throughput. The spatial resolution can be achieved in the range between 0.3 and 1 cm^{-1}. The optics also carry the scattered light back into the spectrometer, which disperses the scattered signal into its constituent parts and onto the detector.

The system adopts a CCD-type (Charge Coupled Devices) detector, which is the most common detector used for applications with laser wavelength in the range between 200 and 800 nm [10]. In order to focus the laser to a specific area of the sample, an XYZ stage is mounted beneath the microscope system. The height of the stage is adjustable to achieve the best focus on the sample. The microscope, besides its function to give the desirable optical image magnification (10, 50 and 100 times), also serves as a tool to focus the laser onto the sample. For the UV laser, because it requires very expensive and higher quality optics, the lens used is rated at 40X magnification.

Besides these main components, the system is also equipped with a number of stems (push-pull bars) to allow fast switching between different functionalities. Stem 1 operates the camera beam-splitter, Stem 2 operates switching mirrors for UV-Vis and Vis-NIR lasers and Stem 3 operates the switching mirror for microscope and fibre entrance. Stem 4 is used when there is a need to switch the mirrors for top or side detectors. These stems provide the users a fast and simple way to change the configurations of the system to suit their analytical purposes.

For this system, the scattering configuration is performed in the 180 degree (back-scattering mode) arrangement. In this configuration, the laser is delivered through the lens and the scattered light is also collected back from the same lens. This arrangement is very common in the systems which use microscope to collect the light. In order to separate the actual Raman signal from scattered laser light, a notch filter is employed. The notch filter is designed to absorb a large fraction of the laser light without affecting the Raman signal; the bandwidth of the filter is 200 cm^{-1} beyond the frequency of the incident laser used. Because for monoclinic and tetragonal HfO_2-based materials polymorphs, some of their characteristic lines are very close to the exciting line of the laser used, i.e. in the region between 50 and 200 cm^{-1} beyond the excitation frequency of the laser, the use of such notch filter will inevitably lead to some losses of information.

Before measurements are carried out, the system requires calibrations to ensure that the spectrometer is set up properly. Firstly, white light is us used to calibrate the zero order mode of the spectrometer. This is called "zero calibration".

A known Raman peak from a single crystal silicon reference standard, which gives a very strong Raman band at 520 cm^{-1} is then used to complete the calibration process. Calibration is repeated at the start of each Raman session as small changes in environmental conditions can cause significant drifting. After calibration, the system is ready for data acquisition.

In this work, because all the films were deposited on silicon substrate, it was necessary to undertake a scan for the native silicon substrate prior to the data acquisition of the films. The data from the silicon substrate serves as a background reference spectrum, which is very important for data processing. Because the Raman scattering is quite a fast and effective process, typically a normal acquisition process could be set up using the acquisition time 30 seconds and averaged 4 times, which resulted in the whole scan process with duration about 20 minutes for the scattering range of interest between 200 and 800 cm^{-1}.

3.4.4 Data interpretation

The raw scattering data obtained from the films were fed into Origin and processed in the same way like the XRD data. Similarly to the steps described in the XRD section to process raw data, the Raman peaks were also fitted by using Lorentzian distribution. Unlike the XRD, the Raman spectra mainly yielded qualitative interpretation about the crystal structures and phase evolutions in this work. In fact, for bulk materials or even in nanocrystalline forms [12], quantitative information about peak shifts, crystallite sizes, phase fractions, etc. can be derived from analysing the Raman spectra of the interested materials.

Some preliminary efforts were performed in order to find out such relationships between the Raman peak characteristics and its related crystal or phase information but were not successful. The main reason for this failure was film thickness, which ranged from 15-25nm in the current work. Previous studies have been carried out on either bulk powders or on thick films (in the region of hundreds nanometres or microns), where the Raman signal is much higher due to sampling volume. In addition, defects in thin films themselves coupled with other mismatches in the crystal structures might hinder such typically observed phenomena that commonly

found in other forms. Besides, the strong inference from the silicon substrate, the breakdown of selection rules for distorted fluorite-type structures and small crystallite sizes all contributed to this issue. Nevertheless, the peak shapes were still fitted quite satisfactorily with good accuracy (the uncertainty for the peak positions was in the range between 0.5 and 1.5 cm^{-1}). Hence, by identifying main scattering peaks and deconvoluting overlapped ones, the information extracted from studying these Raman spectra were still very valuable on their own and when combined with results from XRD data, a more thorough insight about the role of cerium to stabilise the potential high-k phases of HfO_2 polymorphs was achieved.

3.5 Electrical characterisations

3.5.1 Introduction

In order to extract electrical information about Ce-doped Hf oxide films, particularly its dielectric constant, electrical measurements were carried out using C-V and I-V techniques. These electrical metrologies were developed and used widely in both academic research and industrial manufacture as standard tools to characterise electronic devices, e.g. CMOS built with SiO_2 as gate dielectric. Since the efforts of looking for alternative materials to replace SiO_2 has begun, these techniques have also been continuously adjusted and modified to stay as the main methods to characterise such new materials.

Due to the fact that most potential high-k materials are quite different from SiO_2 in terms of electrical behaviours and performances, various electrical models have been developed to address these differences and hence, required very complex mathematical treatments and many in-depth electrical expertises. Within the electrical characterisations for all the films in this project, only simple MOS-C structures are used. Because the main aim of the electrical measurements is to derive some basic electrical performances of these films, this structure and its related data interpretation is deemed sufficient to build up preliminary understanding about this potential material.

3.5.2 MOS Capacitor Fabrication

For I-V and C-V measurements, MOS capacitor structures were fabricated for each sample. Firstly, arrays of Gold dots to form the upper metal gate contacts were deposited using plasma sputtering of pure gold. The dots were formed by using a shadow mask, which was fabricated by laser drilling. The size of the dot was defined approximately equivalent to the size of the hole on the shadow mask, which was about 300 μm. Aluminium back contacts were then deposited uniformly over the back surface of each sample using vacuum deposition of pure Al to give Ohmic contacts. This back contact was crucially important to reduce large deviations afterwards in the C-V curves. Large deviations in C-V and I-V curves were observed in some preliminary experiments with films having no back contacts and hence, hindering meaningful information that can be extracted.

3.5.3 C-V profiler

The system used to carry out all of the electrical measurements consisted of two main components: the Keithley Model 4200 Semiconductor Characterisation System (4200-SCS) and 4980A Precision LCR meters. The experimental set up is illustrated in Figure 3-11. All of the controlled parameters of the measurements can be either input directly from the front panel of the analyser or by an in-house developed programme, which also serves the purpose of data acquisition. To aid the positioning of the probe on the chosen Gold dot, a microscope coupled with an XY stage is also attached to the main system. If excitation of minority carriers is required (normally for low frequency C-V), a source of light is available to be used. However, for high frequency C-V measurements, the data is taken in the dark only. To maintain a good and consistent back contact, samples are held firmly to the chuck station by vacuum, which is generated by a vacuum pump connected directly to the chuck station.

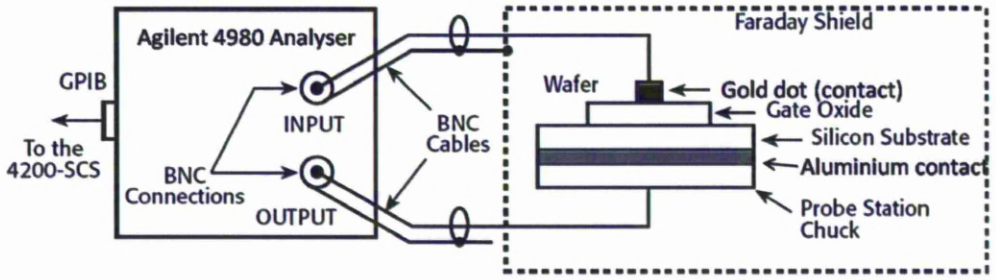

Figure 3-11: C-V test layout (adopted from [13])

The electrical measurements conducted within this work comprise three different types of data acquisition. They are I-V, C-V and C-f characterisations. The I-V test provides information about the leakage current (A) versus gate voltage (V). The data obtained from I-V curves will be used later to convert the leakage versus gate voltage to leakage current density versus (A/cm^2) electrical field strength (MV/cm), which are typically the units used in MOS-C devices metrology. In order to acquire the I-V data, a DC bias voltage is applied to the sample and increased in small steps (0.1V) to a preset voltage value. The current is recorded simultaneously with the voltage applied. The oxide is deemed to be "leaky when the current flowing through it reaches a limit, in practice this value is about some mA. The leakage current density is an important criterion to evaluate the films in terms of their performances and typically quoted at the electrical field strength ± 1 MV/cm. For all samples, at least 3 random dots were measured to ensure consistency. The number of measured dots per sample was in fact normally between 5 and 10 because some dots could be broken down during measurements.

The C-V and C-f are interrelated techniques. However, while the former test provides information about how capacitance changes with bias voltage at a fixed frequency, the latter reveals how the capacitance changes with varying frequency at a fixed bias voltage. To undertake a C-V test, a small AC signal (50mV) is applied to the chuck with a probe pick-up at the Gold gate. The frequency is set by the operator either at 10 KHz, 100 KHz and 1 MHz (for medium and high frequency C-V measurements) or over a wide range between 20 Hz to 2.5 MHz (for a C-f characterisations). The DC bias voltage is varied slowly in small step (0.1V) with an interval 10 ms between each recorded data point.

The range of DC bias voltage selected for each sample is normally the range of applied voltage determined from the I-V test done beforehand to ensure that full saturation of capacitance can be achieved.

The C-f measurement commonly follows afterwards the C-V test. Typically, the lower end of the frequency range was limited to around 10 KHz. The reason for this lower limit is that lower frequencies are of little interest for device applications. The bias voltage used for C-f measurements was set to the highest voltages from the C-V tests. If necessary, one or two more other lower but within close proximity to the highest bias voltage can also be measured.

Among these test, the high frequency C-V is the most important as it provides a means of calculating the k-value as well as other qualitative information about the oxide charges and interface states. Hence, trials and errors are used to obtain the best results possible for C-V curves. Variables can be voltage sweeping direction (from negative to positive bias voltage and vice versa), voltage step and delay time. In theory, the sweeping direction should not affect the C-V curves if the dielectric oxide layer is free from defects and relatively thick. However, in reality, this is normally not the case due to the effect of charge modulation amongst others. Because all the films in this work were deposited on *n*-type silicon substrates, the sweeping direction was from negative to the positive bias voltages to ensure that the films always kept under their equilibrium conditions. The bias voltage step and delay time were justified after many trials with different sources of dielectric films previously and determined accordingly to yield reliable and reproducible data.

3.5.4 MOS-C modelling and data interpretations

Prior to extracting electrical information from the samples, a simple MOS-C model is required. Figure 3-12 shows a simple MOS-C construction that will be used as the basis for constructing this model. A SiO_2 interfacial layer is included in this structure as all of the films investigated in this work were deposited on top of the native silicon oxide.

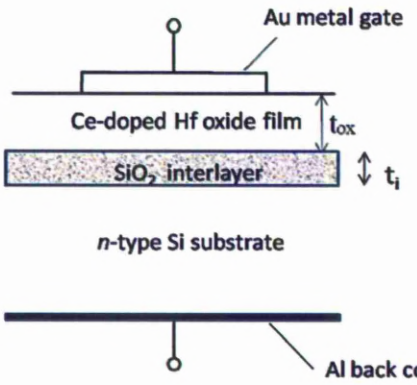

Figure 3-12: MOS-C structure for electrical characterisation

Consider an *n*-type silicon substrate; theoretical C-V curves can be illustrated as the following Figure 3-13 with different regions responding to the bias voltage applied.

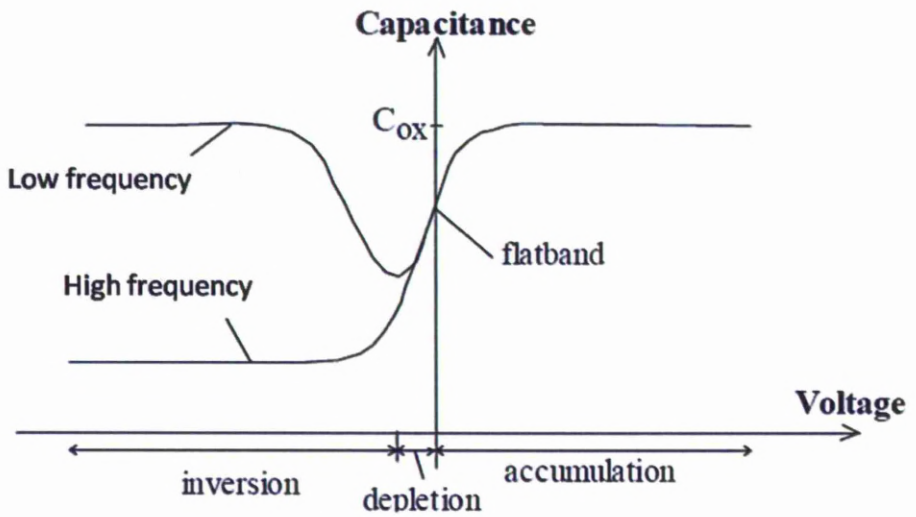

Figure 3-13: Theoretical C-V curves for an n-type Si substrate

For high frequency C-V measurement, the maximum capacitance obtained from the accumulation is used to calculate the dielectric constant of the oxide film. For the structure illustrated in Figure 3-12, this can be done using the following relationship:

$$\frac{1}{C_{max}} = \frac{1}{C_{ox}} + \frac{1}{C_i} \qquad \text{(Equation 3.5)}$$

If C_i (capacitance of the interfacial state) is neglected, then C_{ox} is equivalent to C_{max}, and the dielectric constant can be estimated by using equation 3.6:

$$\varepsilon_{ox} = 10^{-19}\frac{C_{ox}t_{ox}}{A}$$ (Equation 3.6)

ε_{ox}: oxide permittivity (F/cm), C_{ox}: oxide capacitance (pF), t_{ox}: oxide thickness (nm), A: gate area (cm^2)

The equation above is normally used when the interfacial layer is very small compared to the oxide film. However, in this work, due to the presence of the interfacial layer and the low film thicknesses, an alternative method was required, namely CET (Capacitance Equivalent Thickness). This method also provided easier data manipulation with Excel spreadsheets. Moreover, because the aim of using this potential material to replace SiO_2 in MOS devices, the calculation of CET based on SiO_2 permittivity would give an idea how scaling varied with other operational parameters such as bias voltage, frequency, etc.

The maximum capacitance obtained in the accumulation region from a high frequency C-V curve is used to estimate the dielectric constant of the films (typically at 100 KHz) by using equation 3.7:

$$k_{ox} = \frac{k_{SiO_2}t_{ox}}{CET - \frac{t_i}{k_i}k_{SiO_2}}$$ (Equation 3.7)

CET: Capacitance Equivalent Thickness, t_i: interlayer thickness, k_i: interlayer permittivity, k_{SiO2}: SiO_2 permittivity

The equation above allows the value of dielectric constant to be calculated if the interlayer's parameters are known, regarding the value of SiO_2 permittivity (k = 3.9) and its CET (in nm), which can be calculated by applying equation 3.8:

$$CET = 10^{-9}\frac{\varepsilon\varepsilon_0}{C_{max}}A$$ (Equation 3.8)

ε: relative permittivity of SiO_2 ($\varepsilon = 3.9$), ε_0: electric constant ($\varepsilon_0 = 8.854\times10^{-12}$ F m^{-1}), A: gate area (m^2), C_{max}: maximum capacitance (F).

In this work, from TEM and MEIS studies, the interlayer was determined as SiO_2 and its thickness was assumed to be unchanged hence, equation 3.7 yields:

$$k_{ox} = \frac{3.9t_{ox}}{CET - t_{SiO_2}}$$ (Equation 3.9)

In addition to the k-value, other qualitative information can also be revealed by studying the shapes of C-V curves. The oxide charges and density of interface states can be calculated using complicated electrical modelling and related algorithms [14]. However, as stated before, such complicated treatments are beyond the scope of this work and hence, only qualitative conclusions derived from the C-V curves alone are concerned. The effects of fixed oxide charges and surface states can be illustrated in Figure 3-14 for an *n*-type substrate.

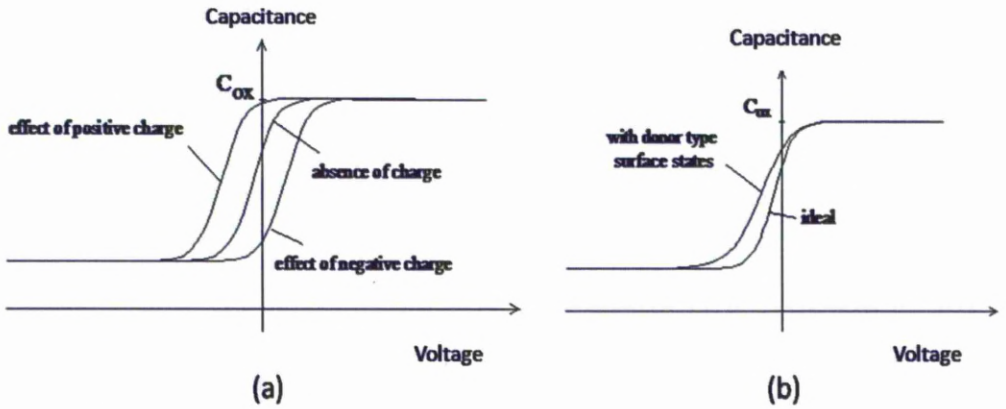

Figure 3-14: Distortions to an ideal C-V curve with (a): effect from fixed oxide charges and (b): from surface states with a donor type.

In the case of fixed oxide charges, the C-V curve will be shifted along the x-axis depending on the sign of charges but the overall shape of curve remains unchanged as illustrated in Figure 3-14a. In this case, the density of oxide charge is independent of the bias voltage. By observing the hysteresis of the C-V curves, the effect of annealing and doping concentrations on the oxide charge within the film can be determined.

The second source of C-V curve stretch out is the surface states, which basically belong to the semiconductor substrates and their related trap density. Because the occupancy of these traps depends on the bias voltage, the C-V curve is distorted asymmetrically as illustrated in Figure 3-14b. The surface states can either be donor-type vacancies (positive when empty, neutral when filled) or acceptor-like vacancies

(neutral when empty, negative when filled). In practice, both fixed oxide charges and surface states can coexist in the films resulting in a combined effect on the C-V curves. Therefore, by studying the shape of the C-V curves, important information can be deduced about the quality of the films and how the growth conditions and heat treatments affect them.

3.6 Atomic Force Microscope (AFM)

3.6.1 Introduction

Atomic Force Microscope (AFM) and Scanning Tunneling Microscope (STM) are the two most well-known representatives of a collective set of techniques commonly known as Scanning Probe Microscopy (SPM). STM was firstly invented by Binnig and Rohrer in 1981 and AFM followed in 1985 by the work of Binnig, Quate and Gerber. In principle, all of the techniques in this group utilise a sharp probe to "image" the surface and to generate topographical information about the sample surface at the atomic scale. The high resolution offered by these techniques, coupled with the relative ease of sample preparation, has made these techniques very popular for surface characterisation of thin films.

Although similar in principle, ATM and STM differ to from each other in the way the sample is "imaged" and hence, the choice of use for a particular sample. STM utilises a sharp metal tip to probe a conductive surface by using a very small bias voltage applied between the tip and the surface in an order of nanometres. This leads to a tunnelling effect, which in turn is used to map the electronic states of the surface and thus, topography of the surface can be built indirectly from that. In contrast, AFM employs a different mechanism to "image" the surface. The topography can be directly built by measuring different types of interactive forces via deflection of a cantilever when a tip is brought very close to the surface. Depending on the applications, the forces of interest can be attractive, repulsive, Van der Waals, magnetic, electrostatic, .etc. One distinctive advantage that AFM has over STM is that the sample does not need to be conductive. Given the context of this work, where all films are insulators, AFM is clearly the method of choice to study the surface profiles. It also gives true 3D images with higher resolutions than Scanning

Electron Microscopy (SEM) and thus, will be used as the main tool to study the surface and topography of all films in this thesis.

3.6.2 Background

In order to "image" the surface, AFM utilises a tip which is scanned over a specified area of the sample under investigation. The interaction between the tip and the surface is the very underlying principle of this technique. In order to understand how this works, a visualisation of interactions that happen when a tip is brought close to the surface is illustrated by its force-distant curve in Figure 3-15.

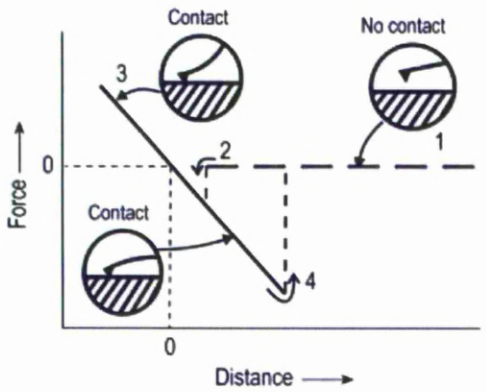

Figure 3-15: Force-distant curve in different interactional stages [15].

When the tip is still far away from the sample (between position 1 and 2), effectively there is no force observed assuming no electrostatic interaction between the tip and the surface. When the tip is brought close enough to the surface (position 2), contact can be made by the van der Waals interaction. As the tip keeps moving toward the sample, the total force exerted on the cantilever will become repulsive. If the sample is then retracted from the tip afterwards, the interactional force is reduced between the line connecting position 3 and 4. When the force is below the zero line and moving toward position 4, the total force now becomes attractive due to the adhesion between the tip and the surface. At position 4, the adhesion will be balanced by the load of the cantilever and the tip moves away from the surface, further retracting the sample. In practice, the force is set up somewhere between position 3 and 4, ideally very close to 4, in order to minimise the contact force.

The force-distant curve illustrated above is the fundamental principle of AFM measurement for the "contact mode", which is by far the most common type. For soft surfaces, i.e. biological or soft materials, another method is used instead namely "tapping mode". In this mode, the cantilever with the tip attached to it is vibrated very close to its resonance frequency via the control of a piezo oscillator.
In this way, only sporadic contact between the tip and the sample is stimulated. As a result, lateral force can be reduced and hence, scratching of soft surfaces can be avoided. Both of these modes can be presented by a similar schematic principle in Figure 3-16.

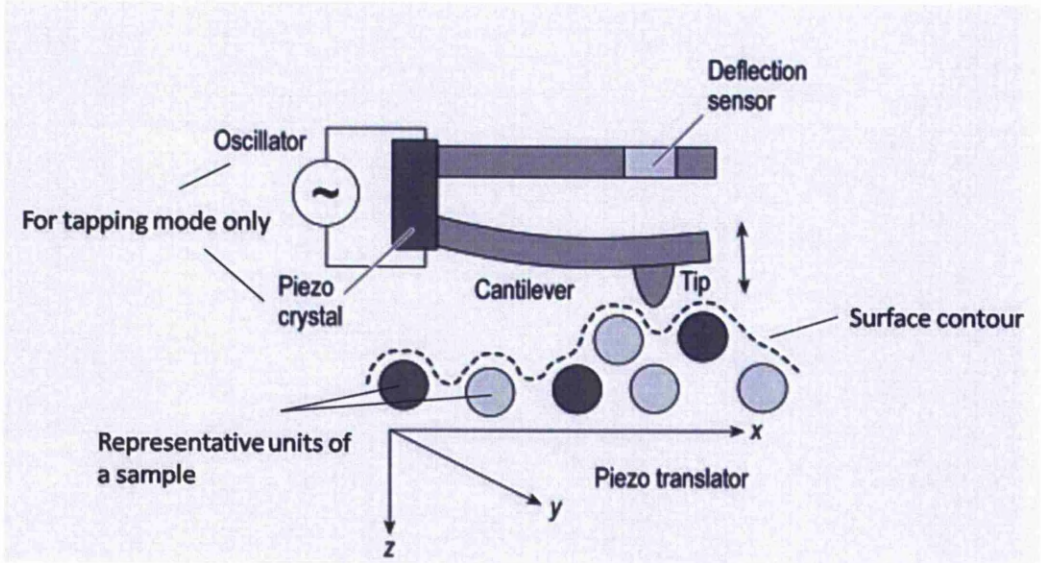

Figure 3-16: AFM schematic principle (adopted from [15]).

Whichever mode is employed, the deflection of the cantilever is then monitored and recorded by means of a complex optical system utilising a laser beam to "sense" the movements of the cantilever.

This process is used to control the force acting on the cantilever through a feedback system and when coupled with an imaging system, eventually produces an image of the surface.

3.6.3 Nanoscope III (Digital Instrument)

The equipment used to obtain topographic data of all the films within this work is an AFM system manufactured by Digital Instrument, Nanoscope III. A schematic representation of main components is presented in Figure 3-17.

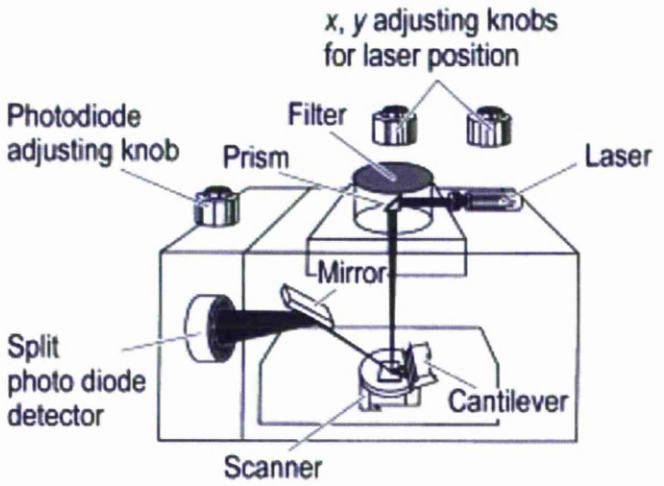

Figure 3-17: Schematic layout of Nanoscope III system.

The system was designed to perform a range of topographic studies for both STM and AFM, depending on the types of materials of interest. In this work, all the films were surveyed in AFM contact mode to yield information about their surface profiles and roughness. The system could be set up to scan the surfaces in two different modes: constant height or constant force. The former mode was employed to study the topography of the films as it helps to eliminate thermal drift which can affect high resolution imaging.

The "image" or topography of the films can be built up by tracking the deflection of the AFM tip cantilever. The motion of the cantilever is monitored and recorded using a four sector photodiode. Laser light reflected from the cantilever is directed towards the photodiode, which senses the difference signals created by different positions of the laser beam. Hence, the deflection of the cantilever can be measured very precisely with high resolution. In order to enhance the reflection of the laser, the cantilever is normally coated with a highly reflected material such as gold.

The tip made from SiN and has a very small radius of curvature and high aspect ratio, enabling it to trace very fine details from the surfaces. By employing the line-by-line scan mode, the force exerted on the tip translates to the defection of the cantilever, which in turn is monitored by the laser and the photodiode and eventually, images of the films are generated. The built-in software allows converts the raw data into a topographical map of the scanned area, which can be displayed as a colour map of as a 3D topography.

The surface roughness can be expressed by various mathematical definitions. In this study, the arithmetic average of absolute values was used and is defined by Equation 3.10:

$$R_a = \frac{1}{n}\sum_{i=1}^{n}|y_i| \qquad \text{(Equation 3.10)}$$

3.7 Ellipsometry

3.7.1 Introduction

To monitor the growth process and the influence of annealing on the physical properties of the films, thickness is very important. The thickness is not only an important metrological parameter but also necessary to extract reliable information for subsequent electrical measurements. Moreover, due to a relatively large number of samples, the measurement of thickness should be fairly fast and simple to enable the data processing and gathering. Ideally, TEM needs to be employed as it gives the most accurate physical thickness. However, TEM cross-section sample preparation and the measurements themselves are costly and very time-consuming, hence limiting its use for characterising large numbers of samples. In comparison, ellipsometry is advantageous in terms of its simplicity and speed in order to handle a number of films within a short period. In addition, extra information such as refractive index of the films can also be determined using ellipsometry. As a result, it was used as the main tool to measure the thickness of all films in this study.

3.7.2 Background

Ellipsometry, like many other optical techniques, utilises light as the main source of investigation and analysis. Basically, it relies on one specific properties of light, polarisation. Therefore, prior to introducing the principle of ellipsometry, it is necessary to briefly discuss polarisation and how this property changes when light interacts with matters. The polarisation of light was first discovered by Malus in 1808 during experiments of the optical behaviours of calcite crystals [16]. Later, together with classical theory of electromagnetic waves and the well-known treatments by Maxwell on this subject, this property of light has become an important tool to study structures of matter. Essentially, polarisation is described as an attribute of light by specifying its orientation during the course of travelling in space. Since light has been treated as an electromagnetic wave, its propagation is characterised by its electric field intensity vector (the induced magnetic vector is neglected). This vector in turn can be represented by two main constituents: one is *p*-component (*p* for parallel) and another is *s*-component (*s* for senkrecht, German for perpendicular). Both of these components are perpendicular to each other, and to direction of the light's propagation. The plane created by these two components is called the plane of incidence. Depending on the ratio of amplitudes between these components and their related phases, three main types of polarisation can be observed. They are linear, circular and elliptical polarisation states, which illustrates the shape of these two components when being projected on the wave plane. Mathematical descriptions of these polarisation states can be found in many excellent textbooks on ellipsometry such as [16] among others. One important note in these treatments is the use of complex number to describe the state of those components. Because light is treated as electromagnetic waves, it is necessary to describe them with both amplitude and phase and thus, it is most commonly parameterised by using complex number. Let consider a simple case where light is directed to and reflected from a flat surface. Assuming that this light is linearly polarised, its polarisation state will be changed after reflection from the surface as depicted in Figure 3-18.

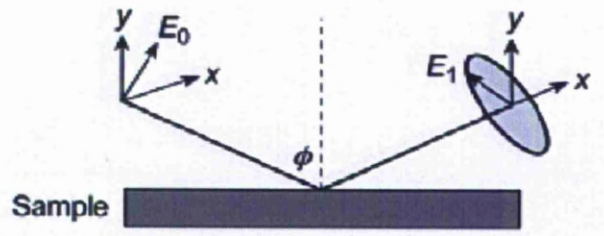

Figure 3-18: Principle of ellipsometry (adopted from [15]).

The change in amplitudes of the two components of the light during the course of reflection induced by the sample can be described by the complex ratio ρ and can be measured by ellipsometry. This principle is illustrated by the fundamental equation of ellipsometry as the following:

$$\rho = \frac{r_p}{r_s} = \tan(\psi)\, e^{i\Delta} \qquad \text{(Equation 3.11)}$$

r_p, r_s : amplitudes of p and s components after reflection and normalised to their initial values, tan(Ψ): amplitude ratio upon reflection, Δ: phase difference.

In principle, the equation above can only be solved analytically for pure substrate or isotropic and homogenous film with indefinite thickness (which is the simplest case) to generate information such as refractive index and extinction coefficient. In all other cases, a layered model has to be constructed which included each of the individual layers in the optical structure. Because ellipsometry actually measures Ψ and Δ, direct conversion to yield physical parameters is not possible. An iterative routine is therefore required to home in on the unknown parameters within the model until the experimental and theoretical values reach agreement.

In most cases, the model requires certain parameters to be fixed before a sensible solution can be obtained. The choice of a correct and sensible model is very important to the interpretation of ellipsometry data and hence, the physical parameters calculated.

The calculations involved in ellipsometry are very complicated and can be done by using either the Jones or the Mueller formalisms employing Stokes vectors and matrices [16]. These detailed calculations and related procedures are beyond the scope of this study.

Instead, to extract such physical parameters from the films, an Excel-sheet program, called Ellipsheets was used together with its customised layer model, which allows up to a maximum of a four layer structure to be modelled [17]. The measured values Ψ and Δ from the films can be compared and matched with simulated values generated from the model to give the best estimation of the thickness and refractive index. In fact, if the films are relatively thick, i.e. more than 10 nm, the ellipsometer can give values of thickness and refractive index using its own built-in calculating procedures and models. However, for thinner films, the calculations for these parameters do not yield sensible results. Hence, regardless of the film thickness to be measured, the use of the Ellipsheet spreadsheet combined with measured data for Ψ and Δ have been employed routinely to deduce information about the films.

3.7.3 Auto EL ellipsometer

A Rudolph Research Auto EL ellipsometer has been used throughout this work. It is a single-wavelength ellipsometer, which means that it operates only at one specific light wavelength and hence, only one pair of Ψ and Δ is generated for each measurement. Depending on the types of sample, three different choices of wavelength can be used: 633, 546 and 405 nm. In this study, all films were measured using 633 nm light; this is typically used in the semiconductor industry for metrology and inspection.

The configuration of this ellipsometer can be schematically presented in Figure 3-19. The main components of this equipment are the Polariser (P), Compensator (C), Sample (S) and Analyser (A), hence the name of its configuration PCSA. Both the polariser and analyser have the same function as linear polarisers. The compensator (also called retarder, in this case is a quarter-wave type) functions as an elliptical polariser. Instead of employing a laser as a light source, this equipment uses an

incandescent light bulb from a lamp. As a result, the specific wavelength used for measurement is achieved via means of a wavelength filter before the photodetector.

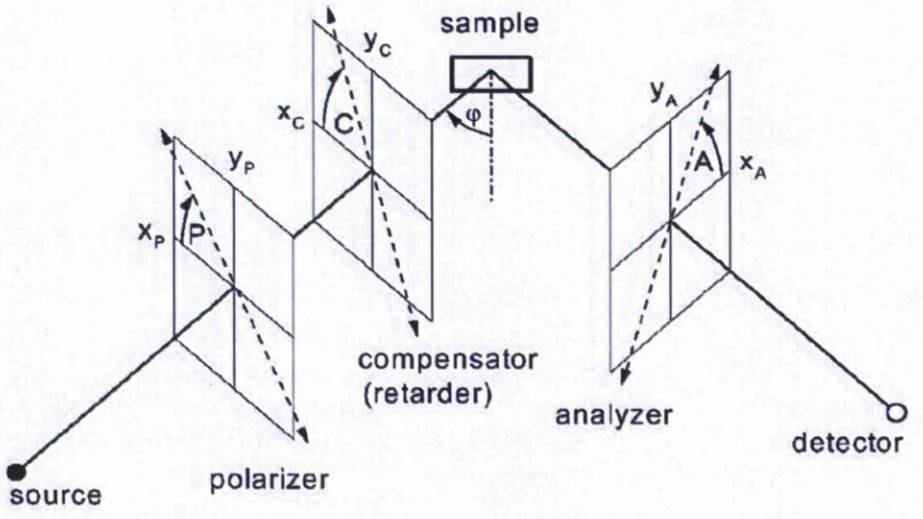

Figure 3-19: PCSA ellipsometer configuration [16].

Basically, the operational procedure comprises the following steps. Unpolarised light from the source passes through the polarizer which can be rotated to any angle, this produces linearly polarised light. The light then passes through the compensator which changes the linear polarized light into elliptically polarised light. The elliptically polarized light is then reflected off the sample and into the analyzer, which contains another rotatable polarizer. The shape and orientation of the incident elliptically polarized light can be changed by rotating the angle of the polarizer. The target is to set this angle so that the elliptically polarized light becomes linearly polarized after it is reflected from the sample. The ellipsometer finds this polariser angle by iterative steps of the polariser and the analyser until the signal hiting the detector is minimised. Thus, this operational mode is named "nulling ellipsometry". The rotation of the incident and reflected polarisers is done automatically by step motors in such a way that the polarizer and analyzer angles are found for the "null" position. The incident angle is fixed for all measurements and set at 70 degrees.

Before any measurement can be done, calibration is required to ensure that all the moving components of the ellipsometer are correctly set up. The calibration process is performed routinely using a standard sample, which is a Si wafer with a SiO_2 film on the top. The thickness and refractive index of this sample is provided by the supplier (t = 1100 Å, n = 1.455 ~ 1.465). By using a simple two layer model as a built-in function from the control console, the check on this sample is performed on a daily basis. Due to very high resolution of all the optical components and excellent accuracy in measured parameters (polariser or analyser: 0.05° Δ: 0.05°and Ψ: 0.1°), the results from calibration with this standard sample normally fall inside the permitted accuracy for a SiO_2 film (between 3 Å to 10 Å in thickness and 0.01 in refractive index). This ensures that the equipment is properly aligned and set up for actual measurements.

3.7.4 Data acquisition and processing

To improve the accuracy of the data acquired as well as check the film's uniformity, normally five measurements randomly chosen throughout the sample were performed. The average value of Ψ and Δ could then be calculated from these five pairs of acquired data and then used to compare with the values generated by the Ellipsheets spreadsheet model.

As mentioned before, although the ellipsometer can calculate thickness and refractive index from the measured values of Ψ and Δ, it can only do so for relatively thick films. For thinner films, the built-in functions were not able to give the value of thickness without being given a refractive index. This problem can be be understood by plotting Ψ versus Δ for films with different refractive indices as shown in Figure 3-20. This diagram was produced using the three layer model in Ellipsheets. Due to the lack of experimental data for Ce-doped HfO_2 films, the refractive index used was taken to be the same as the value reported for HfO_2 films [18]. To a first approximation, it is assumed that low doping levels of cerium would not significantly affect the refractive index of HfO_2 films.

The model was built with a SiO_2 interlayer sandwiched between the high-k film and the Si substrate (the thickness of this SiO_2 layer was taken to be 2.1 nm as determined for one of the samples by TEM). Another assumption was also made that the films were flat and pinhole free (as shown in AFM study).

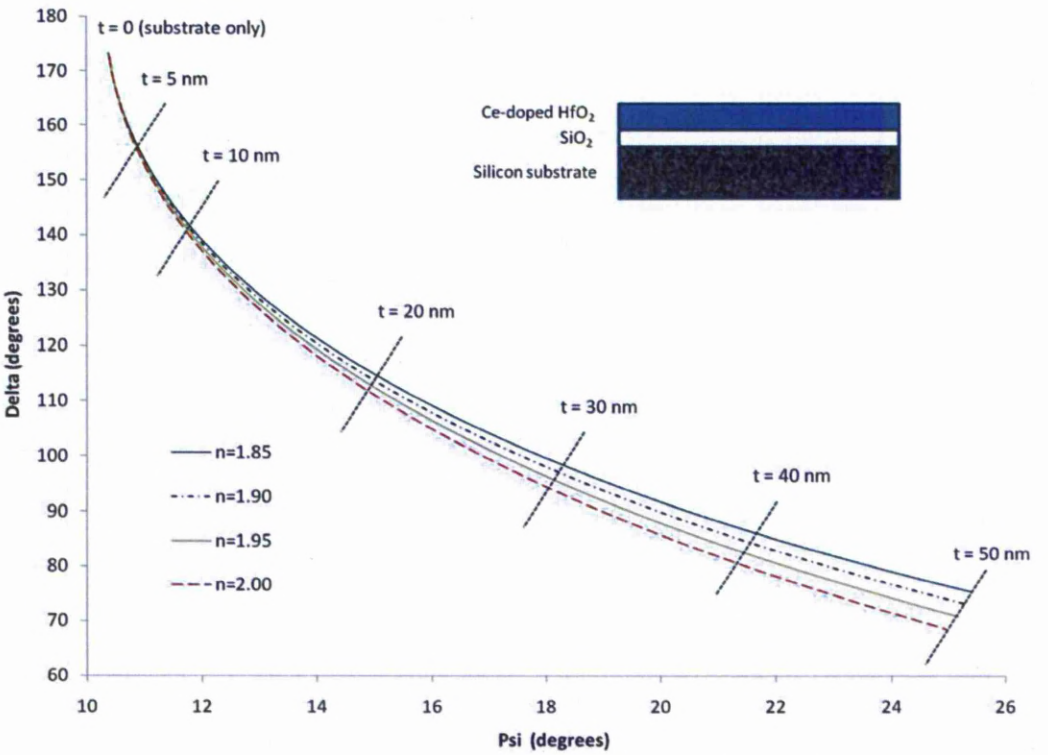

Figure 3-20: Ψ – Δ plot with various refractive indices. The value of t denotes film's thickness.

As can be seen from Figure 3-20, for very thin films ($t \leq 5$ nm), regardless of refractive indices chosen, the value of Ψ changes very little compared to the value of Δ. Quite often, this change falls inside the uncertainty range of the instrumental resolution. In other words, the measured values of Ψ and Δ from the ellipsometer for any given film can only generate the value of thickness if the refractive index is known beforehand. As a result, for thin films, in order to estimate their thicknesses, the value of refractive index has to be input to the layer model in the spreadsheet. In this study, a refractive index value of 1.9 was used throughout the data processing for thin films and it showed a good agreement between "theoretical" and experimental values of Ψ and Δ.

For the films with thicknesses of more than 10 nm, the change in Ψ becomes large enough to generate both values of thickness and refractive index for a given pair of measured values of Ψ and Δ. It means that by applying the aforementioned layer model to the built-in program of the ellipsometer, the values for both refractive index and thickness can be generated.

As a result, the values of thickness and refractive index can be obtained automatically and later can be compared with the values obtained from the spreadsheet for cross-checking in terms of Ψ and Δ matching as a figure of merit (with the input value of refractive index obtained from ellipsometer served as starting point to fine-tuned the alterations in the spreadsheet). After trial and error, it has been found that for all the films, their refractive indices changed very little and typically having the values between 1.890 and 1.910). To ensure consistency and reduce systematic error, an average value of 1.90 was used for all films regardless of their thicknesses to obtain the "theoretical" calculations for Ψ and Δ. The films' thicknesses determined from this method and based on the aforementioned refractive index were found to have the error in the range between 0.05 to 0.2 nm.

Besides the dependence of refractive index on the film thickness, some other sources of errors can also contribute to the differences between the experimental and "theoretical" values of Ψ and Δ. They can be the surface roughness, the voids inside the films and the uniformity of the films. These issues can mean that the model needs to become more complicated to accommodate those contributions. The SiO_2 interlayer thickness can also vary slightly between samples deposited from different substrates or between the as-grown and vacuum annealed samples. However, based on results from TEM, MEIS and AFM, all of these factors can be safely neglected from the data processing mentioned above. The good agreement between measured and simulated values for Ψ and Δ from all the films proved that by using that three layer model, it was sufficiently reliable to extract the value of film thickness within the work of this study.

3.8 Medium Energy Ion Scattering (MEIS)

3.8.1 Introduction

The chemical compositions of as-grown and selected annealed films in this project were acquired and analysed by employing MEIS at Daresbury Laboratory (UK). Besides critical data about the compositions of the films such as the amount of cerium and hafnium incorporated into the oxides, important information about the interface structure between the oxide films and Si substrates were also provided. Such results were crucial to understand the growth process, the ability to control doping level during the growth and the interactions between deposited films and the underneath Si for different annealing conditions.

3.8.2 Introduction

MEIS is a technique utilising ions for the analytical purpose of surfaces and interfaces in the medium energy range (50-300 keV) and belonging to the bigger ion scattering method group. This group comprises of conventional high energy Rutherford back scattering (RBS) and low energy ion scattering (ISS) [19]. The differences between MEIS and the other two techniques are mainly due to the range of ion energy employed and hence, the mechanism of interaction with matters. MEIS differs from ISS in the way that the interaction law of the latter method is much more complex and ISS is essentially sensitive only to the top layer because of its low energy. Compared to RBS, MEIS is more surface sensitive, and more complex instrumentally. As a result, MEIS is a method of choice when information about the film surface, bulk film microstructure and interface between film and substrate are all required from a single technique.

The main principle of MEIS can be described by considering basic physics of ion scattering and two other important experimental configurations: channelling and blocking. Firstly, the interactions of ions with solid matters are briefly reviewed. Due to the region of ion energy used, it is sufficiently high so that the ion-surface interaction law is simple and well characterized, essentially only classical Rutherford scattering is involved and sufficiently low so that the surface specificity can be optimized. Also due to the high energy, the diffraction and other quantum effects can

be neglected (the de Broglie wavelength of ions in MEIS is in the order of 10^{-3} Å). The basic quantities measured in MEIS are the energy and angular distribution of backscattered ions. The technique derives elemental specificity from the fact that the energy of a backscattered ion is a strongly dependent on the mass of the target atom(s). As the ions propagate through the sample, they also will lose smaller amounts of energy to the target electrons. Considering energy and momentum conservation, the energy loss in the collision can be calculated by knowing scattering angle (θ_s) and the ratios of the ion and target masses ($\rho = m_1/m_2$). For an incident energy E_0 (and exit energy E_1), the fractional energy loss (also known as kinematic factor) can be expressed as:

$$K^2 = \frac{E_1}{E_0} = \left[\frac{\rho \cos\theta_s + \sqrt{1-\rho^2 \sin\theta_s{}^2}}{1+\rho}\right]^2 \qquad \text{(Equation 3.12)}$$

The dependence on target mass makes MEIS ideally suitable for the study of multi-element systems, providing that these elements are not so close to each other in the periodic table. By increasing the incident ion mass, the energy separation between different elements becomes larger but at the price of potential damage created by ion-induced. This problem can be mitigated by a combination of very low beam dose and efficient data collection (multi-detection techniques), or by moving the ion beam to fresh spots on the sample and averaging the results.

One important issue in MEIS is the way the beam is configured to propagate through the sample, i.e. channelling and blocking. Figure 3-21 presents an example of channelling and blocking as ion paths are illustrated. A well collimated beam of ions is incident along a high symmetry (channelling) direction of the target (a single crystal). Most of the incident ions will propagate in the large channels between the nuclei, where they will lose energy quasi-continuously to the electrons in the target. These energy losses are not large enough to lead to large angular deviations because of the large mismatch of the ion-electron masses. However, a few ions will collide with the first atom along a row of target nuclei. The energy loss is such a collision may be large enough to create a significant angular deflection. The angular distribution of the backscattered ion flux from the atoms in the first layer will be

smooth. Due to geometrical distortions in the surface (contractions, reconstructions, etc.) or thermal vibrations, there may be a finite collision probability for deeper layers also. Ions scattered from the second layer will have their outward paths blocked at certain angles by first layer atoms and so on. The variation in scattered ion intensity with angle thus relates to the geometrical arrangement of surface atoms. As a result, the backscattered ion flux will be reduced in directions corresponding to a vector joining two atoms in different layers and that the angular distributions will be marked with pronounced blocking dips, which contain direct information about the relative position of atoms in the first few layers of the crystal. The experimental parameters (the beam energy, the incident direction, etc.) are usually set up such that the collision probabilities form a rapidly converging series, i.e. only three or four layers contribute. A complete solution of surface structure requires a comparison between experiment and simulation for several scattering geometries.

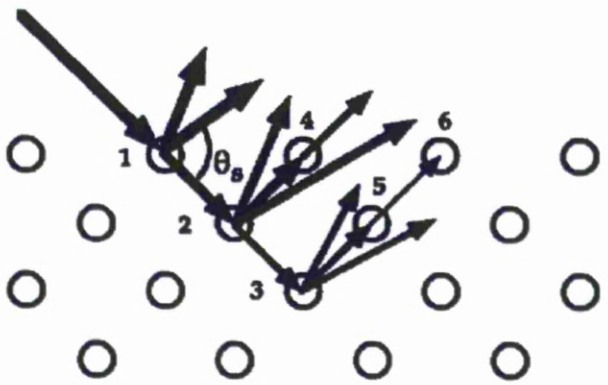

Figure 3-21: Ion paths demonstrate MEIS and the phenomena of channelling and blocking. The widths of the arrows indicate the intensity of the ion flux at each point [19].

3.8.3 MEIS facility at Daresbury

The MEIS facility in Daresbury comprises of three main sections: an accelerator, which consists of a high voltage supply and accelerating lens (designed to operate at energies up to 400 keV), a beam line for transport of the positively charged ion beam and a multi-chamber ultra-high vacuum (UHV) experimental end-station [20]. A schematic illustration of main components of the system is given in Figure 3-22.

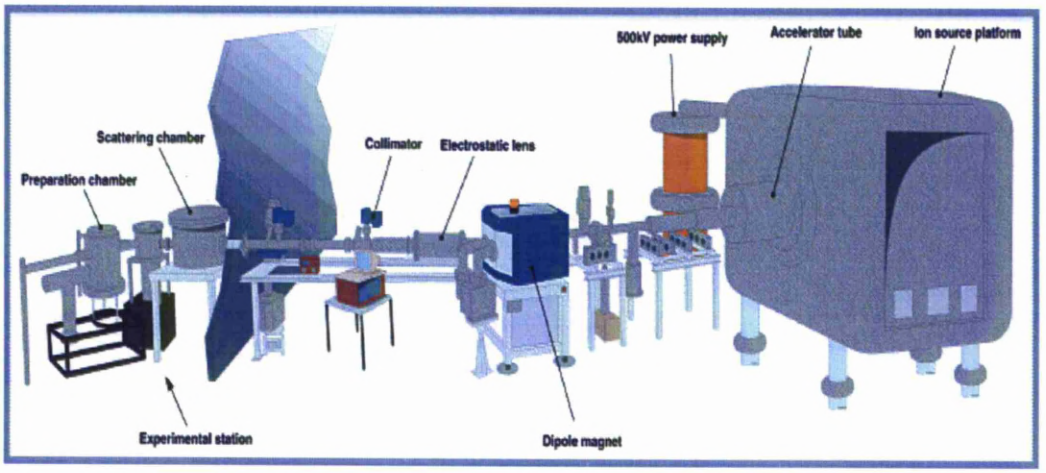

Figure 3-22: schematic view of MEIS main components [21].

The ion source platform houses a dual ion source, which in turn is generated by duo-plasmatron. He^+ or H^+ ions are initially accelerated with energy about 20 keV from the source and then the ions are accelerated again to the required energy with a second power supply. Within this work, a flux of He^+ ion with energy around 200 keV was typically employed.

The beam line is pumped to high vacuum and consists of a bending magnet, several electrostatic lenses, and steering components. Collimating slits equipped along the beam line are employed to create a beam with a divergence of 0.1° and a standard spot size of 1mm wide by 0.5 mm height on target. Beam parameters can be remotely controlled from a control console nearby, allowing the beam to be focused or defocused during the course of an experiment to acquire the optimum conditions. The beam current is monitored using a thin wire grid placed in the beam, enabling the beam current on target to be known. To ensure a reproducible beam dose on target, the beam current is monitored by a current integrator.

The experimental station contains three ultra high vacuum (UHV) chambers: a scattering chamber, a preparation chamber and an interconnecting one, together with a fast entry vacuum load-lock. Samples are mounted on holders that can be transferred from one chamber to the next via transfer arms. The scattering chamber houses a goniometer accommodating a sample holder and position the sample into the beam. The goniometer can be adjusted in three different ways, namely rotation,

spin and tilt axes respectively. This allows the position of the beam on the sample can be moved so the sample can be aligned to the beam. Each of those movement axes can be actuated and adjusted by a step motor via the control console. Figure 3-23 demonstrates the alignment axes provided by the goniometer. The scattering chamber is also equipped with a toroidal sector electrostatic analyser (TEA), which is fitted with a two-dimensional position-sensitive detector to allow parallel detection of a range of ion emission (scattering) angles and scattered ion energies (see Figure 3-24). These form one composite unit that can be moved around the goniometer-sample system in the plane of the beam. The analyser has a 27° acceptance angle and the energy window of the analyser is 2% of the pass energy. The angular resolution of the detector is 0.3° and the energy resolution is 3.5E-3.

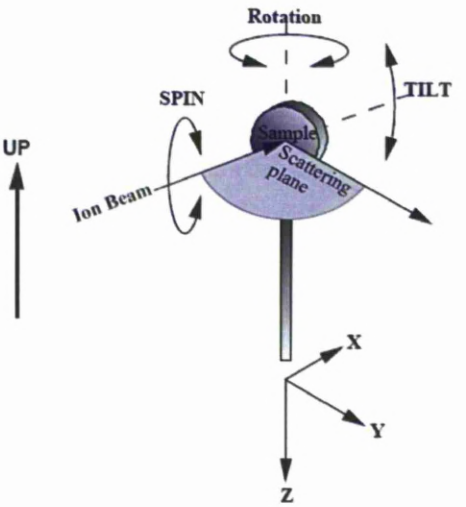

Figure 3-23: MEIS axes of alignment [22].

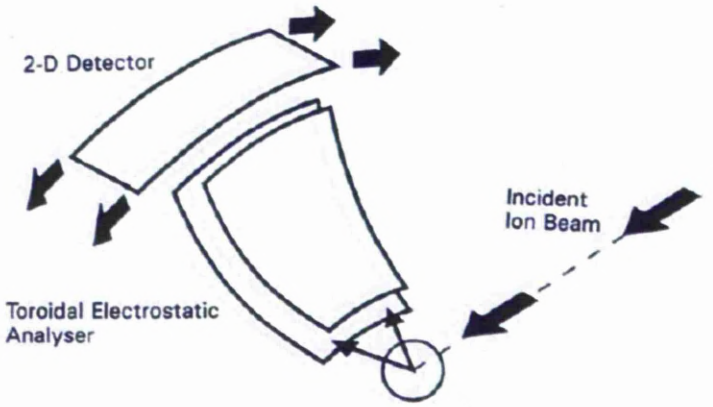

Figure 3-24: Schematic illustration of the angle-resolving toroidal-sector electrostatic for the ion-energy analyser and its detector [20].

3.8.4 Experimental set up and data processing

MEIS measurements were taken using the following conditions as standards.

Ion source	200 keV He^+
Beam current	~200 nA
Substrate	Si n-type (100)
Beam dose	2.5 μC
Energy pass	1.6%
Ion incidence angle	(111) Si crystal angle (channel)
Scattered ion angle	125.3° (100) direction, 70.5° (111) direction
TEA angle	125°
TEA range	27°

In this experimental set up, the ions collected at the scattering angle along (100) direction (effectively down to about 50 nm from the surface) allow the Ce and Hf content of the films to be effectively mass separated, enabling the film composition to be estimated. The utilisation of scattering angle along the (111) direction enables the heavy ions (Ce and Hf) to be collected as well as the oxygen and silicon signals. At this geometry, the silicon from the deeper silicon substrate is suppressed by channel "shadowing" and "blocking". Only silicon atoms from the top few atomic layers or any amorphous silicon in the interlayer oxide are evident. As a result, information about the interfacial layer can be deduced.

Data acquisition comprises many scans, of which to detect high energy and surface scattering followed by lower energy and deeper scattering. These scans eventually create a data tiles, i.e. 2D plots of the yield at each point on the analyser. By stepping the pass energy down and joining together the individual tiles, a continuous energy spectrum can be produced. The compositions of the films, i.e. Ce/Hf ratio can be estimated from the ratio of normalised integrated peak areas with respect to one chosen element in the case of 125.3° scattering angle. For instance, the integrated peak area of Ce can be normalised with respect to Hf by multiplying its integrated area with the ratio of the scattering cross sections, which essentially proportional to the square of the atomic number ratio between these two elements (Z_{Ce} = 58, Z_{Hf} =72) so in this case, this ratio is equivalent to $(72/58)^2$.

For the 70.5° scattering angle, peaks of Ce and Hf no longer separate like in the case of 125.3° scattering angle but merge as a single peak. However, the peaks of Si and O are observable in the energy spectrum, enabling the assessment of interlayer as previously mentioned. The more detailed insight about the interaction between the oxide film and the substrate or the chemical composition of the interfacial layer can be revealed by studying the depth profiling (depth scales) [23].The depth scales can be converted from energy for any elements by calculating the instantaneous rate of inelastic energy loss along the ion path. This numerical method was encoded as a computer programme, developed and refined by Dr. Matthew Werner [22] and was used to generate the depth scales for some films within this work.

3.9 Weight gain analysis

To monitor the deposition, weight gain measurement provides a quick and simple way to obtain information about the deposited mass after each growth and usually is the first check performed to ensure that the growth has been successful. Moreover, when films with different compositions from two sources of precursors are grown and the ALD cycle ratios is known, weight gain measurement also can help estimate approximately the growth behaviours. For instance, consider two constituent materials with known bulk densities.

Assuming that the density of the film deposited from each material is similar to the respective bulk value, it can be deduced that if the film composition changes, the deposited mass will also vary accordingly in a proportional way. Hence, if a sets of films with different ALD cycle ratios grown after a number of comparable cycles, the weight gain per cycle for each film can be plotted against the ALD cycle ratio to Investigate the growth efficiency.

Weight gain analysis was performed by using a Mettler Toledo XS 205 DualRange analytical balance. The range offered by this balance is 220/81 g with the deviation 0.1/0.01 mg respectively. In this study, due to small total weight of the deposited film and the silicon wafer (less than 2 g), the latter range was used to maximise the accuracy. In order to check the consistency and reduce errors, weight data of a reference wafer has been recorded regularly before and after each growth. In addition, this record has been used as way to check the stability of the balance. A value between 1.36664 g and 1.36667 g was observed during the period of three years, confirming the high reliability of the measured data.

To perform the analysis, weight measurements for the sample were carried out three times before and after the growths, resulting in two average values for the sample before and after the growth respectively. The difference between these two values is the deposited mass after the growth.

3.10 Post-growth heat treatments

3.10.1 Air & N_2 annealing

Films subject to air and N_2 annealing were undertaken by using a Carbolite horizontal tube furnace (maximum temperature up to 1200 °C). The ramp rate was set at 5 °C/min to ensure an even heating process throughout the equipment. After the set temperature was reached, it was held at least 2 hours before the samples were loaded in to ensure the stability of the system. The samples during the annealing were kept inside a ceramic crucible, which has been always kept inside the tube all the times (the tube has been kept at 300 °C when not in operation) to avoid

contaminations. The only difference in terms of system setup between air and N_2 annealing was the requirement of some specific parts of the system, which were not used for air annealing. In order to undertake N_2 annealing, a gas regulator (1L/min ~ 10L/min) connecting to a N_2 bottle (zero grade from BOC) was open to connect to one end of the furnace. The regulator was set at 3L/min while the N_2 bottle was set at 1 bar. Prior to each time the samples were loaded in for N_2 annealing, the N_2 flow was allowed to pass the tube in 15 minutes to prevent humidity and other contaminations penetrate the furnace from the ambient environment. Both ends of the furnace were equipped with stainless steel and anti-flame material seals.

3.10.2 Vacuum annealing

All the films subject to vacuum annealing were undertaken at MEIS facility, Daresbury Laboratory (UK), using the high vacuum chamber (~10^{-8} torr) and heating devices (up to 1000 °C) within the MEIS system. The annealing temperature could be controlled via the adjustment of a current flowing through a high resistance W filament mounted at the back of the sample holder. If very high temperature (more than 900 °C) was required, an electron beam could be focused on the back of the sample to provide extra heating.

3.11 TEM

All TEM images in this work were kindly acquired and provided by Dr. Bob Murray and Dr. Simon Romani, using the TEM facility at the electron microscopy centre (Department of Engineering, University of Liverpool).

References

1. Potter, R. J., Marshall, P. A., Chalker, P. R., Taylor, S., Jones, A. C., Noakes, T. C. Q. and Bailey, P. (2004) Characterization of hafnium aluminate gate dielectrics deposited by liquid injection metalorganic chemical vapor deposition. *Applied Physics Letters,* **84** (20), 4119-4121.
2. Potter, R. J., Chalker, P. R., Manning, T. D., Aspinall, H. C., Loo, Y. F., Jones, A. C., Smith, L. M., Critchlow, G. W. and Schumacher, M. (2005) Deposition of HfO_2, Gd_2O_3 and PrO_x by liquid injection ALD techniques. *Chemical Vapor Deposition,* **11** (3), 159-169.
3. Gaskell, J. M., Jones, A. C., Aspinall, H. C., Przybylak, S., Chalker, P. R., Black, K., Davies, H. O., Taechakumput, P., Taylor, S. and Critchlow, G. W. (2006) Liquid injection ALD and MOCVD of lanthanum aluminate using a bimetallic alkoxide precursor. *Journal of Materials Chemistry,* **16** (39), 3854-3860.
4. Gaskell, J. M., Jones, A. C., Chalker, P. R., Werner, M., Aspinall, H. C., Taylor, S., Taechakumput, P. and Heys, P. N. (2007) Deposition of lanthanum zirconium oxide high-k films by liquid injection ALD and MOCVD. *Chemical Vapor Deposition,* **13** (12), 684-690.
5. Maruyama, T. (2000) Cerium dioxide thin films prepared by chemical vapor deposition from cerium dipivaloylmethanate. *Journal of Materials Science Letters,* **19** (19), 1723-1725.
6. Paivasaari, J., Putkonen, M. and Niinisto, L. (2002) Cerium dioxide buffer layers at low temperature by atomic layer deposition. *Journal of Materials Chemistry,* **12** (6), 1828-1832.
7. Birkholz, M. (2006) *Thin film analysis by X-ray scattering,* WILEY-VCH Verlag GmbH & Co. KGaA, Weinheim,
8. *Rigaku Miniflex manual instruction,*
9. Pecharsk, V. K. and Zavalij, P. Y. (2005) *Fundamentals of powder diffraction and structural characterizations of materials,* Springer Science & Business Media, Inc.,
10. McCreery, R. L. (2000) *Raman Spectroscopy for Chemical Analysis,* John Wiley & Sons, Inc.,
11. *LabRAM HR - Software and Hardware User Guide,*
12. Gouadec, G. and Colomban, P. (2007) Raman Spectroscopy of nanomaterials: How spectra relate to disorder, particle size and mechanical properties. *Progress in Crystal Growth and Characterization of Materials,* **53** (1), 1-56.
13. Gate Dielectric Capacitance-Voltage Characterization Using the Model 4200 Semiconductor Characterization System. *Keithley - Application Note Series,* (2239).
14. Mitrovic, I. Z. Metrology of oxides using C-V, I-V & C-t techniques.
15. Bubert, H. and Jenett, H. (2002) *Surface and thin film analysis: Principles, Instrumentation, Applications,* Wiley-VCH Verlag GmbH,
16. Tompkins, H. G. and Irene, E. A. (2005) *Handbook of Ellipsometry,* William Andrew, Inc.,
17. Jun, E. K. (1999) http://www.ccn.yamanashi.ac.jp/~kondoh/ellips_e.html.

18. Kaupo Kukli , Tero Pilvi , Mikko Ritala , Timo Sajavaara, Jun Lu , Markku Leskela¨ (2005) Atomic layer deposition of hafnium dioxide thin films from hafnium tetrakis(dimethylamide) and water. *Thin Solid Films,* **491**, 328-338.
19. Brundle, C. R., Evans, C. A. and Wihon, S. (1992) *Encyclopedia of Materials Characterisations: Surfaces, Interfaces, Thin Films,* Butterworth-Heinemann,
20. Bailey, P., Noakes, T. C. Q. and Woodruff, D. P. (1999) A medium energy ion scattering study of the structure of Sb overlayers on Cu(111). *Surface Science,* **426** (3), 358-372.
21. http://www.dl.ac.uk/MEIS/facility/.
22. Werner, M. (2006) *Damage formation and annealing studies of low energy ion implants in Silicon using medium energy ion scattering (PhD thesis).* The University of Salford, UK,
23. Gustafsson, T., Lu, H. C., Busch, B. W., Schulte, W. H. and Garfunkel, E. (2001) High-resolution depth profiling of ultrathin gate oxides using medium-energy ion scattering. *Nuclear Instruments & Methods in Physics Research Section B-Beam Interactions with Materials and Atoms,* **183** (1-2), 146-153.

Chapter 4 FILM GROWTH

4.1 Introduction

The studies described in this chapter are concerned with the development of liquid-injection ALD (LIALD) for the controlled deposition of Ce-doped HfO_2 with a varying range of Ce doping levels. Firstly, the ALD growth of HfO_2 and CeO_2 films were investigated separately to establish the growth characteristics of each system. From these initial studies, it was possible to establish a suitable temperature for the combined oxide growth and make initial predictions about the incorporation rate of Ce in the Hf-oxide under various ALD sequences. Once the individual growth characteristics were established, the feasibility of growing Ce-doped HfO_2 films was investigated. MEIS analysis of the films were carried out to determine the chemical composition of the films and the results are used to establish the incorporation efficiency of Ce in Hf-oxide. A table of all samples and their details relevant for further studies is provided at the end of the chapter to summarise the work within this film growth section.

4.2 Growth of HfO_2 and CeO_2 films

This section will present and discuss the studies of each single precursor source to grow HfO_2 and CeO_2 in ALD mode and eventually, the combination of these sources to create Ce-doped HfO_2 films. The characterisation of HfO_2 and CeO_2 growth is important to understand the behaviour of each individual process such as growth rate, ALD window, the influence of oxidising agent and whether any overlap in ALD regimes between these two growth processes can be observed. The last issue is vital to establish the parameters that can be used to grow the aimed ternary alloy films.

4.2.1 HfO_2 growth

4.2.1.1 Cambridge Nanotech reactor

Initially, growth studies of HfO_2 were conducted using a modified Cambridge Nanotech Savannah S100 reactor with a home built liquid injection system attached.

These initial studies were used to study the feasibility of using liquid injection precursor delivery instead of conventional heated source delivery methods such as vapour draw or bubbling. As a result, the chosen precursor to grow HfO_2 was $Hf[N(CH_3)_2]_4$, which was one of the newly developed type at that time and also showed good ALD growth characteristics as demonstrated by Kukli et at [1]. Hence, the data collected from LIALD growth of the same precursor could be compared directly to the published results from this precursor to evaluate the growth characteristics between two techniques.

In the growth study of LIALD, the precursor, $Hf[N(CH_3)_2]_4$, was dissolved in anhydrous toluene to produce a 0.05M solution. The co-reactant used for growing HfO_2 together with this precursor was water. The thicknesses of all films were determined by ellipsometry for both conventional ALD in the work of Kukli and LIALD in this work.

Figure 4-1 presents the growth curves of the aforementioned precursor obtained from LIALD and from the work of Kukli obtained by conventional ALD. In the case of LIALD, growth rates were obtained at temperatures between 200 °C and 350 °C by depositing 300 growth cycles. Details about the growth results of conventional ALD for this precursor can be found in [1] together with the extraction of film thicknesses and refractive indices.

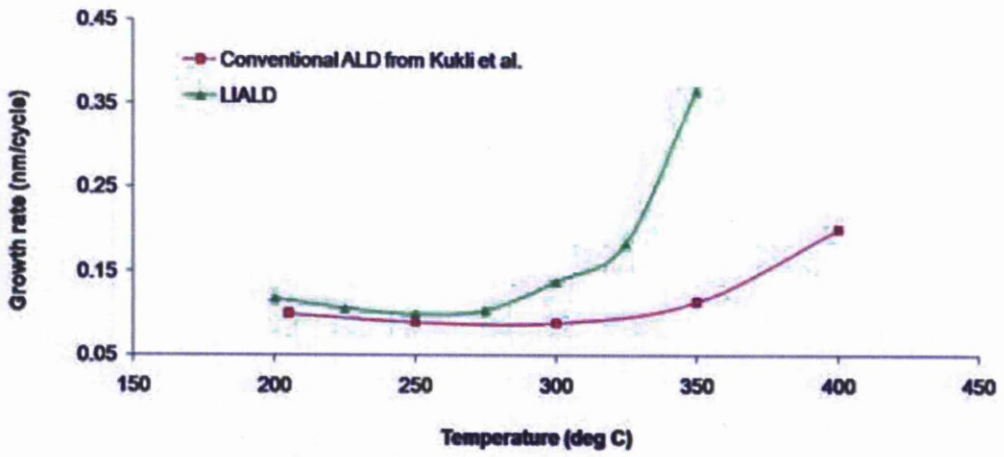

Figure 4-1: Comparison of growth curves between LIALD and conventional ALD for $Hf[N(CH_3)_2]_4$.

As can be seen from the figure above, in the regime between 200 °C and 275 °C, the growth rates of these two techniques show very similar values. However, they begin to differ quite markedly beyond 300 °C though still share the same tendency of increasing rates at higher temperatures. The exact reason why the growth rate was much higher at temperatures beyond 300 °C in LIALD compared to the results from conventional growth is still not clearly understood. However, one likely reason was the behaviour of the growth beyond 300 °C. As can be seen for both growth curves, the growth characteristic was no longer ALD but CVD-type, illustrated by the increase in growth rate with increasing temperature. Hence, it could be the CVD contributions to the growth rate beyond 300 °C were much higher in this work compared to the work of Kukli. Another factor could also contribute to the unmatched growth rate from this work compared to the conventional ALD study at high temperature was the thermal decomposition of the precursor, which was also the cause of the CVD-type growth pattern observed for both studies. Nevertheless, this initial study proved that the ALD regime of this precursor for both techniques can be achieved in the temperature range quite closely and similarly.

4.2.1.2 Aixtron reactor

The initial plan was to continue the growth work using the modified Cambridge Nanotech reactor, however, initial Ce-oxide growth studies using $Ce(thd)_4$ with H_2O as a co-reactant were unsuccessful. Water is simply not a strong enough oxidising agent to react with the (thd) ligands, and as a result, co-reactants such as ozone are required with this type of precursor as demonstrated in [2]. Unfortunately, our Cambridge reactor does not currently have the option of ozone and as a result, further growth work moved over to an Aixtron AIX200FE system, which has been modified for ALD deposition.

4.2.2 CeO_2 growth

In order to characterise the growth of CeO_2, a solution of 0.05M $Ce(thd)_4$ in anhydrous toluene was prepared (thd = tetrakis(2,2,6,6-tetramethyl-3,5-heptanedionato)).

Unlike Hf-precursors, the choice of Ce-precursors is much more limited and as a result, $Ce(thd)_4$ was employed because it has been used and well-characterised [2].

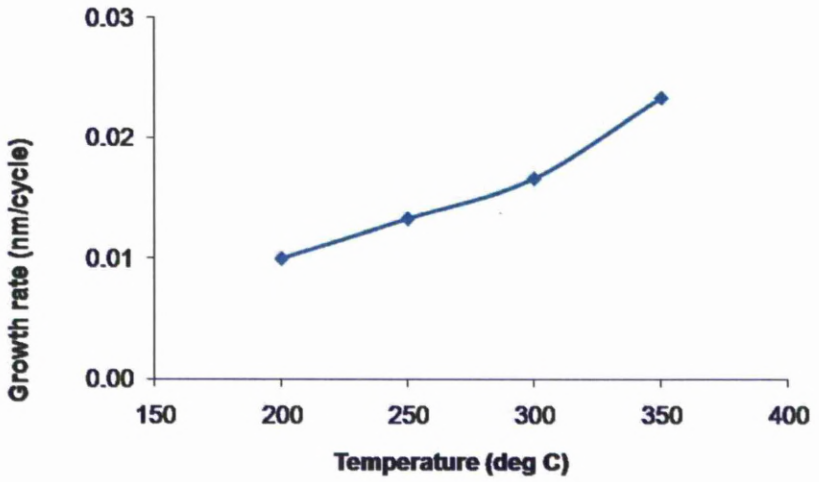

Figure 4-2: Growth curve of $Ce(thd)_4$ with ozone.

Figure 4-2 shows the ALD growth curve of this Ce-precursor with ozone to 350 °C. Similar to the characterisation of Hf-precursor, all films were deposited with 300 cycles and their thicknesses were measured by ellipsometry. The result above is quite comparable to the growth curve obtained by Paivasaari et al in their study about ALD CeO_2 from $Ce(thd)_4$ [2]. However, an ALD regime was not clearly observed from this growth curve as opposed by the narrow ALD "window " reported in the study previously mentioned (175 °C – 250 °C). The growth rate from this growth curve was also lower compared to the growth rate observed in the study of Paivasaari, possibly because the ozone pulse length used in this study (0.5s) was much shorter the chosen pulse length in his study (2.5s). Another noticeable observation from this study is the low growth rate of CeO_2. This phenomenon can be attributed to the fact that $Ce(thd)_4$ is a very stable precursor (just slightly decomposes at temperatures beyond 275 °C as shown in [2]).

4.2.3 HfO_2 growth

In addition, to accommodate a more suitable growth conditions that match better with the cerium-precursor, another type of Hf-precursor had to be used.

As a result, the source of Hf-precursor was changed from $Hf[N(CH_3)_2]_4$ to $[(MeCp)_2$ HfMe(OMe)] (Me = CH_3, Cp = C_5H_4); a relatively new precursor, which could provide many improvements compared to previous types [3] and already characterised extensively in previous studies within our research group. Hence, the growth curve for $[(MeCp)_2HfMe(OMe)]$ was performed with ozone instead of water to simplify the growth process because $Ce(thd)_4$ was shown to react sufficiently with ozone. Similar to the previous Hf-precursor, a solution of 0.05M of this source was prepared in anhydrous toluene.

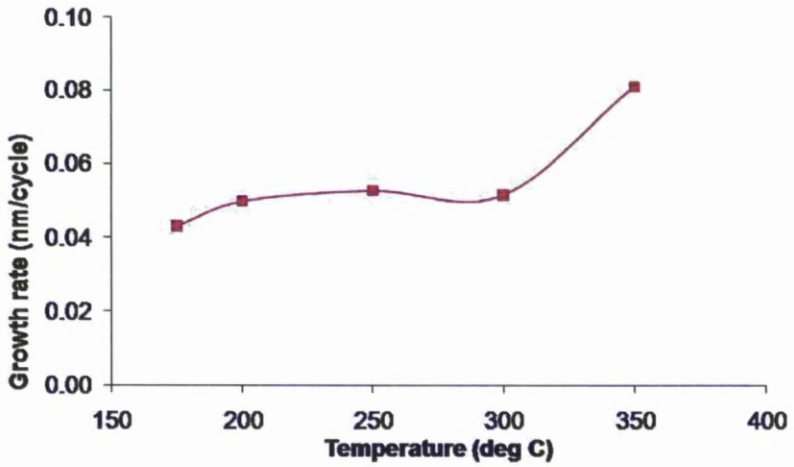

Figure 4-3: Growth curve of $[(MeCp)_2$ HfMe(OMe)] with ozone.

Figure 4-3 shows the growth rate of the Hf-oxide as a function of temperature determined by depositing 300 ALD cycles and measuring film thicknesses using ellipsometry. An ALD window for this precursor is observed in the temperature range between 200 °C and 300 °C, where the growth rate is essentially independent of temperature. This ALD "window" is the temperature range over which growth is dominated by self limiting ALD behaviour. At lower temperatures, the growth rate starts to fall due to the insufficient reactivity of this precursor while at higher temperatures the growth rate increases because of thermal decomposition. The overlap of ALD windows of the Ce and Hf precursors will be of central importance for growing a ternary alloy film because it dictates the range of growth temperatures that can be employed for controllable growth.

To find out the overlap of ALD regimes between these two precursors, their respective growth curves will be plotted together over the same range of temperatures as presented in Figure 4-4 below. The dotted box indicates the range of temperatures that the ALD window can be assigned for these two precursors.

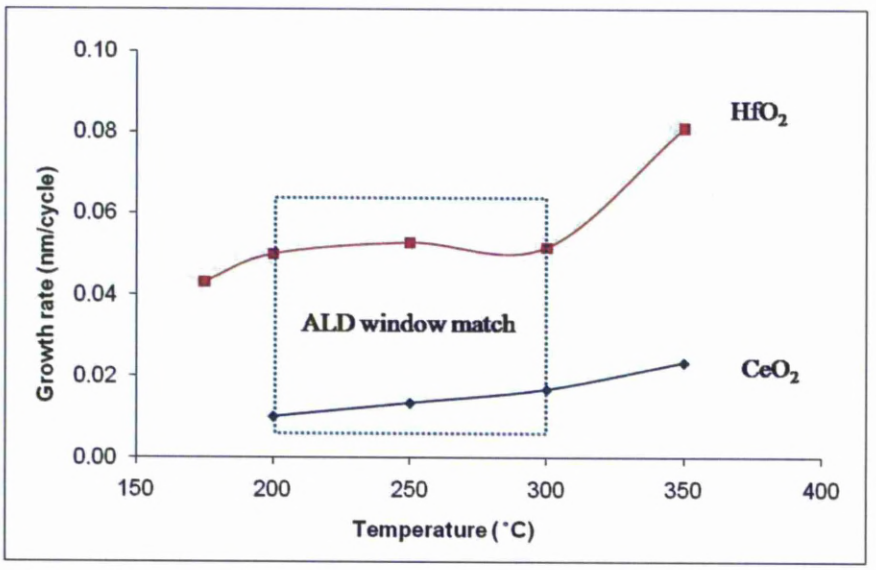

Figure 4-4: ALD window overlap for HfO_2 and CeO_2 growths.

As discussed in previous sections, a true ALD regime is only observed for the growth of HfO_2 over the range of temperatures between 200°C and 300°C. As a result, a true ALD window overlap could not be strictly determined for these two precursors. However, because the growth rate of HfO_2 was much higher than CeO_2 and the aimed doping levels of cerium would not be too high, this non-ideal ALD growth behaviour of CeO_2 was deemed to be practically acceptable. Therefore, in order to determine the growth temperature for the ternary oxide films, it was possible to choose any temperature within the ALD region of HfO_2. However, due to the fact that the growth rate of CeO_2 was very low compared to HfO_2, the growth temperature for the ternary oxide films later was chosen at the highest possible value, i.e. 300 °C to ensure the best compromise between the ALD window overlap and the growth rate of CeO_2.

4.3 Growth of Ce-doped hafnia

In this section, key details of the LIALD Ce-doped HfO_2 growth will be presented and analysed to characterise the process. The compositions of samples were determined using MEIS analysis to find out the relationship between growth parameters and their corresponding cerium incorporations. Initially, all the films were grown in two separate batches for different targets. The first batch was grown mainly for the purpose of studying phase stabilisation during post growth annealing in different environments, followed by a specific interest of electrical characterisations in the aimed 10% Ce sample, which was close to the theoretically calculated value to give the optimal stabilising effect to the higher-k phases of HfO_2 [4]. Hence, in this batch, a wide range of cerium doping levels, from approximately 5% to 30% were investigated and consequently subjected to various post-growth treatments to characterise the phase stabilisation and evolution in those films. The second batch was designed to focus on more detailed investigations of electrical properties of Ce-doped HfO_2 films with a very narrow range of concentration around 10% Ce. Therefore, the growth results of these two batches and their corresponding composition analysis will be discussed in parallel to extract important information about the growth process and some observed discrepancies between these two batches. This section will be concluded with a table of as-grown samples with their corresponding information such as compositions and thicknesses.

4.3.1 Growth data

A detailed description of the deposition technique has been presented previously in chapter 3. Hence, this section only describes briefly the method used and some key parameters involved during the growth process.

$Ce_xHf_{1-x}O_2$ films were deposited by LIALD on as-received *n*-type Si (100) substrates. The precursors (described in the previous sections) were dissolved in anhydrous toluene at a concentration of 0.05M and were injected into the vaporiser which was held at 160 °C. Argon gas at a flow rate of 200 sccm was used as a carrier gas to help transfer the precursor vapour to the reaction chamber while the reactor pressure was maintained at 5 mbar.

The growth temperature of 300 °C was chosen as the optimum for matching the ALD windows of CeO_2 and HfO_2, presented above. Ozone was used as a source of oxygen and introduced at the inlet of the reactor controlled by a pneumatic valve. The cerium incorporation in the films was controlled by changing the ratio of Ce-oxide ALD cycles to the Hf-oxide ALD cycles. Each ALD cycle consist of a four step process following a sequence: precursor-dose/purge/O_3-dose/purge. Hence the growth of a Ce-doped Hf-oxide sample can be described by the following sequence:

$$n\times\{i\times(\text{Hf-precursor/purge/}O_3\text{/purge})\ j\times(\text{Ce-precursor/purge/}O_3\text{/purge})\}$$

where i and j are integer numbers of Hf-oxide and Ce-oxide deposition cycles and n is the number of times that the sequence is repeated.

From the previous results obtained for each individual precursor, it is possible to estimate the expected composition that will be obtained with a given ALD sequence based on relative deposition rates. The growth rate of HfO_2 is roughly three times higher than CeO_2, hence a 1:1 ratio should require j to be three times the value of i. However, previous studies for various other compound oxide systems from the same reactor indicate that this is not always the case. This added complexity may be due to interface interactions between one material and the next affecting surface absorption or even etching effects. As a result of this potential complexity, the value of j was fixed as 1 for all the subsequent film growths as a starting point. For the first batch, the value of i were chosen as 2, 4, 9, 12 and 19, which translated to the Ce/Hf pulse ratio as 1/2, 1/4, 1/9, 1/12 and 1/19 respectively. Following initial analysis of the composition of these samples, which will be described shortly, the second batch of samples were deposited with cycle ratios of 1/7, 1/9 and 1/11. The total number of ALD growth super cycles defined by, n, was varied from 30 to 200, with the aim of achieving nominal film thicknesses between 3 and 30 nm. The reason for targeting films with such a large range of thicknesses is related to the measurement techniques used to characterise these films. For example, XRD and Raman require relatively thick films towards the higher end of the targeted range, while MEIS requires significantly thinner films.

As films with compositions close to 10% Ce were expected to be of significant interest, the films thicknesses in the second batch were designed to cover the whole thickness range, i.e. films with increasing thicknesses in relatively even steps.

In order to characterise the growth process of Ce-doped Hf-oxide films by alternating the Ce/Hf pulse ratios, weight gain of each sample was measured after each growth run. Because of the difference between the bulk densities of HfO_2 ($d=9.68$ g/cm^3) and CeO_2 ($d=7.3$ g/cm^3), it was expected that the weight gain per cycle for each specific sample should vary in relation to the Ce/Hf ratio. Therefore, the weight gain per cycle is a low cost tool for evaluating the growth process; by understanding the relationship between the input (ALD cycle ratio) and the output (mass deposited). Figure 4-5 demonstrates the variation of weight gain per cycle of the first batch against the Ce/Hf ALD cycle ratio (represented by the cerium ALD cycle fraction, for instance a pulse ratio 1/9 is equivalent to a fraction of 0.1). This cerium ALD cycle fraction can be assumed to be equivalent to the theoretical cerium concentration incorporated into the film if the difference in growth rate between CeO_2 and HfO_2 in temporarily ignored. Samples of pure HfO_2 and CeO_2 are also included for illustration.

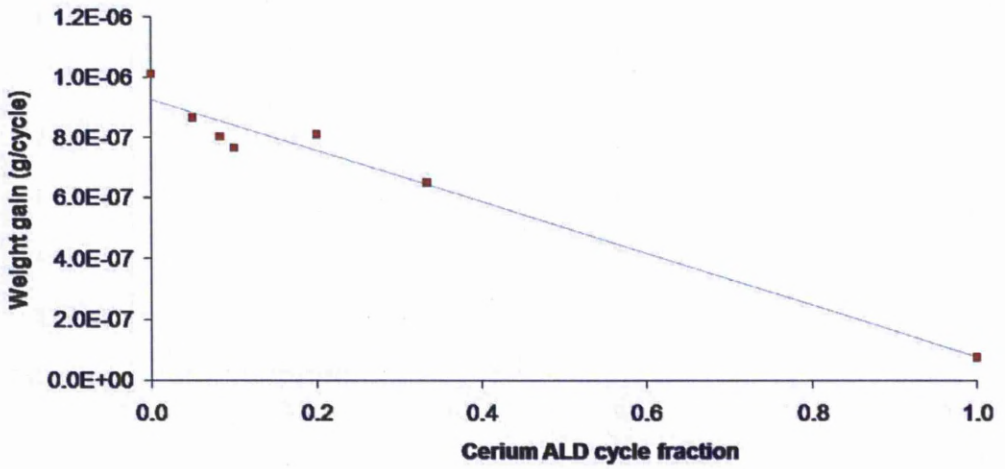

Figure 4-5: Dependence of weight gain upon theoretical percentage of Ce atomic incorporation.

As can be seen from the above figure, a linear relationship between the weight gain per cycle and the theoretical Ce concentration data can be observed. This implies that instead of different growth rates for each constituent, the ternary oxide films still showed a tendency to response proportionately to the ALD cycle ratios.

For the second batch, the tendency of weight gains per cycle against the Ce/Hf ALD cycle ratios was also expected to behave similarly. However, the data from this batch did not correspond to the same trend previously observed in the first one. The set of films with the pulse ratio 1/7 showed a much higher value compared to the other two sets, which were relatively similar to each other. This odd behaviour, though not fully understood, could be explained by the fact that the second batch was undertaken about one year after the first one and still employed the same precursor stocks. This inevitably would lead to some degree of inconsistencies in terms of the precursors' qualities and their consequent chemical properties even though they were stored properly in reasonable conditions. Another possible reason was the inconsistent behaviour of the injector, particularly with the one used to inject $Ce(thd)_4$ precursor. Figure 4-6 shows the recorded data from the flow meter sensors installed at the inlet of the reaction chamber to monitor the liquid injected for individual precursor solution.

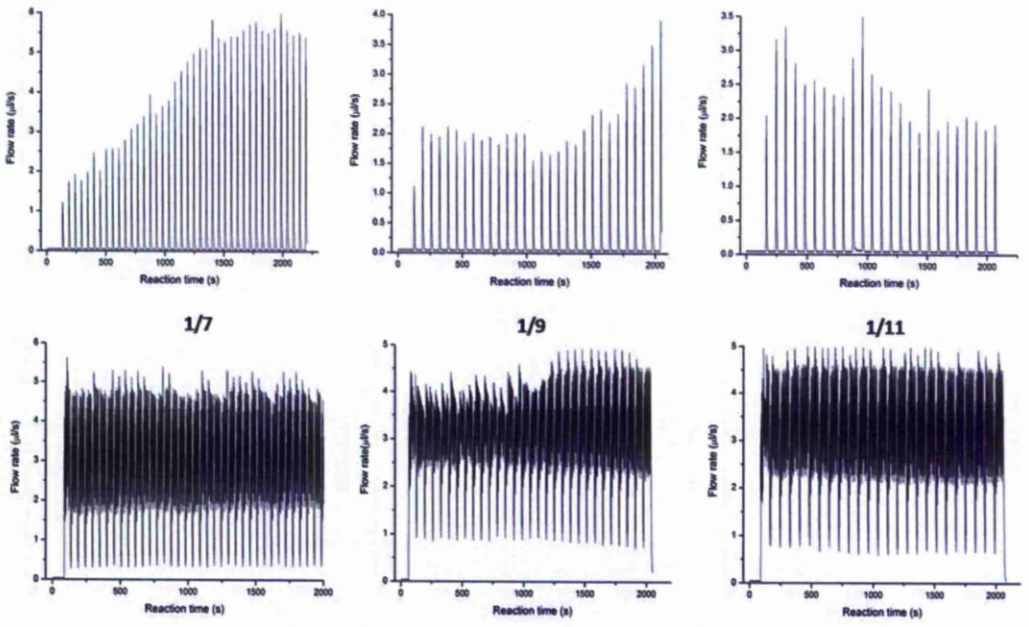

Figure 4-6: Flow rate records for Ce precursor solution (top images) and Hf precursor solution (bottom images).

As can be seen from the flow rate patterns above, while the Hf flow rate was quite consistent and similar in all cases, the Ce counterpart showed a significant variation both in value and pattern shape. Particularly in the case of sample with the ALD cycle ratio 1/7, the cerium flow rate was much higher and was maintained so nearly half of the growth time. Because of this irregular behaviour, the Ce incorporations for the second batch were thought to be quite different from the first batch.

4.3.2 MEIS analysis for compositions

MEIS was used to investigate the composition of selected films to establish the efficiency of cerium incorporation in the films. Three samples from the first batch with Ce/Hf ALD cycle ratios of 1/2, 1/4 and 1/9 respectively were initially selected for MEIS measurements, these samples were kindly measured at the Daresbury MEIS facility by Dr M. Werner et al [5], together with raw data processing. The MEIS energy spectra were recorded at a scattering angle of 125.3°to collect ions emerging from the (100) direction. This scattering angle was selected to give good mass discrimination between the cerium and hafnium, hence allowing these elements to be effectively resolved and the atomic composition of the films to be determined.

Figure 4-7 shows the MEIS spectra of the three samples. Although the cerium peaks overlapped partially with hafnium peaks, Ce/Hf ratios can still be obtained by deconvoluting the peaks. This process in turn was simplified by assuming that the ratios of integrated peak areas for each element were similar to their corresponding ratios of peak heights. Consequently, the Ce/Hf ratios were calculated using the peak heights normalised using "scattering cross-section" factors (see chapter 3 for more details of the experimental setups and data analysis). The error in MEIS for estimating element concentration was less than 10% [5, 6].

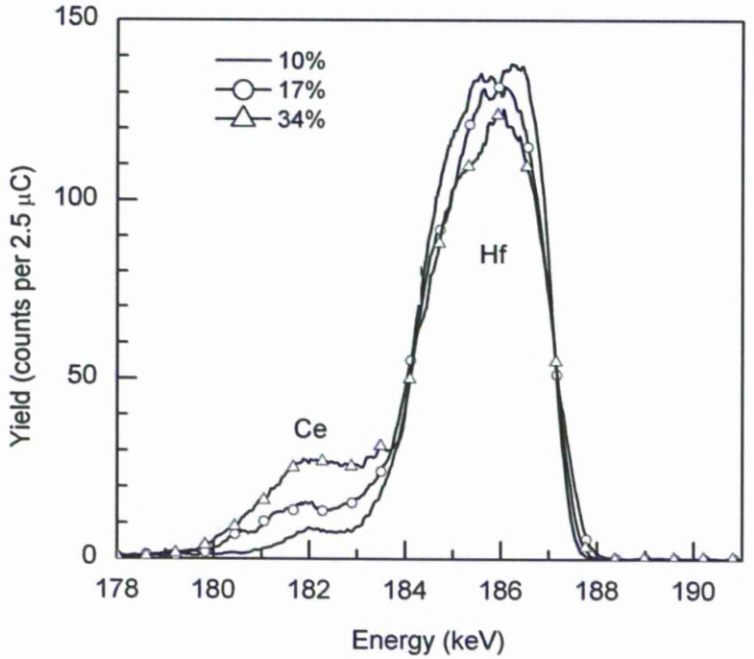

Figure 4-7: MEIS energy scan for 1:9, 1:4 and 1:2 samples with the estimated cerium concentration 10%, 17% and 34% respectively (125.3° scattering angle) [7].

Another MEIS measurement for the film with 1/12 Ce/Hf ALD cycle ratio was performed in another later session yielded the estimated cerium content about 8%. The relationship between cerium atomic incorporation (derived from Ce/Hf ALD cycle ratios) during the growths and the actual cerium concentrations in the films therefore can be plotted (see Figure 4-8) to investigate the growth process from all the results mentioned above. This relationship is of crucial importance to understand the growth of this ternary oxide in terms of the controllability of the process to reach a specific cerium doping level and hence, prove the feasibility of such LIALD process to deposit films with required doping concentrations.

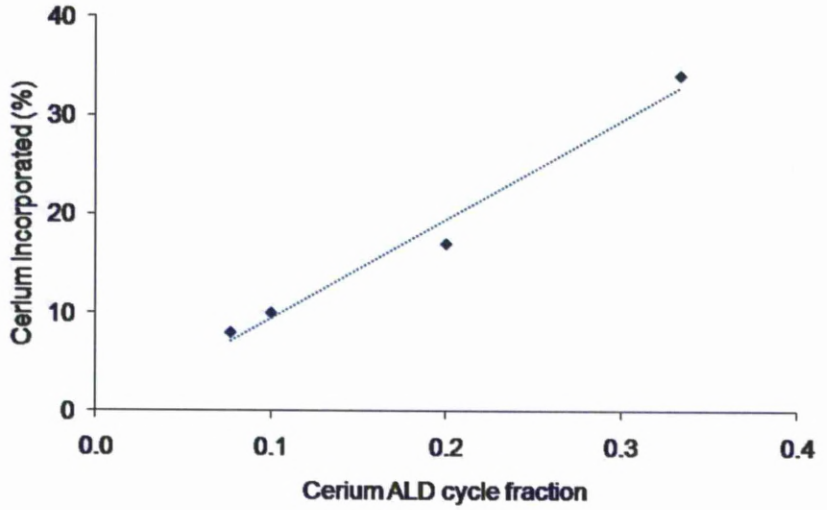

Figure 4-8: Cerium incorporated into films as a function of cerium ALD cycle fraction (1st batch)

As can be seen from the above plot, a linear relationship between the cerium atomic percentages incorporated and their corresponding cycle fractions injected can be observed. This result confirms a proportionate response of the cerium concentrations in deposited films with the Ce/Hf ALD cycle ratios, which was also demonstrated previously by the weight gain per cycle against pulse ratios. From this relationship, the cerium concentration of the last sample of the first batch with the Ce/Hf ratio 1/19 can be extrapolated to yield a result of approximately 5%.

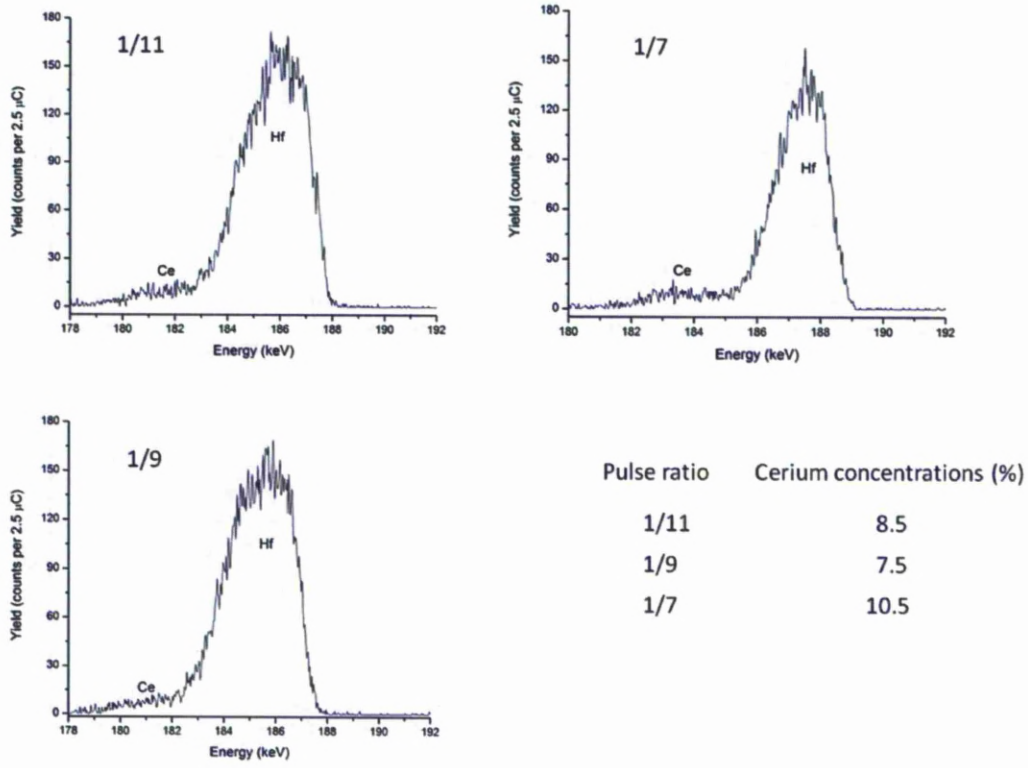

Pulse ratio	Cerium concentrations (%)
1/11	8.5
1/9	7.5
1/7	10.5

Figure 4-9: MEIS energy spectra and estimated cerium concentrations for the films of the second batch (125.3° scattering angle).

The composition analysis was also conducted to determine the cerium doping levels for the films in the second batch. Their MEIS energy spectra, together with corresponding cerium estimated concentrations, are presented in Figure 4-9. As mentioned in previous section, the behaviour of the growth in the second batch of samples was suggestive of a small discrepancy compared to the first batch as can be seen from Figure 4-10. In this figure, cerium concentrations of three samples from the second batch are incorporated into the linear relationship observed for the first batch to compare growth behaviour between these two batches. While the sample with the ALD cycle ratio 1/11 showed a similar cerium concentration to the 1/12 sample in the first batch, somewhat lower percentages of Ce than expected were found for the other two, especially with sample grown with the cycle ratio 1/9. This result confirms that the growth of the second batch did not achieve the exact results planned. Nevertheless, because the sample with 1/7 pulse ratio was found to contain about 10% cerium, it could still be used to investigate the electrical characteristics for this specific doping level.

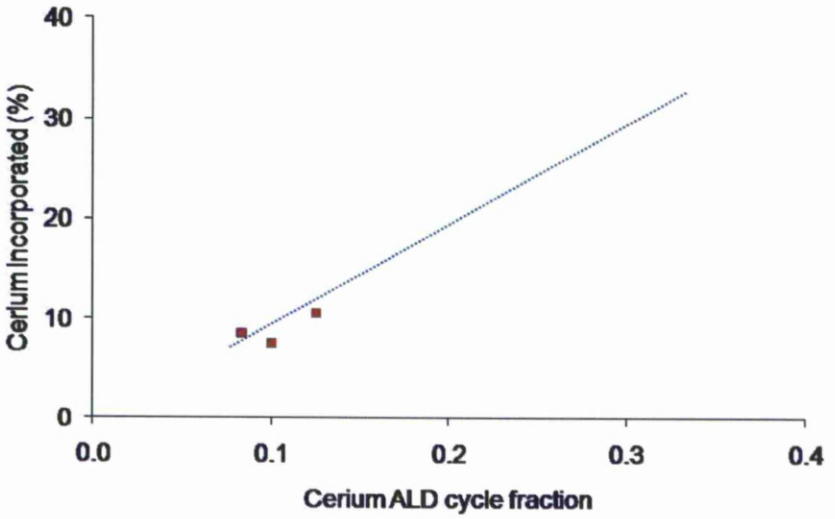

Figure 4-10: cerium incorporated into films as a function of cerium ALD cycle fraction (2nd batch)

All the growth data of samples from these two batches destined for subsequent analysis are tabulated in Table 4-1, with details of sample names, cerium concentrations and thicknesses.

Table 4-1: Summarised data for all as-grown samples from two batches. The thicknesses were calculated from Ellipsheets (see section 3.7.4 for more details) with a fixed refractive index 1.9 for all films.

Sample	Ce/Hf Pulse ratio	Cerium %	Thickness (nm)
First batch			
1329	1/19	5	27.5
1331	1/12	8	18.0
1318	1/9	10	23.0
1320	1/4	17	31.3
1321	1/2	34	24.9
Second batch			
1527	1/11	8.5	20.4
1528	1/9	7.5	16.3
1531	1/7	10.5	3.0
1532	1/7	10.5	6.4
1533	1/7	10.5	11.5
1534	1/7	10.5	17.5
1535	1/7	10.5	20.5

4.4 Summary

In this chapter, the main results related to the growths of Ce-doped HfO_2 films are presented, together with corresponding composition analysis by MEIS. The LIALD process was firstly characterised for two separate single source precursors chosen to grow HfO_2 and CeO_2 respectively. After growth parameters were established from these initial studies based on the concept of ALD window overlap, the compound oxide was grown subsequently in a wide range of cerium doping levels in two separate batches. Growth and MEIS data from the first batch showed that by alternating the Hf/Ce cycle ratio, the cerium concentration incorporated into films could be controlled in a predictable manner. While these analyses demonstrated a controllable and predictable LIALD process in terms of cerium incorporated into the films against the Ce/Hf cycle ratios from the first batch, the second batch showed some degree of disparity in terms of growth behaviour. As a result, these unexpected results inevitably would narrow the aimed investigations initially planned for the second batch though subsequent key experiments involved the samples from this batch can still be undertaken with considerations to the specific interest of the 10% Ce sample.

References

1. Kukli, K., Pilvi, T., Ritala, M., Sajavaara, T., Lu, J. and Leskela, M. (2005) Atomic layer deposition of hafnium dioxide thin films from Hafnium tetrakis(dimethylamide) and water. *Thin Solid Films,* **491**, 328-338.
2. Paivasaari, J., Putkonen, M. and Niinisto, L. (2002) Cerium dioxide buffer layers at low temperature by atomic layer deposition. *Journal of Materials Chemistry,* **12** (6), 1828-1832.
3. Jones, A. C., Aspinall, H. C., Chalker, P. R., Potter, R. J., Manning, T. D., Loo, Y. F., O'Kane, R., Gaskell, J. M. and Smith, L. M. (2006) MOCVD and ALD of high-k dielectric oxides using alkoxide precursors. *Chemical Vapor Deposition,* **12**, 83-98.
4. Fischer, D. and Kersch, A. (2008) The effect of dopants on the dielectric constant of HfO_2 and ZrO_2 from first principles. *Applied Physics Letters,* **92** (1).
5. Werner, M. (2006) *Damage formation and annealing studies of low energy ion implants in Silicon using medium energy ion scattering (PhD thesis).* The University of Salford, UK,
6. Chu, W. K. and Mayer, J. W. (1978) *Backscattering Spectrometry,* Academic Press, New York,
7. Chalker, P. R., Werner, M., Romani, S., Potter, R. J., Black, K., Aspinall, H. C., Jones, A. C., Zhao, C. Z., Taylor, S. and Heys, P. N. (2008) Permittivity enhancement of hafnium dioxide high-k films by cerium doping. *Applied Physics Letters,* **93** (18).

Chapter 5 PHASE STABILISATION OF Ce-DOPED HAFNIA FILMS

5.1 Introduction

As mentioned previously, one of the main interests within the semiconductor industry is finding alternative materials to replace SiO_2 for gate dielectric applications. HfO_2 and its derivatives have been extensively investigated and are now being used in some of latest generations of microprocessors, particularly from Intel in their 45 nm node chip production. While HfO_2 in its current form will probably be used for at least the next couple of technology node generations, ongoing research into higher-k dielectrics is still essential to meet future scaling requirements By doing so, the rate of device scaling and better performance demanded from the market can be maintained satisfactorily. One promising trend, at least for near-future applications, among many ways to keep up with the pace from production demand, is looking for other HfO_2-based systems which can offer good dielectric performances similar to HfO_2 on its own but with higher k-value. Some recent theoretical [1-3] and experimental [4] studies have demonstrated that by doping HfO_2 with some elements, the higher-k phases (tetragonal or cubic) can be stabilised at room temperature. These positive results also provided the main motivation for the experimental work of this research and helped build up the framework to conduct the studies of various rare earth-doped HfO_2 thin films within the functional materials research group at the University of Liverpool. Among different studies carried out, Ce-doped hafnia has been the focal point of this study and hence, all the following results and discussions in this chapter will focus on the influence of using cerium as a dopant to improve the dielectric performance of hafnium oxide by studies of phase stabilisations in this binary oxide films.

The chapter will be organised as follows. The first four sections will present and discuss the results from different annealing environments: air, N_2 and vacuum. The influences of these post-growth treatments and cerium doping levels to the phase stabilisation and crystal structures will be demonstrated via data obtained from XRD,

UV Raman, AFM, MEIS and TEM. In terms of electrical characterisations, all results will be specifically focused on the sample with the aimed 10% cerium.

According to a theoretical first-principle study by Fisher et al.[2], approximately 10% cerium doping is required to stabilise the tetragonal phase of HfO_2 and hence, obtain the highest permittivity increase. As a result, the sample with a target composition of 10% cerium was specifically selected for full and detailed electrical analysis to verify the enhancements of adding cerium to hafnium oxide thin films, especially in term of boosting the k-values. In the last section, the effect of film thickness to the phase stabilisation and consequent dielectric properties will be discussed, also with purposeful considerations to the sample with the target of approximately 10% cerium.

5.2 Air annealing study

The effect of the annealing temperature on the crystal structure and the relating phases were firstly surveyed in air. Although air annealing is not used for industrial processing, it is a practical way of providing an oxygen-rich environment, which ensures that films have stoichiometric composition (fully oxidised). It is therefore, a good starting point to build up initial knowledge about the crystal structure and phase evolution with annealing temperatures in an increasing manner.

In this section, results for phase and crystal structure analysis of all the films covering the whole range of cerium doping levels will be presented and discussed. The data collected from XRD and UV Raman will be thoroughly analysed firstly for the sample with 10% Ce, followed by the other samples to yield important information about the phase assignments and the evolutions of crystal structures.

5.2.1 XRD phase analysis

Figure 5-1 shows the evolution of XRD spectra with annealing temperature for the 10% Ce sample after 15 minutes air annealing between 600°C and 1000 °C. The spectrum of the as-grown sample is also shown for comparison. The scan was performed in the 2theta angle range between 20° to 40°as the characteristic peaks of

all three main polymorphs of HfO_2, namely monoclinic, tetragonal and cubic, could be found between 27°and 33°. From experimental results and literature data, all three polymorphs also possess another peak at ~35.5° which is nearly identical for each of the phases and hence, is of little use for phase identification.

Another assumption made here is the possibility of orthorhombic phases occurring in the films. Because such phases only exist under high pressure conditions, it is very unlikely that they could be formed during film growth or subsequent annealing processes, which were deemed stress-free and hence, would be excluded from the phase investigations.

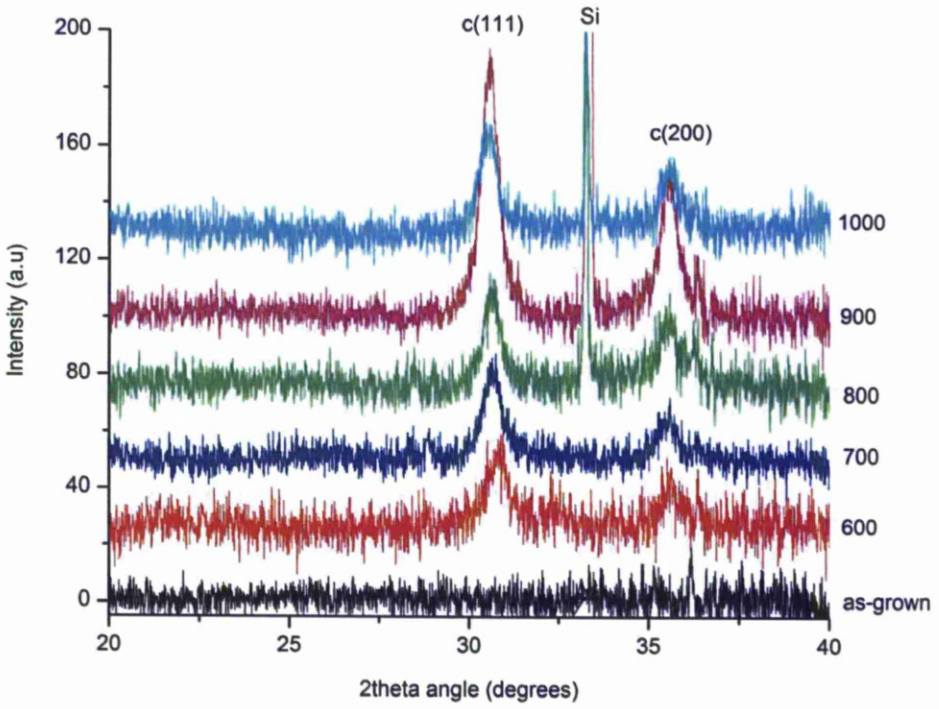

Figure 5-1: XRD spectra of 10% Ce sample annealed in air for 15 minutes at various temperatures

Except for the as-grown example which was amorphous, all other films showed some degree of crystallinity as can be seen from their spectra (Figure 5-1). For this 10% Ce sample, the dominant feature around 30.5° was consistently observed and assigned with the index (111) on the basis of fluorite-type cubic structure as firstly reported by Passerini in [5] and later from ICDD card [53-550], both of which shows

a very close match to the experimental patterns in Figure 5-1 above.The peak at 35.5° is attributed to the plane (200) from the same cubic structure mentioned above, while the narrow features at approximately 33° and 36° are attributed to the silicon substrate.

By using a peak-fitting process adopting a Lorentzian-type distribution (more details can be found in chapter 3) combining with Bragg's law for diffraction and Debye-Scherrer equation for crystallite estimation, a detailed analysis of these films was conducted. The results of this analysis are tabulated and shown graphically in Table 5-1 and Figure 5-2 respectively.

The results from these analyses revealed very small uncertainties providing that all other factors affecting the data acquisition from the XRD equipment were sufficiently stable, namely the systematic error (goniometer accuracy) within ± 0.01°. However, due to the polycrystalline nature of the films and their relatively small crystallites, most spectra contained different degrees of background noise and the peaks in general did not have sharp and well-defined shapes as usual in the case of powder diffraction. Nevertheless, after following a peak-fitting process, meaningful data could still be extracted within acceptable accuracy that the method could offer at its best. A snapshot of one peak-fitting result window is shown in Figure 5-3 as an illustration for this data processing.

Table 5-1: Detailed peak analysis for (111) plane and its relating crystal structure estimation for 10% Ce air annealed sample with reference cubic data from ICDD card [53-550].

Annealing temperature (℃)	600	700	800	900	1000	Reference cubic data
2theta angle (degrees)	30.80	30.65	30.63	30.55	30.51	30.38
d-spacings (Å)	2.90	2.92	2.92	2.93	2.93	2.9394
Cubic cell (Å)	5.03	5.05	5.06	5.07	5.07	5.096(9)
Crystallite size (nm)	11.85	12.98	13.69	14.36	14.46	

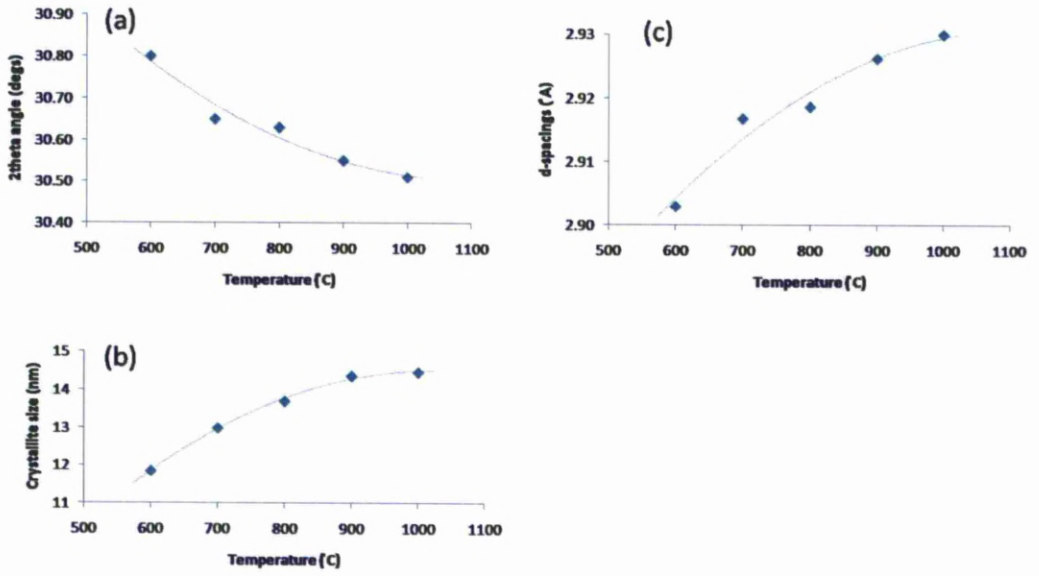

Figure 5-2: Plots of (111) peak analysis of (a): 2theta angle, (b): crystallite size and (c): d-spacings against annealing temperatures for 10% Ce air annealed series

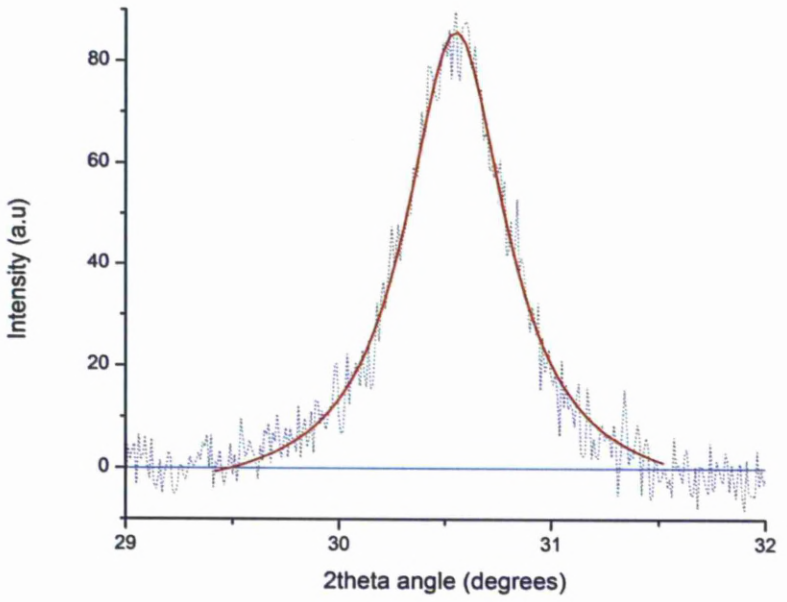

Figure 5-3: Illustration of peak-fitting process adopting Lorentzian distribution for 10% Ce sample annealed in air at 900 °C.

Figure 5-2a shows the effect of anneal temperature on the peak position of the main "cubic" (111) XRD peak. The peak clearly shifts to the left with increasing temperature. This peak can be attributed to the high-temperature cubic phase and the peak position tends to approach the reference value (Table 5-1) as the annealing temperature is increased. It should however, be noted than the reference value quoted in Table 5-1 are for pure hafnia and hence, some degree of lattice distortion is to be expected when cerium is introduced into the matrix. This distortion is caused by the larger size of Ce^{4+} (111pm) compared to Hf^{4+} (97pm) [6] and is likely to cause a reduction in the d-spacing compared to the ideal CaF_2-type cubic.

The effect of phase stabilisation ("cubic" in this case) was clear even at quite low annealing temperature. While pure hafnia becomes monoclinic after annealing, the Ce-doped hafnia crystallises into the stabilised high temperature cubic phase. In terms of d-spacing (Figure 5-2c), which represents the distance between parallel planes, the value became larger indicating that the unit cell is increasing in size. All of these trends could be graphically demonstrated by a form of a polynomial trend line as shown in the aforementioned plots.

In term of crystallite size, a similar trend was observed though with a little difference. As the annealing temperature increased, the crystallite size also increased but seemed to approach to a maximum value after 900℃. From the viewpoint of crystal growth, this can be understood as an effect of space constraint. Because the films are relatively thin, typically 20-30 nm, they are constrained in the z-direction and hence, have a limited maximum crystallite size. Moreover, the crystallite size is directly dependent on the thermodynamic equilibrium when different grains formed and hence, likely reached its maximum size at around 900°C. This postulation is supported by the observation of island-growth seen with the AFM image in Figure 5-4. While the as-grown sample was quite smooth and showed no indication of crystallization, the air annealed one was appreciably rougher, with clear differences caused by annealing environment. The increased roughness can be attributed to crystallisation of the films following annealing. Complete details about AFM studies for different samples in various annealing environments will be presented later in section 5.5.

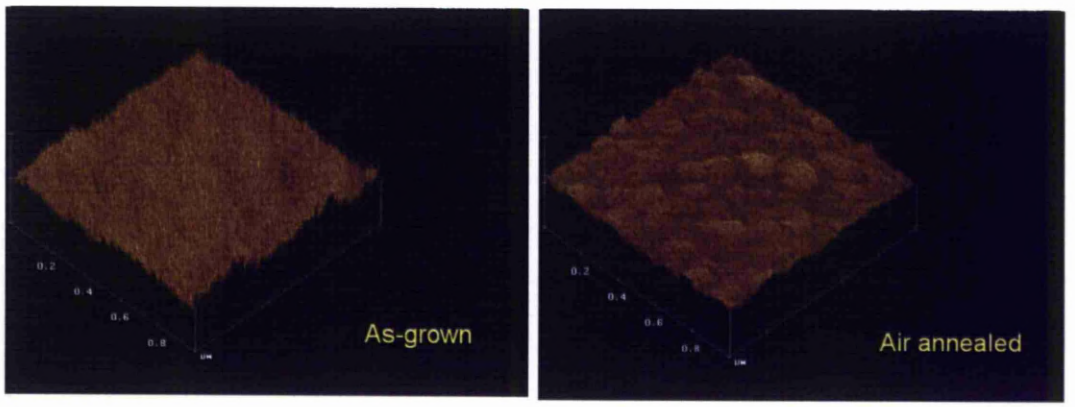

Figure 5-4: AFM images of 10% Ce as-grown and air annealed samples at 900℃, 15 minutes .

Following the XRD study of the 10% Ce sample, all the others were also subjected to air annealing over the same range of temperatures. Their XRD spectra will be presented in the following figures for all samples at each annealing temperatures to compare directly the differences in phase composition(s) and their corresponding evolutions.

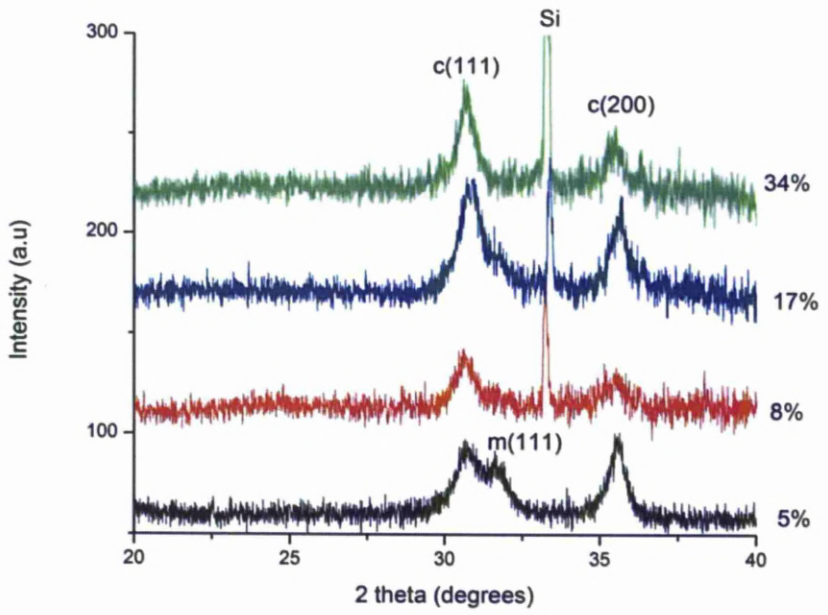

Figure 5-5: XRD spectra of 600℃ air annealed samples.

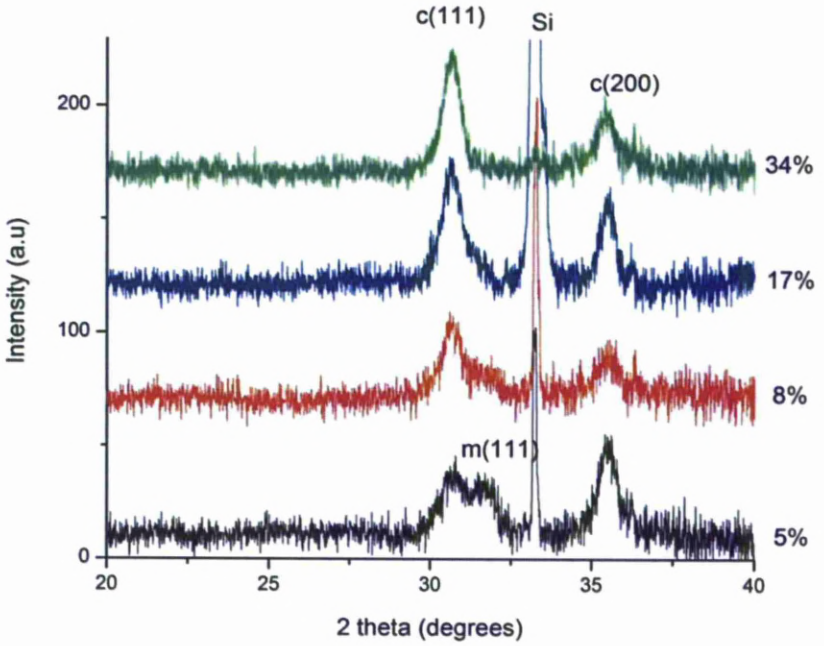

Figure 5-6: XRD spectra of 700℃ air annealed samples

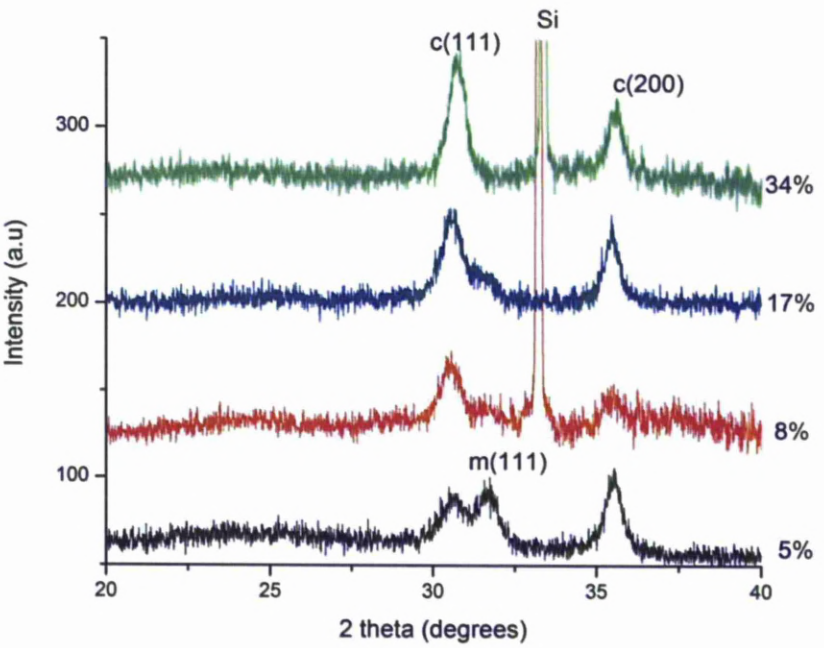

Figure 5-7: XRD spectra of 800℃ air annealed samples.

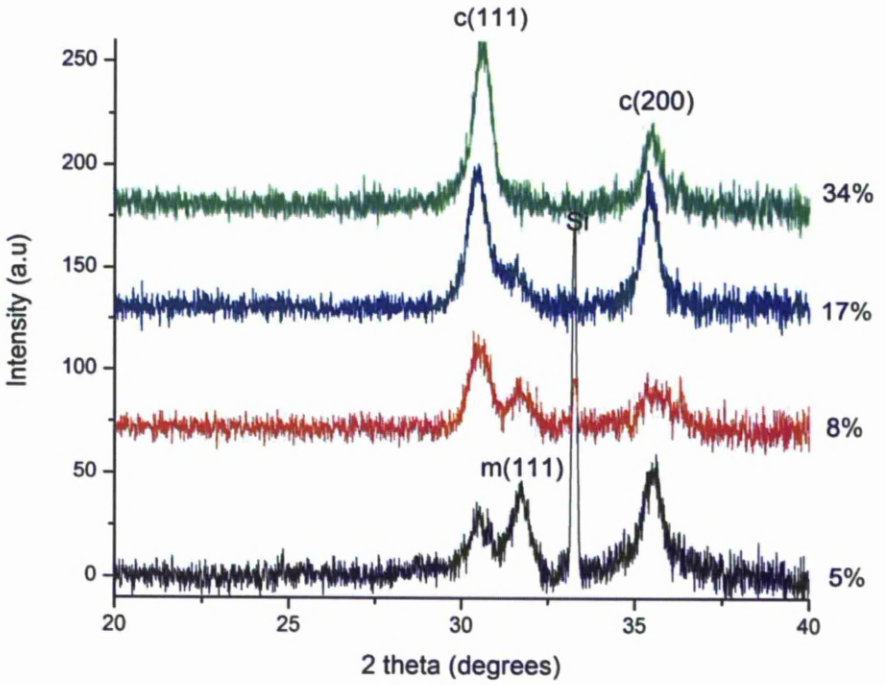

Figure 5-8: XRD spectra of 900℃ air annealed samples.

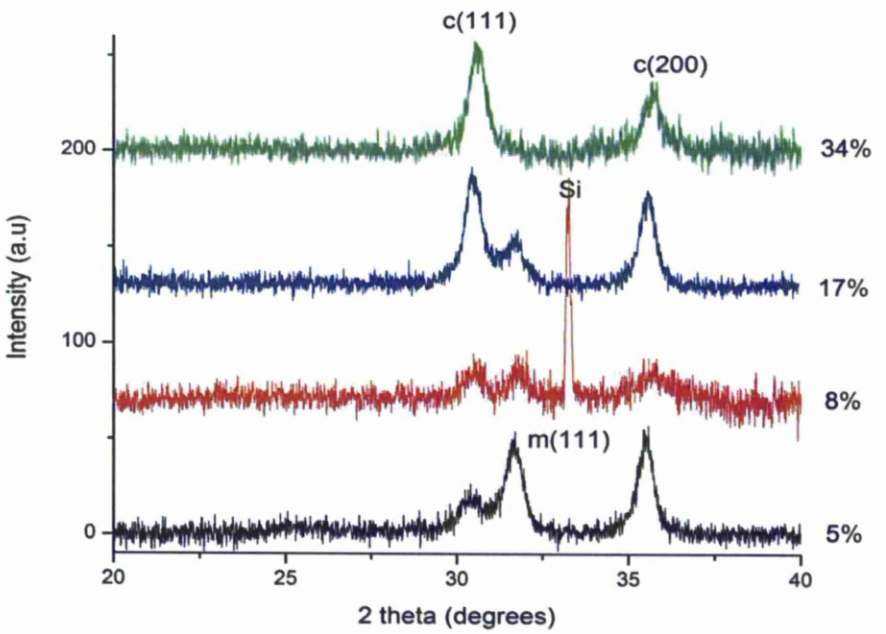

Figure 5-9: XRD spectra of 1000℃ air annealed samples.

The main features of the diffraction patterns were assigned as c(111) and m(111) representing the plane (111) of "cubic" (the high temperature fluorite-type) and monoclinic phases respectively. Additionally, a peak whose position is at around 35.5° consistently appeared in all spectra and labelled as c(200) [5].Therefore, two peaks contributing to the cubic phase from all of these XRD results are identical to the patterns of the 10% Ce sample mentioned previously. After assessing all of the XRD results, some qualitative observations can be deduced. Firstly, with the exception of the 34% Ce sample, all show signs of being a mixed phase containing both monoclinic and cubic phases regardless of the annealing temperatures. For low doping concentrations, i.e. 5% and 8%, the monoclinic phase increases substantially with annealing temperature, particularly beyond 800°C. This tendency indicates that low doping concentrations have a limited ability to stabilise the high temperature "cubic" phase. The stabilisation effect is not strong enough to fully suppress the formation of monoclinic phase. In the case of 17% sample, the cubic phase remains dominant although the monoclinic still existed with relatively constant percentage except at 1000°C with even more significance. The co-existence of two phases in the 17% Ce doped samples is somewhat unexpected in light of the predicted results obtained previously for the 10% Ce sample, as well as when being compared to the other samples. If the analogy between ZrO_2 and HfO_2 is assumed then it might be due to the solubility of different polymorphs during air annealing at some specific temperatures with varying cerium concentrations. For example, at around 17% cerium doping level, there would be a phase separation from a tetragonal parent phase to monoclinic and cubic at high temperature [7] due to the solubility limit of tetragonal phase beyond 17% Ce.

To have a more thorough understanding about the phase stabilisations as well as the effect of cerium and annealing temperature to the crystal structure of Ce-doped hafnia films, a detailed analysis of c(111) peak positions, crystallite sizes and cell parameters were performed. All the data is presented in the following tables and plotted against either cerium concentrations or temperatures. A peak-fitting process similar to the method used with the 10% Ce sample was also employed for the sample with 34% Ce because these two samples just only showed a single peak at approximately 30.5°.

For the other three samples which show a mix of phases, deconvolution of XRD peaks was required to extract information about the c(111) peak and additionally, the fraction of monoclinic phase by using the method proposed by Schmid in [8]. The analysis of this monoclinic fraction against cerium concentration and annealing temperature will be discussed after the results of the main c(111) peak.

Table 5-2 summarises the peak position data for the cubic (111) feature which have been extracted from peak-fitting process. As can be seen, a general trend is observed between the peak position and annealing temperature. If the reference peak position of HfO_2 is recalled ($2\theta_{c\,(111)} = 30.38^{\circ}$), differences between the peak positions of any given sample and of the reference cubic one ($\Delta\,(2\theta)$) against annealing temperatures can be plotted as shown in Figure 5-10. It can be seen from this figure that with increasing annealing temperatures, the peak positions of all samples consistently shift to the left, i.e. towards the position of the high-temperature cubic phase of pure HfO_2. This tendency indicates that the higher the annealing temperatures, the closer the "cubic" form in those films approaches the reference structure of pure HfO_2.

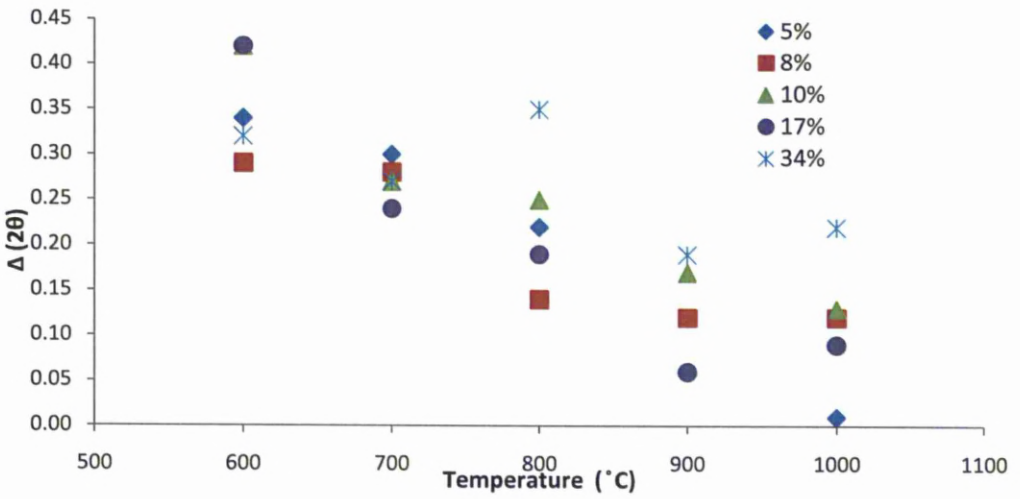

Figure 5-10: Variations of Δ (2θ) against temperatures for air annealed samples. The data points were within the experimental accuracy (see section 3.3.4 for more details).

Table 5-2: Peak positions of c(111) in 2θ degrees of all air annealed samples

Ce (%)	Annealing temperature (°C)				
	600	700	800	900	1000
5	30.72	30.68	30.60	30.50	30.39
8	30.67	30.66	30.52	30.50	30.50
10	30.80	30.65	30.63	30.55	30.51
17	30.80	30.62	30.57	30.44	30.47
34	30.70	30.65	30.73	30.57	30.60

With the exception of the 5% Ce sample, which has a c(111) peak which approaches the high-temperature cubic peak position ($2\theta_{c\,(111)} = 30.38^{\circ}$), all of the other samples have XRD peaks that converge towards higher angles. This is believed to be due to the low level of cerium doping, which means the distortion that cerium introduces to the hafnia matrix is quite modest. As a result, the unit cell could gradually approach the cell size of the undoped cubic form. Because the peak position is directly linked to the degree of distortion of the "cubic" unit cell, it can be suggested that all of the samples, other than the 5% one, has a degree of unit cell distortion retained even at high temperatures. This tendency is also supported by the data of unit cell for all samples presented in
Table 5-3 below.

Table 5-3: Crystallite size and cubic unit cell of air annealed films as a function of cerium doping levels and annealing temperatures.

Ce (%)	Crystallite size (nm)				
	600	700	800	900	1000
5	8.75	8.64	8.11	9.68	8.48
8	12.92	11.04	10.92	10.94	12.78
10	11.85	12.98	13.69	14.36	14.46
17	10.24	11.06	10.38	11.70	13.80
34	12.84	11.91	12.84	13.17	14.16
d-spacing (Å)					
	600	700	800	900	1000
5	2.91	2.91	2.92	2.93	2.94
8	2.91	2.92	2.93	2.93	2.93
10	2.90	2.92	2.92	2.93	2.93
17	2.90	2.92	2.92	2.94	2.93
34	2.91	2.92	2.91	2.92	2.92
Lattice parameter (Å)					
	600	700	800	900	1000
5	5.04	5.05	5.06	5.08	5.09
8	5.05	5.05	5.07	5.08	5.08
10	5.03	5.05	5.06	5.07	5.07
17	5.03	5.06	5.07	5.09	5.08
34	5.04	5.05	5.04	5.07	5.06

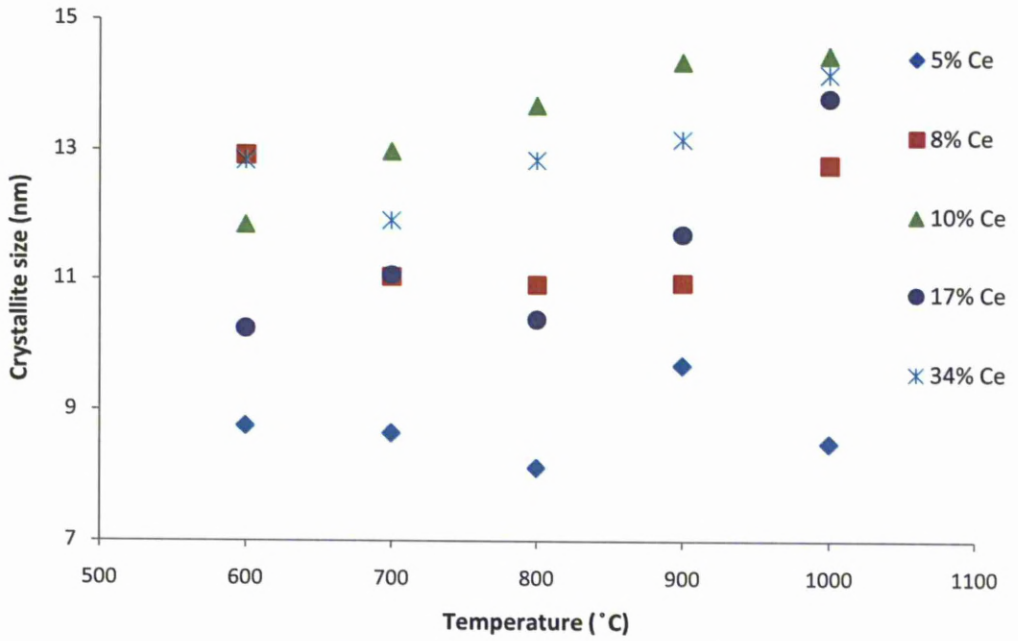

Figure 5-11: Variations of crystallite sizes against temperatures for air annealed samples. The data points were within the experimental accuracy (see section 3.3.4 for more details).

Figure 5-11 depicts graphically the influence of annealing temperature on the crystallite size of all samples. It can be seen from the above plot that these samples behaved quite differently in response to annealing temperatures. For the 5% Ce sample, the crystallite size does not vary significantly with increasing temperature. This observation agrees to some extent with the previous observation in Figure 5-10 for this low doping level. It may be suggested that at such low dopant content, the "cubic" form reaches a limit of crystallite size even at low annealing temperature and hence, with increasing annealing temperatures, the growth of "cubic" structure is virtually unaffected by thermodynamic driving force. In contrast, a different tendency can be observed for all other samples. For the samples with 8%, 17% and 34% Ce, all of them follow a similar trend though the 8% one seems to be slightly different from the other two at low temperatures. The crystallite sizes for these three tend to increase in a non-linear fashion with annealing temperature. The crystallite sizes fluctuate between the ranges of 600 ˚C to 800 ˚C and gradually increase afterwards. This observation indicates that for these samples, while at low and intermediate annealing temperatures, the growth of "cubic" structures is not strongly dependent on the thermodynamic driving force, it is at high temperatures.

In other words, this behaviour is suggestive of an activation threshold for crystallisation in these samples. For the 10% sample, the data shows a linear increase in crystallite size with temperature, but appears to saturate as the annealing temperature exceeds 900°C. When being directly compared to the 34% Ce sample, which also contains only one form of crystal structure, i.e. without the existence of monoclinic phase, a dissimilar crystal growth and/or crystallisation can be suggested. This can be due to the formation of different types of "metastable tetragonal phases" (see chapter 2 for more details) and/or co-existence of various intermediate phases resembling the high-temperature cubic phase of HfO_2. This issue will be discussed more in details in the following section about Raman characterisations of these films.

As mentioned previously, it is also of interest to evaluate the fraction of monoclinic phase in the samples containing 5%, 8% and 17% Ce as the monoclinic phase could not be fully suppressed by the stabilised "cubic" as in the case of the 10% and 34% Ce samples. A noteworthy detail from the aforementioned deconvolution process required for peak analysis of these three samples is only a small degree of monoclinic phase can be detected visually in some of their XRD spectra. This observations holds true for the 17% Ce sample annealed at 600 °C and 700 °C as well as for the 8% Ce sample annealed at 600 °C (see Figure 5-5 and Figure 5-6). Consequently, it was nearly impossible to fit a meaningful peak during the deconvolution process and hence, all of these monoclinic peaks have been omitted. Figure 5-12 presents the fraction of monoclinic phase obtained after XRD pattern analysis for these three samples as a function of annealing temperature.

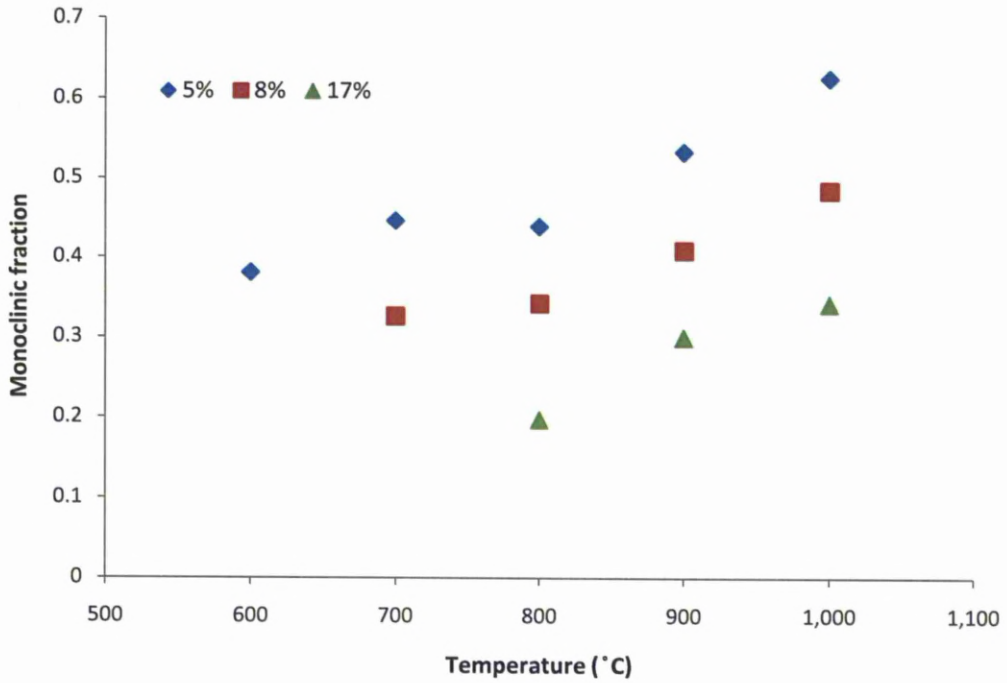

Figure 5-12: Monoclinic fraction against temperatures for air annealed samples

It can be suggested from Figure 5-12 that with increasing annealing temperatures, the fractions of monoclinic phase also increase in a seemingly linear fashion for both 5% and 8% Ce samples. In the case of 17% Ce example, it reveals that the monoclinic fraction seems likely to follow the similar trend. However, as stated previously, at annealing temperatures beyond 900 °C, a phase separation is likely to take place. If this tendency is held true for this 17% Ce sample, a constant fraction of monoclinic can co-exist with "cubic" phase and hence, can partly explain the seemingly equal values of monoclinic fraction at 900 °C and 1000 °C.

5.2.2 Raman phase analysis

Prior to the Raman results and discussions, it may be useful to recall briefly some key points regarding crystal structure and phase stabilisation in HfO_2-based materials and its twin oxide ZrO_2. Besides three main well-known structures, namely monoclinic, tetragonal and cubic, the occurrence of many other "metastable phases", particularly t' and t" forms, have been proposed and verified by both theoretical and experimental approaches (see chapter 2 for more details).

Some of these "metastable phases", in fact, exhibit a very similar structure as the high-temperature cubic one. Therefore, it is a very important issue to identify the true crystal structure as much as possible within these samples. Moreover, it is also a matter of great interest because this finding can play a key role in terms of the k-value associating with such phase as predicted in literature [1-3, 9]. For instance, the doping level approximately 10% cerium was shown theoretically by Fischer to favour a stabilised tetragonal phase in [2], which was predicted by Zhao and Vanderbilt to achieve a k- value of 70 [9].

From the previous XRD section, phase determination (mainly concerned with the assignment of cubic phase) can be established for all the films annealed in air. However, XRD suffers one main drawback for the current task of differentiating between the phases of interest here. While XRD is sensitive to the displacement of heavy atoms within the structure, it is far less sensitive to lighter elements such as oxygen due to the significantly lower scattering cross section. Many of the stabilised phases are characterised by a displacement of the oxygen sub lattice along the z-axis [10, 11]. Therefore, XRD has limited use for establishing the phase of the films without additional results from Raman scattering, which is much more sensitive to the oxygen atoms.

The Raman features of the three polymorphs of ZrO_2 and HfO_2 in terms of their active modes have been well established for some time [12]. In fact, most of the arguments about mode assignments have been around the tetragonal active modes. The situation has become further complicated since the discovery of "metastable phases" within this fluorite-related structures. As far as doping is concerned, it is not surprising to understand that this problem is due to the formations of oxygen vacancy, defects and the order-disorder phenomenon. All of them add complexity to interpreting the Raman data as selection rules can be broken down within the proximity of Brillouin zone, enabling the activations of forbidden vibrational modes.

With all of this knowledge beforehand, the Raman results of this 10% Ce sample will be treated as a starting point to assert and clarify the proposed "cubic" structure assigned previously from the XRD study. Spectra of this sample are shown in Figure 5-13 along with a spectrum of the silicon substrate.

The scan was performed in the range between 200 cm^{-1} to 1200 cm^{-1}, of which characteristic peaks of various phases can be found [10, 13].

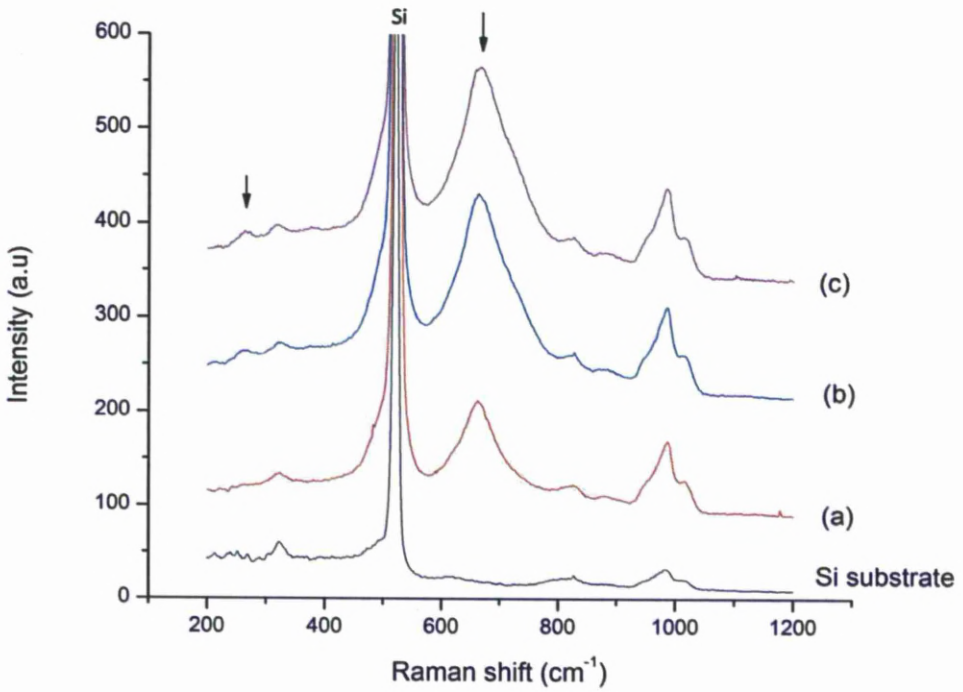

Figure 5-13: Raman spectrum of 10% Ce sample for (a): film annealed at 700°C, (b): film annealed at 900 °C, and (c): film annealed at 1000°C.

The first noticeable observation from the above figure is that the interference from the Si substrate was quite strong and thus, impeded the identification of Raman peaks from the film. The range most affected is between 450 cm^{-1} to 550 cm^{-1} which can potentially affect the observation of the expected cubic feature band around 460 cm^{-1} [12]. The presence of the film seems to have an enhancement effect on the intensity of the Si features and so far, the reason for this is still not clear. It might be that the UV laser excites the SiO_2 layer beneath the films, resulting in resonance enhancement of the Raman scattering. The same phenomenon can also be pointed out for the features around 1000 cm^{-1}, which is probably some kind of second-order mode from the Si substrate itself or from some form of carbon-contained impurity on the surface of the specimen.

The main peak of interest which consistently appeared in all the films is the one whose position is around 660-670 cm^{-1}. Another peak which can also belong to these films though with a much lower intensity is the one at approximately 260 cm^{-1}. Due to its weak signal, its contribution to the crystal structure will be revised and discussed in more details when dealing with other samples, which show more noticeable evolutions to annealing temperatures and cerium contents.

Using the peak-fitting procedure, it was found that a peak was identified around 664 cm^{-1} in all air annealed 10% Ce films and hence, should have a direct link with the "cubic" structure assigned from XRD study. Except the film annealed at 700°C, the other two show that a degree of asymmetry towards the higher wave-number range with their peaks. This phenomenon is depicted in Figure 5-14 and Figure 5-15 for samples annealed at 700°C and 1000°C respectively.

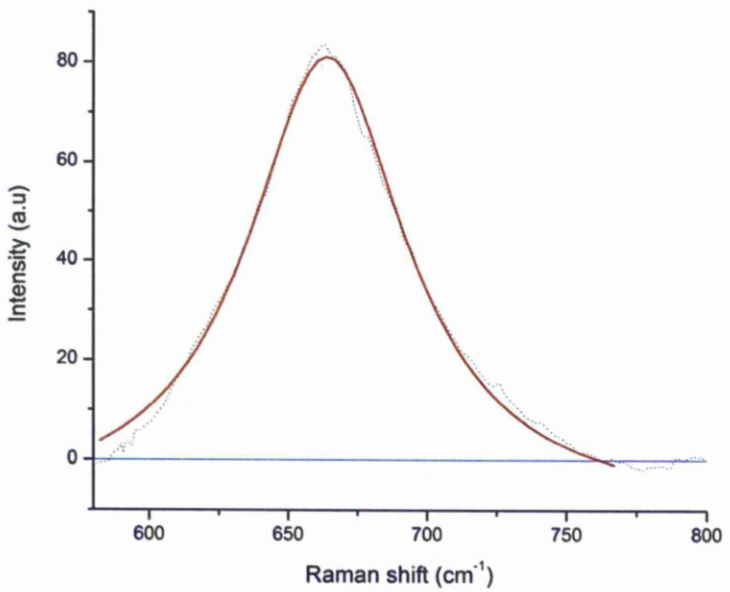

Figure 5-14: Raman peak-fitting for 10% Ce 700°C air annealed film. The dotted line represents the experimental data; the solid line assumes a Lorentzian distribution. The horizontal line represents the baseline after background subtraction.

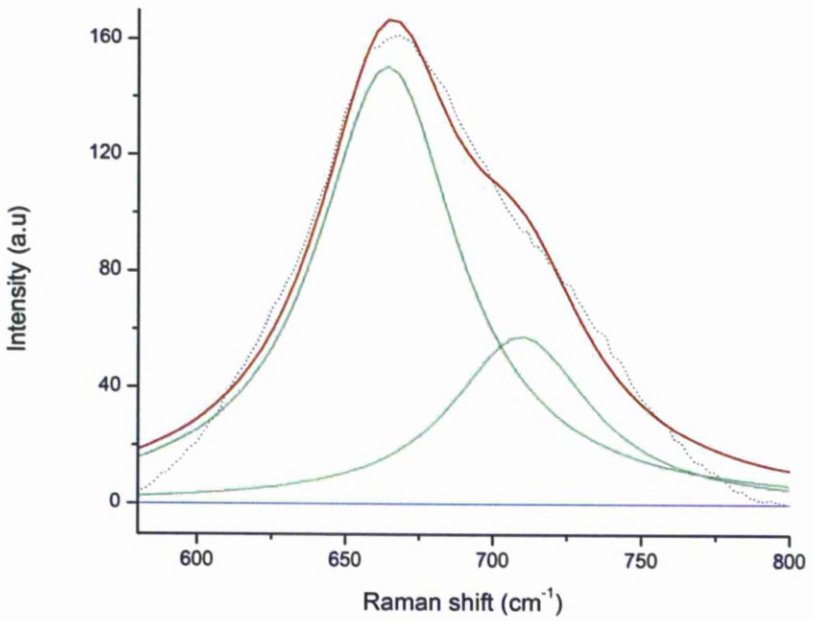

Figure 5-15: Raman peak-fitting for 10% Ce 1000 °C air annealed film. The dotted line represents the experimental data; the solid line assumes a Lorentzian distribution. The horizontal line represents the baseline after background subtraction. After the deconvolution process, it can be split into 2 other primary curves as shown in the graph.

The shoulder feature observed for the sample annealed at 1000°C is also observed for the one annealed at 900 °C, which in turns immediately raised the question about the occurrence of this asymmetry compared to the one annealed at 700 °C. The asymmetry observed can be explained by the presence of a second peak to the right of the main peak. If this peak is purely thought as a convolution of the other two main peaks, it is probably that besides the main characteristic peak at 664 cm^{-1}, another one around 710 cm^{-1} also exists. According to Yashima et al [10], this peak either can belong to a cubic structure or be assigned as a defect-induced tetragonal mode. Because no more experimental data from available literature dealing with this specific peak could be found and due to its minor importance and contribution to the characteristic peak, it is accepted here that the aforementioned hypothesis is true.

Based on the XRD study and the main peak of all films from this Raman characterization, it is reasonable to assign this Raman reflection (the peak around 660-670 cm^{-1}) belonging to a form of "cubic" structure.

However, none of such characteristic peak of AO_2 fluorite-type cubic structure [12] around 460 cm^{-1} occur nor any similar one from stabilised cubic form [14] observed when a tetragonal zirconia doped with ceria to form a solid solution. Hence, it seems at this stage, this characteristic peak cannot be assigned to a high-temperature cubic structure although the unit cell parameters calculated from XRD study still remain valid considering the "metastable cubic" configuration. Therefore, based on these results, it can be proposed that the crystal structure of 10% Ce sample possibly rendering a form of tetragonal configuration mentioned previously. This proposition will be revisited and discussed further when other samples are concerned in terms of its "tetragonality". Moreover, the appearance of the aforementioned subordinate peak somehow complicates the interpretation of this peak and therefore, creates some significant difficulties to gain any better understanding about its evolution. Nonetheless, it is still an important finding to having determined the direct relationship between the "cubic" peak from XRD study and the characteristic peak from the Raman spectra of this specific sample, which can pave the way for further insights about the phase evolution and stabilisation analysis. Raman spectra of other samples will be presented as follows, together with tabulated data for the previously discussed main feature in the case of the 10% Ce sample. The errors in the determination of peak position and FWHM were previously mentioned in section 3.4.4.

Table 5-4: Peak positions (cm^{-1}) of all air annealed samples.

Ce %	Temperature (°C)				
	600	700	800	900	1000
5	664	666	669	669	670
8	662	665	667	666	668
10	n/a	663	n/a	662	664
17	657	656	661	661	663
34	659	660	664	667	665

Table 5-5: FWHM (cm^{-1}) for the main feature of all annealed samples

Ce %	Temperature (°C)				
	600	700	800	900	1000
5	66.3	68.1	70.4	74.8	69.4
8	48.1	72.2	68.0	64.0	66.0
10	n/a	69.6	n/a	57.0	57.9
17	52.0	50.2	55.2	55.6	58.6
34	69.4	68.5	49.9	54.9	59.5

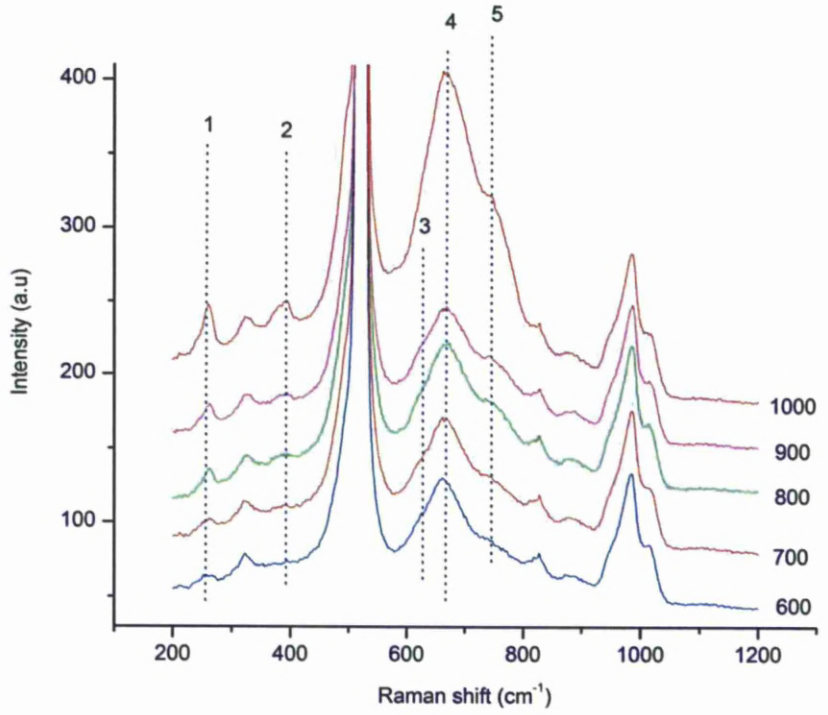

Figure 5-16: Raman spectrum of 5% Ce sample at various annealing temperatures.

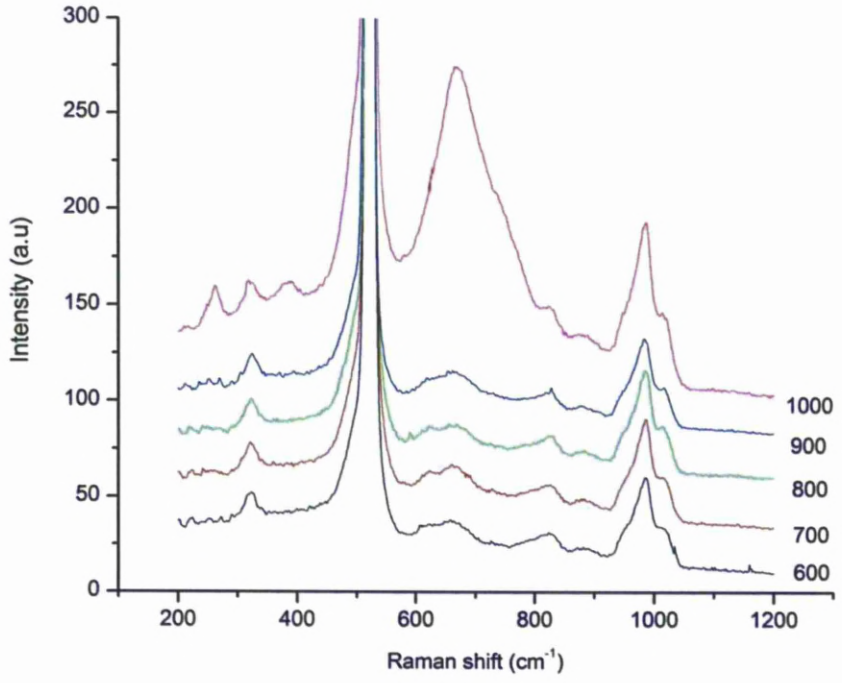

Figure 5-17: Raman spectrum of 8% Ce sample at various annealing temperatures

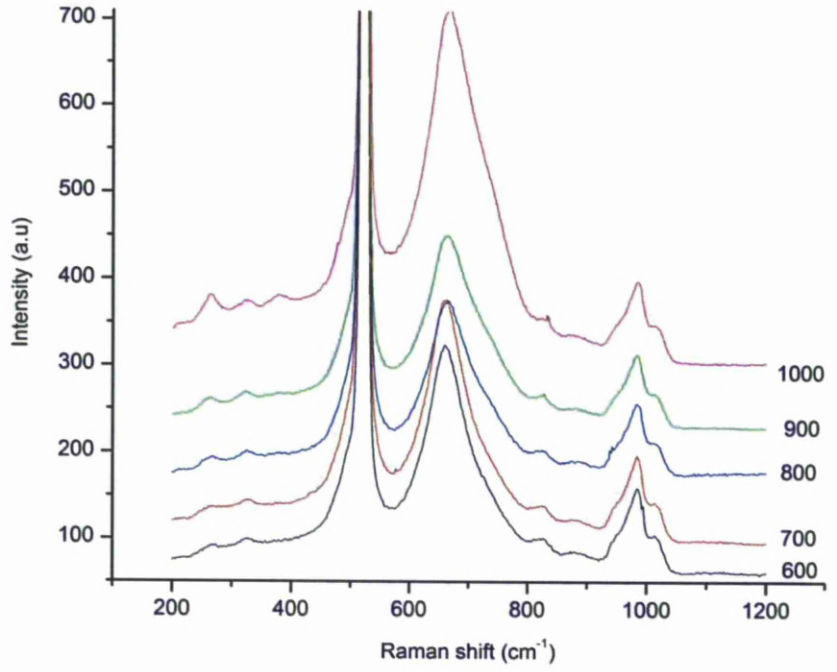

Figure 5-18: Raman spectrum of 17% Ce sample at various annealing temperatures

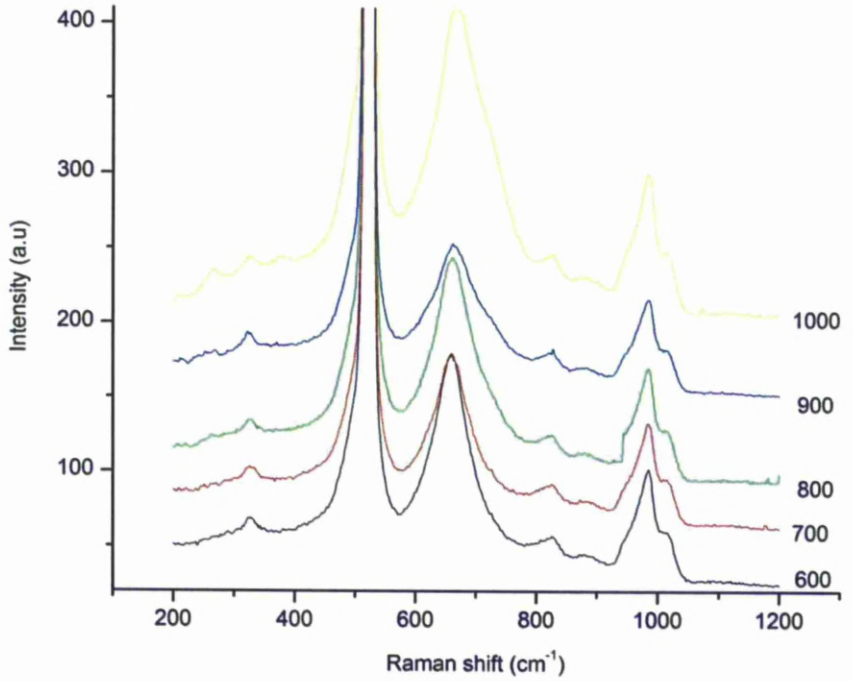

Figure 5-19: Raman spectrum of 34% Ce sample at various annealing temperatures

The Raman spectra of the air annealed 5% Ce films are shown in Figure 5-16. There are 5 main peaks associated with the actual films and these are labelled from 1 to 5 accordingly. It has already been established that a fraction of this sample is in the monoclinic phase; hence it is necessary to assign the monoclinic features of the Raman spectra first. It can be done by comparing Raman spectra of films with different monoclinic fractions, for instance between pure HfO_2 (only monoclinic), 5% Ce (mix of monoclinic and "cubic") and 10% Ce (only "cubic"). Therefore, a pure HfO_2 film with similar thickness was annealed at 900°C in air and its Raman was recorded as shown in Figure 5-20 below together with its 5% Ce and 10% Ce counterparts.

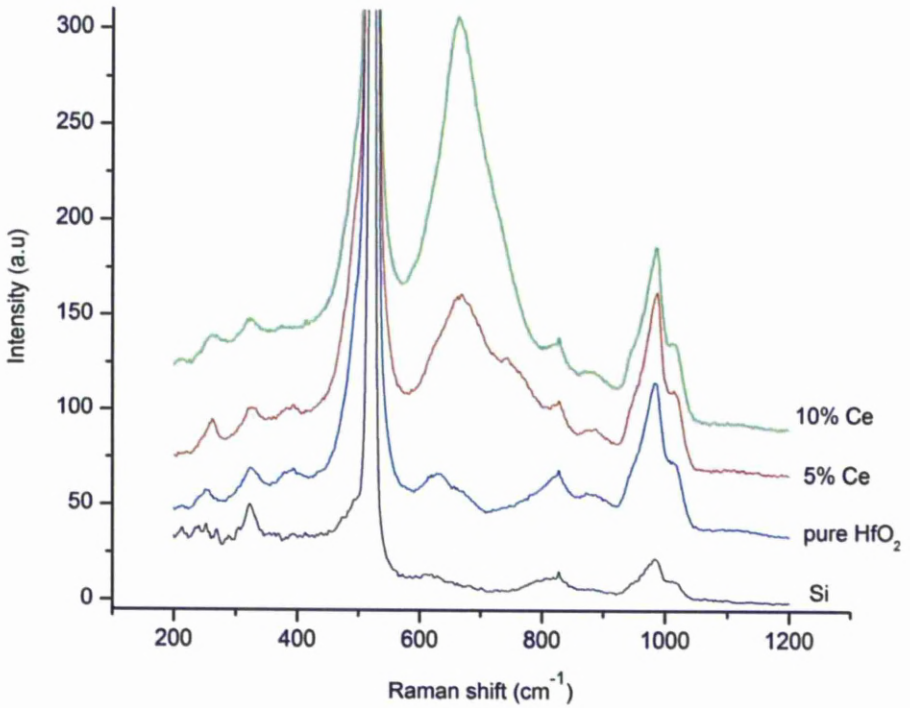

Figure 5-20: Raman spectra of air annealed films at 900°C

As can be seen from this comparison, the only peak contributed to the spectrum of 5% sample is the one around 390 cm^{-1} (peak 2). This is supported by the data given in reference [10] which indicates that monoclinic features are at 383 cm^{-1} and 399 cm^{-1} respectively while no peak within this proximity of wavenumber was reported either for tetragonal or cubic phase.

It is quite interesting to note that in this case and for other samples containing a fraction of monoclinic such as 8% Ce (Figure 5-17) and 17% Ce one (Figure 5-18), this peak is only noticeable in air annealing condition and high temperatures (900°C and 1000 °C).The monoclinic film also shows another peak around 253 cm^{-1}, which is also very close to another one belonging to the monoclinic phase (255 cm^{-1}) reported in [10]. In the case of both Ce-doped Hf -oxide films, their spectra both contain a peak appearing approximately at 262 cm^{-1} (peak 1). This peak, according to the peak assignment also from [10], might belong to some form of tetragonal structures.

The main difference and clearly, the most distinguishable feature between the HfO_2 film and the other two is the pattern appearing within the wavenumber range from 600 cm^{-1} to 800 cm^{-1}. In the case of HfO_2, its monoclinic form was characterised by two blended peaks (after deconvolution and peak-fitting, their positions are determined at 630 cm^{-1} and 668 cm^{-1} respectively). For the other two samples, while the 10% shows a dominant peak at around 662 cm^{-1}, the one with 5% cerium shows two additional shoulders (labelled as peak 3 & 5). Based on the phase determined from preceding XRD studies and the differences pointed out from this comparison, it can be proposed that this very main feature (peak 4), as already pointed out in the discussion of 10% sample before, is the main peak of interest and belongs to the dominant phase ("cubic") occurred in all samples.

Having assigned peak 2 the monoclinic phase, only four peaks (1, 3, 4 and 5) remain of interest for further investigation. The assignments for peak 3 and 5 are pretty difficult because of some reasons. It is due to the very nature of thin films in this study (between 20-30 nm), i.e. low signal-to-noise and the fact that some different polymorphs from these Ce-doped Hf oxides likely co-exist as demonstrated in various studies before, e.g. [10, 11, 14-16]. In the case of peak 3, due to its close proximity to another possible peak from the monoclinic phase, it is very difficult to sufficiently distinguish them. Another obstacle is the broadening effect of the main feature (peak 4), which has been observed in many similar Raman studies, for instance in [14]. Therefore, it can be considered a kind of defect-induced band rather than a peak except possibly in some cases presented later.

In the case of peak 5, though it is better separated from the main feature (peak 4) and hence can be sufficiently fitted with higher degree of confidence, a survey from literature did not return any likely feature at that position (around 740 cm^{-1}). Therefore, it remains unclear that this feature is likely a peak or just a defect-induced band. In a study of Ytria-doped hafnia [11], a very similar feature at that range of wavenumber is assigned as defect-induced band. Thus it can be reasonable to assign this peak in the same way, i.e. a defect-induced feature, which is considered as a feature of a defect or disorder arising from air annealing condition.

Fortunately, of all the concerned features which can correlate to any significant insights about the phase stabilisation, peak 1 and 4 are the most important ones due to the fact that they represent the vibrations of two different bonds between Hf-O_{II} and Hf-O_I respectively if an analogy between ZrO_2 and HfO_2 is assumed. In this context, peak 1 corresponds to the stretching mode of Hf-O_{II} while peak 4 depicts the one of Hf-O_I [14]. Based on the viewpoint of tetragonal ZrO_2, which has been normally considered as a layer structure [17], it can be also similarly applied to this scenario with HfO_2 (see chapter 2 for more details). Thus in this picture, tetragonality of a doped-HfO_2 system with oversized cation (Ce^{+4} in this study) is attributed to the strong bonding of Hf-O_I within the layers (shorter bond-length) and the weak bonding of Hf-O_{II} between the layers (longer bond-length). In order to demonstrate the tetragonality (c/a ratio) and the influence of Ce^{4+} cation to the crystal structure of HfO_2, a schematic adopted from [17] will be presented in Figure 5-21 below. In this figure, Zr-O_I and Zr-O_{II} bonds are illustrated to give a visualisation of these different characteristic cation-oxygen links within tetragonal structure as a distorted fluorite-type cubic configuration.

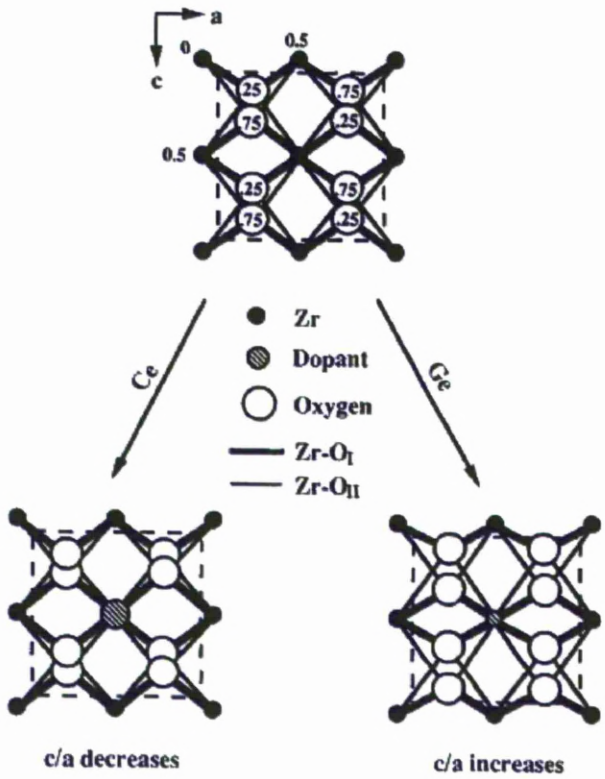

Figure 5-21: A schematic illustration how tetragonality (c/a ratio) of ZrO_2 varies with oversized dopant (cerium) and undersized dopant (Germanium). The numbers indicate the position of atoms in *b*-direction (perpendicular to the paper plane).

A graphical demonstration of six vibrational modes of tetragonal ZrO_2 [18] and their corresponding peak positions is shown in Figure 5-22. While for the peak assignment for the band at 265 cm^{-1} (E_g (2)) is generally agreed between researchers, there have been some disparities in the assignment of other bands. In a more recent study about Raman vibrational modes of tetragonal zirconia [19], Naumenko et al proposed a different band assignment of which the band at 645 cm^{-1} was assigned as A_{1g} instead of B_{1g} (1). Because the tetragonal phase is considered as a distorted fluorite-type cubic and its different metastable configurations thought only due to the oxygen displacement along c-axis [10, 15, 16], it may be more reasonable to assign the band at 645 cm^{-1} (peak 4 in this study) as A_{1g} as mentioned above rather than B_{1g} (1). So, based on these discussions, it is now available to assign peak 1 as E_g (2) mode which involves both Hf and O atoms movement (in *b*-direction) and peak 4 as A_{1g} mode which only Oxygen displaced along the *c*-direction.

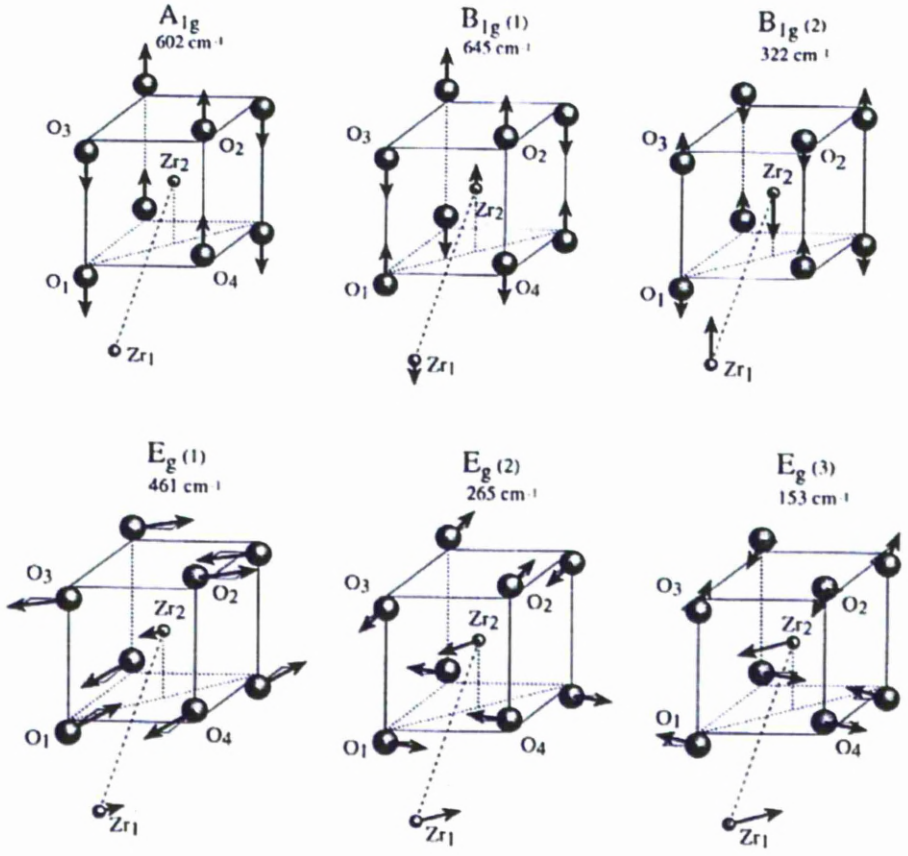

Figure 5-22: Six normal Raman active modes of tetragonal ZrO_2

As can be seen from Figure 5-16 for 5% Ce sample and other Raman spectra of other different doping levels, peak 1 is relatively small compared to peak 4 and just only appears at high annealing temperatures, i.e. beyond 800°C. This observation can be explained regarding the nature of this mode. This active mode, E_g (2), involves movements from both Hf and O atoms which in turn require a degree of disorders and oscillations within the material matrix. Thus this sort of stretching mode might appear more likely at higher annealing temperatures. Although this mode did not appear consistently in all samples at different annealing temperatures, it is still a good evidence to indicate that some form of tetragonal structures does exist in all films.

After the assignments for all peaks, the main interest and focus therefore remain on peak 4, which was the main feature in all films. An attempt was firstly tried to see if any linear relationship between the crystallite sizes determined from XRD study and FWHMs of this peak (see Table 5-5) could be observed as reported in [20] for nanomaterials. However, as the result turned out, no such relationship or any similar one could be observed. It might be due the complexity of phases within thin films, small crystallites or poor signal-to-noise ratio. However, in terms of phase evolution and its implication about the effect of using cerium on the stabilisation of phases in HfO_2, the analysis of the peak position still gave many meaningful insights of these issues. In order to illustrate how this main peak position (after deconvolution) varies with annealing temperature and cerium concentrations, the data in Table 5-4 is plotted in Figure 5-23 and Figure 5-24 respectively.

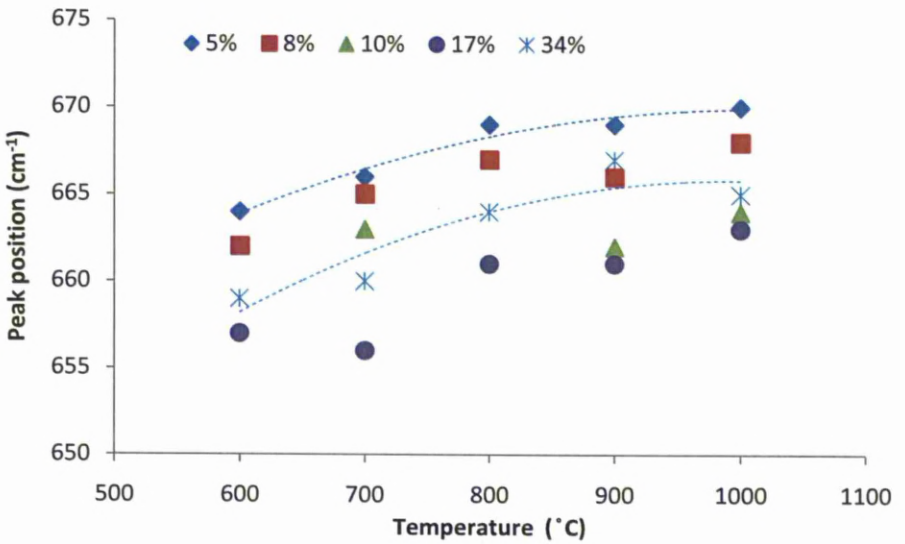

Figure 5-23: Variations of Raman peak position against temperatures for air annealed samples. The top trend-lines is for 5% Ce sample, the bottom one is for 34% Ce one. The errors in the determination of peak position were previously mentioned in section 3.4.4.

As can be seen from the figure above, all samples show quite a similar trend. The peak position shift towards higher wavenumber value as temperature increased regardless of cerium contents. This tendency means that with higher temperature, the crystal structure will render a higher tetragonality (c_f/a_f ratio) as being similarly observed in [14].

In fact, this observation agrees with the previous XRD study about the unit cell parameter if one considers the pseudo-flourite cubic cell ($a_f = a\sqrt{2}$) proposed by Teufer [21] in his study about crystal structure of tetragonal ZrO_2. According to the XRD study previously conducted, the unit cell of this "cubic" structure will increase as temperature increases. From the viewpoint of XRD alone, it either means that (i): the high-temperature cubic cell expands or (ii): some other forms of tetragonal or its metastable structures have the expansion on both the *a*- and *c*- directions as pointed out in [14]. Based on the results illustrated in Figure 5-23, it is sufficiently reasonable to conclude that for air annealed samples, the crystal structures of all films adopt a form of tetragonal or metastable derivatives and their tetragonality slightly increases with annealing temperature regardless of cerium concentrations.

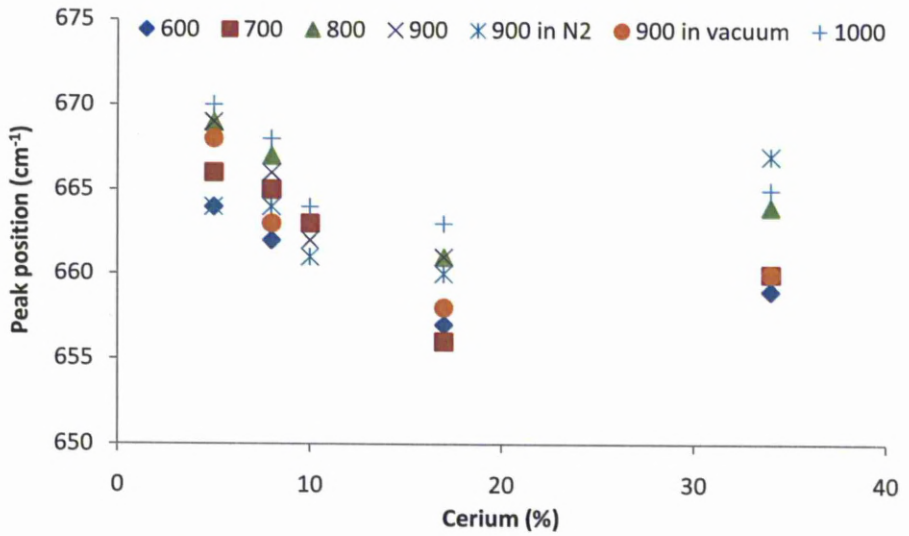

Figure 5-24: Variations of Raman peak position against cerium concentrations. The trend-line is added to guide the eye only.

The influence of cerium on the phase stabilisation of HfO_2 films is revealed in Figure 5-24. It was reportedly demonstrated that with increasing amount of dopants, such as Ce^{4+} [14] or Y^{3+} [10, 11, 15], the intensity ratio of two peaks I_{609}/I_{640} in the case of cerium doping or I_{480}/I_{640} in the case of Ytrium doping would dictate the ratio of tetragonal to cubic transition. Such a tendency cannot be observed in any Raman spectra of all the samples because of some reasons. Firstly, the strong interference from the silicon substrate with its large peak at around 520 cm^{-1} prevents the clear observation of Raman signals from the film at around 500 cm^{-1}.

This impedes the observation of the characteristic feature of tetragonal phase as in [11]. Another reason is the broadening of peak 4 on its own, which was also observed in many previous studies of the tetragonal-cubic phase transition in ZrO_2 or HfO_2 (see [10, 11, 14]for instance). This broadening phenomenon was generally explained by the disorder, created by substitutional dopant atoms introduced into the films, that normally observed in solid solution [14]. In addition, the broadening of this peak, together with the shift towards lower frequency, was related to the decrease in tetragonality when the amount of oversized doping cation (Ce^{+4}) is increased. This results in a shift of the peak towards low wavenumber value at 620 cm^{-1} [14] when a specific cerium content was reached (21%). This observation also meant that at that specific cerium concentration, the tetragonal-cubic transition was complete and the stable phase at that cerium doping level would be cubic [14]. Although such features at around 500 cm^{-1} or 610 cm^{-1} are not possible to be detected in any Raman spectra of these air annealed samples, the decrease in frequency of peak 4 as cerium concentrations increases can be observed as shown in Figure 5-24. In the range between 5% and 17% cerium, the frequency of this peak depicts a linear shift towards lower wavenumber at any given temperature. This trend is in good agreement with the result from [14] and other studies related to phase stabilisation of ZrO_2 and HfO_2 mentioned before. A more detailed assessment of this plot also reveals that the slope of the trend-lines decreases with increasing temperature. This means that the influence of cerium is more significant at lower annealing temperatures and became lesser at higher temperature.

What is irregular from this trend mentioned above is the result obtained from 34% Ce sample. As pointed out previously, a stable cubic configuration should be reached for samples with more than 21% cerium doping level. As a result, it is expected that the frequency of the main peak should shift towards 610 cm^{-1}. However, this is not observed for the 34% sample at any given annealing temperature. Instead, the frequency of this peak increases again. This phenomenon can be partly explained if the solubility limit of CeO_2 in ZrO_2 is taken into account and the same behaviour is assumed for HfO_2.

The solubility limit of CeO_2 in ZrO_2 was reported to be about 18% [7, 22] for temperatures below 1400°C thus if the amount of cerium exceeds this limit, then it is likely that cubic ZrO_2 solid solution will co-exist with a form of metastable tetragonal (t'), a product of diffusionless transformation of tetragonal phase [14]. If a similar process also occurs in Ce-doped hafnia, then it is likely that the 34% Ce sample will behave in the same manner. As a result, it is likely one of the reasons why the variation of tetragonality in this sample does not follow the same trend as the others.

5.2.3 Summary

The phase composition and crystal structure analysis for air annealed samples over the range between 600 °C and 1000 °C were conducted to investigate the influence of cerium to the stabilisation of the higher k-value phases in hafnia. The results established from XRD study confirm that by introducing cerium to hafnia, high temperature phase found in pure HfO_2 can be stabilised regardless of annealing temperatures for 10% and 34% doping concentration, while a mix of "cubic" and monoclinic can be observed for the samples with 5%, 8% and 17 % Ce and the fraction of monoclinic in these samples shows a dependence upon annealing temperatures. In addition, crystal structure of this stabilised phase and its corresponding crystallite sizes can also be deduced from this study with the reference to the high temperature cubic structure found in pure HfO_2. The results from the Raman study, however, reveal that the stabilised phase existing in these samples are more likely a form of "metastable tetragonal" or mixed phases of tetragonal and its metastable forms. Although the tetragonality of these phases is not fully resolved due to the limited resolutions from Raman spectra of those films, it can be suggested that this stabilised phase resembles the stable cubic phase in pure HfO_2 very closely, particularly for the films annealed at high temperatures (with the exception of 34% Ce sample). Therefore, for convenience, the crystallographic assignment for this characteristic stabilised phase in all samples is still kept on the basis of the high temperature cubic phase from pure HfO_2, i.e. c(111).

5.3 N_2 annealing at 900°C

In this section, XRD and UV Raman results for phase and crystal structure analysis of all the samples annealed in N_2 with duration of 15 minutes at 900 °C will be presented and discussed. This is followed by that is the electrical characterisation of the 10% Ce sample to investigate the dielectric properties of the N_2 annealed films in terms of dielectric constant and leakage current. The electrical data analysis of this 10% Ce sample will be supplemented by a TEM image to give necessary information about the interfacial layer and its thickness, which are important parameters to understand the behaviour of the electrical behaviours from this sample.

5.3.1 Phase analysis

Similar to the study of air annealing, all samples were subjected to XRD and Raman investigations. Firstly, the XRD results are presented in Figure 5-25 and Table 5-6 as follows.

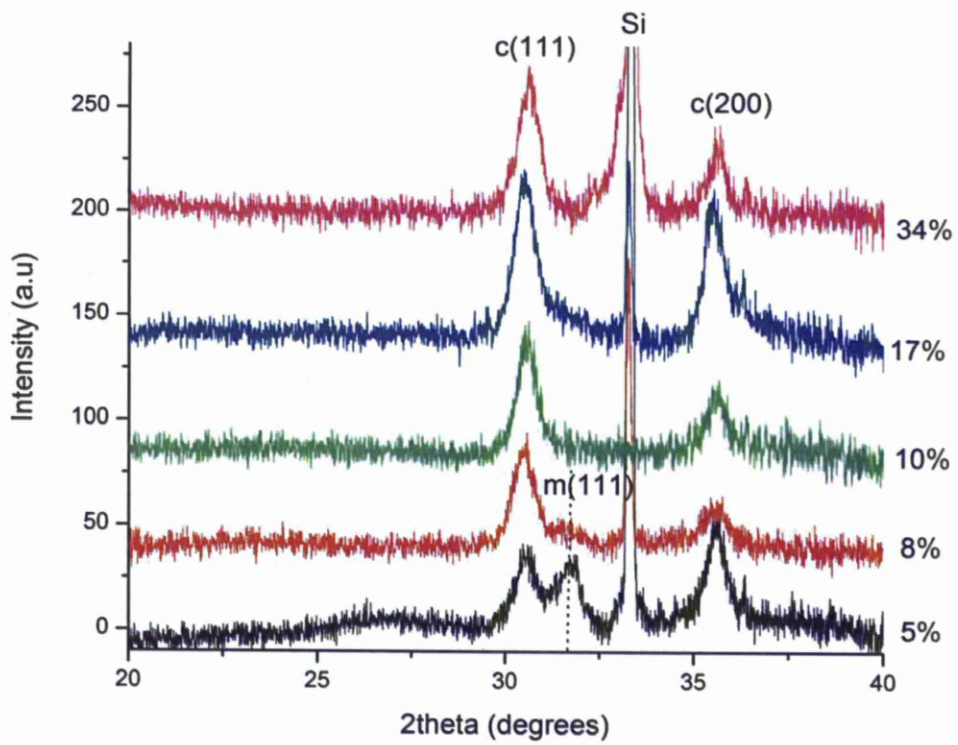

Figure 5-25: XRD spectra of all samples annealed in N_2 for 15 minutes.

Table 5-6: summarised XRD data analysis for all N_2 annealed samples

5% Ce	8% Ce	10% Ce	17% Ce	34% Ce
c(111) peak position (degrees)				
30.52	30.47	30.57	30.50	30.60
c(111) unit cell (Å)				
5.07	5.08	5.07	5.08	5.06
crystallite sizes (nm)				
9.81	11.56	13.40	12.35	10.93

Compared to the data obtained for air annealed samples at 900°C (see Table 5-2 and Table 5-3), the results from all N_2 annealed samples for the stabilised phase of interest show a high degree of similarity. Therefore, it is reasonable to conclude from the XRD results that the effect of N_2 annealing is quite similar to air at 900°C for all samples. However, a closer assessment of the diffraction patterns of 5%, 8% and 17% Ce samples reveal that the fraction of monoclinic in these films decreases compared to the air annealed samples. This indicates that in N_2 annealing, monoclinic phase is less favourable than air annealing for these specific cerium concentrations. This observation will be revisited and discussed in more details in section 5.4.

Based on the findings about the phase assignment from the Raman study for air annealed samples, it is of interest to compare the response of samples with 5%, 10% and 34 % Ce. While the first one represents the lowest range of doping level and shows a significant amount of monoclinic phase, the other two only show a single phase from their XRD patterns. However, as illustrated previously, the sample with 34% Ce may differ with the 10% Ce one in terms of their tetragonalites due to the difference of solubility of tetragonal phase regarding cerium concentration. Figure 5-26 shows the Raman spectra for these three samples after annealing in N_2 for 15 minutes.

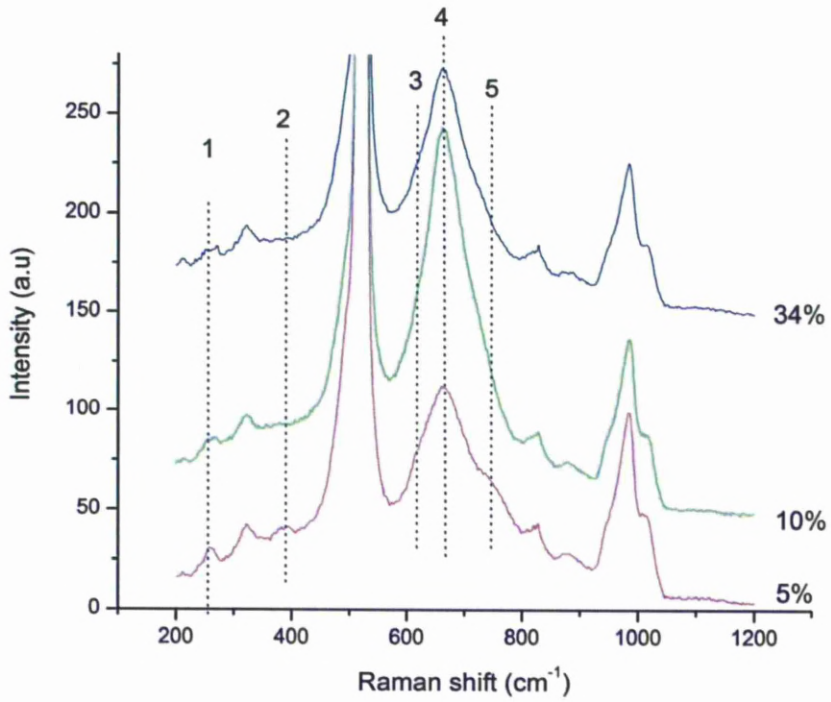

Figure 5-26: Raman spectra for N_2 annealed samples

Compared to previous Raman spectra for each sample annealed in air at the same temperature, the results illustrated in Figure 5-26 also show a degree of similarity, which agrees with the same observation made from the comparison of XRD studies mentioned above. As a result, it can be concluded that in N_2, the influence of cerium to all samples annealed at 900 °C is pretty much the same as in air in terms of phase evolution and crystal structure (with the exception of decreasing monoclinic fractions in three samples with 5%, 8% and 17% Ce).

5.3.2 Electrical characterisation of 10% Ce sample

As Ce-doped Hf oxide films are of interest for replacement for SiO_2 in CMOS devices, it is important to consider the electrical characterisations of the films. Because of the specific interest on the sample with approximately 10% Ce, all the electrical characterisations within this study will focus only on this doping concentration, firstly with the N_2 annealed films in 15 minutes.

In order to conduct electrical characterisations of these films, simple MOS capacitor structures were fabricated resulting in a (Au/$Ce_{0.1}$–$Hf_{0.9}$ O_{2-x}/ Si/Al) structure. Au contacts with a diameter of 300 μm were deposited on the films by sputtering and a blanket Al backside contact was deposited by vacuum evaporation. Capacitance-Voltage (C-V), Current-Voltage (I-V) and Capacitance-Frequency (C-f) responses over a range of frequency from 20 Hz to 2 MHz with different DC voltage bias were measured for each MOS-C structure. Their correspondent dielectric constants (k-values) and leakage current density were consequently extracted using calculations derived from references [23, 24] (see chapter 3 for detailed descriptions of these measurements).

Before discussing the electrical data, it is necessary to know the thicknesses of the films before and after N_2 annealing and their corresponding interfacial layers because these parameters are the primary factors in determining the k-value from the C-V curve. From a TEM image for the as-grown 10% Ce sample (see vacuum annealing section), the SiO_2 interfacial layer thickness is determined approximately 2.1 nm, which is slightly thicker than the native SiO_2 found on as-received Si substrate prior to the growth (1.8~2.0 nm). Ellipsometry measurement for this as-grown film gives a value of 23 nm (with the interlayer taken into account by applying the 2-layer model, see chapter 3 for more details). Therefore, in order to determine the thickness of the film after annealing, the interlayer thickness needs to be determined beforehand. Figure 5-27 shows a TEM image taken for the annealed film, revealing the interfacial layer between the film and the Si substrate. From this image, a thickness approximately 3.7 nm of the interfacial layer is revealed while the film thickness after annealing is estimated about 20 nm. This value, in turn, is in good agreement with the result given by the ellipsometry. Therefore, it can be reasonably assumed that for further electrical data analysis of other films, the film thickness can be based mainly on the input data of thickness measurement from ellipsometry.

In contrast to the hypothesis that annealing in N_2 will not alter the interlayer, this TEM study shows a considerable increase in the interfacial layer thickness. This increase is surprising due to the fact that ideally, within an inert environment such as N_2, there should be no source of oxygen that might diffuse through the film and oxidise the substrate. The most likely explanation is oxygen ingress into the furnace during annealing either due to oxygen impurities in the nitrogen or insufficient seals. Moreover, because the annealing was performed in a tube furnace, it was also very likely that oxygen could be introduced during the course of sample loading/unloading.

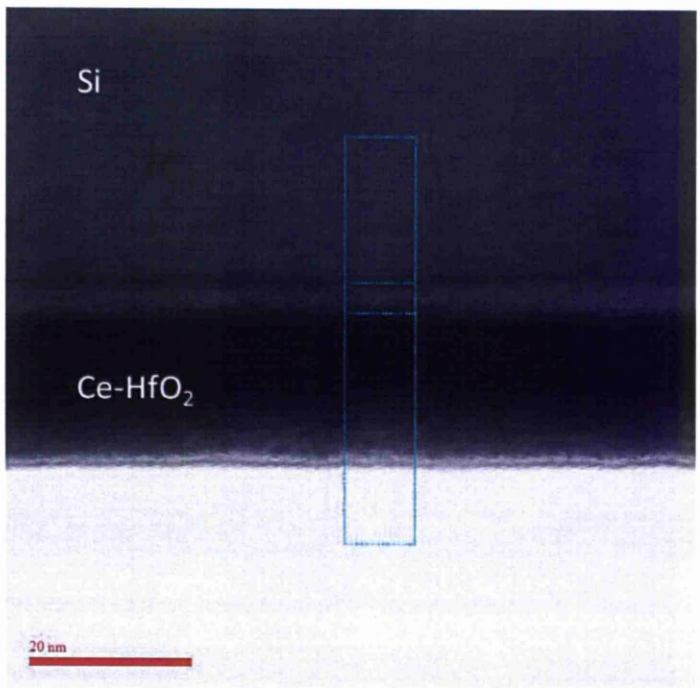

Figure 5-27: TEM image of a 10% Ce thick sample (about 23 nm) after N_2 annealing at 900℃/15 minutes

The increase in the thickness of the interfacial silicon oxide is highly undesirable for high-k applications; hence the use of N_2 as an annealing environment for any subsequent meaningful electrical measurements will be excluded for the rest of this research. As will be demonstrated later in the vacuum annealing section, in order to maintain the prevention of mixing up/diffusion of elements to other layers and undesired oxidation, vacuum is mandatory to undertake the post-growth treatment to satisfy these requirements.

After the thickness of the film and the interlayer had been established by TEM and ellipsometry for both as-grown and annealed films, interpretation of the C-V curve can take place to yield their dielectric constants besides many other important information about the electrical properties from those films. Figure 5-28 shows the C-V curves for both as-grown and N_2 annealed 10% Ce samples at three different frequencies: 10 kHz, 100 kHz and 1 MHz respectively. The arrows indicate the direction of the ramped bias voltage during the measurements. The dielectric constant was calculated from C-V curves at 100 KHz as commonly used to extract this information from dielectric thin films [4].

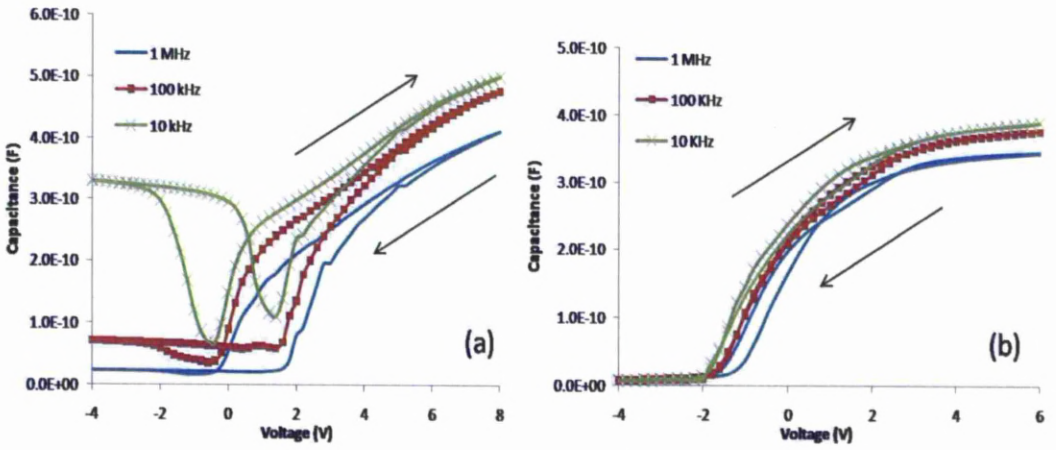

Figure 5-28: C-V curves for 10%Ce sample (a): as-grown and (b): N_2 annealed in 15 minutes

Firstly, as can be seen from Figure 5-28 (a), the C-V curves of the as-grown example show a very high degree of hysteresis and frequency dispersion, especially at the lower frequency. The frequency dispersion at lower frequency, which is the characteristic response of insulating oxide film on n-type Si substrate, can be attributed to the response of the dielectric film in the inversion regime. However, as this kind of response is normally only found at low and intermediate frequency (10 kHz in this study) hence, the clear reason for that phenomenon is still not understood. Another noticeable observation is that at all frequencies tested, none of C-V curves for the as-deposited samples show full accumulation region saturation. From the shapes of these plots, it is revealed that the curve itself showing a degree of both fixed oxide charge and density of interface (surface) states (see [23] for more details).

The fixed oxide charge contributes to the shift of the curve to the right, i.e. towards positive bias voltage, which means that some forms of negative charges existing inside the as-grown films. The origin and formation of these negative charges have been proposed in [25] as a form of oxygen vacancy. Besides these negative charges, another type of charge, namely interface (surface) states, can also be found from the C-V plot as it introduces a non-parallel stretch-out towards the positive bias voltage. Based on that behaviour, this kind of trap can be assigned to an "acceptor like" state, which means it remains neutral when empty and becomes negative when filled. A detailed study of oxygen vacancies in transitional and rare-earth metal oxides [26] offers an excellent study about the neutral oxygen vacancy that may occur within different oxide surfaces. However, it is noteworthy to point out that in this study, the high-k oxide films were grown on top of native SiO_2 layer. Therefore, the effect of interface (surface) states, which is primarily thought of the intrinsic property of the semiconductor substrate [23, 24], might be far more complicated compared to the interpretation of such phenomenon when dealing with conventional SiO_2 MOS structure.

The effect of N_2 annealing on the electrical responses of this sample is illustrated in Figure 5-28(b). Improvements are apparent in terms of hysteresis, frequency dispersion, reductions in fixed charges and density of interface (surface) states. For instance, the hysteresis has been significantly reduced and hence, indicating a reduction in fixed oxide charge and some reduction in interface. However, in terms of dielectric constant, the N_2 annealed film shows a very close result (k~28) to the as-deposited sample (k~29) at 100 kHz. Not only the k-value measured at this specific frequency, both films also show a nearly identical behaviour over the range of tested frequency, i.e. between 10 kHz and 2MHz. Plots of k-f relationship are presented in Figure 5-29 (a) for both films over the frequency range mentioned above, with the k-value measured and calculated at the highest bias voltage on the accumulation regime from the C-V curves.

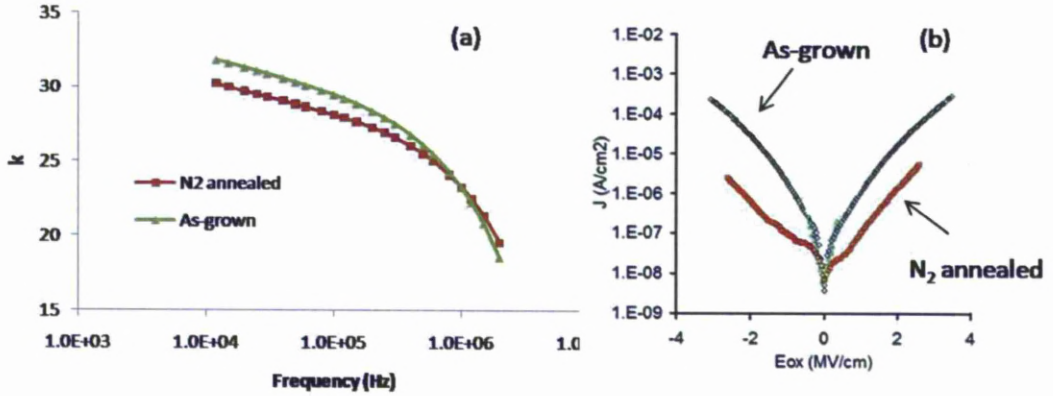

Figure 5-29: (a) Permittivity against frequency and (b): Leakage current density against electric field strength for 10 % Ce sample (the frequency and the leakage current density are presented in log scale)

The effect of annealing on the leakage current density against electric field strength is examined and presented in Figure 5-29 (b). It was thought that the as-grown sample should possess much better leakage current density versus any types of annealed ones due to its amorphous nature [27]. However, in the case of N_2 annealing, the opposite result was observed, with the leakage clearly decreasing after treatment. This reduction in leakage can be attributed to the increase in the thickness of the SiO_2 interfacial layer. This amorphous layer acts as a secondary insulating layer, to prevent carriers that may have leaked through the high-k layer from reaching the silicon beneath. Therefore, although the N_2 annealed film has a crystallite structure, it still shows a much lower leakage current density compared to the amorphous as-deposited samples. The value for the leakage current density at ±1MV/cm of the as-grown film is between 1.45E-06 ~ 1.6E-06 A/cm^2, while it is approximately 9.0E-08 A/cm^2 for the N_2 annealed sample.

5.3.3 Summary

Phase evolution and crystal structure analysis were performed for all samples annealed in N_2 at 900 °C in 15 minutes. The results obtained from XRD and Raman show that the influence of N_2 on all samples is quite similar to air annealing at the same temperature, except a decrease in monoclinic fraction is observed for samples with 5%, 8% and 17% Ce. However, a TEM study revealed that annealing in N_2 resulting in an increase of the interlayer between the oxide film and the silicon substrate.

This finding effectively excludes the option of investigating the electrical properties for subsequent characterisations of other samples. Lastly, electrical characterisations were undertaken for the sample with 10% Ce. Although the k-value was found quite similar for both as-grown and annealed films, the as-deposited film suffers from severe hysteresis and a combination of fixed charges and interface states. The annealed film, on the other hand, shows significant improvements on these issues. Contrary to the presumption about the superiority of as-grown film over annealed example on the leakage current density, it was found that the annealed film exhibiting a lower value compared to the as-deposited one. The reason is likely attributed to the thicker interfacial layer found from the annealed film.

5.4 Vacuum annealing

Similar to the previous studies in air and N_2, the same routine of phase evolution and crystal structure analysis for all annealed films were also performed in vacuum at 900 °C. However, aside from the phase analysis for all samples, the electrical characterisations of sample with approximately 10% Ce was extended further compared to the case of N_2. Besides the vacuum annealed 10% Ce sample at 900 °C, another series of films with similar Ce concentration were subjected to different annealing periods at 800 °C to investigate the influence of annealing duration to the crystallite sizes and/or unit cell of the films, which in turn were expected to show some effects to the dielectric properties. The results will comprise XRD and TEM alongside electrical data including C-V, I-V and k-f measurements.

5.4.1 Influence of annealing at 900°C in 15 minutes

5.4.1.1 Phase analysis

Firstly, XRD spectra of all samples are presented in Figure 5-30 and the results from the peak analysis is shown in Table 5-7. An assessment of Raman spectra for all samples gives quite similar results to air and N_2 annealed ones before, hence they will not be shown here. Unfortunately, due to the extensive use of the 10% Ce sample, it was not available to obtain a Raman spectrum from it. Therefore, the phase evolution and crystal structure analysis will be focused only on the XRD data.

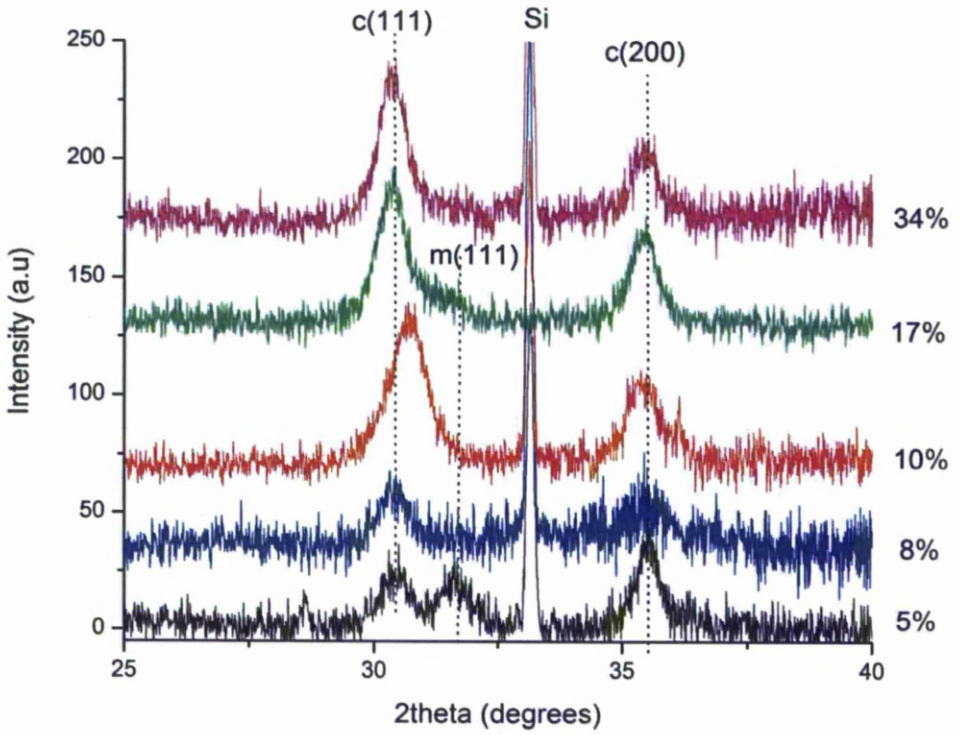

Figure 5-30: XRD spectra of all samples annealed in vacuum for 15 minutes

Table 5-7: summarised XRD data analysis for all vacuum annealed samples

5% Ce	8% Ce	10% Ce	17% Ce	34% Ce
c(111) peak position (degrees)				
30.42	30.40	30.68	30.35	30.36
c(111) unit cell (Å)				
5.09	5.09	5.05	5.10	5.10
crystallite sizes (nm)				
12.15	10.50	9.06	11.28	12.39

The first noticeable observation is the response of the 10% Ce sample compared to all the others in terms of c(111) peak position. It can be depicted clearly by the shift of this peak further away from the reference cubic value, while all the other samples' peaks show a similar position. As a result, the d-spacing and its "cubic" cell are slight smaller when compared to the others also to the air and N_2 annealed values obtained before for this sample. The same tendency can also be observed for this sample's crystallite size.

The large deviation from the reference cubic unit cell may indicate that the "cubic" structure for this 10% Ce film having the most distorted configuration. In other words, it may have the largest tetragonality if it adopts some forms of "metastable tetragonal", i.e. t' or t". All of those results also suggest that in vacuum, at 10% doping level, Ce-doped hafnia system shows a quite different response towards the crystallization and some prohibitions may be induced to the crystal growth, i.e. the crystallite size, as being reported in various literature references (see chapter 2 for more details about phase stabilisation mechanism in Hf-oxides).

For the other samples, another interesting observation is the absence of monoclinic phase at 8% Ce, while samples with 5% and 17% still show the existence of monoclinic phase. This observation, coupled with the behaviour from the 10% Ce sample, may suggest that the influence of vacuum annealing on the phase evolution of Ce-doped Hf-oxide films is quite different with air or N_2 annealing, especially when the tetragonality of the crystal structure is concerned in the proximity of 10% Ce concentration. This issue will be discussed in more details in section 5.4 when the comparisons are made for all annealing environments.

5.4.1.2 Electrical characterisations of 10% Ce sample

In a similar manner to the electrical characterisations for the N_2 annealed film, the vacuum annealed one for this sample was prepared using the same procedure and MOS structure to record its C-V, I-V and k-f plots. As mentioned previously in the case of N_2 annealing, knowledge of the interlayer thickness before and after annealing is crucial to extract useful information from the C-V curve. Therefore, TEM was performed to reveal the influence of vacuum annealing to this 10% Ce sample. Figure 5-31 shows the TEM image for as-deposited and vacuum annealed films. As can be seen from this TEM image, the interfacial layer is nearly identical for both as-grown and annealed films. This indicates that vacuum annealing did not introduce any substrate oxidation or interaction from the high-k oxide film on top. As a result, the thickness of this interlayer (~2.1 nm) remained unchanged after vacuum annealing. Moreover, this TEM image also shows that the interlayer after vacuum annealing remained amorphous; hence it can be determined to be a SiO_2 layer.

This conclusion, therefore, will be assumed for any further vacuum annealing samples destined later for electrical characterisations.

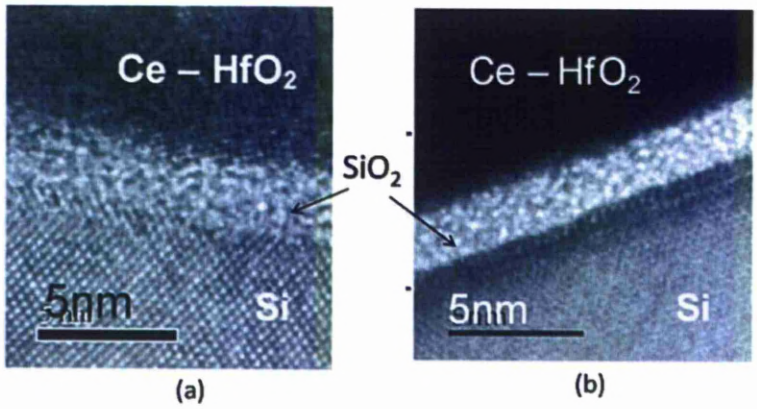

Figure 5-31: TEM images of 10% Ce sample (a): as-grown and (b): vacuum annealed at 900°C, 15 minutes

The thickness measurements by ellipsometry for this sample reveal that the film did not change its thickness vacuum annealing, i.e. ~23 nm for both as-grown and annealed films. This data is supported by a MEIS study for as-deposited and vacuum annealed 10% Ce sample, which is shown in section 5.5.

Firstly, C-V curves for both as-deposited and annealed films will be shown in below. The arrows indicate the direction of the bias voltage applied during the measurements.

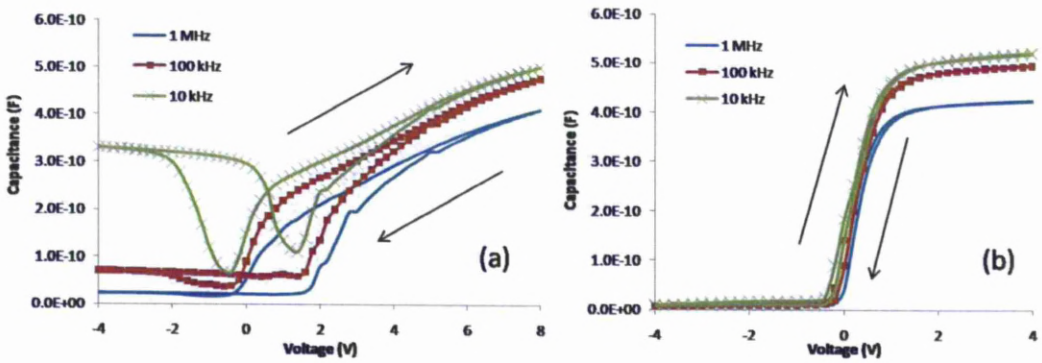

Figure 5-32: C-V curves for 10%Ce sample (a): as-grown and (b): vacuum annealed in 15 minutes

As can be seen from Figure 5-32 (b), the vacuum annealed one shows superior frequency dispersion as well as huge improvement in hysteresis compared to the as-grown film. The shape of the C-V curves of the vacuum annealed film, regardless of frequency, also show a nearly identical path for both the sweeping directions. The gap between these two paths is very narrow (approximately 0.07V), which indicates a very small amount of fixed charges inside the film. Moreover, these two paths are nearly parallel to each other, which means the interface states was much reduced after annealing. Recall the C-V curves of the N_2 annealed film from the same sample in Figure 5-28 (b), it can be concluded that the film annealed in vacuum shows a much better quality. In terms of dielectric constant, a calculation for the C-V curve at 100 kHz in the accumulation regime yields a value of 34. This result is in very good agreement with the theoretical prediction for a stabilised tetragonal phase in Ce-doped HfO_2 (k ~32) from Fischer in [2]. This is further supporting evidence suggesting that the phase existing in this 10% Ce vacuum annealed sample very likely adopting a kind of tetragonal phase.

Plots of k-f relationship are presented in Figure 5-33 (a) for both films over the frequency range between 10kHz and 2 MHz, with the k-value measured and calculated at the highest bias voltage on the accumulation regime from the C-V curves. The leakage current density against electric field strength is shown in Figure 5-33 (b).

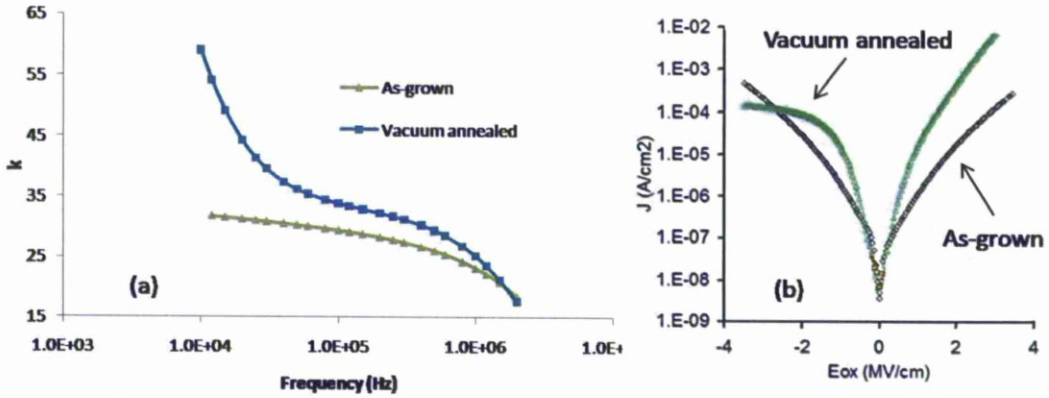

Figure 5-33: (a) Permittivity against frequency and (b): Leakage current density against electric field strength for 10 % Ce sample (the frequency and the leakage current density are presented in log scale)

As can be seen from Figure 5-33 (a), the vacuum annealed film shows a significantly higher k-value over this range of frequency, particularly between 10 kHz and 100 kHz. This behaviour is also quite different to the response of the N_2 annealed one presented previously in Figure 5-29 (b), which can lead to the postulation that the crystal structure from the vacuum annealed film is different to the N_2 annealed one. The difference may lie on the ionic polarisation that contributes to the overall permittivity at this intermediate frequency range as well as the soft phonon associating with the vibrations of the crystal lattice.

In terms of the leakage current density, values of 9.9E-06 ~ 2.2E-05 A/cm^2 are found at ±1 MV/cm from Figure 5-33 (b) for vacuum annealed film. They are about one order of magnitude higher compared to the values of the as-grown film. The high leakage observed for the vacuum annealed film can be attributed to the crystallisation of the film which provides more leakage pathways through grain boundaries. An increase in the surface roughness can also partly contribute to this behaviour of the vacuum annealed film (see section 5.5 for details about the AFM study).

5.4.2 Influence of annealing duration at 800 °C to the electrical properties

In this section, effect of different annealing durations to the crystal structures, crystallite sizes and their corresponding dielectric responses is presented for the vacuum annealed films from sample 1534 (see chapter 4 for more details). This sample is found to contain approximately 10.5 % Ce, hence this study also gives additional details about the electrical responses of the 10% Ce vacuum annealed at 900 °C in 15 minutes discussed above. The reason about a drop from 900 °C to 800 °C for this 1534 sample was mainly because this could provide more manoeuvrability in terms of annealing duration, i.e. the time setup for each annealed film could be varied in a wide range of durations between 1 minute and 100 minutes. Hence, the crystal structure and its crystallite size were allowed to expectedly develop in observable change.

Firstly, XRD results are presented in Figure 5-34 below, followed by tabulated data for c(111) peak analysis in Table 5-8.

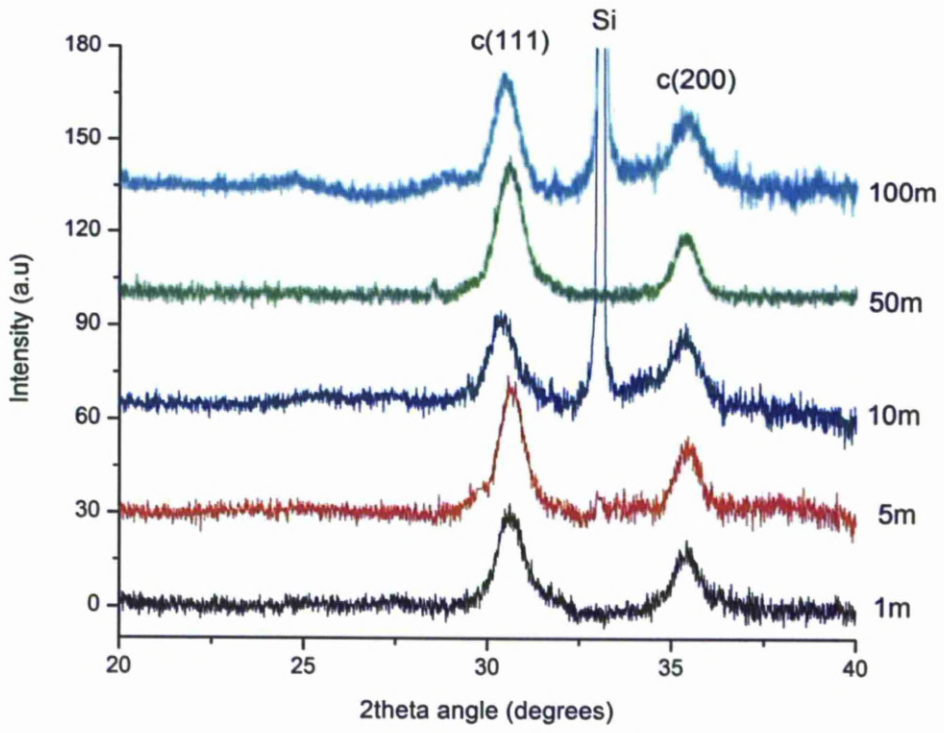

Figure 5-34: XRD spectra of 1534 sample annealed at 800 °C with various durations.

Table 5-8: Summarised data for c(111) peak analysis of 800 °C vacuum annealed 1534 sample.

Duration (mins)	2theta (degs)	Crystallite size (nm)	d-spacings (Å)	Unit cell (Å))
1	30.62	8.49	2.92	5.06
5	30.67	10.04	2.91	5.05
10	30.38	9.11	2.94	5.10
50	30.59	9.45	2.92	5.06
100	30.49	8.69	2.93	5.08

As can be seen from these XRD data, no obvious relationship about the influence of annealing duration on the unit cell of "cubic" phase and its corresponding crystallite size can be deduced. However, it seems that the effect of vacuum annealing at this temperature is quite drastic at short durations, for instance between 5 and 10 minutes, resulting in a significant change in the position of c(111) peak between these two. Hence, it is expected that there is a large difference in terms of electrical properties between these two films.

Based on the previous electrical study of the 10% Ce vacuum annealed sample at 900°C in 15 minutes, the electrical properties of the film annealed in 5 minutes is expected to be comparable because of their high similarity in crystal structure.

The electrical characterisations for all films from this vacuum annealed sample will be shown in the following figures, together with summarised key results extracted from these C-V and I-V curves presented in Table 5-9.

Table 5-9: Summarised data for electrical measurements from vacuumed annealed 1534 sample at 800°C in different durations

Annealing duration (mins)	Annealed film thickness (nm)	k (100 kHz)	J (A/cm2) at -1 MV/cm	J (A/cm2) at 1 MV/cm	ΔV hysteresis at midgap
1	17.0	25	2.12E-05	5.07E-03	0.5
5	15.0	38	4.48E-05	3.69E-03	0.2
10	16.0	23	4.09E-04	1.29E-03	0.8
50	14.0	21	7.76E-05	1.55E-03	0.3
100	15.0	44	2.81E-04	6.51E-03	0.2

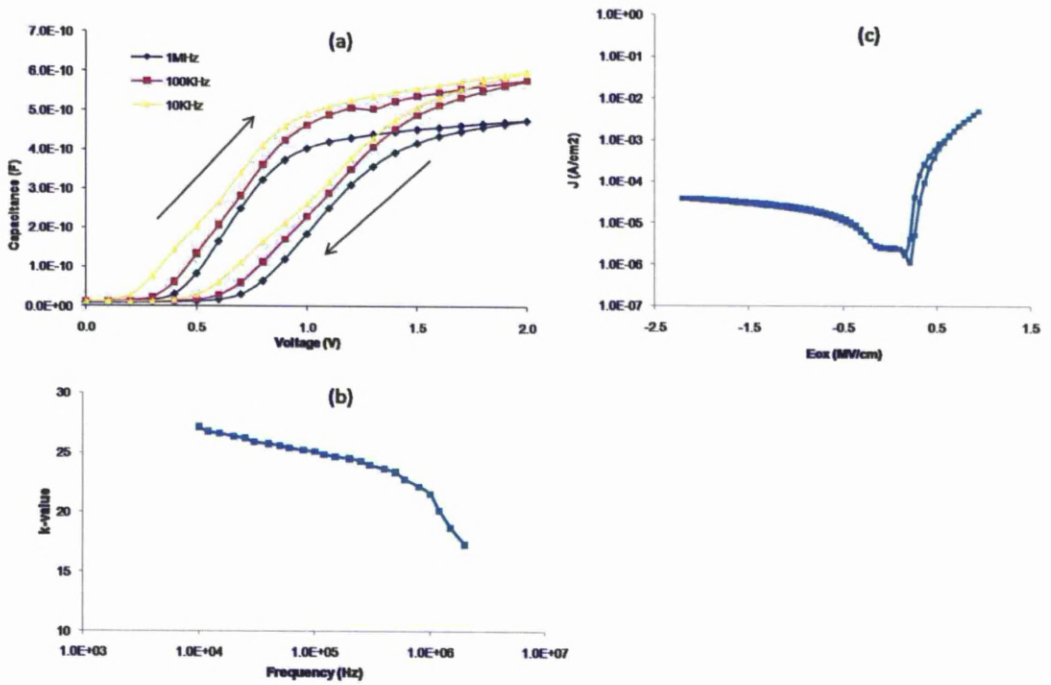

Figure 5-35: (a): C-V curves, (b): k-f plot and (c): leakage current density against electric field strength for 1534 vacuum annealed sample at 800℃, 1 minute.

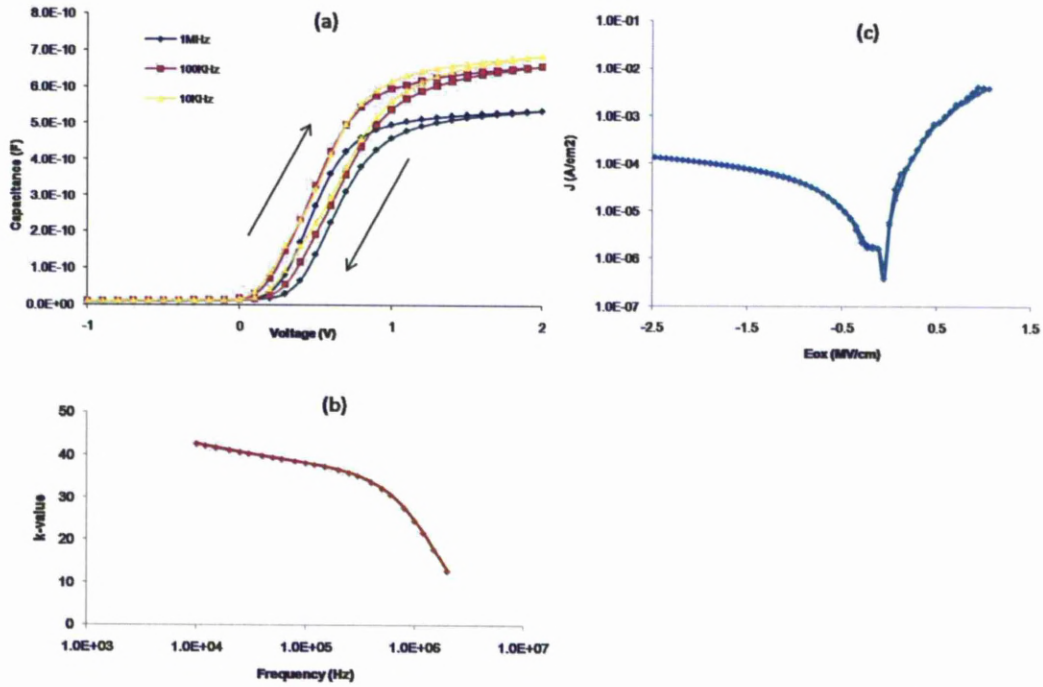

Figure 5-36: (a): C-V curves, (b): k-f plot and (c): leakage current density against electric field strength for 1534 vacuum annealed sample at 800 °C, 5 minutes.

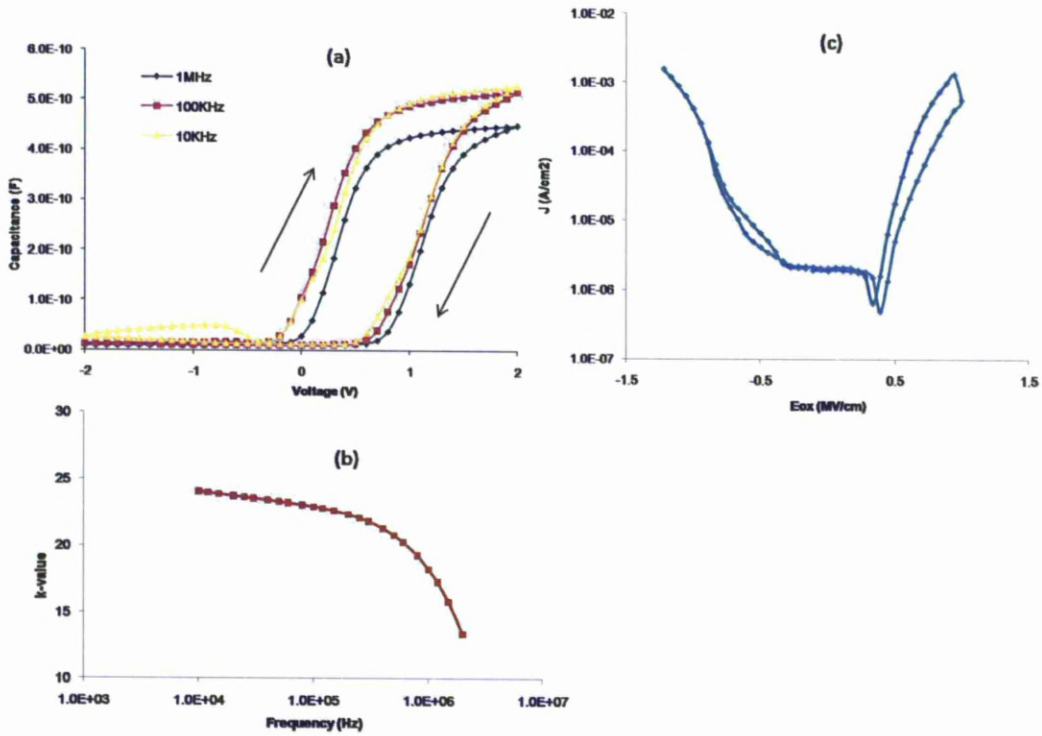

Figure 5-37: C-V curves, (b): k-f plot and (c): leakage current density against electric field strength for 1534 vacuum annealed sample at 800 °C, 10 minutes.

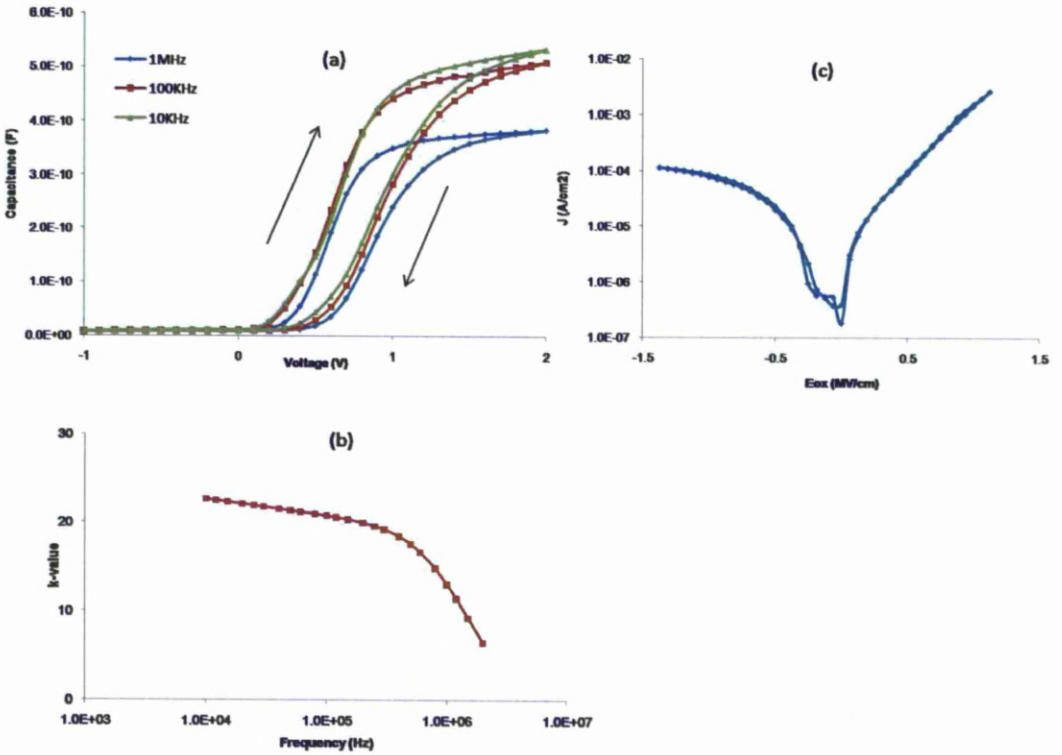

Figure 5-38: C-V curves, (b): k-f plot and (c): leakage current density against electric field strength for 1534 vacuum annealed sample at 800 °C, 50 minutes.

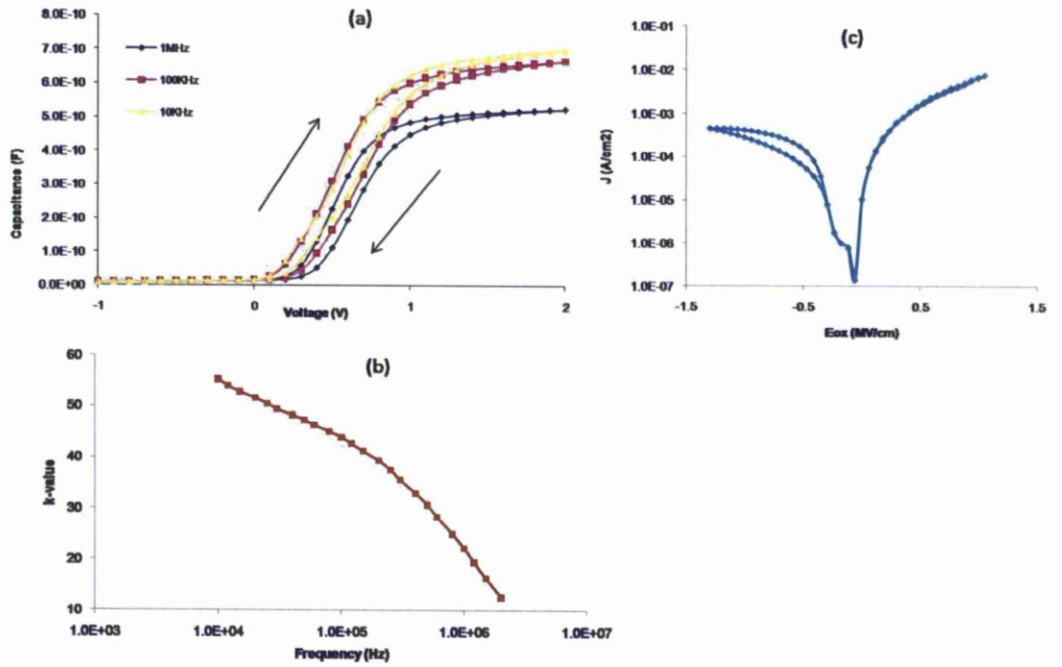

Figure 5-39: C-V curves, (b): k-f plot and (c): leakage current density against electric field strength for 1534 vacuum annealed sample at 800 °C, 100 minutes.

As can be seen from Table 5-9, among all the films in this annealing study, the ones with the duration of 5 and 100 minutes yield the best performance in terms of dielectric constant (k~ 38 and 44 respectively). The amount of fixed oxide charge, which is directly proportional to the degree of hysteresis from the C-V plot, also shows the same tendency with the results of k-values. The shapes of all the C-V curves from all films show that the amount of interface states should be quite low, as indicated by the nearly parallel paths from both sweeping directions. As mentioned in the XRD data analysis for all of these films, the film with the duration of 5 minutes was expected to give a permittivity similar to the previous 10% Ce vacuum annealed sample at 900 °C, 15 minutes. An even much higher value obtained from the film with the duration of 100 minutes is quite surprising though. In terms of leakage current density, all films show quite similar behaviours, especially at the regime of positive electric field strength. All samples show very similar frequency dispersion as can be seen from their k-f plots (with the exception of the one with the duration of 100 minutes, which illustrates a steeper gradient).

Initially, it was presumed that within a very narrow range of thickness, the electrical performance of those films would be dictated by the annealing durations, i.e. the variations from crystal structure parameter should have a clear effect on electrical properties. However, as the results of this study turn out, no such clear and sensible relationship can be observed. The reason for this phenomenon remained unknown though the homogeneity across the original 1534 sample, which was subsequently cut into smaller pieces to conduct various annealing durations, might be a questionable factor, as can be seen from different annealed film thickness.

5.4.3 Summary

Crystal structure and phase analysis were conducted for all samples with various cerium concentrations. The results from this analysis reveal that all except for the sample with 5% and 17% Ce still retaining a fraction of monoclinic, all the others show only a stabilised single phase, which is likely a distorted cubic structure or a form of "metastable tetragonal". Particularly, the 10% Ce sample shows the most distorted structure from the reference high temperature cubic phase, suggesting the influence of vacuum annealing on this sample is the most significant.

The analysis from the crystal structure and phase evolution suggests that the sample with 10% Ce will have a higher-k value due to its likely high tetragonality. This deduction is confirmed with the results obtained from electrical characterisations for this 10% Ce annealed at 900 °C in 15 minutes, yielding a k-value of 34. Besides an enhancement in dielectric constant, vacuum annealing is also found to improve other electrical properties of 10% Ce sample such as low amount of both fixed charges and interface states compared the as-grown one. However, the leakage current density is found to increase after annealing. This behaviour is attributed to the crystallisation of the film after annealing, enabling leakage pathways compared to the amorphous as-grown film.

Another set of films with approximately 10% Ce was also subjected to annealing at 800 °C with various durations to investigate the effect of crystal structure and crystallite size variation to the electrical properties. The results, however, are seemingly suggestive of no such clear relationship as being assumed. Of all the films subjected to this study, the films with duration 5 and 100 minutes show the best dielectric performances, resulting in k-values of 38 and 44 respectively. They also show the lowest amount of fixed charges compared to other films. These findings are indicative of some interesting yet unclear influences of the annealing duration to the associating phases in those two films and hence, resulting in quite high k-values.

5.5 Discussion about the influence of annealing environments on phase stabilisation and microstructure of Ce-doped hafnia films

In this section, the influence of different annealing environments to the phase stabilisation and microstructures of all annealed films at 900°C in 15 minutes over the whole range of cerium doping level will be discussed. The discussion will focus on the results from phase and crystal structure (XRD), film microstructure (MEIS) and surface roughness (AFM).

5.5.1 Phase and crystal structure analysis

Firstly, the XRD results for all samples with consideration to crystallite sizes and unit cell will be presented in Figure 5-40 and Figure 5-41 below.

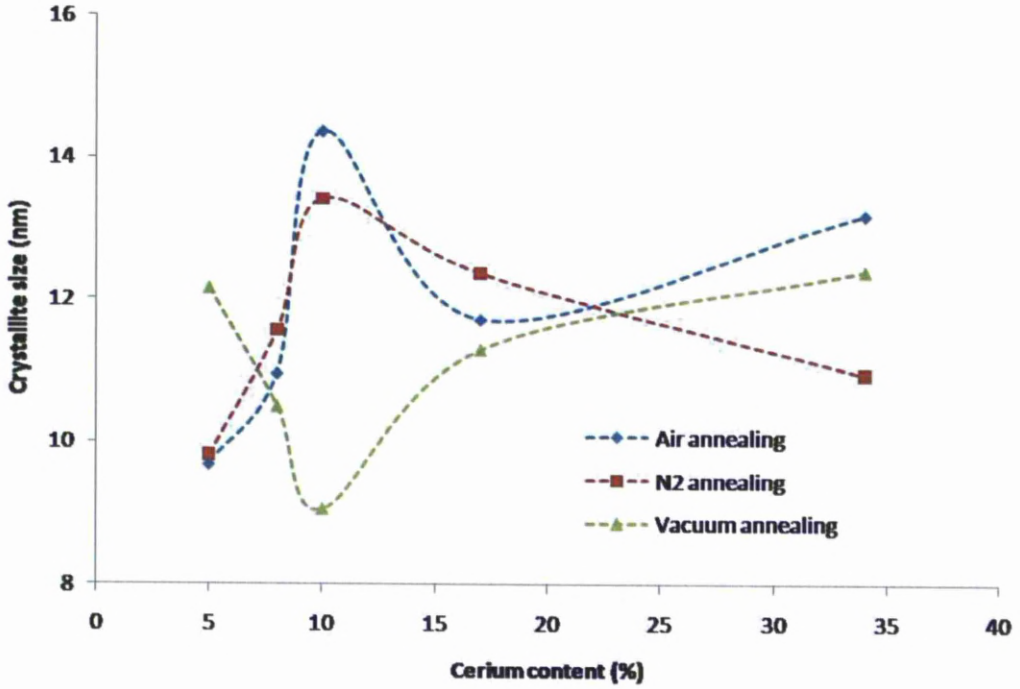

Figure 5-40: Variation of crystallite size against cerium concentration for different annealing environments at 900˚C, 15 minutes.

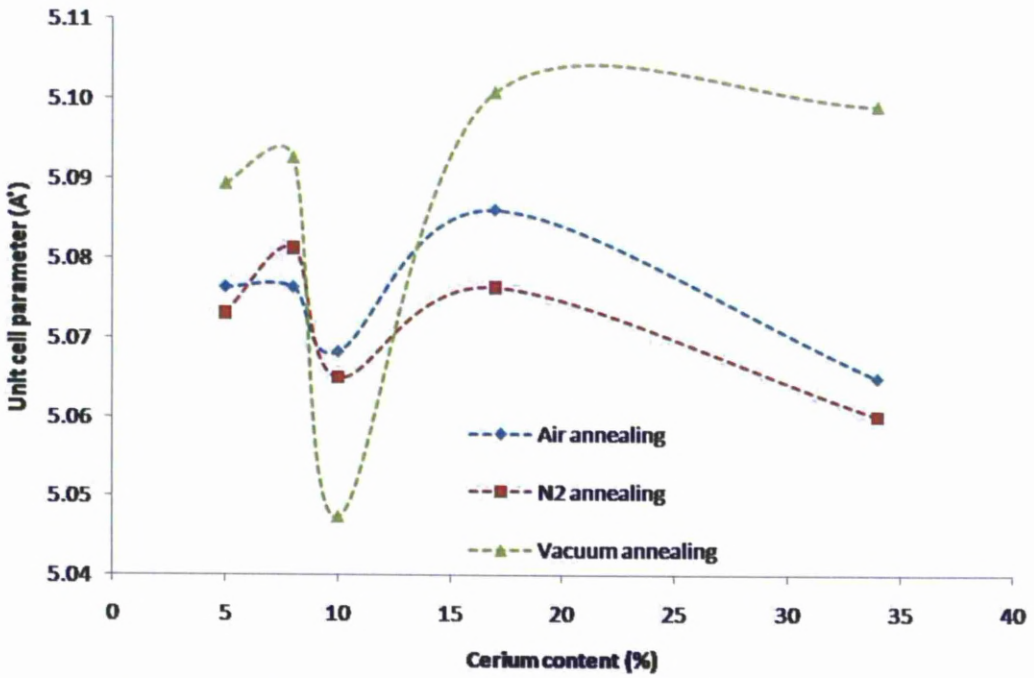

Figure 5-41: Variation of "cubic" unit cell against cerium concentration for different annealing environments at 900˚C, 15 minutes.

In terms of crystallite size, Figure 5-40 shows that while films annealed in air and N_2 show a degree of similarity, the ones annealed in vacuum present a very different trend. It is quite interesting though that the positions of the maximum (in the case of air and N_2 annealing) and the minimum (in the case of vacuum annealing) of those curves coincidentally appeared at 10% cerium concentration.

When the unit cell parameter on the basis of a cubic fluorite-type is concerned, all annealing environments consistently show similar trend though for vacuum annealing, it is much more profound and again, all minimum of these curves appearing at 10% of cerium doping level (see Figure 5-41). If the data for the 10% sample is temporarily excluded, then the remaining data follows quite ordinary curves. However, the 10% sample data cannot simply be ignored as it systematically and consistently deviates from the other sample data regardless of annealing conditions. It can well be that the films with doping at around 10% cerium possess some very unique crystallographic characteristics and thus, quite distinct from the others. As discussed previously in separate annealing section, it is very likely that at this doping level, the tetragonality of the stabilised phase is much higher compared to other concentrations. The "cubic" structure of 10% sample possibly evolved to some kind of distortions more substantially under oxygen-poor condition, e.g. vacuum and hence, its tetragonality would be higher than the others. Given the known observations about the stability of tetragonal phase in ZrO_2 for oversized tetravalent dopant (cerium in this case) from Li et al in [17] and the theoretical study of Fischer for stabilised tetragonal of Ce-doped HfO_2 in [2], it can be postulated that in vacuum, sample with 10% Ce achieved the highest degree of tetragonality while the other samples seemed to adopt a less-distorted cubic phase.

For samples with 5%, 8% and 17% Ce, another concern related to the influence of annealing environments is their monoclinic fraction. Figure 5-42 presents the monoclinic fraction for these 3 samples in different annealing conditions.

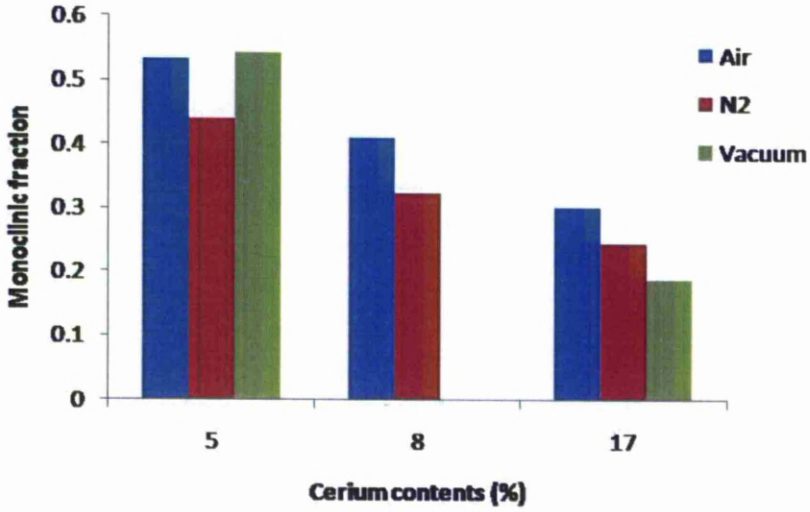

Figure 5-42: Monoclinic fraction for 5%, 8% and 17% annealed samples at 900°C, 15 minutes.

As can be seen from Figure 5-42, while the influence of annealing conditions on 5% Ce sample is virtually insignificant, other two samples consistently show a decrease in monoclinic fraction. This behaviour confirms the effect of cerium in suppressing monoclinic phase in annealed films (with the exception of 5% Ce doping, which is deemed too low to be effective). The existence of the monoclinic phase in 17% Ce sample was already explained in the section of air annealing, which can be likely attributed to a phase separation due to solubility limit of tetragonal phase around 18% Ce. In the case of vacuum annealed 8% Ce sample, the monoclinic is not detected from its XRD spectrum. The reason why an abrupt change in terms of monoclinic suppression observed for this sample is still not clearly understood. It can be hypothesised that under the condition of poor-oxygen condition such as vacuum, Ce-doped hafnia around 8% concentration possibly crystallise into a much more favourable structure of some sort of tetragonal rather than monoclinic. The true reason demands a more thorough and detailed investigation though.

5.5.2 Film microstructure analysis

Besides the effect of annealing environments to the phase and crystal structure, it is also of important to understand their effects to the film microstructure such as the interaction of the film with the Si substrate and the interfacial layer in-between.

In chapter 4, MEIS data were presented for the chemical composition analysis of selected films. Here, some other MEIS data are shown to investigate the aforementioned issues for annealed films in N_2 and vacuum.

Firstly, the influence of vacuum annealing to the film microstructure is assessed for the 10% Ce sample. Figure 5-43 shows MEIS energy scan for this sample before and after vacuum annealing at 70.5° scattering angle, followed by a depth scale plots for two different scattering angles in Figure 5-44. The use of this 70.5°scattering angle was because information about interfacial layer and light element (oxygen) only available from this scattering configuration. The other scattering angle (125.3°) on the other hand was to make peak separation for heavy elements (Hf and Ce) possible.

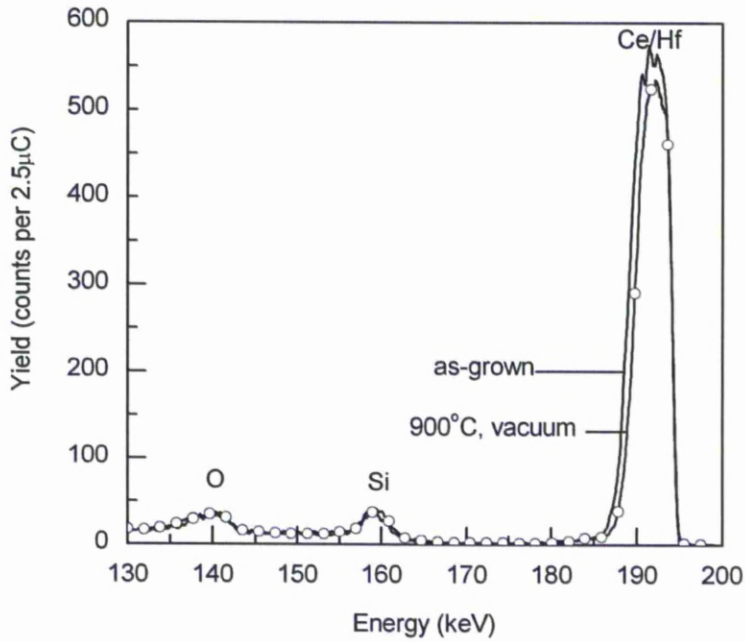

Figure 5-43: MEIS energy scan of as-grown and vacuum annealed 10% Ce sample (70.5° scattering angle)

As can be seen from Figure 5-43, the two plots of as-grown and 900°C vacuum annealed films show nearly identical profiles, especially in terms of the positions and intensities of Si and O peaks. In other words, the films virtually remained chemically unchanged before and after vacuum annealing. However, a small change in the film thickness, corresponding to densification of the film is seen for the annealed sample as a slight reduction in the height and width of Hf/Ce peak shape.

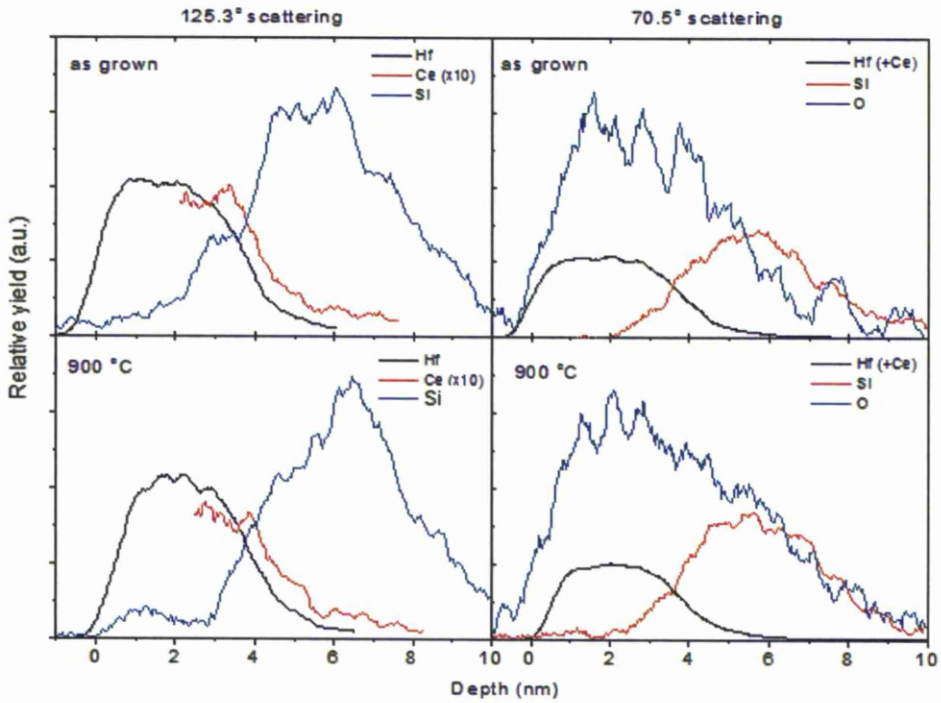

Figure 5-44: Depth profile analysis of 10% Ce sample before and after vacuum annealing

Figure 5-44 shows detailed depth profile analysis from the 10% Ce sample after having been normalized and scaled up (in the case of cerium profile) for easier comparison and matching. It is quite clear from this set of data that the film thickness reduction is quite small yet detectable. The internal oxidation of the SiO_2 interfacial can also be observed though somewhat negligible, which is supported by the TEM study for this sample (see Figure 5-31).In the case of 125.3° scattering angle, it is also possible to resolve a little degree of migration of cerium into the SiO_2 interfacial layer. This observation complicates the determination of the interfacial layer composition which was initially assumed to be SiO_2. Nevertheless, it can be proposed that although the interfacial layer probably might not be purely SiO_2, this inhomogeneity is very small and therefore, can be neglected. In the case of N_2 annealing, substrate oxidation and/or interaction was observed by the TEM image for the 10% Ce sample (see Figure 5-27). MEIS data were also collected for two other samples with 17% and 34% Ce, also at two different scattering angles.

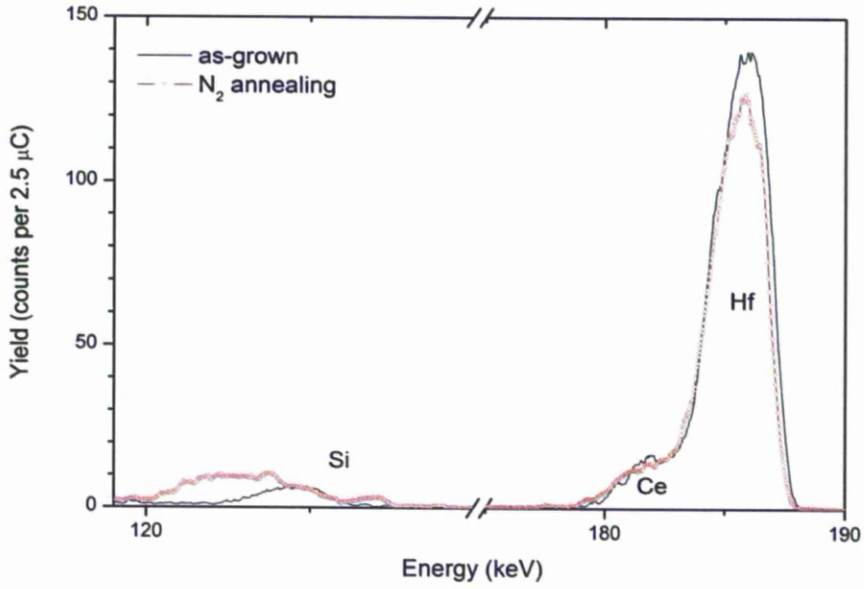

Figure 5-45: MEIS energy scan of as-grown and N_2 annealed 17% Ce sample (125.3°scattering angle)

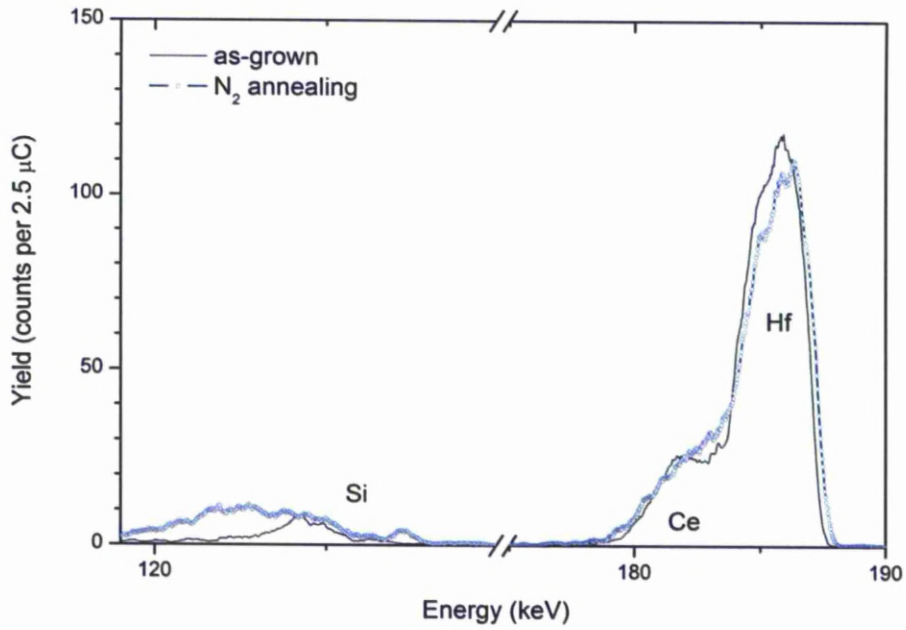

Figure 5-46: MEIS energy scan of as-grown and N_2 annealed 34% Ce sample (125.3°scattering angle)

From Figure 5-45 and Figure 5-46 above, the effects of N_2 annealing on the films are quite apparent in terms of increasing amount of silicon appearing in the films, illustrating by significant increase in Si peak width from both figures. With this scattering configuration, the oxygen feature cannot be readily resolved from silicon. However, the combining intensities of these two peaks before and after annealing regarding the drop of hafnium peak intensities and widths, i.e. the films becoming denser as observed in the case of 10% Ce sample vacuum annealed, while the cerium peak intensities virtually remains unchanged suggesting that there was possibly an intermixing of cerium to the interfacial layer. In other words, the interfacial layer in both these films got thicker and its chemical might not be SiO_2 anymore as in the case of vacuum annealing. In order to understand the effect to the interfacial layer more clearly, another MEIS energy scan was performed with 70.5 ˚scattering configuration for 17% Ce sample. The spectra is shown in Figure 5-47 and followed by a depth profile analysis in Figure 5-48.

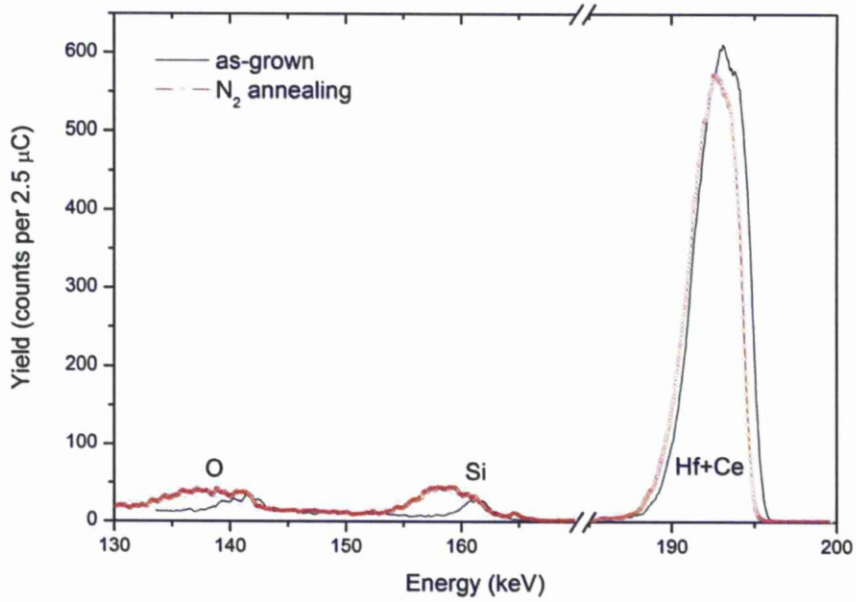

Figure 5-47: MEIS energy scan of as-grown and N_2 annealed 17% Ce sample (70.5° scattering angle)

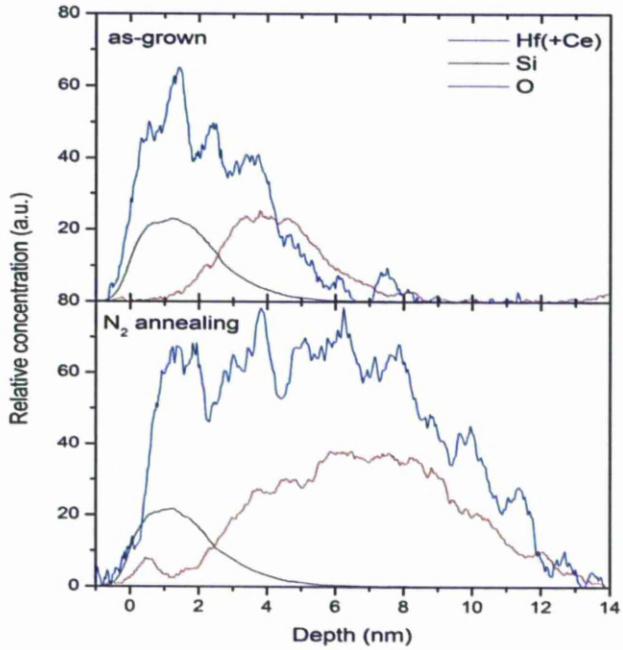

Figure 5-48: Depth-profile analysis for as-grown and N_2 annealed 17% Ce sample

As can be seen in Figure 5-47, after N_2 annealing, the combining peak of (Hf+Ce) drops slightly in term of intensity and gets somewhat narrower, which is the result of the densification after annealing. In contrast, the opposite trend is seen in the case of silicon and Oxygen peaks, which indicates there is a substantial growth of SiO_2 interfacial layer after the film was annealed. This tendency is supported in Figure 5-48 by comparing the depth-profile analysis before and after annealing in N_2, illustrated by the reduction in (Hf+Ce) peak width while a profound increase both in intensity and relative yield are observed for silicon and Oxygen profiles. In short, these results together with the aforementioned TEM data for N_2 annealed 10% Ce sample confirm the phenomenon of interfacial layer built-up in N_2 annealed samples.

5.5.3 Surface roughness analysis

To investigate the effect of different annealing conditions and cerium concentrations to the surface roughness of the films, AFM was employed to study the morphology of the films. AFM images of all samples are presented in the following figures, followed by a summarized set of arithmetic surface roughness (Ra) tabulated in Table 5-10.

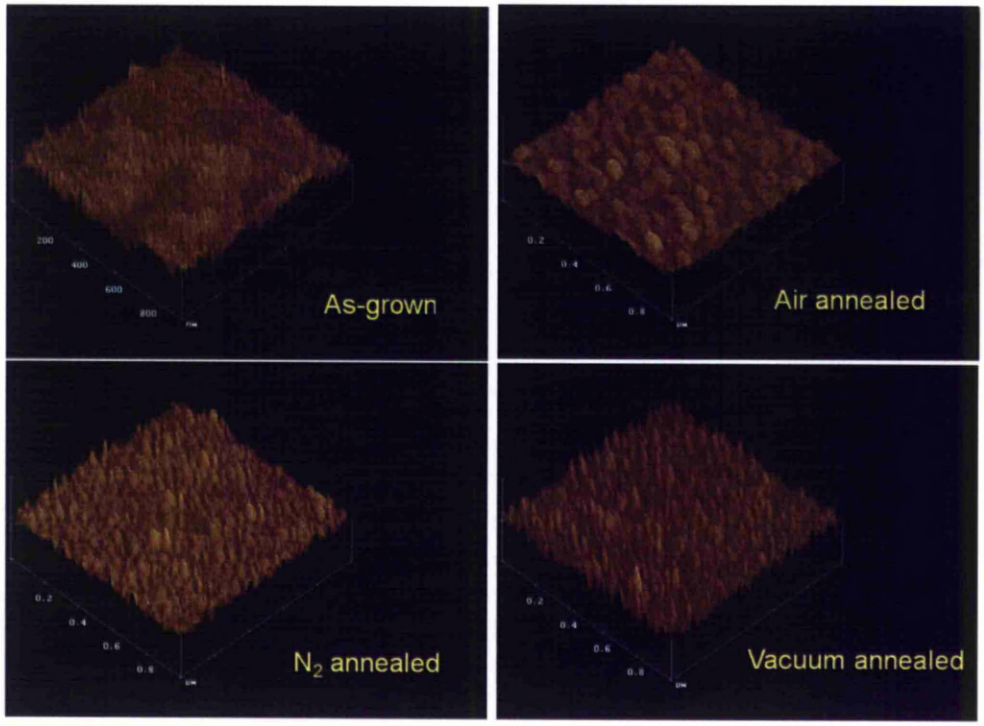

Figure 5-49: AFM images of 5% Ce sample under different annealing conditions at 900˚C, 15 minutes.

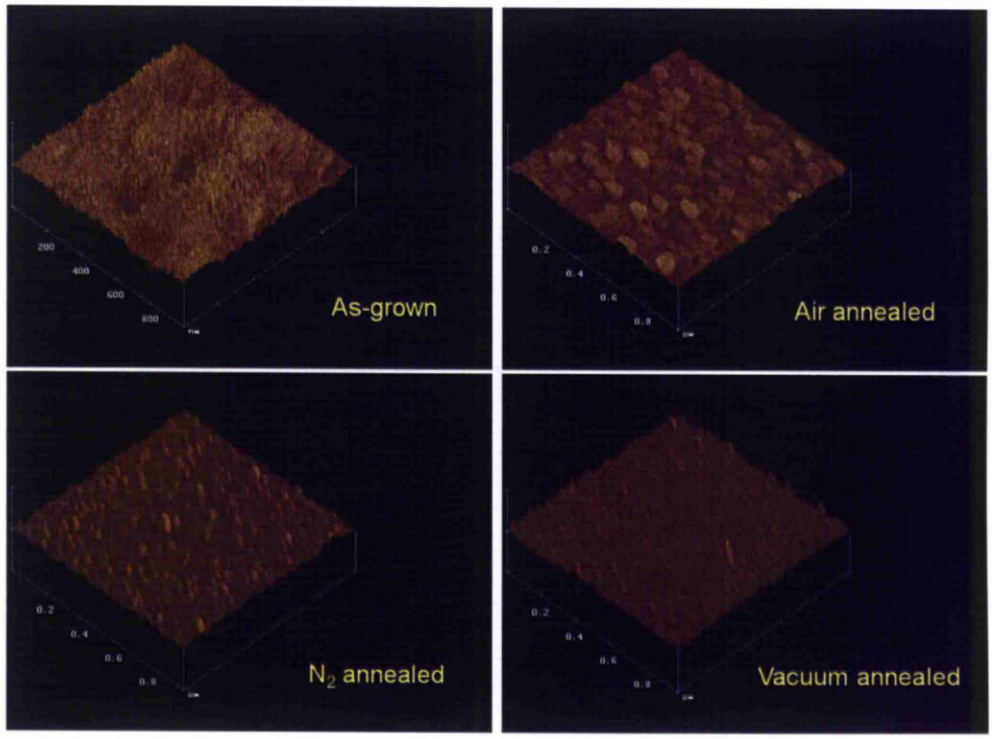

Figure 5-50: AFM images of 8% Ce sample under different annealing conditions at 900˚C, 15 minutes.

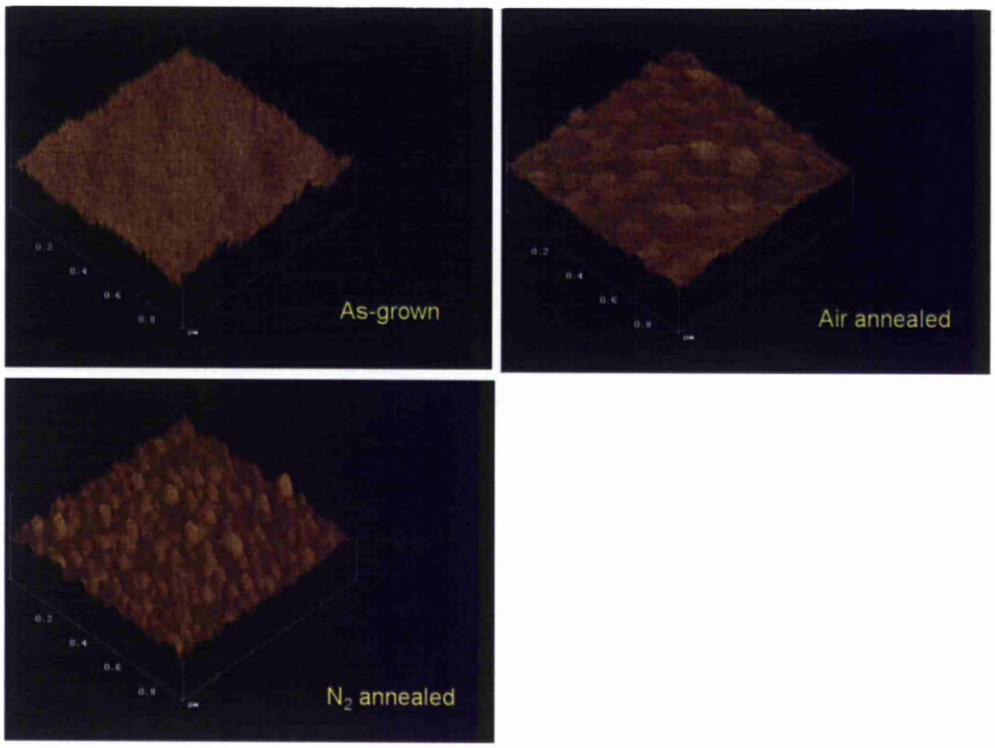

Figure 5-51: AFM images of 10% Ce sample under different annealing conditions at 900˚C, 15 minutes.

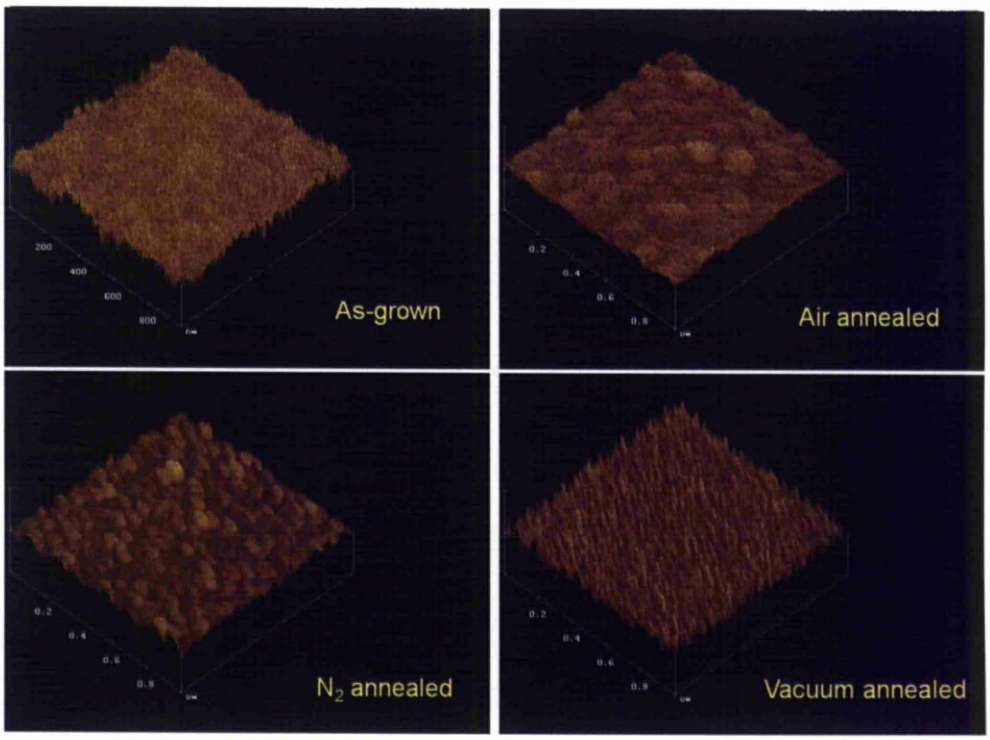

Figure 5-52: AFM images of 17% Ce sample under different annealing conditions at 900˚C, 15 minutes.

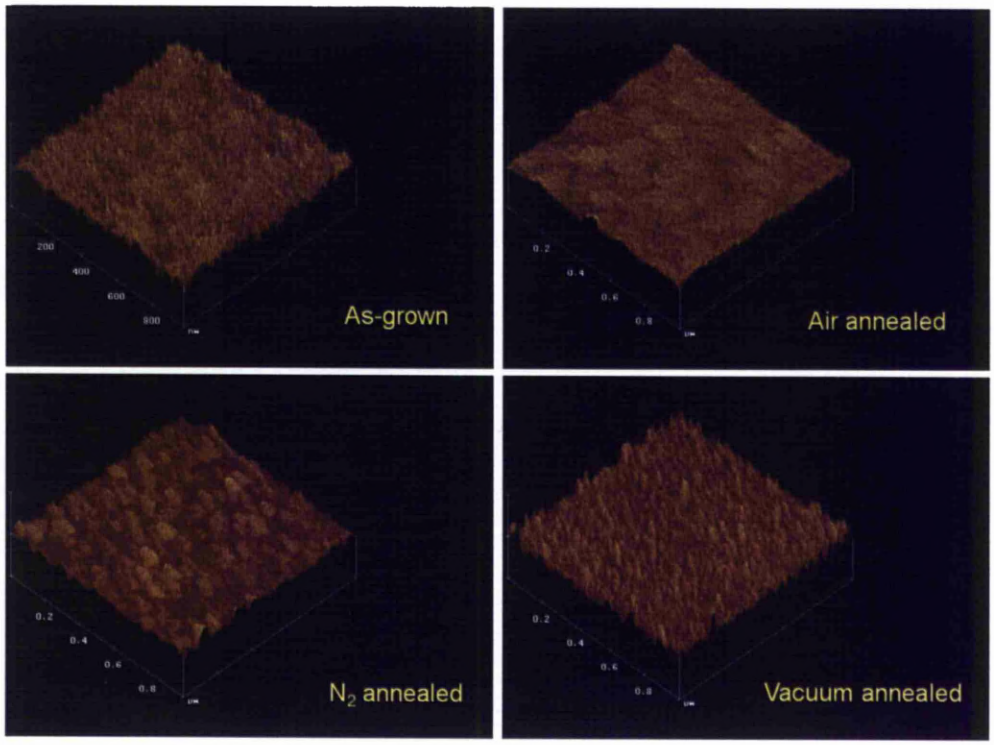

Figure 5-53: AFM images of 34% Ce sample under different annealing conditions at 900˚C, 15 minutes.

Table 5-10: Summary of surface roughness measurements from all samples under different annealing conditions at 900˚C, 15 minutes.

Surface roughness Ra (nm)				
Cerium content	As-grown	Air annealed	N2 annealed	Vacuum annealed
5%	0.491	0.561	0.728	0.926
8%	0.275	0.369	0.416	0.482
10%	0.378	0.482	0.669	n/a
17%	0.484	0.545	0.578	0.888
34%	0.512	0.513	0.578	0.656

The AFM images above from all samples indicate that the films are smooth and pin hole free after annealing. The roughness is found to be significantly smaller than the overall thickness of the actual film, which means that annealed films are quite smooth. As can be seen from Table 5-10, a consistent trend is observed for each of the different cerium concentrations, the surface roughness is lowest for air-annealed films and highest for vacuum-annealed ones. In terms of surface topography, large "islands" are seen for the air-annealed samples, while columnar structures are observed for the vacuum-annealed ones. In all cases, the N_2-annealed examples show a trend somewhere in between these two other annealing environments.

From these observations, it is reasonable to hypothesise that the surface roughness is inversely proportional to the oxygen partial pressure within the annealing environment. This hypothesis is supported by XRD data presented previously about the influence of annealing environments on the crystallite sizes. One likely reason for this phenomenon is due to possible different crystallisation pathways involved during the transitions of the films from amorphous state to polycrystalline structures.

5.6 Effect of film thickness to electrical properties

The dependence of dielectric constant on film thickness was reported in [28] for Al_2O_3 and stimulated for materials with very high-k values such as $(Ba,Sr)TiO_3$ in [29]. Some recent studies also confirm such dependence for epitaxial $SrTiO_3$ [30] or epitaxial ZrO_2 [31]. From these studies, a common observation was found that when the film thickness decreases, the dielectric constant also decreases from its "bulk" value though with different trends. The reason for this behaviour in thin film was explained either because of the film quality degradation with decreasing thickness [28] or an intrinsic effect due to the presence of a film surface without taking into account film quality change [29] among other hypotheses. Whatever the true and dominant reasons for this phenomenon, it is important to realise about such existing effect to the film's permittivity. As discussed previously in chapter 2, scalability is one of the key factors to assess any high-k materials. In contrast to SiO_2 which is an amorphous material and hence has an unchanged permittivity, most of the potential high-k oxides investigated so far are crystalline ones, including the Ce-doped hafnia in this research. It is well-known that when the thickness changes, the crystal structure, phase stability and other related properties will also change (see also chapter 2 for examples of pure ZrO_2). This, in turn, will have a direct effect to the dielectric constant, which is strongly dependent on the crystal structure and phase composition of such crystalline materials. As a result, in order to maintain a good scaling demand, it is of great concern to understand the behaviour of any high-k material at different physical thickness.

In an attempt to find out if such a strong dependence of permittivity on thickness exists with these Ce-doped hafnia films, a set of samples containing approximately 10.5 % Ce with various thicknesses (see chapter 4 for more details) were subjected to vacuum annealing at 800 °C in 10 minutes. XRD analysis and electrical characterisations were carried out to investigate whether any influence of film thickness on dielectric constant could be observed and if any, to which extent it might affect to the potential scalability of the film.

5.6.1 Phase and crystal structure analysis

Figure 5-54 shows the XRD spectra of three vacuum annealed 10.5% Ce samples, followed by a summarised peak analysis in Table 5-11. Because the other two films are quite thin (thickness below 10 nm); their XRD spectra and related crystal analysis are not available.

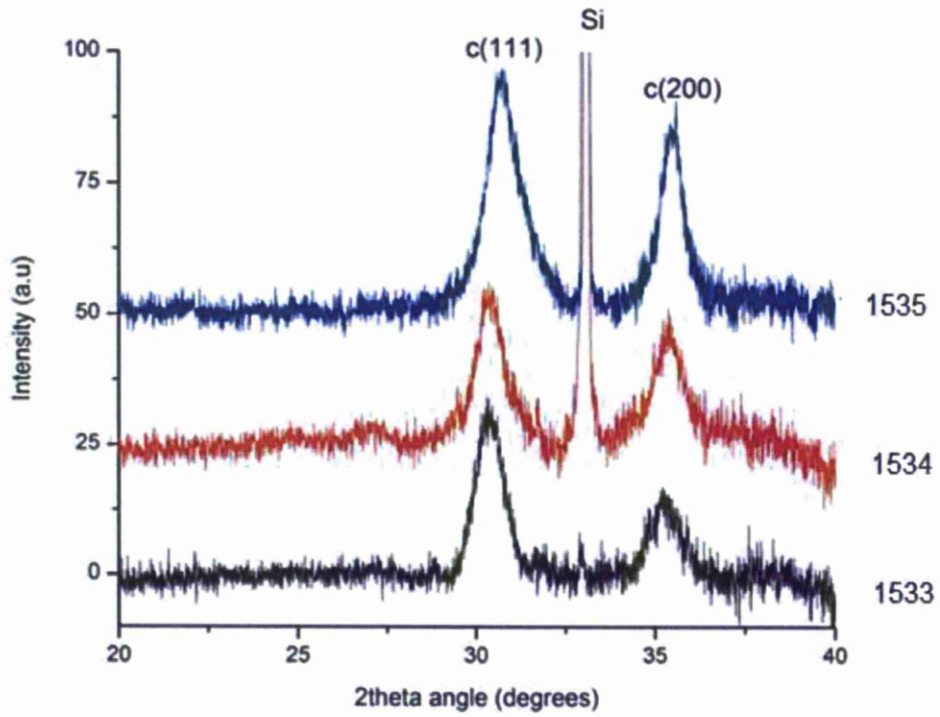

Figure 5-54: XRD spectra of vacuum annealed 10.5% cerium films (800 °C, 10 minutes) with varying thicknesses.

Table 5-11: Summarised crystal structure analysis for vacuum annealed samples at 800 °C, 10 minutes together with their respective thickness.

Sample	Thickness (nm)	2theta (degs)	Crystallite size (nm)	d-spacings (Å)	Unit cell (Å)
1531	2.5	n/a	n/a	n/a	n/a
1532	6.0	n/a	n/a	n/a	n/a
1533	10.5	30.38	6.87	2.94	5.10
1534	16.0	30.38	9.11	2.94	5.10
1535	19.5	30.76	7.15	2.91	5.03

As can be seen from the figure and table above, sample 1533 and 1534 show that their phases are identical with the reference cubic data while sample 1535 depicts a high distortion from that structure. Accordingly, the unit cell of sample 1535 is much smaller compared to the other two. In terms of crystalline size, sample 1533 and 1535 are quite similar while sample 1534 shows a higher value.

The XRD results obtained for these three samples are quite interesting and may be suggestive of some hidden details about the phase evolution. Because the difference in thickness between sample 1533 and 1534 is quite large, it is thought that they should have some distinguishable features in terms of their structures. An effort to find out whether any such difference can be observed thus is expectedly to appear in their Raman spectra. Figure 5-55 shows Raman spectra for these 3 samples (after background subtraction). As can be seen from these Raman spectra, these three samples in fact have quite different main feature related to their "cubic phase" within the wavenumber range between 600 cm^{-1} and 700 cm^{-1} (see section 5.2 for detailed discussion). After deconvolution process, it is revealed that this main feature from these 3 samples is a product of merging from two subordinate peaks at approximately 620 cm^{-1} and 665 cm^{-1} respectively but with different proportions. While sample 1533 has the highest contribution from the peak at 665 cm^{-1}, sample 1533 has the highest fraction of the peak at 620 cm^{-1} and sample 1534 stays in-between these two extremes. As mentioned in section 5.2, the peak at 665 cm^{-1} can be assigned to the vibrational mode of tetragonal and the one at 620 cm^{-1} was assigned as vibrational mode of stabilised cubic form according to Kim et al [14].

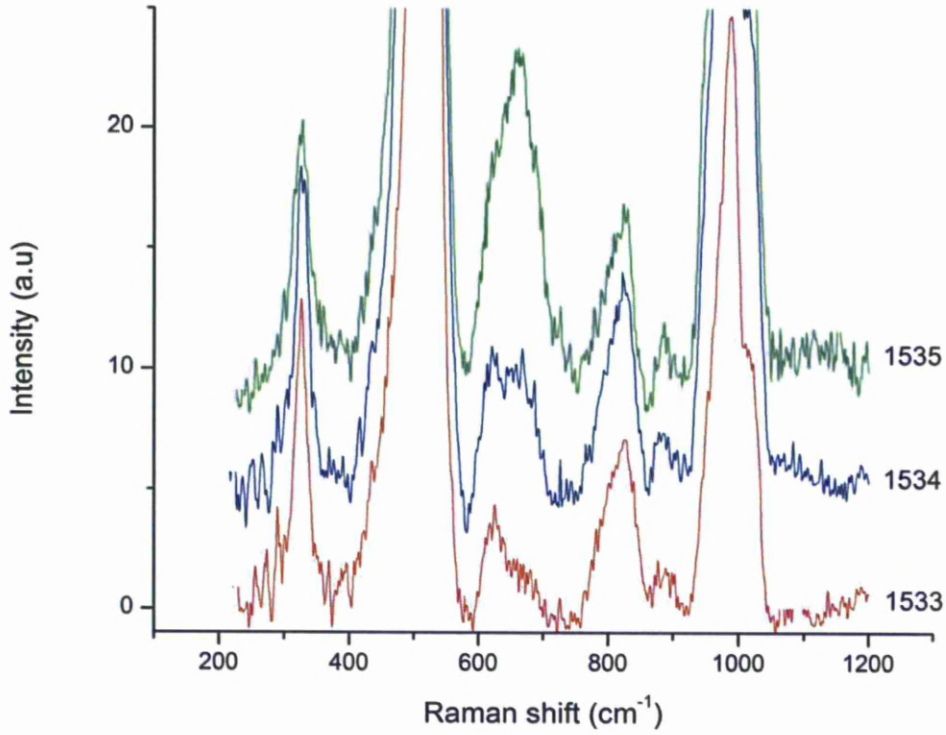

Figure 5-55: Raman spectra for vacuum annealed samples at 800 °C, 10 minutes.

Therefore, based on these Raman spectra in Figure 5-55, it can be concluded that while the dominant phase in sample 1535 is some form of tetragonal, the main phase existing within sample 1533 is very likely a cubic structure. Sample 1534 adopts a mix of these two phases although its XRD diffraction pattern is identical to the one from sample 1533.

5.6.2 Electrical characterisations

The electrical characterisations for this set of films were carried out in the same procedure described previously for other samples. The results for all films from this vacuum annealed sample will be shown in the following figures, together with summarised key results extracted from these C-V and I-V curves presented in Table 5-12.

Table 5-12: Summarised data for electrical measurements from different vacuum annealed samples at 800 °C in 10 minutes.

Sample	Thickness (nm)	k (100KHz)	J (A/cm2) at -1 MV/cm	J (A/cm2) at 1 MV/cm	ΔV hysteresis at midgap
1531	2.5	4.3	2.26E-05	2.50E-03	0.05
1532	6.0	33	1.18E-03	3.24E-03	0.3
1533	10.5	34	6.39E-05	4.34E-05	0.6
1534	16.0	23	4.09E-04	1.29E-03	0.8
1535	19.5	30	2.81E-04	6.51E-03	0.2

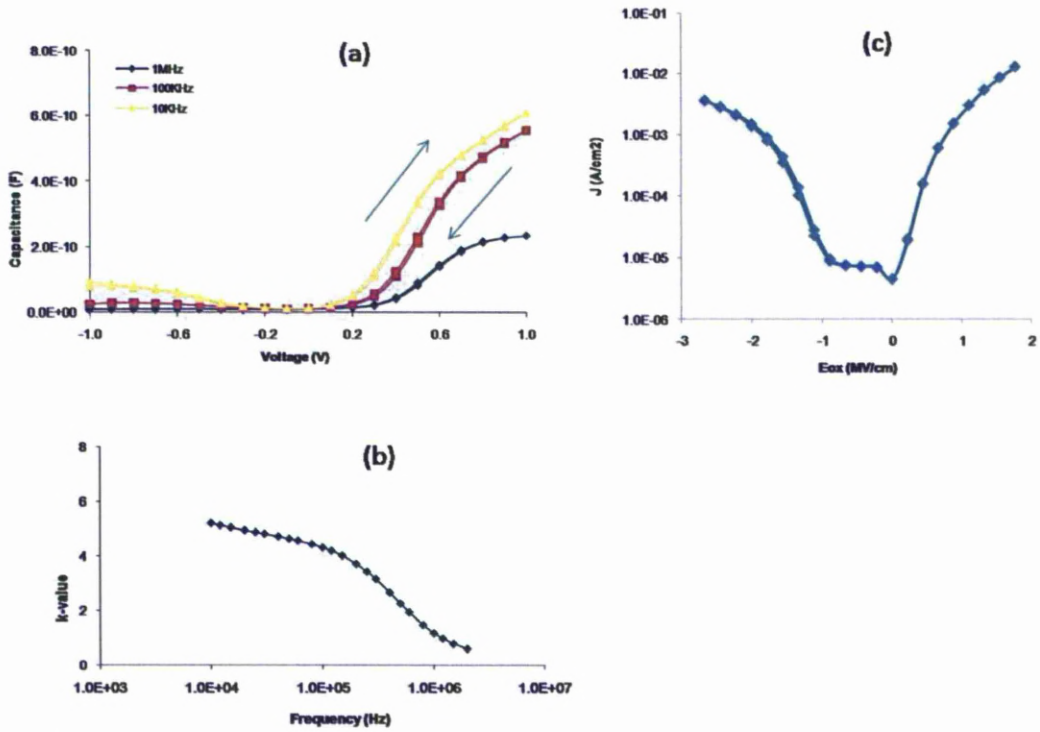

Figure 5-56: C-V curves, (b): k-f plot and (c): leakage current density against electric field strength for 1531 vacuum annealed sample at 800 °C, 10 minute.

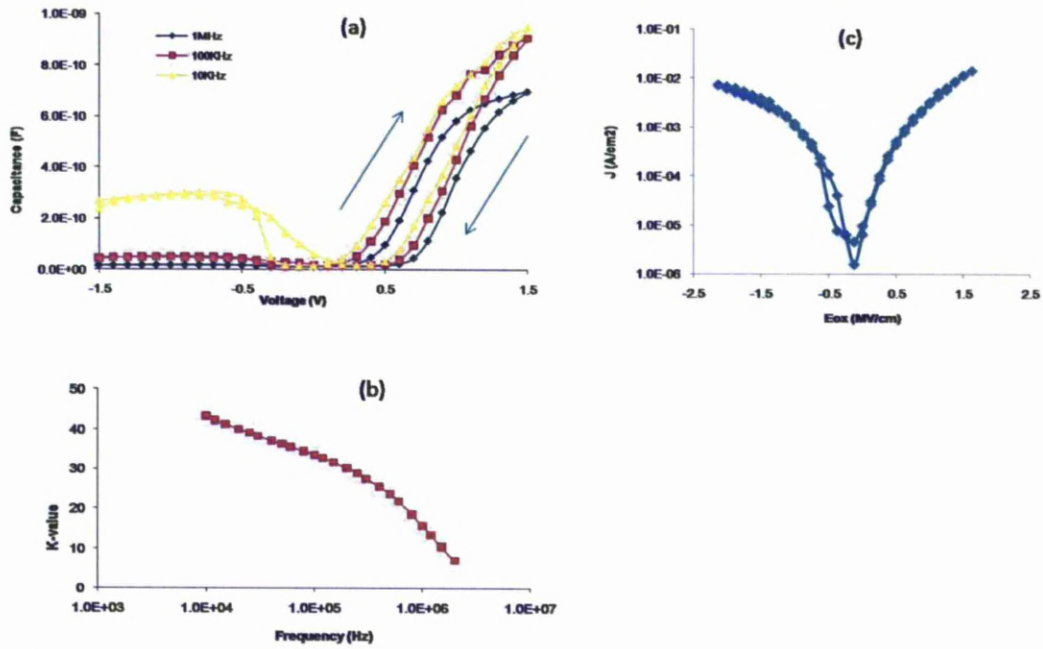

Figure 5-57: C-V curves, (b): k-f plot and (c): leakage current density against electric field strength for 1532 vacuum annealed sample at 800 °C, 10 minute.

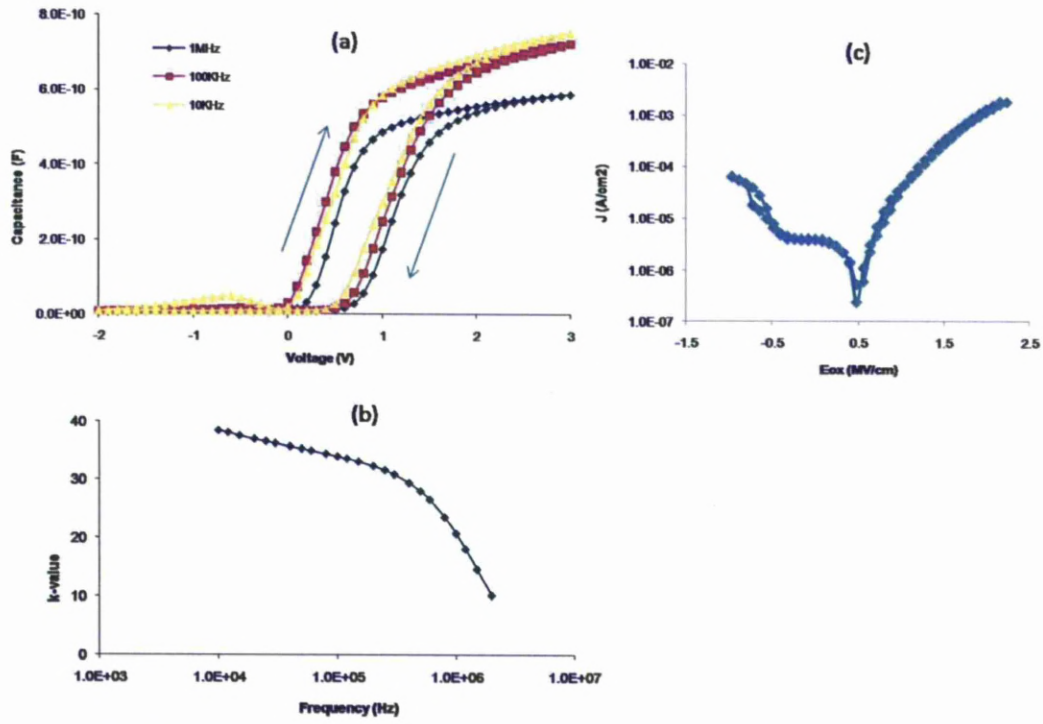

Figure 5-58: C-V curves, (b): k-f plot and (c): leakage current density against electric field strength for 1533 vacuum annealed sample at 800 °C, 10 minute.

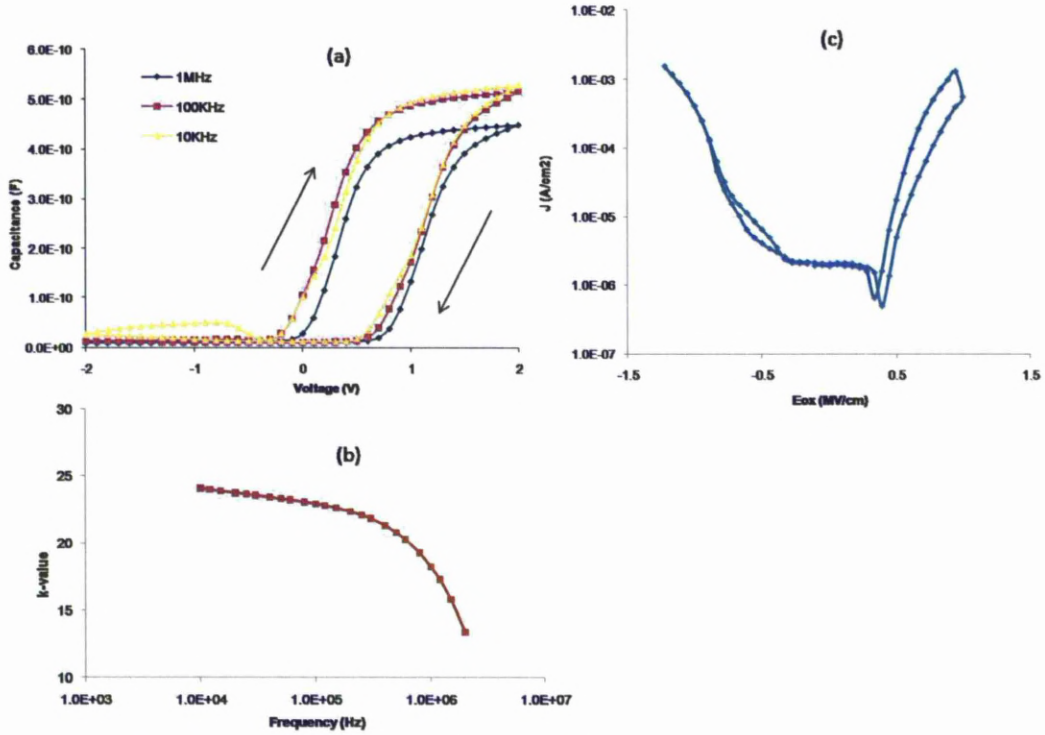

Figure 5-59: C-V curves, (b): k-f plot and (c): leakage current density against electric field strength for 1534 vacuum annealed sample at 800˚C, 10 minute.

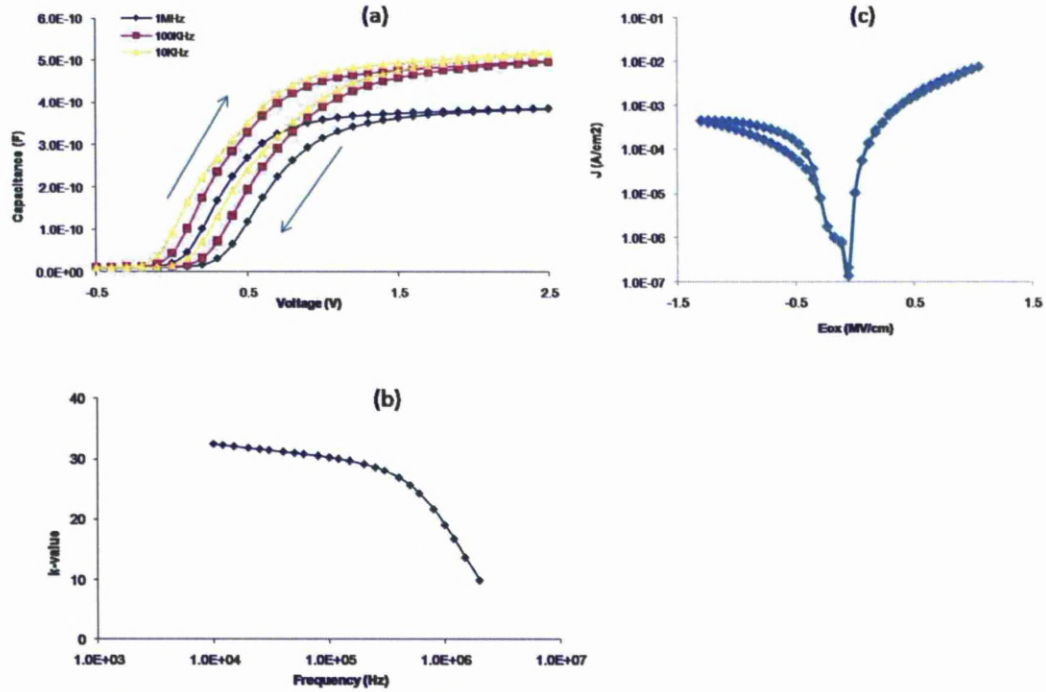

Figure 5-60: C-V curves, (b): k-f plot and (c): leakage current density against electric field strength for 1535 vacuum annealed sample at 800˚C, 10 minute.

As can be seen from the electrical data presented in all the C-V plots above, for sample 1531, 1532 and 1533, they show varying degrees of frequency dispersion at 10 kHz. The reason for that behaviour remains a subject of further investigation though it might be that at such small thickness range, the films might behave differently from their thicker counterparts. This is also supported by the fact that none of these samples show clear saturation in the accumulation regime, especially at 10 and 100 kHz.

Except sample 1531 which shows a very low k-value likely due to the fact that it is extremely thin, all the other samples (with the exception of sample 1534) show quite a stable dielectric constant and in very good agreement with the values obtained from the electrical characterisation of previous vacuum annealed samples in section 5.4. It is still not clear why a drop in permittivity observed for this specific thickness However, as discussed previously about the Raman spectra of 3 thickest samples, a possible explanation can be deduced if the phase composition of this sample is concerned. Given the fact that the other two next to this sample mainly just contain a single phase, it can be proposed that the mix of phases in this 1534 sample might have some adverse effects to the overall permittivity of the film and hence, cause this unexpected drop. However, the overall trend for all samples suggests that in terms of scalability, it is reasonable to expect a stable dielectric constant from this 10.5% Ce-doped Hf-oxide sample between quite a good range of physical thickness (6.0 nm ~ 23 nm).

In terms of leakage current density and fixed oxide charges, the data obtained from electrical measurement do not seem to suggest any sensible relationship between the physical thicknesses of the films and their corresponding electrical properties. Hence, there is no clear conclusion can be derived for the dependence of these parameters upon film thickness.

5.7 Chapter summary

Results of phase stabilisation and crystal structure analysis of samples covering the Ce doping range between 5% and 34% are presented for three different annealing environments: air, N_2 and vacuum. The effect of cerium in stabilising the higher-k phase in hafnia is confirmed by the study of XRD and Raman data for annealed films at 900 °C in 15 minutes. Of all samples, the films with 10% and 34% Ce are found to contain a single stabilised phase regardless of annealing environments or temperatures. On the other hand, samples with 5%, 8% and 17% are found to adopt a mix of monoclinic and the stabilised phase. The proportion of the monoclinic phase for each of those samples is dependent on the annealing environments and cerium doping levels. Determination of the stabilised phase in annealed samples based on the combination of XRD and Raman analysis suggests that the crystal structure adopts some form of "metastable tetragonal", although this structure resembles very closely to the high temperature cubic phase of pure HfO_2. Of all cerium concentrations, the sample with 10% Ce is demonstrated to have the most distinct structure compared to the others, particularly under vacuum annealing condition. In terms of annealing environments, film microstructure and surface roughness are also found strongly dependent on the partial oxygen pressure within annealing conditions. Results from MEIS and TEM demonstrates that only films annealed in vacuum show no or little interactions with the silicon substrate whereas films annealed in N_2 show significant intermixing and internal oxidation with the substrate, resulting in substantial interfacial increase. The influence of annealing environments on film roughness is found to be highest for vacuum annealed samples and lowest for air annealed ones, with N_2 annealed examples somewhere in the middle.

Electrical characterisations were firstly carried out to investigate the dielectric behaviour of films containing approximately 10% Ce. N_2 and vacuum annealed films were measured to investigate the dependence of their electrical properties on the annealing conditions at 900 °C in 15 minutes. Results from this study reveal that both annealed samples show significant improvements in terms of fixed oxide charges and interface states compared to the as-grown example.

However, while the vacuum annealed film shows an enhancement in permittivity (k~34) compared to the as-deposited one (k~29) at 100 kHz, the N_2 annealed film does not show any improvement. The dielectric constant for the vacuum annealed film is found to be in good agreement with a theoretical value predicted for stabilised tetragonal Ce-doped HfO_2 with a similar cerium doping dose. The leakage current density in vacuum annealed film is found to be higher than the as-grown one and is attributed to the leakage pathways induced by the crystallisation. On the other hand, the N_2 annealed film show a lower leakage current density compared to the as-deposited example and can be explained by the fact that a thicker interlayer is observed after N_2 annealing. Following these results, another set of vacuum annealed films at 800 °C from a sample with approximately 10.5% Ce was measured electrically to investigate the effect of annealing duration between 1 and 100 minutes to the electrical properties. The results from this study show that some of these films demonstrating quite good dielectric performance. Film annealed for 5 minutes was found to yield a dielectric constant about 38 while the one annealed for 100 minutes even showed a higher k-value of 44. The exact reason why these two show superior permittivity compared to other films annealed in different durations is still not clear as the phase and crystal structure analysis for this set of films seemingly do not hint any clear explanation.

A set of 10.5% Ce films with varying thickness (2.5 nm~19.5 nm) was also subjected to vacuum annealing at 800 °C in 10 minutes to study the effect of physical film thickness to the dielectric properties. Except for the thinnest film and another one with the thickness 16 nm, all other three samples show comparable permittivity (30~34), which is in the range of predicted k-value from the preceding electrical characterisations of 10% Ce vacuum annealed sample. Phase analysis from XRD and Raman from three thickest films is suggestive of an effect from the dominant stabilised phase, which is likely responsible for a drop in permittivity from the sample 16 nm thick. The overall results from this study indicates a good scaling potential for this Ce-doped hafnia vacuum annealed films with approximately 10.5% Ce over a range of investigated thickness, which is also a promising proposition to the use of this high-k oxide when the scalability is concerned.

References

1. Cockayne, E. (2008) Effect of ionic substitutions on the structure and dielectric properties of hafnia: A first principles study. *Journal of Applied Physics,* **103**.
2. Fischer, D. and Kersch, A. (2008) The effect of dopants on the dielectric constant of HfO_2 and ZrO_2 from first principles. *Applied Physics Letters,* **92** (1).
3. Lee, C. K., Cho, E. N., Lee, H. S., Hwang, C. S. and Han, S. W. (2008) First-principles study on doping and phase stability of HfO_2. *Physical Review B,* **78** (1).
4. Govindarajan, S., Boscke, T. S., Sivasubramani, P., Kirsch, P. D., Lee, B. H., Tseng, H. H., Jammy, R., Schroder, U., Ramanathan, S. and Gnade, B. E. (2007) Higher permittivity rare earth doped HfO_2 for sub-45-nm metal-insulator-semiconductor devices. *Applied Physics Letters,* **91** (6).
5. Passerini, L. (1930) Isomorphism among oxides of the quadrivalent metals : the systems CeO_2-ThO_2, CeO_2-ZrO_2, and CeO_2-HfO_2. *Gazzetta Chimica Italiana,* **60**, 762-776.
6. Chalker, P. R., Werner, M., Romani, S., Potter, R. J., Black, K., Aspinall, H. C., Jones, A. C., Zhao, C. Z., Taylor, S. and Heys, P. N. (2008) Permittivity enhancement of hafnium dioxide high-k films by cerium doping. *Applied Physics Letters,* **93** (18).
7. Tani, E., Yoshimura, M. and Somiya, S. (1983) Revised phase diagram of the system ZrO_2-CeO_2 below 1400 degrees C. *Journal of the American Ceramic Society,* **66** (7), 506-510.
8. Schmid, H. K. (1987) Quantitative analysis of polymorphic mixes of zirconia by X-ray diffraction. *Journal of the American Ceramic Society,* **70** (5), 367-376.
9. Zhao, X. and Vanderbilt, D. (2002) First-principles study of structural, vibrational, and lattice dielectric properties of hafnium oxide. *Physical Review B,* **65** (23), 233106.
10. Yashima, M., Takahashi, H., Ohtake, K., Hirose, T., Kakihana, M., Arashi, H., Ikuma, Y., Suzuki, Y. and Yoshimura, M. (1996) Formation of metastable forms by quenching of the HfO_2-$RO_{1.5}$ melts (R=Gd,Y and Yb). *Journal of Physics and Chemistry of Solids,* **57** (3), 289-295.
11. Fujimori, H., Yashima, M., Sasaki, S., Kakihana, M., Mori, T., Tanaka, M. and Yoshimura, M. (2001) Cubic-tetragonal phase change of yttria-doped hafnia solid solution: high-resolution X-ray diffraction and Raman scattering. *Chemical Physics Letters,* **346** (3-4), 217-223.
12. Michel, D., Perezyjorba, M. and Collongues, R. (1976) Study by Raman-spectroscopy of order-disorder phenomena occurring in some binary oxides with flourite-related structures. *Journal of Raman Spectroscopy,* **5** (2), 163-180.
13. Fujimori, H., Yashima, M., Sasaki, S., Kakihana, M., Mori, T., Tanaka, M. and Yoshimura, M. (2001) Internal distortion in ceria-doped hafnia solid solutions: High-resolution X-ray diffraction and Raman scattering. *Physical Review B,* **64** (13).

14. Kim, D. J., Jang, J. W. and Lee, H. L. (1997) Effect of tetravalent dopants on Raman spectra of tetragonal zirconia. *Journal of the American Ceramic Society,* **80** (6), 1453-1461.
15. Sheu, T. S., Tien, T. Y. and Chen, I. W. (1992) Cubic-to-tetragonal (t') transformation in zirconia-containing systems. *Journal of the American Ceramic Society,* **75** (5), 1108-1116.
16. Yashima, M., Morimoto, K., Ishizawa, N. and Yoshimura, M. (1993) Diffusionless tetragonal-cubic transformation temperature in zirconia-ceria solid solutions. *Journal of the American Ceramic Society,* **76** (11), 2865-2868.
17. Li, P. and Chen, I. W. (1994) Effect of dopants on zirconia stabilization - An X-ray Absorption study .2. Tetravalent dopants. *Journal of the American Ceramic Society,* **77** (5), 1281-1288.
18. Bouvier, P., Gupta, H. C. and Lucazeau, G. (2001) Zone center phonon frequencies in tetragonal zirconia: lattice dynamical study and new assignment proposition. *Journal of Physics and Chemistry of Solids,* **62** (5), 873-879.
19. Naumenko, A. P. (2008) Vibrational analysis and Raman spectra of tetragonal zirconia. *Physics and Chemistry of Solid States,* **9** (1), 121-125.
20. Gouadec, G. and Colomban, P. (2007) Raman Spectroscopy of nanomaterials: How spectra relate to disorder, particle size and mechanical properties. *Progress in Crystal Growth and Characterization of Materials,* **53** (1), 1-56.
21. Teufer, G. (1962) Crystal structure of tetragonal ZrO_2. *Acta Crystallographica,* **15** (Nov), 1187.
22. Duwez, P. and Odell, F. (1950) Phase relationships in the system zirconia-ceria. *Journal of the American Ceramic Society,* **33** (9), 274-283.
23. Mitrovic, I. Z. Metrology of oxides using C-V, I-V & C-t techniques.
24. Hall, S. (2000) Lecture: MOS/MIS Dielectric characterisation.
25. Foster, A. S., Gejo, F. L., Shluger, A. L. and Nieminen, R. M. (2002) Vacancy and interstitial defects in hafnia. *Physical Review B,* **65** (17).
26. Ganduglia-Pirovano, M. V., Hofmann, A. and Sauer, J. (2007) Oxygen vacancies in transition metal and rare earth oxides: Current state of understanding and remaining challenges. *Surface Science Reports,* **62**, 219-270.
27. Robertson, J. (2006) High dielectric constant gate oxides for metal oxide Si transistors. *Reports on Progress in Physics,* **69** (2), 327-396.
28. Birey, H. (1977) Thickness dependence of dielectric constant and resistance of Al_2O_3. *Journal of Applied Physics,* **48** (12), 5209-5212.
29. Natori, K., Otani, D. and Sano, N. (1998) Thickness dependence of the effective dielectric constant in a thin film capacitor. *Applied Physics Letters,* **73** (5), 632-634.
30. Boesch, D. S., Son, J., LeBeau, J. M., Cagnon, J. and Stemmer, S. (2008) Thickness dependence of the dielectric properties of epitaxial $SrTiO_3$ films on (001)Pt/$SrTiO_3$. *Applied Physics Express,* **1** (9).
31. Zhou, Y., Sasaki, K., Kawae, T. and Morimoto, A. (2009) Thickness dependence of the structural and dielectric properties of epitaxial ZrO_2 films grown by limited reaction sputtering. *Journal of Physics D-Applied Physics,* **42** (20).

Chapter 6 CONCLUSIONS AND RECOMMENDATIONS FOR FUTURE WORKS

6.1 Summary of key results and main conclusions

The studies presented in this thesis are mainly concerned with issues relating to stabilising the higher-k phases in hafnia film by cerium doping as a potential high-k oxide in future CMOS devices. The focus is on (i): feasibility of the growth of Ce-doped Hf-oxide films with varying cerium concentrations by using the state-of-the-art LIALD technique and (ii): phase and crystal structure analysis of annealed films at various temperatures and annealing environments over a wide range of cerium doping levels. In addition, specific considerations are concentrated on the electrical characterisations of films with approximately 10% Ce annealed in vacuum condition.

The study of the LIALD growth and its associated parameters, succeeding the separate studies of each individual precursor source with co-reactant as ozone, revealed that the cerium doping dose for this ternary oxide film could be controlled and altered by varying the ratio of cerium ALD cycle against hafnium ones, which was illustrated by MEIS data analysis. Altering the ALD cycle ratio between these two precursors as 1/2, 1/4, 1/9, 1/12 and 1/19 resulted in the cerium incorporation into the films as 34%, 17%, 10%, 8% and 5% respectively. A linear relationship between the ALD cycle ratio and cerium concentrations within the films was clearly observed. This linear relationship is indicative of the ALD nature of the growth process for this ternary oxide system though the growth of CeO_2 was demonstrated not a strict ALD process on its own. Another set of samples were grown with a much narrower range of cerium concentrations targeting compositions close to 10% with the purpose of carrying out more detailed investigations of electrical properties of these materials. The ALD cycle ratio for the second set was set as 1/11, 1/9 and 1/7 respectively. However, MEIS composition analysis from this set showed that only one of them (1/11) reached the expected concentration predicted from the linear relationship observed in the first set of samples. The other two showed some deviations from their expected cerium contents. The cerium contents were found to be 7.5% and 10.5% for the sample with ALD cycle ratio 1/9 and 1/7 respectively.

Nevertheless, the sample with the ALD cycle ratio 1/7 was shown to contain approximately 10.5% Ce, which was close to the target composition and hence useful for detailed electrical measurements for films subjected to varying annealing parameters and films with different thicknesses. The technique was proven capable of growing such films in a quite controllable manner though some inevitably unexpected deviations existed from batch to batch. However, this was very likely due to some problems associated with the reactor behaviour rather than the LIALD growth process.

Results of phase stabilisation and crystal structure analysis of samples covering the Ce doping range between 5% and 34% were established for three different annealing environments: air, N_2 and vacuum. The annealing study was initially carried out in air over a wide range of temperatures from 600°C to 1000°C. Phase analysis conducted for air annealed films confirmed the effect of cerium as a stabiliser and its interplay with annealing temperature. Based on the XRD and Raman analysis of these air annealed samples, the stabilised phases existing in different films were shown being slightly different with various degrees of distortion from a reference high temperature cubic phase. This distortion was demonstrated to be dependent on both cerium doping levels and annealing temperatures. It can be concluded from this air annealing study that the stabilised phase found in all samples adopted some form of "metastable tetragonal" rather than the reference cubic structure though indistinguishable from XRD results.

The influence of cerium on higher-k phase stabilisation in hafnia was then specifically focused on annealed films at 900°C in 15 minutes under different annealing environments. The reason this annealing condition was chosen for N_2 and vacuum study because they provided a comparable condition to the typical annealing step in CMOS flow process. Therefore, films annealed in vacuum and N_2 could be subjected to subsequent electrical tests. Of all samples, the films with 10% and 34% Ce were found to contain a single stabilised phase similar to the one identified in previous air annealing study, regardless of annealing environments or temperatures. On the other hand, samples with 5%, 8% and 17% were discovered to adopt a mix of monoclinic and the stabilised phase.

It was found that the fraction of monoclinic in these three samples decreased in a descending order of air, N_2 and vacuum (with the exception of 5% sample, which showed an equivalent fraction for air and vacuum). Determination of the stabilised phase in annealed samples based on the combination of XRD and Raman analysis suggested that the crystal structure adopted some form of "metastable tetragonal", although this structure resembled very closely to the high temperature cubic phase of pure HfO_2. The tetragonality of the stabilised phase(s) could not be accurately determined due to the nature of thin films, which gave poor signal-to-noise ratio in XRD and Raman spectra. Of all cerium concentrations, the sample with 10% Ce gave the most distinct structure compared to the others, particularly under vacuum annealing condition. This behaviour of the 10% Ce sample was in good agreement with theoretical prediction about the stabilised tetragonal phase in Ce-doped HfO_2 with doping level about 12.5%. All of these results could be drawn to some important conclusions as follows. Firstly, the effect of cerium was shown to be dependent on the annealing environments in terms of suppressing monoclinic phase at low doping levels with vacuum annealing being demonstrated to be the most effective. Beyond 10% Ce concentration, the influence of annealing environments was shown to be on the distortion of the stabilised phase, which was illustrated in the case of 10% and 34% samples. For sample with 17%, a monoclinic phase always existed regardless of annealing conditions. This irregular behaviour was attributed to the solubility limit of tetragonal phase, resulting in a phase separation to cubic and monoclinic for doping level around 17% Ce. Of all samples, the one with 10% Ce was found to be the most distorted structure from the fluorite-type cubic phase, especially in vacuum. In other words, this behaviour of 10% Ce supported the theoretical simulation about stabilising tetragonal phase in HfO_2 by doping with cerium mentioned above.

In terms of annealing environments, film microstructure and surface roughness were also found to be strongly dependent on the partial oxygen pressure within annealing conditions. Results from MEIS and TEM demonstrated that only films annealed in vacuum showed no or little interactions with the silicon substrate.

On the other hand, films annealed in N_2 showed significant intermixing and internal oxidation with the substrate, resulting in substantial interfacial increase (2.1 nm interfacial layer thickness for both as-grown and vacuum annealed, 3.7 nm thickness for N_2 annealed 10% Ce sample). The influence of annealing environments on film roughness was found to be highest for vacuum annealed samples and lowest for air annealed ones, with N_2 annealed examples somewhere in the middle.

Electrical characterisations were firstly carried out to investigate the dielectric behaviours of films containing approximately 10% Ce. N_2 and vacuum annealed films at 900°C in 15 minutes were measured to investigate the effect of phase stabilisation on their corresponding dielectric properties. Results from this study revealed that both annealed samples showed significant improvements in terms of fixed oxide charges and interface states compared to the as-grown example. Calculations of dielectric constants for these films were performed by using a simple 2-layer MOS model comprising the high-k oxide and the interlayer. However, only the vacuum annealed film showed an enhancement in permittivity (k~34) compared to the as-deposited one (k~29) at 100 kHz. The N_2 annealed film did not yield any improvement. The permittivity measured for the vacuum annealed film was found to be in good agreement with a theoretical value predicted for stabilised tetragonal Ce-doped HfO_2 with similar cerium doping level. The leakage current density in vacuum annealed film was observed to be higher than the as-grown one. This phenomenon was attributed to the leakage pathways induced by the crystallisation after annealing. On the other hand, the N_2 annealed film showed a lower leakage current density compared to the as-deposited example and could be explained by the fact that a thicker interlayer was formed after N_2 annealing. Following these results, another set of vacuum annealed films at 800°C from a sample with approximately 10.5% Ce was measured electrically to investigate the effect of annealing duration between 1 and 100 minutes on the dielectric responses. The results from this set showed that some of these films demonstrating quite good dielectric performance though an overall trend was not clearly depicted. The calculations of dielectric constant for these films were performed by using the similar model described previously.

A surprisingly high k-value of 44 was found for sample annealed in 100 minutes, followed by another one of 38 for sample annealed in 5 minutes. Another set of 10.5% Ce films with varying thickness (2.5 nm~19.5 nm) was also subjected to vacuum annealing at 800°C for 10 minutes to study the effect of physical film thickness to the dielectric properties due to the importance of scalability demand and the dependence of dielectric constant on film thickness. Except the thinnest film and another one with the thickness 16 nm, all other three samples with thickness 6.0 nm, 10.5 nm and 19.5 nm respectively showed similar permittivity to the preceding electrical characterisations for the 10% Ce vacuum annealed sample. Phase analysis from XRD and Raman from three thickest films in this set showed that all of these samples contained two phases but with different proportions. These two phases were identified as stabilised cubic and some form of tetragonal. The sample 10.5 nm thick was found to contain mostly of stabilised cubic phase with a minor fraction of tetragonal while the sample 19.5 nm thick showed an opposite trend. The sample 16.0 nm was shown to contain an equivalent fraction of both phases. This phase composition of sample 16.0 nm was thus likely responsible for an irregular result encountered from the permittivity calculation. In the case of the thinnest sample, very low k-value could be attributed to a very small thickness which could result in an abrupt change in dielectric performance. Nonetheless, it could be reasonably assumed that for this 10.5% Ce vacuum annealed sample, a good scaling capability was achievable.

6.2 Recommendations for future works

It is clear from the results and conclusions above that significant work can still be carried out in several areas. Firstly, there is scope for improving the understanding of phase stabilisation, the assignment and identification of such phase(s). More improved and more detailed of XRD spectra can be made possible by employing an X-ray source of shorter wavelength and/or utilisation of Grazing Incidence XRD. While the former can provide better peak separation especially at high 2theta angles, the latter can help reveal the crystal structure of very thin films. Because a high-k oxide film is subjected to continuous scaling, the crystal structure of thin film is important to understand and optimise the dielectric performance.

Similar improvements can also be achievable by utilising a lower wavelength UV laser, a by-pass filter capable of recording Raman shift right after the laser excitation wavelength and the use of polarised laser to suppress the strong interference from the silicon substrate. The use of polarised laser is particularly helpful to monitor separate vibrational modes of interest. Also within this scope, more experiments can be carried out over a wider range of annealing temperatures in vacuum and possibly N_2 (or any equivalent inert gas), providing that the annealing system is also improved. Because the dielectric properties for any film at a given thickness and doping level is strongly dependent on the post-growth treatment, a wider range of annealing temperatures can give many further insights about the crystallisation and consequently, its influence on dielectric characteristics. It also helps optimise the annealing conditions required to achieve the highest possible k-value for a specific doping concentration and film thickness, which i